DEPARTAMENTO DE ASTROFISICA

Universidad de La Laguna

Detección y caracterización de exoplanetas mediante el método de los tránsitos

Memoria que presenta
D. Roi Alonso Sobrino
para optar al grado de
Doctor en Ciencias Físicas.

INSTITUTO Ð ASTROFISICA Ð CANARIAS
enero de 2006

Examination date: January 16, 2005
Thesis supervisor: Juan Antonio Belmonte
Thesis co-advisor: Timothy M. Brown

©Roi Alonso Sobrino 2005
ISBN: xx-xxx-xxxx-x
Depósito legal: TF-xxxx/2006
Some of the material included in this document has been already published in *The Astrophysical Journal, Astronomy & Astrophysics, The Astronomical Journal, Astronomische Nachrichten and Astrophysics and Space Science*.

A todos aquellos que dieron su vida
por decir verdades.
A mi familia.
A Mar.

Resumen

1.- Introducción

Un *exoplaneta* o *planeta extrasolar* es un objeto, con masas por debajo del límite necesario para que se produzca la fusión termonuclear del deuterio (en la actualidad estimada en unas 13 veces la masa de Júpiter), que orbita estrellas o restos de estrellas distintos de nuestro Sol. En esta introducción, tras esta definición de exoplaneta y de otros conceptos como *Júpiteres calientes* y *Júpiteres muy calientes*, se describen las distintas técnicas existentes para la detección de estos objetos, poniendo especial énfasis a los éxitos, ventajas y desventajas de cada método. De esta forma, se pincela el método de medida de los tiempos de llegada de los pulsos procedentes de los púlsares, que permitió la detección de los primeros exoplanetas en el año 1992 (Wolszcan & Frail 1992). Desafortunadamente, la mayoría de los púlsares carecen de compañeros planetarios (Lorimer, 2001).

El método de las velocidades radiales es hasta la fecha el que ha producido mayor número de detecciones de exoplanetas. Se describen someramente cómo se realizan estas observaciones, y las amplitudes del movimiento de la estrella para objetos con masas distintas. La diversidad de exoplanetas encontrados con este método permite extraer una serie de características comunes de los exoplanetas conocidos o de las estrellas en torno a las que orbitan, tales como la fracción de éstas que poseen planetas (hasta un cierto valor inferior de la masa), la función de masas del objeto secundario, la distribución de las excentricidades, la dependencia de la metalicidad de la estrella con la tenencia de exoplanetas, o la distribución del periodo frente a la masa de estos objetos.

Se describen también en esta introducción otras técnicas de detección de exoplanetas, como las microlentes, la imagen directa, y la astrometría, destacando sus éxitos más recientes. En el año 2004, tanto las microlentes como la imagen directa han tenido sus primeras detecciones confirmadas.

El método de los tránsitos se explica con especial detalle, prestando atención a los parámetros físicos del planeta que son solamente accesibles mediante la combinación de este método con el de las velocidades radiales. Sólo con la curva de luz se pueden medir el cociente entre el radio del planeta R_p y el de la estrella R_s, la inclinación de la órbita i (o bien el parámetro de impacto b), la razón entre el radio de la órbita a y el radio de la estrella, y la densidad de la estrella. Combinando los resultados con las medidas de velocidad radial, se puede determinar además la masa exacta del planeta M_p y su densidad ρ_p. El interés por el conocimiento de estos parámetros ha motivado diversas búsquedas de exoplanetas que produzcan tránsitos. Un estudio de Brown (2001) estima los ritmos esperados de detección tanto de exoplanetas como de falsas alarmas en este tipo de búsquedas fotométricas. Para un proyecto como el STARE en un campo en el plano galáctico, estima que deberían haber 1.4 exoplanetas en tránsito y 7.2 falsas alarmas por cada 10000 estrellas observadas con una precisión mejor que 0.01 magnitudes.

El primer planeta que producía tránsitos se detectó en el 2000 (Charbonneau et al. 2000, Henry et al. 2000), si bien su descubrimiento fue realizado con el método de las velocidades radiales (Mazeh et al. 2000). Recibe el nombre de HD 209458b, y es en la actualidad el exoplaneta más estudiado y mejor conocido. Resumimos en una sección las observaciones más emblemáticas de este sistema, y los hallazgos que de estas observaciones se derivaron. De este modo, los estudios realizados por diversos equipos de investigación con el HST (Brown et al. 2001, Charbonneau et al. 2002, Vidal-Madjar et al. 2003, 2004) han permitido conocer los parámetros del planeta y de la estrella con una precisión exquisita, realizar búsquedas de hipotéticos satélites orbitando en torno al planeta así como de posibles anillos, e incluso detectar componentes de la atmósfera. Estos últimos estudios parecen probar que la alta atmósfera de HD 209458b se halla en proceso de evaporación debido a su cercanía a la estrella.

Sin embargo, parece que hay una cierta discrepancia entre el tamaño medido del exoplaneta y el que debería tener de acuerdo con los modelos de formación y evolución de exoplanetas. El radio medido para HD 209458b es entre un 20% y un 30% mayor que el predicho por estos modelos. Dedicamos una sección a abordar este tema, señalando las posibles soluciones al problema que existen en la literatura. Varias de estas soluciones implicarían que, en el caso de encontrar nuevos exoplanetas transitantes, todos deberían mostrar un tamaño mayor al estimado por los modelos, mientras que otras suponen ciertas anomalías en el caso de HD 209458b, como pudieran ser las perturbaciones producidas por un tercer cuerpo en el sistema.

Una técnica para estudiar las atmósferas de estos lejanos planetas, que ya ha sido utilizada con éxito en el caso de HD 209458b, es la espectroscopía de transmisión. Dedicamos una sección para describir esta técnica y para comparar los dos principales estudios teóricos que se han realizado encaminados a aplicar este método a los exoplanetas en tránsito: los trabajos de Seager & Sasselov (2000) y Brown (2001). Esta técnica la pondremos en aplicación durante el tránsito de Venus del 2004, tal como se describe en el Capítulo 6.

Finalmente, se pincelan en la introducción las dos hipótesis principales para explicar la formación de los exoplanetas hasta ahora detectados.

En el momento de comenzar esta tesis, tan sólo HD 209458b producía tránsitos, y ya existía controversia acerca de la explicación para su radio aparentemente grande. Se desconocía si nuevos planetas que transitasen frente a su estrella tendrían su radio incrementado frente a lo predicho por los modelos, o si tendrían un radio "normal", en cuyo caso HD 209458b sería el caso anómalo. Por ello, el objetivo principal de esta tesis fue el descubrimiento de nuevos planetas transitantes, para así poder establecer qué es lo común y qué lo anómalo en este tipo de objetos. Para cumplir con este objetivo (con el instrumento STARE descrito en el Capítulo 2), hubo que superar una serie de obstáculos, como el establecimiento de unas técnicas de seguimiento que permitiesen descartar los falsos positivos (configuraciones estelares que producen señales fotométricas similares a las de un planeta en tránsito). Estas técnicas se describen en el Capítulo 3 y se proporciona una cadena ordenada de pruebas (un protocolo) que ha de superar un candidato para ser confirmado como un exoplaneta transitante. El Capítulo 4 describe una campaña de observación con el instrumento STARE en la constelación de Lyra, y el resultado de las observaciones de seguimiento en los 16 candidatos obtenidos. Uno de los candidatos es el primer exoplaneta descubierto con el método de los tránsitos en torno a una estrella relativamente brillante, TrES-1. Todas las observaciones que condujeron a esta conclusión se describen en el Capítulo 5. Finalmente, la oportunidad de aplicar la técnica de la espectroscopía de transmisión en un planeta cuya atmósfera ha sido atravesada por sondas espaciales vino dada con el tránsito de Venus de 2004. Estas observaciones y sus resultados preliminares se describen en el Capítulo 6.

2.- El instrumento STARE

Este capítulo está dedicado a la descripción del instrumento STARE, un pequeño telescopio de diseño Schmidt con una apertura de 102 mm y una distancia focal efectiva de 296 mm, y del modo en que los datos provenientes de este instrumento son tratados para buscar las señales producidas por exoplanetas en tránsito. El instrumento toma datos (una imagen cada 2 minutos) de forma semi-automática de grandes regiones del firmamento (6.1×6.1 grados^2) en las que estén contenidas varias decenas de miles de estrellas. Se observa el mismo campo durante largos periodos de más de un mes de observación. Los datos son analizados utilizando la moderna técnica de la sustracción de imágenes (Alard 2000), en la que a una imagen de referencia tomada en buenas condiciones fotométricas se le sustrae cada una de las imágenes (debidamente alineadas y compensadas de posibles cambios en la PSF de las estrellas), y posteriormente se realiza fotometría de apertura en las imágenes residuo que se obtienen tras esta sustracción.

Las curvas de luz de las estrellas que se obtienen poseen aún efectos instrumentales que se corrigen mediante el uso de la técnica de descomposición en valores singulares (SVD, las siglas en inglés de *Singular Value Decomposition*). En este capítulo se describe dicha técnica.

Finalmente, se realiza un modelado de las fuentes de ruido presentes en los datos del instrumento, para evaluar la bondad tanto de la instrumentación como de los algoritmos de análisis de datos utilizados.

Las ventajas de utilizar otros instrumentos similares en distintos emplazamientos se perfilan al final del capítulo, lo que justifica que el instrumento STARE sea en la actualidad un nodo de la red de tres telescopios TrES (Transatlantic Exoplanet Survey). Los otros dos nodos se encuentran en Arizona y California, ambos en los Estados Unidos de América.

3.- Las técnicas de seguimiento

En este capítulo proponemos, estudiamos y revisamos las distintas técnicas que se pueden utilizar para esclarecer la verdadera naturaleza de los objetos que producen señales fotométericas similares a las de un planeta transitante. Existen diversos tipos de sistemas estelares eclipsantes que pueden mimetizar la señal de un exoplaneta. La confirmación última de un exoplaneta se puede realizar tan sólo en unos pocos telescopios en el mundo, por lo que se hace necesario desarrollar otros métodos menos costosos que permitan descartar la mayoría de los candidatos.

En primer lugar se describen las distintas configuraciones estelares que pueden resultar en falsos positivos de una búsqueda fotométrica de exoplanetas mediante el método de los tránsitos. Estos falsos positivos pueden ser sistemas estelares binarios con cocientes de sus radios similares a los provocados por un exoplaneta gigante y una estrella de tipo solar, o bien estar causados por dos estrellas con eclipses rasantes. Una tercera opción es que se traten de sistemas triples (o múltiples), en los que la luz proveniente de una tercera estrella diluye la profundidad de los eclipses de un sistema eclipsante. Esta tercera estrella puede estar físicamente ligada al sistema binario, o bien estar en la línea de visión del sistema eclipsante.

Como primer método, se describe el análisis cauteloso de la curva de luz original. Este análisis conlleva en primer lugar un estudio de la modulación de la curva de luz fuera de los periodos de eclipse. Los sistemas binarios típicamente producen fuerzas de marea que deforman la estrella primaria. Por consiguiente, la curva de luz fuera del eclipse posee una modulación sinusoidal con un periodo que es la mitad del orbital. Describimos la técnica utilizada para discernir esta señal. En segundo lugar, se estudia la forma del tránsito en detalle. Mediante un ajuste por mínimos cuadrados a una función en la que los parámetros libres son la duración total del eclipse, la de la parte plana de éste, su profundidad, y su punto central, es posible estimar la densidad promedio de la estrella central del sistema. Si esta densidad es muy diferente de la estimada por otros métodos (por ejemplo, la resultante de una estrella de secuencia principal con una temperatura efectiva idéntica a la estrella, y que haya sido medida bien mediante fotometría o mediante espectroscopía), se puede descartar o restar prioridad al candidato.

La medida de la dependencia de la profundidad de los eclipses con el color puede ser indicativa de un sistema estelar triple no resuelto espacialmente. En la sección 3.3, se describen en detalle las variaciones en el color del sistema esperadas, para estrellas de secuencia principal. Estas variaciones, en caso de existir, permiten descartar al candidato. En el caso de que el cambio en color entre el sistema fuera del eclipse y dentro del eclipse no sean detectables, señalamos las distintas restricciones que se pueden poner a un hipotético sistema no resuelto. Se discuten en esta sección dos casos: dos estrellas eclipsantes idénticas con eclipses diluidos por una tercera estrella en la línea de visión (no necesariamente parte del sistema), y dos estrellas eclipsantes en las que el eclipse secundario no es detectado en los datos, también afectadas por la contribución de una tercera estrella. Este segundo caso es harto más complicado de ser detectado mediante esta técnica desde observatorios en tierra, pues los cambios en color son del orden de la milimagnitud.

Si bien los sistemas triples físicamente ligados son complicados de resolver mediante técnicas de alta resolución espacial, la probabilidad de detectar una tercera estrella fortuitamente alineada con el sistema eclipsante es alta cuando se pasa de un telescopio con una PSF de $\sim 15''$ a las modernas técnicas de óptica adaptativa, en la que se pueden alcanzar PSFs mejores que $0.2''$. Proporcionamos una estimación de esta probabilidad, y mostramos un caso de un candidato en la constelación del Cisne, observado con óptica adaptativa en el telescopio de 4.2 m William Herschel (WHT, situado en el Observatorio del Roque de los Muchachos) en el que se detectaron al menos 4 compañeros del candidato a una distancia menor de $1''$. Ninguno de ellos puede ser la causa de los eclipses en la estrella principal.

Las medidas de velocidades radiales de la estrella proporcionan la prueba última de que un candidato es en realidad un exoplaneta. Pero también sirven, de forma muy efectiva, para detectar los sistemas estelares eclipsantes, bien mediante observaciones de variaciones en velocidad radial mucho mayores de las esperadas para exoplanetas, o bien mediante la medida de velocidades de rotación de las estrellas que estén sincronizadas con el periodo del compañero. En el caso de que el compañero sea un planeta, los tiempos de sincronización de la estrella son del orden de 10^{13} años, y por lo tanto no debe haber sincronía entre la estrella y el planeta.

Finalmente, proporcionamos un esquema ordenado de las distintas pruebas que ha de ir superando un candidato a exoplaneta para ser finalmente confirmado, o para descartarlo como sistema estelar eclipsante. El orden de este esquema es por esfuerzo y necesidades de telescopio. Este esquema está especificado en el apartado 7 de este resumen.

4.- Resultados en un campo de la constelación Lyra

Se describen en este Capítulo las observaciones realizadas con los telescopios STARE y PSST, de la red TrES, en una campaña efectuada en un campo de la constelación de Lyra. Con el telescopio STARE se observó durante un total de 49 noches, lo que permitió la detección de 16 candidatos a planetas transitantes. Se proporcionan las curvas de luz dobladas de cada uno de estos candidatos, las características de las estrellas y de los eclipses observados, y posteriormente se procede a realizar y analizar las observaciones de seguimiento descritas en el Capítulo anterior. De esta forma, se comienza con un estudio detallado de la curva de luz original, tanto de la variación en los momentos fuera de los eclipses como de la forma de dichos eclipses. Podemos comprobar cómo este estudio es capaz de descartar el origen planetario para 15 de los 16 candidatos.

Para esclarecer la verdadera configuración estelar de cada uno de los candidatos, se realizaron diversas observaciones tanto fotométricas como espectroscópicas de estos objetos. Se describen en este Capítulo, uno por uno, cada uno de los candidatos obtenidos y la configuración estelar más probable dilucidada tras las diversas observaciones realizadas. Destacamos en este resumen, a modo de ejemplo, el caso de T-Lyr0-03679, en el que unas observaciones tomadas en el telescopio IAC-80 del Observatorio del Teide permitieron detectar eclipses profundos en una estrella situada a $7.9''$ del candidato principal. Se muestra cómo, aún en el caso de que el sistema no hubiese sido resuelto en estas observaciones, la información acerca del color del sistema permitiría haberlo descartado como candidato a exoplaneta transitante.

Se describen también las observaciones realizadas en el telescopio WHT utilizando la técnica de óptica adaptativa. Dichas observaciones sirvieron para detectar un sistema triple, T-Lyr0-01100.

En total, de los 16 candidatos obtenidos, 6 mostraron ser sistemas estelares binarios, 7 sistemas estelares triples (bien ligados gravitacionalmente o no), 2 casos no resueltos (pero descartado su origen planetario), y un exoplaneta transitante, rebautizado como TrES-1, y que se describe en detalle en el Capítulo siguiente.

Un candidato de la red TrES especialmente arduo de resolver, GSC 01944-02289, se describe en una sección aparte. Todas las observaciones de seguimiento de este candidato parecían indicar la presencia de una enana marrón en tránsito frente a una estrella de tipo F. Sin embargo, un estudio detallado de los bisectores de las líneas espectrales permitió concluir que se trataba de un sistema triple, en el que una estrella de tipo espectral F5 evolucionada diluye los eclipses de un sistema eclipsante binario compuesto por una estrella primaria de tipo G0V y una secundaria de tipo M3V. Hasta la fecha, este candidato ha sido el más complejo de identificar, pues superó todos los pasos previos al último paso del esquema de confirmación de planetas propuesto en el capítulo anterior.

Finalmente, se resume el estado de las observaciones de seguimiento de la red TrES, que ya ha identificado un total de 46 falsos positivos en 9 campos reducidos.

5.- TrES-1: El planeta transitante de una estrella brillante tipo K0V

En este Capítulo se describen las observaciones de seguimiento que condujeron al descubrimiento del primer exoplaneta (y hasta la fecha el único) detectado mediante un proyecto de búsqueda de exoplanetas utilizando imágenes de campo amplio, y denominado TrES-1. Una primera búsqueda en la literatura de los parámetros de la estrella en torno a la que orbita, sugería que se trataba de una estrella de tipo G tardío o K temprano, y el movimiento propio catalogado en los archivos del USNO-B1.0 mostraba que la estrella se encontraba relativamente cerca, a unos 150 pc, pues el movimiento que exhibía era el típico para estrellas de campo de baja masa en la vecindad solar. Los parámetros de la estrella en torno a la que orbita TrES-1 se resumen en la Tabla 5.1. Las observaciones tomadas en distintos filtros desde 3 telescopios diferentes mostraron un tránsito básicamente acromático, descartando de esta forma la mayoría de los sistemas triples discutidos en el Capítulo anterior. Se describen en detalle las observaciones realizadas desde el telescopio IAC-80 en el Observatorio del Teide, como muestra del tipo de análisis empleado. Los parámetros orbitales y físicos obtenidos para TrES-1 se proporcionan en la Tabla 5.2. Destacamos en este resumen el periodo orbital de 3.030065±0.000008 d, la masa de 0.75±0.07 M_J, y el radio de $1.08^{+0.18}_{-0.04}$ R_J. Este último parámetro está limitado por el desconocimiento del radio de la estrella, pues el cociente entre el radio del planeta y de la estrella (obtenidos a partir de las curvas fotométricas del tránsito) se conocen con mayor precisión: $R_p/R_s=0.130^{+0.009}_{-0.003}$.

Las medidas de velocidad radial de baja señal a ruido llevadas a cabo con los *CfA Digital Speedometers* proporcionaron un límite mínimo a la masa del compañero de la estrella en unas 5 M_J, y la comparación de los espectros con espectros sintéticos permitieron estimar la temperatura efectiva de la estrella en T_{eff}=5250±200 K, la gravedad superficial en log$g$=4.5±0.5, y la velocidad de rotación en $v \sin i \leq 5$ km/s. La metalicidad medida resultó idéntica a la solar, dentro de los márgenes de error. La medida de la baja rotación de la estrella fue de nuevo una señal positiva, pues indicaba que la estrella no había sido acelerada por interacciones de marea con un compañero estelar, y significaba que las medidas de velocidad radial con alta señal a ruido no se verían complicadas por unas líneas espectrales ensanchadas. Un espectro tomado en el telescopio de 1.5 m del Observatorio de Monte Palomar, y que cubría todo el rango espectral visible, permitió clasificar la estrella como K0V.

Se tomaron ocho medidas de velocidad radial, con alta relación señal a ruido, utilizando el espectrógrafo HIRES en el telescopio Keck I. El análisis de la velocidad radial de la estrella resultó en una medida de la masa de TrES-1 en 0.75±0.07 M_J, alcanzando unas precisiones en cada una de las velocidades radiales de 10-15 m/s, y sin indicios de variaciones en los bisectores de las líneas espectrales. Estas medidas proporcionaron la confirmación final del origen planetario de la señal fotométrica de tránsitos detectada con el telescopio STARE.

Al contrario de lo ocurrido con el exoplaneta que transita frente a HD 209458, el radio medido para TrES-1 está bien explicado por los modelos actuales de planetas irradiados, sin la necesidad de fuentes de energía internas al planeta.

Un trabajo posterior (Sozzetti et al. 2004) incrementó la precisión de los parámetros orbitales y físicos, tanto de la estrella como del planeta. Con estos parámetros, TrES-1 es en la actualidad el segundo exoplaneta mejor conocido de los más de 150 descubiertos hasta la fecha.

Presentamos un análisis preliminar de unas observaciones que hemos realizado utilizando la cámara ACS/HRC con un grisma a bordo del telescopio espacial HST. Estas observaciones permitirán reducir aún más la incertidumbre en los parámetros tanto de la estrella como del planeta. A pesar de que la estrella es unas 40 veces menos brillante que HD 209458, estimamos que con esta configuración instrumental podemos alcanzar una precisión tan sólo un factor 2.2 peor que la obtenida en HD 209458 con el espectrógrafo STIS a bordo de HST (Brown et al. 2001). Este primer análisis muestra una estructura cerca del centro del tránsito que interpretamos preferentemente como causada por una mancha en la superficie de la estrella que es ocultada al pasar TrES-1 por delante de ella. Un estudio de las curvas de luz originales del telescopio STARE de las estrellas de TrES-1 y de varias estrellas cercanas parece mostrar una mayor dispersión de los datos en la estrella de TrES-1, lo que es consistente con la presencia de actividad magnética en esta estrella. Hay también indicaciones de actividad en la estrella a partir del indicador de Ca II (Sozzetti et al. 2004).

En un rango espectral diferente, hemos buscado el eclipse secundario de TrES-1, producido cuando éste pasa por detrás de su estrella. Para ello, hemos utilizado el detector IRAC a bordo del telescopio espacial infrarrojo Spitzer durante 5.6 horas, realizando observaciones en las bandas centradas en 4.5 y 8 μm. La detección del secundario en ambas bandas (Charbonneau et al. 2005) constituye la primera detección directa de emisión térmica proveniente de estos objetos[1]. Esta detección ha permitido medir la temperatura efectiva del planeta en T_{eff}=1060$\pm$50 K, y, si se supone que la emisión se produce de forma isotrópica, el albedo se estima en A=0.31$\pm$0.14. La medida de la hora en la que ocurre el centro del secundario permite restringir la excentricidad de la órbita a básicamente 0 (i.e. órbita circular), a no ser que la línea de los nodos esté alienada con nuestra línea de visión.

6.- Soñando con el futuro: El tránsito de Venus de 2004

En un experimento sin precedentes, el tránsito de Venus del 8 de Junio de 2004 proporcionó una oportunidad ideal para poner a prueba la técnica denominada espectroscopía de transmisión, descrita en la Introducción. La atmósfera de Venus está mejor estudiada y conocida que la de los lejanos exoplanetas, y en el 2004 Venus pasaba por delante del Sol (visto desde la Tierra) por vez primera desde 1882. En este Capítulo se describen las observaciones realizadas en la Vacuum Tower Telescope (VTT) situada en el Observatorio del Teide, que permitieron detectar líneas de absorción del $^{12}CO_2$ y $^{13}CO_2$ mediante esta técnica.

Se comienza con una recopilación del conocimiento existente en la parte de la atmósfera de Venus de la que la espectroscopía de transmisión nos puede

[1]Junto con la detección anunciada simultáneamente de emisión térmica en 24 micras de HD 209458b (Deming et al. 2005).

proporcionar información. Esta parte es la mesosfera de Venus, situada entre los aproximadamente 65 y 100 km de altura sobre la superficie. Casualmente, es una región en que la única información acerca de las velocidades de los vientos en estas alturas proviene de unas pocas sondas que penetraron en la atmósfera; por lo tanto, esta información está muy sesgada, consistiendo en datos para una única latitud y longitud, en un momento determinado. En esta región se espera que cambie el régimen de vientos, del flujo zonal retrógrado que se observa en las capas de nubes (a unos 60-65 km de altura), al régimen subsolar-antisolar detectado a alturas superiores a unos 120 km. Se estimaba que las líneas de absorción en tránsito del CO_2 muestrearían este rango de alturas. Las observaciones se planearon para medir desplazamientos Doppler en estas líneas, proporcionando así datos acerca de los vientos en un amplio rango de latitudes (moviendo la rendija del espectrógrafo) y alturas (distintas líneas muestrearían diferentes alturas en el rango de 65-100 km).

Se realizaron observaciones con el Polarímetro Infrarrojo TIP, utilizando óptica adaptativa siempre que fuese posible (después de la primera hora de adquisición de datos, cuando Venus estaba a una altura suficiente sobre el horizonte), en tres bandas centradas en 1.5969, 1.5979 y 1.6129 μm. Describimos detalladamente el proceso de calibración de las imágenes, al que se ha prestado especial atención, debido a la presencia de franjas de interferencia en las imágenes, y al amplio rango de intensidades muestreado (desde el centro del limbo de Venus, en el que la señal era de varios centenares de ADUs, hasta el disco solar, con señales de decenas de miles de ADUs); una mera división por una imagen de campo uniforme tomada moviendo el telescopio no fue suficiente, y describimos el proceso con el que mejores resultados obtuvimos para la eliminación de las franjas interferenciales.

Dividiendo la señal en la posición del limbo de Venus entre la señal 11 pixeles ($\sim$3.8$''$) alejados del limbo en la dirección del disco solar, se detectan líneas de absorción en la atmósfera del planeta. Promediando varios centenares de exposiciones de 1 s de integración se obtienen espectros de transmisión en los que se detectan claramente líneas de absorción de $^{12}CO_2$ y $^{13}CO_2$. Sin embargo, la relación señal a ruido de los datos no es suficiente como para intentar una medida del desplazamiento Doppler con la precisión requerida (del orden de 10 m/s), en parte por los problemas con las franjas de interferencia. Finalmente, se promedian los espectros en función de la latitud en la región con las líneas de transmisión detectadas más claramente. Aparentemente, se observan diferencias en las profundidades de las líneas entre las regiones a bajas y altas latitudes venusianas. El trabajo futuro irá dirigido a estudiar el origen de esta dependencia, no descartándose un origen instrumental.

Estas observaciones demuestran la utilidad de este método para detectar componentes en las atmósferas de los exoplanetas transitantes, con todas las aplicaciones que estas detecciones conllevan para comprender mejor el origen de estos objetos, y, en el futuro, para potencialmente estudiar las atmósferas de planetas similares a nuestra Tierra.

7.- Conclusiones y trabajo futuro

El campo de la investigación en exoplanetas ha evolucionado a una velocidad asombrosa desde el primer descubrimiento de un exoplaneta alrededor de una estrella de tipo solar, 51 Peg (Mayor & Queloz 1995). Entre las diversas técnicas de detección, el método de los tránsitos constituye la herramienta más potente para medir parámetros físicos de estos intrigantes Júpiteres calientes. Combinado con las medidas de la velocidad radial de la estrella huésped, nos puede proporcionar la densidad del planeta, que acarrea pistas acerca de su historia de formación. El descubrimiento en los próximos años de nuevos planetas en tránsito por proyectos diversos, tanto desde tierra como desde el espacio, aumentará nuestro conocimiento acerca de estos objetos. Estamos comenzando a ser capaces de realizar "planetología comparada", y nuevas perspectivas acerca de la distribución de masas real de estos objetos surgirán en el futuro cercano. Algunos autores han comparado la situación actual con el estado del conocimiento de la evolución estelar justo antes de que el primer diagrama H-R fuese construido. Con más de 150 planetas descubiertos hasta la fecha, nos aproximamos a la situación en la que los estudios estadísticos de estos objetos comienzan a ser significativos.

7.1.- *Conclusiones en el campo de exoplanetas.*

Las conclusiones del presente trabajo se resumen en los siguientes puntos:

- Hemos descubierto el primer planeta transitante detectado mediante un telescopio de campo amplio (STARE), TrES-1. Orbita a una estrella del tipo K0V moderadamente activa, que no muestra restos de Litio hasta los niveles detectables. Las medidas de la masa, de 0.76±0.05 M_J, y del radio, de $1.04^{+0.08}_{-0.05}$ R_J, hacen que este planeta sea el segundo mejor conocido en términos de precisión en sus parámetros físicos. Al contrario de lo que sucede con el exoplaneta mejor estudiado en la actualidad, HD 209458b, el radio de TrES-1 se explica adecuadamente con los modelos de evolución de planetas bajo una intensa radiación de la estrella huésped. No se necesita una fuente adicional de energía en el planeta. Un trabajo reciente (Charbonneau et al. 2005) nos permitió detectar el eclipse secundario, lo que constituye la primera observación de emisión térmica procedente de un exoplaneta, en 4.5 y 8 μm. Con esta detección, se estima que la temperatura efectiva del planeta es de T_{eff}=1060±50 K, y la excentricidad ha de ser básicamente nula ($e \cos w$=0.0030±0.0019).

- Se ha realizado un análisis detallado de las distintas técnicas de seguimiento que se requieren para confirmar o descartar un candidato a planeta transitante, y se ha propuesto un esquema ordenado de pruebas, que van desde las más económicas en términos de esfuerzo y medios necesarios hasta las más costosas. Este esquema consiste en realizar:
  - Una interpretación cuidadosa de la curva de luz: buscar modulaciones en las partes fuera de eclipse, y ajustar la forma del tránsito.
  - Velocidades radiales con baja señal a ruido, para detectar los sistemas eclipsantes estelares.
  - Fotometría multicolor de los tránsitos, encaminada a detectar sistemas estelares triples.
  - Imagenes con muy alta resolución espacial, para tratar de resolver los sitemas estelares triples (bien jerárquicos o bien no ligados).
  - Velocidades radiales con alta señal a ruido y un análisis de los bisectores de las líneas, para finalmente medir el movimiento de la estrella huésped, y de esta forma inferir la masa del planeta.
- Se ha analizado en detalle un campo de la red TrES en la constelación de Lyra, prestando una atención especial a las observaciones de seguimiento de los 16 objetos que se identificaron como candidatos a planetas transitantes. Estas observaciones dieron lugar a la detección de 6 sistemas estelares binarios, 7 sistemas triples no resueltos en las imágenes de STARE, 2 casos no resueltos y del planeta transitante TrES-1.
- El tránsito de Venus en el 2004 nos ha permitido detectar por primera vez trazas de $^{12}CO_2$ y $^{13}CO_2$ en la atmósfera del planeta mediante el uso de la técnica de espectroscopía de tránsito. El trabajo futuro irá encaminado a interpretar los espectros de transmisión obtenidos, y la aparente dependencia de las profundidades de las líneas en función de la latitud venusiana muestreada.

7.2.- *Conclusiones en el campo de variabilidad estelar.*

Se han realizado varios estudios en el campo de variabilidad estelar utilizando los datos de STARE. Se encuentran resumidos en los dos apéndices de la tesis. Las principales conclusiones que se extraen de estos estudios son:

- Las curvas de luz de STARE (o de cualquiera de los telescopios de TrES) poseen la precisión suficiente como para realizar estudios serios de variabilidad estelar.

- Se ha estudiado en detalle la curva de luz de STARE de la estrella tipo $\delta\tilde{S}$cuti V1821 Cygni, detectando 4 frecuencias de pulsación evidentes. Una de las frecuencias no había sido detectada en estudios anteriores de la estrella. Otras 3 frecuencias cercanas al nivel de ruido podrían servir para explicar la aparente variabilidad de la amplitud de la frecuencia principal de pulsación f_1. Sin embargo, no se puede descartar la posibilidad de que f_1 sea intrinsecamente variable en amplitud, y que las 3 frecuencias cercanas detectadas sean un artefacto de la herramienta utilizada para el análisis de las frecuencias.

- Se han proporcionado frecuencias, amplitudes y fases para 5 nuevos pulsadores descubiertos en la constelación del Cisne, como resultado colateral a la investigacín de V1821 Cygni.

- Un total de 38 estrellas variables han sido descubiertas con STARE en campos potenciales de la misión espacial COROT, como resultado de una colaboración con este proyecto. Algunas son demasiado débiles como para ser observadas con las CCDs de sismología de COROT, o bien están demasiado lejos de los objetos principales; aún así 18 estrellas han sido identificadas como potenciales objetivos secundarios para las CCDs de sismología de COROT. La mayoría son estrellas del tipo δ Sct, si bien también se han descubierto variables γ Dor y binarias eclipsantes.

7.3.- *Trabajo futuro*

Un análisis preliminar de las observaciones de TrES-1 utilizando HST/ACS resulta en una determinación de los parámetros del planeta que están dentro de las barras de error proporcionadas en este trabajo. El estudio detallado de la forma de la entrada y salida del tránsito en estos datos permitirá buscar anillos en TrES-1. La medida precisa de los tiempos en los que ocurren los tránsitos, y los residuos del ajuste del tránsito serán utilizados para buscar hipotéticos satélites de tamaño del orden de la Tierra en torno a TrES-1.

Se necesita más trabajo para interpretar las observaciones llevadas a cabo durante el tránsito de Venus de 2004. Especialmente, para tratar de comprender o interpretar el origen de la aparente dependencia de la profundidad de las líneas de transmisión con la latitud. En particular, una medida de los cocientes entre las anchuras equivalentes de dos líneas claras de $^{12}CO_2/^{13}CO_2$ puede proporcionar pistas acerca de las temperaturas en las alturas en las que dichas líneas se vuelven opacas a los rayos solares tangenciales.

Aunque muchos de los candidatos de la red TrES se descartan como sistemas eclipsantes binarios (o triples), hay bastante información valiosa acerca de los tamaños de las estrellas eclipsantes con una componente de tipo M. Algunos de los miembros de la colaboración TrES están trabajando en obtener los parámetros físicos y orbitales de estos sistemas binarios. Como un primer resultado, se ha encontrado en uno de los campos de TrES en la constelación de Hércules el cuarto sistema binario eclipsante descubierto hasta ahora compuesto por dos estrellas de tipo M (Creevey et al. 2005).

Y, finalmente, la red TrES seguirá en marcha durante al menos tres años más, rastreando el cielo nocturno a la caza de nuevos exoplanetas transitantes.

Cuando se haya detectado un número significante de candidatos a planetas transitantes, tendrá sentido realizar un estudio detallado acerca del ritmo de detección de falsos positivos, conociendo la naturaleza de cada uno de éstos. Un estudio de este tipo podría servir para establecer si el ritmo de detección de los exoplanetas transitantes concuerda con el ritmo de detección de los exoplanetas detectados hasta ahora con la técnica de las velocidades radiales.

8.- Apéndice A: Estudios de δ Scuties con los datos de STARE

En este primer Apéndice, se estudia la curva de luz de una estrella del tipo δ Scuti (V1821 Cygni), obtenida con el telescopio STARE en un campo de la constelación del Cisne. Algunos estudios en la literatura demostraban que la estrella pulsaba de forma multiperiódica, y habían indicios de variaciones en la amplitud de uno de los modos de pulsación. La curva de luz del telescopio STARE sirve para confirmar esta variabilidad en amplitud, investigar acerca de su origen (causada por frecuencias de pulsación cercanas vs. variaciones intrínsecas del modo) y para detectar frecuencias de pulsación que no habían sido observadas en los trabajos de otros autores. Con esto, se demuestra cómo los datos de un telescopio de pequeña apertura (STARE) son capaces de competir con los datos tomados por telescopios bastante más grandes.

Se comienza resumiendo las observaciones previas de esta estrella, realizadas en los trabajos de Delgado et al. (1984) y Zhou, Liu & Du (2001). El segundo trabajo es el resultado de unas observaciones más intensivas que el primero, consistiendo en 21 noches de observación. Los dos grupos de observaciones no proporcionan las mismas frecuencias, y el segundo trabajo fuerza un ajuste de los datos de Delgado et al. a las frecuencias obtenidas en la campaña de 21 noches de observación; de esta forma, concluyen que el modo principal de pulsación es variable en amplitud. Esta introducción finaliza con un breve repaso del tema de las variaciones en amplitud y fase de otras estrellas del mismo tipo en la literatura.

A continuación se describen los datos obtenidos con el telescopio STARE en la constelación del Cisne, durante dos campañas de observación en 2001 y 2002. Un análisis mediante el uso del programa Period98 (Sperl 1998, el mismo programa que el utilizado en el trabajo de Zhou et al.) de la curva de luz combinada de las dos campañas sirve para detectar cuatro frecuencias de la estrella con una amplitud mayor que 4 veces el promedio del ruido en una ventana de una anchura de 5 c/d centrada en cada una de las frecuencias. De estas cuatro frecuencias, una (f_3) no fue observada en los estudios anteriores, y otra (f_4) está publicada en el trabajo de Delgado et al., pero resultó indetectable en el trabajo de Zhou et al. Se evalúa seguidamente la hipótesis de la variación en amplitud de la frecuencia f_1, concluyendo que existen variaciones tanto en amplitud como en fase de esta frecuencia. Para descartar el origen instrumental de estas variaciones, jugamos con la ventaja de que hay varias estrellas con pulsaciones en el mismo rango de frecuencias y amplitudes en las imágenes de STARE; proporcionamos las frecuencias, amplitudes y fases de 5 de estas estrellas, para las cuales no existen trabajos publicados, por desconocerse su naturaleza variable. Una de estas 5 estrellas parece mostrar también variaciones en amplitud y fase.

Una vez confirmada esta variación en la amplitud y la fase de f_1, realizamos un estudio más detallado, encaminado a discernir, entre dos posibles orígenes, la causa de esta varición: intrínseca al modo, o causada por interferencias con frecuencias cercanas de baja amplitud. Para ello, se describe la forma en la que se elimina la contribución de las frecuencias f_2, f_3 y f_4 de la curva de luz, para descartar posibles efectos de interferencia con estos modos. En esta nueva curva de luz, se realiza un ajuste de la amplitud y la fase de la frecuencia f_1 en bloques de 10 días de duración. De esta forma, se obtiene la Figura 8.5, en la que se distingue un cambio en amplitud de unas 4 mmags y un posible cambio en la fase que no ocurre en el momento de mínima amplitud. Esto apunta hacia que el origen de las variaciones de f_1 no puede estar causado por la interferencia de dos frecuencias cercanas. Sin embargo, podemos reproducir los cambios en amplitud y fase de f_1 si consideramos 3 frecuencias adicionales cercanas a f_1 y que se encuentran próximas al nivel de ruido en el espectro. Desgraciadamente, no se puede distinguir con estas herramientas si el origen de estas frecuencias cercanas es intrínseco a la estrella o un resultado de utilizar el análisis de Fourier en señales que son variables con el tiempo. El haber detectado la frecuencia f_4 próxima al nivel de ruido, mientras que en el trabajo de Delgado et al. se veía claramente, y en el de Zhou et al. pasó inadvertida nos hace sospechar que este modo también posee importantes variaciones en amplitud.

9.- Apéndice B: Observaciones de STARE para COROT

Este último Apéndice resume la detección de nuevas estrellas variables en campos potenciales de la misión espacial COROT, utilizando el telescopio STARE. Algunas de estas estrellas variables podrían ser observadas como objetos secundarios en las cámaras de astrosismología de COROT, en sus campañas de observación continuadas de 150 d de duración. La misión COROT tiene previsto su lanzamiento en Junio de 2006.

Se describe someramente la misión COROT, y la motivación para el uso de STARE como instrumento para detectar nuevas estrellas variables accesibles a la misión. De esta forma, se realizaron campañas apuntando tanto al centro como al anticentro galáctico, resultando en 38 estrellas variables detectadas en el anticentro, de las cuales 11 cumplen todas las condiciones para ser observadas como objetivos secundarios de la misión, 18 son más débiles que el límite de magnitud $V<9.5$ impuesto para que un objeto sea observado en las cámaras de astrosismología, y 9 están demasiado alejadas de potenciales objetivos primarios de COROT.

Las observaciones hacia el centro galáctico permitieron detectar 7 estrellas variables con brillo $V<9.5$, y otras 7 más débiles que este valor. De las 7 estrellas variables brillantes, 3 fueron descubiertas en estas observaciones, así como 6 de las 7 estrellas débiles.

CÓDIGOS DE LA UNESCO:

- **21302: Astronomía óptica: Telescopios**
- **21407: Planetología: Planetas**
- **21403: Planetología: Atmósfera planetaria**

Abstract

An exoplanetary transit occurs when it crosses the line of sight between the observer and the star around which it is orbiting. The flux decrease that it provokes allows us to find out certain orbital parameters and some physical characteristics of the planet that are inaccessible through other techniques. The diversity of the performed studies and the acquired knowledge after the detection of HD 209458b's transits motivated the use of this technique as a tool for exoplanet discoveries.

In this thesis, we describe the STARE instrument (a node placed at the Observatorio del Teide that forms part of the TrES network, which is comprised of another two similar instruments at Lowell Observatory, Arizona, and Mount Palomar, California, both in the USA) devoted to the search for exoplanets using the transit method. It consists of a small Schmidt camera (10 cm diameter) that performs differential photometry of wide stellar fields ($6.1^\circ \times 6.1^\circ$). Each of the campaigns lasts several hundreds of hours. We fully describe the analysis tools used to achieve the required precision to detect giant exoplanetary transits (it is necessary to reach a precision of less than 1% in thousands of stars), as well as the noise sources that limit this precision.

There are several stellar configurations that mimic the signal produced by a transiting exoplanet, and follow-up techniques that unveil these false positives are required. We perform a detailed study of these techniques, which start with a careful analysis of the original light curve, without the need for further observations, and end in the precise measurements of the star's radial velocity, the last step necessary for the confirmation of an exoplanet discovery. The fast rate of false positive detections in projects such as TrES have led us to propose an exoplanet confirmation scheme, ordered according to the efforts needed to perform each step.

These follow-up techniques are applied to 16 exoplanet candidates obtained in a TrES observing campaign, in a field of the constellation Lyra. The detailed

analysis of the original light curves allow us to discard 15 of the 16 candidates, while the diverse follow-up observations performed reveal the different stellar configurations causing similar photometric signals as those produced by an exoplanet. Six of these candidates turned out to be binary stellar systems and seven of these triple systems (either physically bound or two bound stars and a third star in the line of sight). For another 2 candidates it was not possible to determine the configuration.

The single candidate that passed all the required tests, TrES-1, is the first exoplanet discovered with the transit method around a relatively bright star. TrES-1 orbits a K0V star, with a period of 3.030065±0.000008 d; it has a mass of 0.76±0.05 M_J, a radius of $1.04^{+0.08}_{-0.05}$ R_J, an almost circular orbit, with an inclination of $i = 89.5^{+0.5}_{-0.3}$ degrees, and an effective temperature of T_{eff}=1060±50 K. The host star has a metallicity of [Fe/H]=0.00±0.09, a T_{eff}=5250±75 K, a surface gravity of log$g$=4.6±0.2, and does not show Lithium remains, while there are clues for stellar activity. With these parameters, TrES-1 is currently the second better known exoplanet, after HD 209458b. Its infrared magnitude turned out to be ideal for the use of the IRAC instrument on board the Spitzer satellite, what allowed the detection of the secondary eclipse. This detection served to estimate the planetary effective temperature and its eccentricity, and it constitutes the first detection of thermal emission from an exoplanet[2].

Finally, we present a preliminary analysis of observations of the June 2004 Venus transit, at the VTT (Vacuum Tower Telescope) solar telescope of the Observatorio del Teide. In these observations, we detect $^{12}CO_2$ and $^{13}CO_2$ of the Venusian mesosphere with the transmission spectroscopy method. This method has already been successfully used to study the atmosphere of HD 209458b, and in the following years it will allow the study of different components of the exoplanetarian atmospheres.

[2]Together with the simultaneously announced detection of thermal emission at 24 micron of HD 209458b (Deming et al. 2005).

Organization

This thesis is organized in 7 chapters and 2 appendices. Firstly, we will summarize the basic knowledge we have of these objects, we will review the most prominent detection techniques, and we will introduce several concepts, such as the method of transits, and transit spectroscopy (Introduction). In Chapter 2, we describe a wide-field photometry search for transiting planets (STARE), with which the bulk of the observations for this thesis were done. A complete description of the instrument, data analysis and noise sources is given in this Chapter. The final products of a STARE transit search consist of a list of transiting planet candidates. The different techniques that have to be applied from this point in order to distinguish the real planets from false positives, and a description of the kind of false positives that arise from these searches is the subject of the Chapter 3. We also propose an ordered scheme to recognize these false positives in an efficient way. One sample field of the STARE project is described in detail in Chapter 4, from the achieved precisions in every star to the follow-up of a list of 16 transiting planet candidates. Most of these candidates are proved to consist of stellar systems in which at least two of the stars are eclipsing. Among these candidates, there is one (TrES-1) that is proved to be a transiting planet, and it is described in Chapter 5. There, we provide all the arguments and observations that lead to this conclusion. An excellent opportunity to test the concept called *transit spectroscopy* came with the June 2004 Venus transit. Absorption from its CO_2 atmosphere was observed from the Vacuum Tower Telescope (VTT) at the Observatorio del Teide. These observations, the data analysis and results are described in Chapter 6. Finally, the conclusions of this work are summarized in Chapter 7. Two appendices, related to the variability studies that can be performed with the STARE instrument, and its utility to bigger projects such as the space mission COROT, are also a part of this thesis.

Contents

1

Introduction

Escribir, por ejemplo: "La noche está estrellada,
y tiritan, azules, los astros, a lo lejos."
Pablo Neruda (Veinte poemas de amor y una canción desesperada)

1.1 Exoplanets

DURING the last decade, we have witnessed the birth of a new branch of astronomy: the study of planets orbiting stars other than the Sun. Three years after the discovery of the first planets around pulsars (Wolszczan & Frail 1992), Mayor & Queloz (1995) announced the first exoplanet orbiting around a Sun-like star, 51 Peg. This first scientific demonstration that the Sun is not the only star which is accompanied by planets, also raised important questions that had no answer with prevailing theories of planet formation: How can a planet be orbiting a pulsar? How can a Jupiter-like planet be orbiting as close to the parent star as to give one whole turn every $\sim$4.5 days? These surprising first results were just the beginning of a whole set of questions that arose almost at the same cadence as planets were detected. One important consequence of these questions was the necessity to find more systems, in order to try to distinguish between regularity and peculiarity in these exo-worlds. As a consequence, and as the refinement of the techniques evolved, more and more planets have been detected, providing clues to the planetary formation in other stellar systems.

Most of the 157 [1] (at the moment of writing these lines) known planets have

[1] as considered by the Extra-solar Planets Encyclopaedia, by J. Schneider: http://www.obspm.fr/encycl/encycl.html

been detected using the same technique, based on the precise radial velocity measurements of the host star. In this Section, we briefly review this and other techniques used to detect exoplanets, paying special attention to their major findings and the current status. After that (Section 1.2), we will concentrate on the transit method, providing the planetary parameters that can be known and reviewing the estimations of the detection rates for transit searches. The first planet that exhibited transits, which is also currently the best-known planet outside our Solar System, is treated in more detail in Section 1.3. This object, according to some authors, turned out to be bigger in size than expected, and several interesting discussions arose from this fact. These are summarized in Section 1.4. A technique that can serve as a diagnostic for exoplanetary atmospheres is described in Section 1.5, and finally we outline the current theories for the formation of these objects (Section 1.6).

1.1.1 Working definitions

Extrasolar planet: We will use in this work the Working Group on Extrasolar Planets (WGESP) of the International Astronomical Union (IAU) definition of a **planet**[2], which states:

1. Objects with true masses below the limiting mass for thermonuclear fusion of deuterium (currently calculated to be 13 Jupiter masses for objects of solar metallicity) that orbit stars or stellar remnants are "*planets*" (no matter how they formed). The minimum mass/size required for an extrasolar object to be considered a planet should be the same as that used in our Solar System.

2. Substellar objects with true masses above the limiting mass for thermonuclear fusion of deuterium are "brown dwarfs", no matter how they formed nor where they are located.

3. Free-floating objects in young star clusters with masses below the limiting mass for thermonuclear fusion of deuterium are not "planets", but are "sub-brown dwarfs" (or whatever name is most appropriate).

As pointed out by this group, this constitutes a reasonable working definition of a *planet*, which is a compromise between definitions based on the deuterium-burning mass and the formation mechanism. A better definition will have to wait until more knowledge is acquired.

[2]http://www.ciw.edu/boss/IAU/div3/wgesp/definition.html

We will use the term *exoplanet* as a synonym of the previous concept, as it is also widely used in the community.

Hot Jupiter: The term "Hot Jupiter" will be used throughout this work to mean the planets with masses $M_P \sin i \leq 13$ M_{Jup} orbiting close to a parent solar-like star (a < 0.1 AU). They are also referred to in the literature as "*51-Peg like objects*" or "*close-in extrasolar giant planets (CEGP)*". Some authors (e.g. Bouchy et al. 2004) have suggested the term "*Very Hot Jupiter*" or "*extremely close-in extrasolar giant planet*" for the planets with periods much lower than 3 days (implying typically orbits with a < 0.025 AU). As there is no clear consensus in the division among these two classifications, we will adopt the more general "Hot Jupiter" denomination as defined above, but we emphasize that it constitutes a *working definition* throughout this work.

1.1.2 Exoplanets around pulsars

Pulsars are the cores that remain after a Supernova explosion of a star with a mass between 15 and 30 $M_{\odot}$. These cores are neutron stars, which host strong magnetic fields. If the spin axis of the star and its magnetic field are not aligned, then a beam of radio waves hits the Earth at extremely regular intervals, which range between 2 milliseconds and 2 seconds. The typical rate of change of the period of these objects is thought to be one second every ten million years (van Straten et al. 2001). Thus, changes in the period faster than this are the effect of orbiting companions to the pulsar. The precision in the pulsar timing is such as to detect objects with Earth masses or even lower. For a detailed review of these concepts and pulsar astronomy in general, we recommend the book by Lorimer & Kramer (2005).

The first indirect detection of an exoplanet was made by Wolszczan & Frail (1992), and in later works (Wolszczan 1994, Wolszczan 2000) the model was refined, in order to establish the existence of one Mercury-sized planet (A), two Earth-sized planets (B and C), and an asteroid-mass object (D, Wolszczan & Konacki 2005), with masses of 0.020, 4.3 and 3.9 $M_{\oplus}$, and 0.15 M_{Pluto} orbiting at distances of 0.19, 0.36, 0.46 and 2.7 AU respectively from the 6.2-millisecond pulsar PSR B1257+12.

The pulsar planets have also provided the first demonstration of orbital resonances between exoplanets (Wolszczan 1994; Konacki, Maciejewski, & Wolszczan 1999), as planets B and C exhibit a near 3:2 mean motion resonance. The gravitational perturbations between the two planets have been detected by the same authors, and used to estimate the masses and inclinations of the orbits of the two most massive planets (Konacki & Wolszczan 2003b). The almost coplanar measured inclinations, and the near 3:2 resonance, strongly support the hypothesis of a disk origin for these planetary system.

It is currently thought that these objects formed in a massive circum-pulsar disk, instead of being remains of an original planetary system of the pulsar parent star that survived the Supernova explosion. Miller & Hamilton (2001) and Hansen (2002) examined the conditions of survival and evolution of these pulsar protoplanetary disks, concluding that these planets should grow in a typical $\sim 10^7$ yr timescale, if the initial disk is sufficiently massive (greater than 10^{28} g). A smaller disk would not survive the evaporation caused by the pulsar accretion flux. There are some proposed schemes for the quick formation of such a massive disk, for instance by tidal disruption of a stellar companion (Stevens, Rees, & Podsiadlowski 1992; Phinney & Hansen 1993) or in the process of a white dwarf merger (Podsiadlowski, Pringle, & Rees 1991; Livio, Pringle, & Saffer 1992). These processes would not be very common. That would explain the lack of planetary companions in the vast majority of millisecond pulsars (48 Galactic pulsars studied by Lorimer, 2001).

1.1.3 The Radial Velocity Searches

The precise study of the radial velocity behavior of nearby dwarf stars has been the most successful method to detect exoplanets to date. Since the first detection of a companion to 51 Peg (Mayor & Queloz 1995), most of the 157 known planets (as of May 2005) have been found as a result of velocity perturbations in the host star induced by the presence of a planetary mass companion. The companion pushes the star back and forth along our line of sight at a velocity with an amplitude of K_s; if we assume that $M_p \ll M_s$, and the eccentricity of the planet's orbit is e, then the minimum mass of the planet is given by the expression:

$$M_p \sin i \simeq \Big(\frac{P}{2\pi G}\Big)^{1/3} K_s M_s^{2/3} (1-e^2)^{1/2} \tag{1.1}$$

and, from the Kepler's laws:

$$a_p \simeq \Big(\frac{GM_s}{4\pi^2}\Big)^{1/3} P^{2/3} \tag{1.2}$$

where M_p is the mass of the planet, a_p is the orbital semimajor axis, M_s is the mass of the star and i is the orbital inclination (see Figure 1.1). Using various identities leads to an expression for the amplitude of the movement in the form:

$$K(m/s) = \frac{30 M_p \sin i}{(a_p M_s)^{1/2}} \tag{1.3}$$

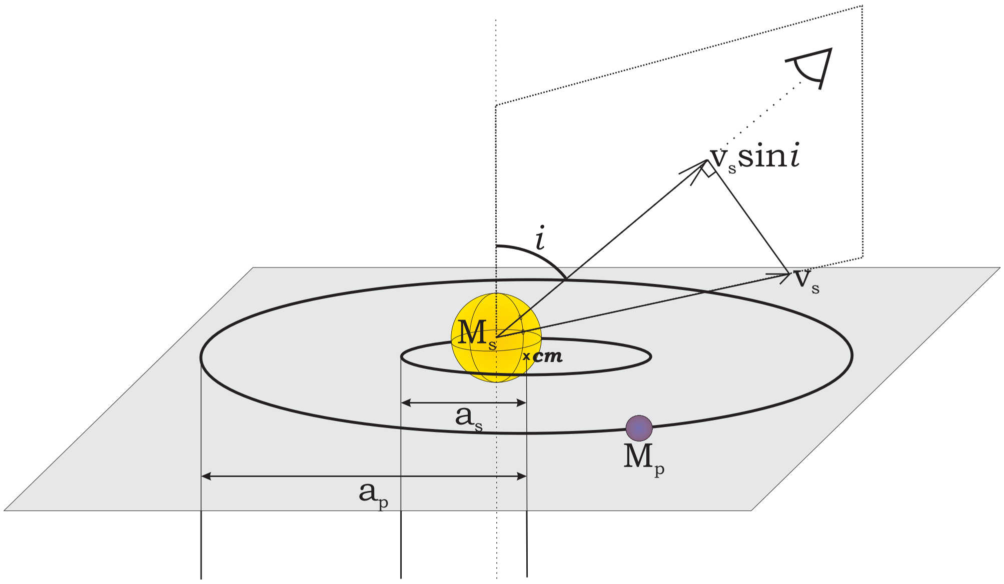

FIGURE 1.1— Schematic view of the main orbital definitions. The star s and the planet p orbit their center of mass cm, in circular orbits with a radius of a_s and a_p respectively. The orbital plane is plotted in gray, and the inclination of the orbit i is defined as the angle between the normal to this plane and the observer's line of sight. The observer is located in the upper right part of the diagram. An edge-on orbit corresponds to an angle of 90°. The reflex motion of the star v_s, when measured along the line of sight, is affected by the sine of this angle.

where the M_p is given in Jupiter masses, M_s in Solar masses and a_p in AU. This movement of the star can be accurately measured using the Doppler effect. The shift produced by a planetary object is of the order of tens or hundreds of m/s (the amplitude of the Sun's movement due to Jupiter is ∼12.5 m/s, due to Saturn ∼4 m/s, and due to the Earth ∼8 cm/s; 51 Peg b moves the host star by 59 m/s), which translates to the necessity to measure shifts in the spectral lines with a precision of roughly 1/1000 of the spectral line width. To achieve this, the radial velocity surveys[3] observe typically sun-like stars (because many spectral lines are needed to improve the measurements) and slow rotators (because fast rotation causes the lines to be broader, and thus the precision is decreased). The information on the radial velocity of the star contained in all spectral lines needs to be concentrated to achieve the required precisions. This is done by computing the cross-correlation between each observed spectrum and a reference spectrum.

[3] see, for instance, *http://www.obspm.fr/encycl/searches.html*

This reference may be the spectrum of a standard star with well-established radial velocity, or one spectrum of the program star itself. The technique of the cross-correlation function was firstly applied to astronomy by Simkin (1974).

The spectrograph behavior has also to be kept under control, to achieve the required precisions, and a radial-velocity reference serves to accomplish this. There are currently two different techniques to establish this reference: a simultaneous thorium-argon lamp observation (see, e.g., Konacki et al. 2003c) and an Iodine absorption cell (see, e.g., Cumming, Marcy, & Butler 1999 and references therein). While the Iodine cell is placed into the path of the star signal, before entering the spectrograph (and thus reducing the signal of the star), the thorium lamp is observed simultaneously as the object (with optical fibers) and thus fainter objects can be measured with the required precision to detect planetary mass objects. It is estimated that the Th-Ar technique is 6 times more efficient than the Iodine absorption cell (e.g., Udry, S. 2004, communication at the XVI Canary Islands Winter School).

Another difficulty with the radial velocity technique is the necessity to maintain good tracking on the star, as its slight movements in and out of the slit can produce spurious radial variations of the star.

State-of-the-art instruments, such as HARPS (Pepe et al. 2002), working at the 3.6 m ESO telescope at La Silla Observatory (Chile), are beginning to obtain precisions of 0.4 m/s. These allow the detection of objects with roughly Neptune's size or even smaller ones (Santos et al. 2004b; McArthur et al. 2004; Butler et al. 2004).

Despite the unquestionable success of this technique in the last decade, there are a few drawbacks. Below 1 m/s, the precision in the radial velocities is not longer determined by the instrument, but by the intrinsic atmospheric pulsations of the star (asteroseismology), which can have amplitudes of several m/s (Mayor et al. 2003), and by the magnetic features on the atmosphere, such as spots, faculae and flares. Even if some of these effects can be modelled and removed (Saar et al. 2003, Kürster et al. 2003), the difficulty increases when trying to reach lower detection thresholds. Thus, it seems difficult for this technique to reach the detection threshold of Earth-sized exoplanets.

Another mayor drawback of the radial velocity searches is that the orbital inclination cannot be known, and thus the exact mass of the planet remains unknown. Actually, only lower limits on the mass can be provided. There are at least two ways to solve the inclination degeneration: astrometric measurements (need to be taken from space to achieve the required precisions) with just one successful case: GJ 876 (Benedict et al. 2002), and the transit method, which will be discussed deeply in this work.

1.1.4 Characteristics of the known exoplanets, derived from the radial velocity surveys

From the sample of 157 planets detected around 138 stars, using mainly the radial velocity technique, a few trends and characteristics of the objects found so far and their host stars are worth mentioning:

- The **fraction of stars** whose planets have masses $M_p > 0.47M_J$, determined from the Elodie survey (S. Udry, communication at the XVI Canary Islands Winter School) is:

  0.7±0.5% of the surveyed stars have planets with periods below 5 d,

  4.0±1.1% with periods below 1500 d (4.1 y) and

  7.3±1.5% with periods below 3900 d (10.7 y).

- The **secondary mass function** is increasing towards low-massive planets, while it also increases toward stellar companions with masses $\gtrsim$0.1 $M_\odot$ (see, e.g. Halbwachs et al. 2003). There is a noticeable lack of brown dwarf companions orbiting close to their host star, which is commonly referred as the "brown dwarf desert". This might point towards a different formation mechanism for the stellar and the planetary companions.

- The **eccentricities** of most of the planets with semimajor axis above 0.06 AU are distributed almost uniformly between 0 and 0.7. All planets with lower semimajor axis reside in circular orbits (see Goldreich & Soter 1966 for an estimation of the circularization timescales). The origin of the eccentricities for single planets is not well understood (see Marcy et al. 2003 and references therein for plausible mechanisms).

- The **stellar metallicity** of the host stars seems higher for stars with detected planets than for those without detected planets (see for Santos et al. 2003 and Israelian 2003 for reviews on studies on the iron content, and on other metals, respectively). For instance, an homogeneous spectroscopic study of the [Fe/H] for 98 exoplanet host stars revealed that, while only about 3% of the stars in the CORALIE sample were found to be orbited by a planet, this number increased to 25% for stars with [Fe/H] above +0.3 (Santos, Israelian, & Mayor 2004). This might be telling us that the metallicity plays a key role in the formation of giant planets; in particular, there seems to be a need for a high metal content to form massive planets (M>4 M_J, Udry et al. 2002).

- The **period-mass distribution** reveals a lack of massive planets in short period orbits (Udry et al. 2002, Zucher & Mazeh 2002). Furthermore, there seems to be a shortage of planets in the 10-100 d period range, and a lack of light planets ($M_p \sin i$ <0.75 M_J) in orbits with periods larger than ~100 d (Udry, Mayor, & Santos 2003). These authors provide possible implications in the distribution of these effects, which seem to be in agreement with the current migration scenarios. Another characteristic of this distribution is an apparent "pile-up" of planets with periods in the 3-3.5 d range. Roughly half of the planets with periods below 10 d have periods in this short range, which may also be providing clues for the migration history of these objects (Gaudi, Seager, & Mallén-Ornelas 2005).

1.1.5 Microlensing

Planets orbiting around other stars can also be detected with the gravitational microlensing effect (Mao & Paczyński 1991; Gould & Loeb 1992). When a star (the *lens*) passes in front of a background *source*, this effect causes a magnification with a well known symmetrical light curve profile. If the star is orbited by a planet, it will also leave a signature on the light curve, which can even potentially serve to discover earth-sized planets (Bennett & Rhie 1996). Several projects have followed this approach (MACHO: Alcock et al. 1993, PLANET: see, e.g., Kubas et al. 2005 and references therein, OGLE: Udalski 2003b, MOA: Bond et al. 2001, MPS: Rhie 2001). Bond et al. (2004) claim the first confirmed detection of a planetary microlensing event (Figure 1.2) detected from two different sites (the event was named OGLE 2003-BLG-235/MOA 2003-BLG-53, O235/M53 hereafter). The shape of the event can provide the mass ratio between the star and the planet, and the distance of the planet to the star at the moment of the event. Unfortunately, these events are unique, and almost impossible to be observed repeatedly. Also, the blend between the source and the lens (which is the system star-planet) makes it difficult to measure the characteristics of the star, and thus to determine the planetary mass. In the case of O235/M53, the proper motion of the star (lens) should allow resolving lens and star in about 10 years, if adaptative optics are used (Bond et al. 2004). Only at that time will the assumed main sequence nature of the lens star be proven.

Apparently, the power of this method resides in its ability to detect planets in many different systems (Bennett & Rhie 2002), which include planets in very wide orbits, low mass planets, and even planets in other galaxies. A space mission proposed by these authors, using a 1-2 m aperture space telescope to monitor $\sim 10^8$ Galactic Bulge main sequence stars, should allow the

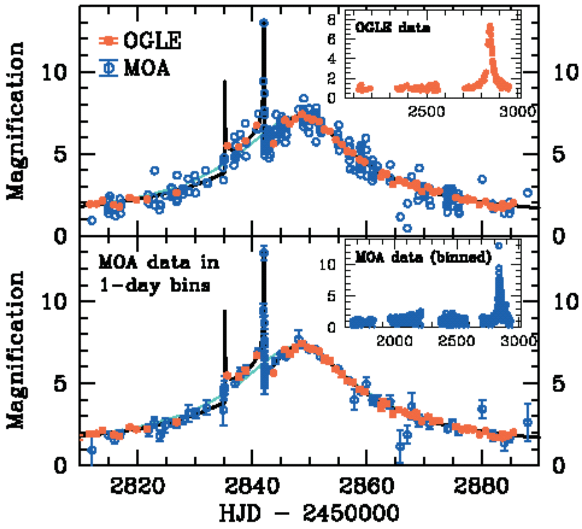

FIGURE 1.2— Light curve with best-fitting and single-lens models of O235/M53 (from Bond et al. 2004).

determination of the average number of planets per star down to 0.1 $M_{\oplus}$ at separations from $\sim$0.7 AU to ∞ for terrestrial planets and from 0 AU to ∞ for giant planets, among other scientific outputs.

1.1.6 Direct imaging

Direct observations of exoplanets face the difficulty of the high contrast between the light coming from the star and from the planet, which is of the order of $\sim 10^9$ in the optical and $\sim 10^6$ above $\sim$10 μm, for a Jupiter-like planet in a Jupiter-like orbit. Coronography and interferometry is planned at the different largest telescopes, both from ground and space (see Lawson, Unwin, & Beichman 2004, table 6, of the NASA TPF Precursor Science document for a review[4]). The most sensitive cases are young big planets orbiting far out from the parent star (d$\gtrsim$50 AU), around nearby stars. These detections, are thus complementary to those of the radial velocity and transit searches, which are more sensitive to planets close to the central star.

A promising candidate for the first detection of a exoplanet with direct imaging techniques is the candidate planetary companion to 2MASS1207334-393254 (hereafter 2M1207, Chauvin et al. 2004). It was detected using the

[4]The file can be retrieved at http://planetquest.jpl.nasa.gov/TPF/tpf_index.html

VLT/NACO adaptative optics system. It is apparently orbiting at a distance of ∼55 AU of the ∼25 M_J brown dwarf 2M1207. Near Infrared photometry (Figure 1.3, left) and spectroscopy are compatible with a spectral type of the companion of L5-L9.5, which places the object in the planetary regime with a mass of M=5±2 M_J, according to different evolutionary models, and a temperature of T_{eff}=1250±200 K (Chauvin et al. 2004). A later study with the HST seems to confirm the planetary nature of this candidate (Schneider et al. 2005, Figure 1.3, right).

New observations with the same optical configuration, taken at three different epochs, show that the candidate shares the same proper motion as the brown dwarf, and thus it is not, with a high confidence level, a stationary background object (Chauvin et al. 2005, accepted).

Another massive planet or minimum mass brown dwarf has been reported recently by the same investigation group, around the young nearby star AB Pic (Chauvin et al. 2005b, accepted). It was detected as a faint, red source located 5.5″ South of the AB Pic star, and apparently it also shares the same proper motion. The evolutionary models predictions, based on the JHK photometry, indicate a mass of 13 to 14 M_J for this object, if its age is ∼30 Myr.

The masses and sizes of these directly detected objects rely on predictions from evolutionary models (such as Burrows et al. 1997, Chabrier et al. 2000, Baraffe et al. 2002), which depend on hard-to-measure estimates of the age of the system. Thus, these mass measurements of the planets do not achieve the precision obtained by the radial velocity surveys.

1.1.7 Astrometry

As in the case of the radial velocity searches, this method relies in the gravitational wobble induced by a planet in its star. If D is the distance to the star (in parsecs) and a is given in AU, then the observed wobble is:

$$r(marcsec) \sim 1000\frac{M_p a}{M_s D} \tag{1.4}$$

It should be noticed that this technique then favors the detection of massive planets in large orbits around nearby stars. If we were observing our Solar System at a distance of 10 pc, then the wobble induced by Jupiter would have a maximum amplitude of r=500 $\mu arcsec$; Uranus would move the Sun by r=100 $\mu arcsec$, and the Earth only r=0.3 $\mu arcsec$.

In this technique, the movement of the star is measured directly from the center of the stellar profile in one image, and thus needs systems with superb resolving power. This implies the use of interferometry, of space-borne telescopes, or both. For this reason, this technique will provide excellent tests and

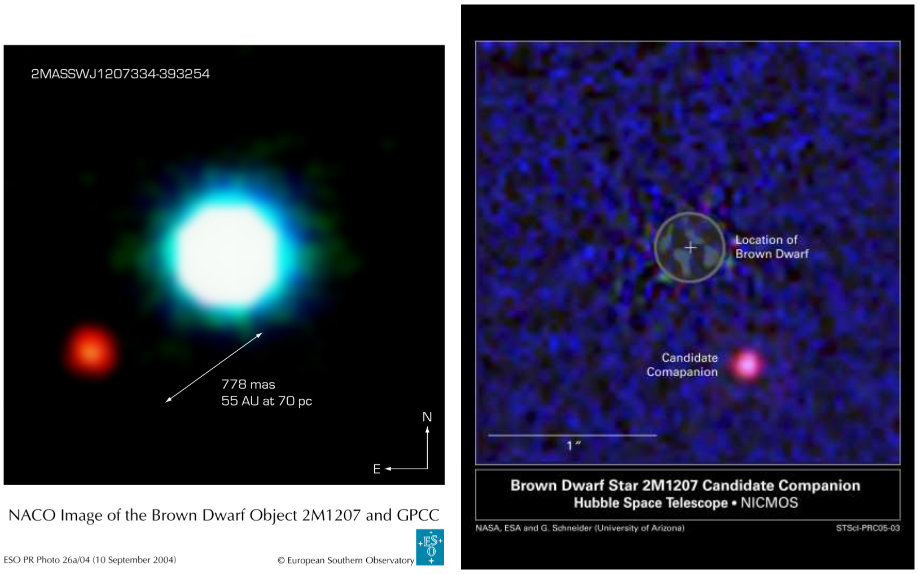

FIGURE 1.3— Left: The possible first exoplanet detected by direct imaging, around the brown dwarf 2M1207, showed in blue (Chauvin et al. 2004). Right: confirmation of the red object with HST data, by Schneider et al. (2005).

technology for the future space interferometric missions, such as Darwin-TPF (see, e.g. Fridlund, Henning, & Lacoste 2003), aimed to take images and spectra of Earth-like planets around nearby stars. But, it seems that it will be very difficult to measure the center of a star with an accuracy better than 1 $\mu arcsec$, because of distortions in the star's image created by stellar spots.

As these lines are written, there has been only one important published success of the astrometric method, when it was used to estimate the inclination of the planet around the M4V star GJ 876 (Benedict et al. 2002). To study the perturbation on the star caused by the most massive planet (1.89 M_J) in the system, GJ 876b, the Fine Guidance Sensors (FGS) on-board HST were used to estimate the amplitude of the astrometric perturbation of the planet as r=250$\pm$60$\mu arcsec$. As a direct consequence, and knowing the orbital parameters (P=61 d, a=0.21 AU, e=0.1, minimum mass=1.89 M_J) from radial velocity measurements (Delfosse et al. 1998, Marcy et al. 1998), the orbital inclination of the planetary companion was estimated as 84$\pm$6°, which, together with the minimum mass determination, resulted in a measured mass of the object of M_p=1.9$\pm$0.5 M_J.

1.2 The transit method

The first reference about the transit method is given in Struve (1952). If a planet with a radius R_p is seen (from a far enough place, such that the perspective effects are negligible) crossing the disk of a star with radius $R_\star$ (causing an event called *transit*), then the flux of the star will decrease by:

$$\Delta F_s = \frac{{R_p}^2}{{R_s}^2} \tag{1.5}$$

In the case of Jupiter passing in front of the Sun, this ΔF_s would be $\sim$1%, that is easily detectable with ground-based photometry. The Earth would produce an $\sim$0.0084% transit, which can be detected with space telescopes (Brown et al. 2001), but is not currently possible from ground. Assuming a circular orbit, the transit would last (Seager & Mallén-Ornelas 2003):

$$t_T = \frac{P}{\pi} \arcsin\Big(\frac{R_s}{a \sin i}\Big\{[1 + (R_p/R_s)]^2 - [(a/R_s)\cos i]^2\Big\}^{1/2}\Big) \tag{1.6}$$

where P, a and i are the period, radius and inclination of the planet's orbit. The inclination is the angle between the normal of the orbital plane and the line of sight. This means that $i = 90°$ is for a planet crossing the star through the middle (solid light curve in Figure 1.4 and 1.5). The typical transit durations for Hot Jupiters are 2-3 hours. Assuming circular orbits for the planets, and with a first order approximation M_s=R_s (in Solar units), Figure 1.6 plots the maximum duration of a 1 R_J planetary transit as a function of the mass of the star and the period of the planet. This maximum duration can be used as a tool to discard false positives in transit searches.

For such an effect to be observable, the orbit of the planet must cross the line of sight of the star. The probability for this to happen is:

$$P_{tran} = \arctan\frac{R_s + R_p}{a_p} \sim \frac{R_s + R_p}{a_p} \tag{1.7}$$

which is low for planets such as Jupiter in our Solar System (P_{trans}=0.089%), but can be as high as 10% for the Hot Jupiter class objects. The existence of this kind of objects, orbiting $\sim$0.7% of the main sequence stars in the solar neighborhood (see Section 1.1.4), and the relatively high probability of transits, have motivated a number of transit searches for exoplanets (see Horne et al. 2002, for a review[5]).

[5] A list of the transit searches is available at: http://star-www.st-and.ac.uk/~kdh1/transits/table.html

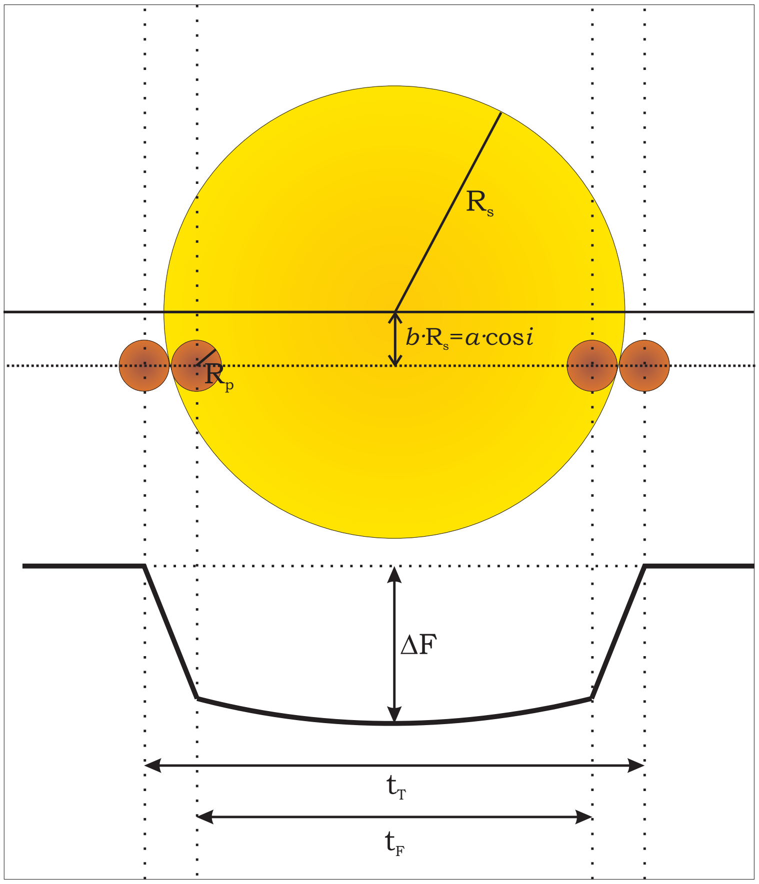

FIGURE 1.4— Schematic view of the main transit definitions. Top: The planet is plotted in four different positions (first to fourth contact). The flux of the star (black solid line) is reduced by an amount ΔF during a transit with a total duration of t_T; the duration between ingress and egress is t_F, and it is also referred as the "flat part" of the transit. The slight curvature of this part is a consequence of the star's limb darkening. Also plotted is the impact parameter b, where the definition of the inclination angle i is represented in Figure 1.1.

The first transiting planet, HD 209458b, was discovered in 2000 (Charbonneau et al. 2000, Henry et al. 2000), but it had been previously detected with the radial velocity method (Mazeh et al. 2000). We will treat this object in detail in Section 1.3.

The success of these transit searches (discovering planets with the transit method, not previously known from any other technique) came from the OGLE-III team (Udalski et al. 2002, 2002b, 2002c, 2003, 2004), who have at this time

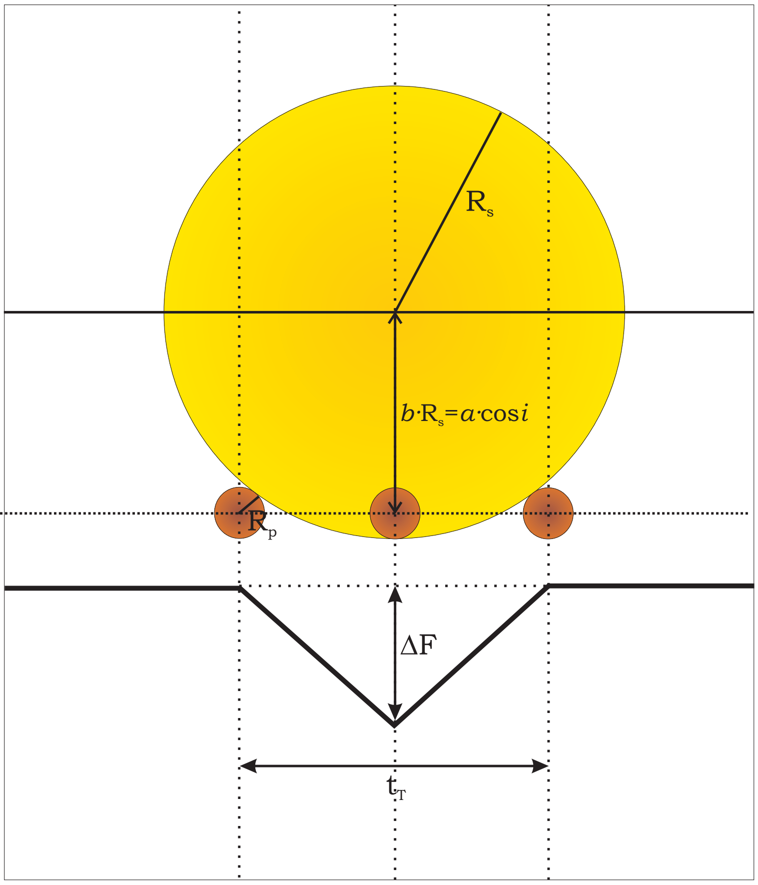

FIGURE 1.5— Same as Figure 1.4, for the case in which the planet is never projected completely on the stellar disk is plotted in the bottom part. In this case, there are no second nor third contacts, an thus there is no "flat part" of the transit (i.e., $t_F = 0$).

published a list of 177 transiting planet candidates. This project uses a 1.3 m telescope placed at the Observatorio de La Silla in Chile, to monitor dense fields for long period of times, with I magnitudes ranging from 13.5 to 17. This places the bulk of the stars at typical distances of ∼1000 pc. Further follow-up works demonstrated that the vast majority of these candidates turned out to be false positives, but 5 planets have been detected to date (OGLE-TR-56b: Konacki et al. 2003a, OGLE-TR-113b and OGLE-TR-132b: Bouchy et al. 2004, independent confirmation of OGLE-TR-113b: Konacki et al. 2004, OGLE-TR-111b: Pont et al. 2004, OGLE-TR-10b: Konacki et al. 2005). Three of these planets, (OGLE-TR-56b, OGLE-TR-113b, OGLE-TR-132b),

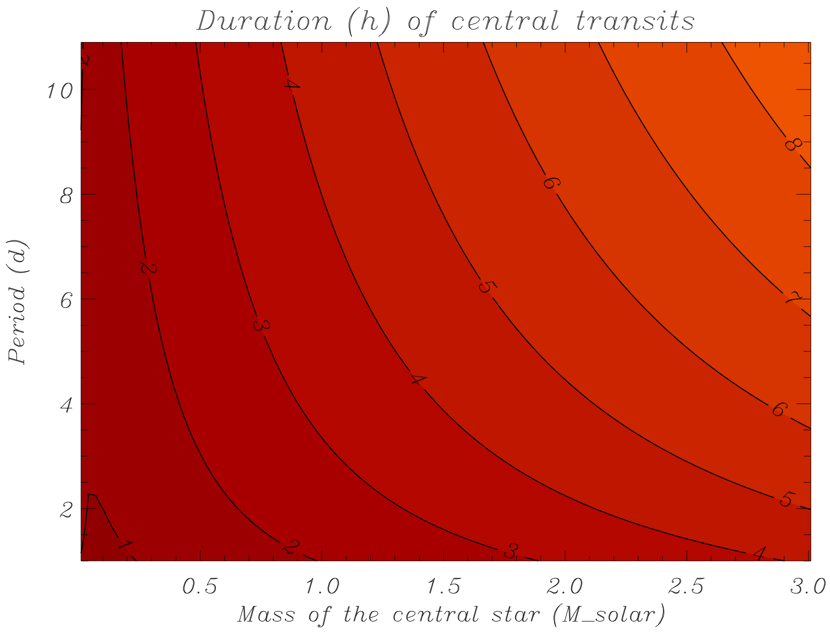

FIGURE 1.6— Maximum duration (in hours) of a central (i=90°) transit, as a function of the star's mass (in Solar units) and the planet's period (in days). Circular orbits and $M_\star$=$R_\star$ (main sequence stars) have been assumed.

apparently orbit their stars with shorter periods than had ever been observed with the radial velocity surveys. This fact led to several authors to group these objects under the terminology of "Extremely Hot Jupiters". As can be seen in Equation 1.7, the probability of observing transits from Earth is bigger as the planet is closer to its host star.

The advantages of these deep-field transit searches are that the population of main sequence stars is constituted of smaller stars on average, which can lead to the discovery of smaller planets. Also, differential atmospheric extinction problems are less important as the field of view gets narrower. The major drawbacks are the difficulty of the follow-up observations and thus the precision with which the planet's parameters can be known. The kind of studies performed in HD 209458 (discussed in next Section) are difficult, if not impossible, to repeat in these much fainter stars.

1.2.1 The measurable parameters

From the shape and period of the photometric transit (depth of the transit ΔF, total duration t_T, duration of the flat part of the transit t_F, period P), four measurable parameters can be calculated (Seager & Mallén-Ornelas 2003):

The planet to star radius ratio:

$$\frac{R_p}{R_s} = \sqrt{\Delta F} \tag{1.8}$$

The impact parameter b:

$$b \equiv \frac{a}{R_s}\cos i = \Big\{\frac{(1-\sqrt{\Delta F})^2 - [\sin^2(t_F\pi/P)/\sin^2(t_T\pi/P)](1+\sqrt{\Delta F})^2}{1-[\sin^2(t_F\pi/P)/\sin^2(t_T\pi/P)]}\Big\}^{1/2} \tag{1.9}$$

The ratio $a/R_\star$:

$$\frac{a}{R_s} = \Big\{\frac{(1+\sqrt{\Delta F})^2 - b^2[1-\sin^2(t_T\pi/P)]}{\sin^2(t_T\pi/P)}\Big\}^{1/2} \tag{1.10}$$

And the stellar density, assuming $M_p \ll M_\star$:

$$\rho_s \equiv \frac{M_s}{R_s^3} = \Big(\frac{4\pi^2}{P^2G}\Big)\Big(\frac{a}{R_s}\Big)^3 = \Big(\frac{4\pi^2}{P^2G}\Big)\Big\{\frac{(1+\sqrt{\Delta F})^2 - b^2[1-\sin^2(t_T\pi/P)]}{\sin^2(t_T\pi/P)}\Big\}^{3/2} \tag{1.11}$$

In these formulas limb darkening has not been considered and circular orbits have been assumed. Combining the measured inclination i (which can be extracted from Equations 1.9 and 1.10), with information on the orbit that results from radial velocity measurements (Equation 1.3), it is possible to solve the degeneracy between the mass and the inclination, and get the exact mass of the planet. Assuming a radius for the star (for instance, from the spectroscopic information and the values tabulated in Cox, 2000), and using Equation 1.8, the radius of the planet can be measured. Combining these two physical quantities, it is possible to measure the mean density of the planet.

1.2.2 Expected detection rates

How many stars do we need to survey to achieve significative chances to detect a transiting planet? How many *false positives* (stellar systems) do we expect to identify in such a survey?, and how can we identify them? The answer to this last question will be treated in detail in Chapter 3, while the other two questions are the subject of a work by Brown (2003). In that work, the possible stellar systems that could produce signals resembling those of transiting planets were categorized in a tree structure, which was defined by the answers to the questions:

- Is the primary of the eclipsing system a main-sequence star (M) or a giant (G)?
- Is the secondary a main-sequence star (S) or a Jovian planet (P)?
- Is the light from the binary undiluted by a third star (U) or diluted (D)?
- If diluted, is the third star a foreground object (F), or is the system a bound triple (T)?

The main configurations that could produce signals similar to the ones produced by a transiting planet are five: MPU (the target of a survey: transiting planets), MSU (grazing transits in systems of two main-sequence stars), MSDF and MSDT (eclipsing systems whose depths are diluted by a third star), and GSU (transits of giants by main sequence stars).

Probability densities for each of these cases were calculated by Brown (2003), under a set of reasonable assumptions and simplifications that could modify the final expected detections by factors of a few. For instance, the luminosity of the secondary component in an eclipsing system was neglected, and circular orbits were assumed. The first of these assumptions might affect the results when compared to the surveys, as the detection of a secondary eclipse in the data is a useful tool to identify a false positive (see Chapter 3).

Integrating the estimated probability densities over all stellar types, over periods in the range 1 d$\leq$P$\leq$30 d, over relative depths 0.01$\leq \delta \leq$0.05, and over transit durations 0.06 d$\leq d \leq$0.25 d, assuming a confusion radius of $20''$, and a limiting R magnitude of 12, Brown gets the results summarized in Table 1.1, which prints the expected detection rates per 10^4 surveyed stars. Detections of at least 3, 2, or 0 transits are printed in that table (0 detections would mean that there are eclipses of that category in the surveyed stars, but they were not observed, i.e. the total number of stars in that category), assuming a single-site typical observing campaign (one STARE run on a field of Cygnus, with 211 h of observation on 38 individual nights, spread over an interval of 91 days). All the calculations were made assuming the observed field was in the Galactic plane. Two consequences of these estimations are the need to improve the duty cycle in transit searches (such as combining data from several telescopes located at different longitudes), and to establish rejection tests that help to identify the false positives (Chapter 3 of this work is devoted to this objective). These are

TABLE 1.1— Expected detection rates for a survey such as STARE per 10^4 stars. From Brown (2003).

Category	n≥0	n≥2	n≥3
MPU	1.43	0.74	0.39
MSU	4.56	2.92	2.27
MSDF	1.90	1.52	1.26
MSDT	1.64	1.20	0.98
GSU	0.00	0.00	0.00

expected to be more numerous than real transiting planet detections, a result that is strongly supported by transit surveys up to date (for instance, the case of the OGLE survey discussed before, or our own work discussed later).

1.3 HD 209458b

Currently, the best-known and best-studied exoplanet is orbiting around the G0V star HD 209458. In this section we describe several studies carried out on this planet, which constitute a benchmark in the field.

The planet was discovered (Mazeh et al. 2000) with the radial velocity technique. The spectra were taken using both the HIRES (Vogt et al. 1994) and ELODIE (Baranne et al. 1996) spectrographs, and completed with spectra from CORALIE (Queloz et al. 2000).

In September 1999, the STARE telescope was used to monitor the first transits of an exoplanet around its star (Charbonneau et al. 2000; Figure 1.7). An independent ingress was observed by Henry et al. (2000).

At that moment, there were only 11 known exoplanets, all of them detected with the radial velocity method (apart from the pulsar planets described in Section 1.1.2). There was also some skepticism from diverse authors, like the observations by Gray (1997) apparently showing distortions in the spectral line bisectors; if confirmed, these would argue against the planetary origin of the radial velocities observed in these stars. These observations could not be reproduced (Gray 1998, Brown et al. 1998), and a definite demonstration of the existence of these exoplanets to the more skeptical community came with the detection of transits in HD 209458. These allowed a determination of the planetary radius.

Combining the data with the radial velocity observations, which give $M_p \sin i$, the mass was measured, and thus the mean planetary density (0.38 g/cm^3 in the work of Charbonneau et al. 2000; refined to 0.35 in Brown et al. 2001). This measurement confirmed the suspected gaseous nature of these objects. Several

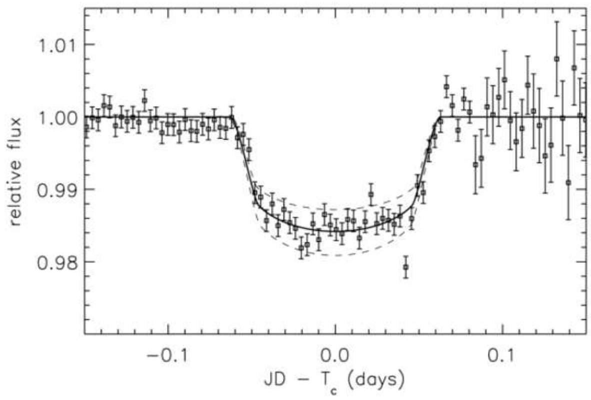

FIGURE 1.7— Transit of HD 209458b observed with the STARE telescope, in September 1999. The curvature at the bottom of the transit is a consequence of the star's limb darkenning. Points are 5 min bins, and the error bars are the standard deviations of the mean in each bin. From Charbonneau et al. (2000).

ground-based multi-color observations were conducted to improve the stellar and planetary parameters, and to measure the limb darkening coefficients, for the first time in a star other than the Sun (Jha et al. 2000, Deeg, Garrido, & Claret 2001).

The best quality light curve was obtained using the spectrograph STIS on board the HST telescope (Brown et al. 2001; Figure 1.8). Attaining an unprecedented precision of $1.1{\cdot}10^{-4}$ per sample point, enough to identify a transit of an Earth-sized object, they improved the parameters of HD 209458b: $R_p = 1.347 \pm 0.060$ R_J, an orbital inclination of $i = 86°.6 \pm 0°.14$, and a stellar radius of $R_s = 1.146 \pm 0.050$ $R_\odot$. The residuals of the fit were used to search for satellites and rings around the planet. Upper limits on the mass and sizes of potential satellites were established in 3 $M_\oplus$ and 1.2 $R_\oplus$, respectively. The presence of large opaque rings was also constrained, to a lesser degree, establishing a maximum size for this structures (if present) of 1.8 radii of the planet.

The spectral information contained in these data set was used by Charbonneau et al. (2002) to detect for the first time an exoplanet's atmosphere. The technique used was transit spectroscopy (described later in this Introduction), whose basic idea consists of measuring the wavelength dependence of the radius of the exoplanet. This dependence is caused by different opacities of the atmosphere components. In a region close to the Na D lines at 589.3

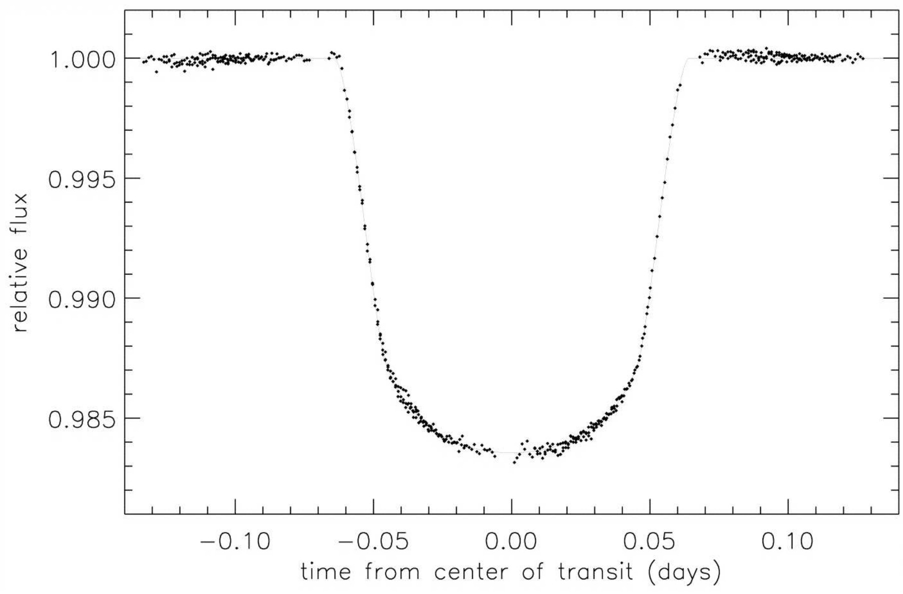

FIGURE 1.8— HST observations of transits of HD 209458 b. The precision per sample point achieved is $1.1{\cdot}10^{-4}$. From Brown et al. (2001).

nm, they compared the ratio of the star's spectrum outside of transit to the spectra when the planet is crossing the disk. Thus, in relative flux, the transit was $0.00023{\pm}0.00006$ deeper in the region where the sodium absorption was expected. The strength of the sodium absorption was $\sim$3 times weaker than that predicted by a fiducial model, which assumed solar sodium abundance for the star. The authors interpret this discrepancy in the measured sodium absorption as a consequence of a high cloud deck, a low atomic sodium abundance, or a combination of both effects. Also, the effect of the strong UV bombardment on the planet might play an important role, with possible formation of photochemical hazes.

Later on, Vidal-Madjar et al. (2003) used STIS on board HST to observe the Lyman-α emission line of the star. When the planet was transiting, the emission was reduced by a $15{\pm}4\%$ (1σ), which according to these authors is a proof for an extended upper atmosphere on HD 209458b. The implied radius of the planet at these wavelengths is 4.3 R_J. This radius suggests that the upper atmosphere material fills and overflows the Roche lobe (which has a radius of 3.6 R_J. Thus, the atmosphere of this planet is in process of evaporation due to the heavy UV-bombardment of the star at such close distance. They estimate the evaporation rate as 10^{10} g/s. In a later work (Vidal-Madjar et al. 2004), they used a lower resolution (and wider spectral range) band to search for different species in the planetary upper atmosphere. The detection of absorption in the H I lines at a 5±2% level in this work is consistent to that detected in the previous study, due to the lower resolution in the line. In this second search, they claim the detection of absorption also in the O I (13±4.5%) and C II (7.5±3.5%) lines. Surprisingly, these results would imply that these components are higher in the atmosphere than the less-massive H I, which seems unlikely, and can not be explained if the molecular diffusion dominates at high altitudes, nor if an extreme eddy diffusion transport is able to transport the oxygen and carbon up to the Roche level. To explain the observation, the authors need a mechanism that is able to transport oxygen and carbon up to about the Roche lobe while maintaining their velocity dispersion of at least ~10 km/s. They propose that the H I is escaping at a high rate, and the hydrodynamical flow of this process drags up the other species, preserving their abundances. This mechanism has been called "blow-off" (Watson, Donahue, & Walker 1981), and it is supposed to keep velocity dispersions for the oxygen and carbon similar or greater than the sound speed (~10 km/s at 10000 K, which is the estimated upper atmosphere temperature). With these velocity dispersions, the conditions at the upper atmosphere would be such that the whole stellar line would be absorbed by the planetary carbon and oxygen, thus allowing a 10% absorption if they flow up to the Roche lobe.

1.4 On the radii of the transiting planets

One important physical parameter that can be obtained with the transit method is the radius of the planet. Soon after the discovery of 51 Peg (Mayor & Queloz 1995), models for strongly irradiated planets appeared in the literature (Guillot et al. 1996). These models predicted that these short period planets, with effective temperatures above 1000 K, should have their radii significantly larger than Jupiter. The first measurement of an exoplanet's radius came with the discovery of HD 209458b's transits (Charbonneau et al. 2000; Henry et al. 2000). The most precise numbers for its radius are given in the work by Brown et al. (2001), where the high-quality HST photometry allowed to fit independently R_s and R_p. The measured radius in that work was $R_p = 1.347 \pm 0.060$ R_J. A subsequent analysis of the same HST data by Cody & Sasselov (2002), state a value of $R_p = 1.42 \pm 0.10$ R_J. In any case, the published value proved that the planet was a gas giant planet, composed basically of hydrogen. A theoretical study of the radius of HD 209458b by Guillot & Showman (2002), required unrealistically hot temperature of the deep atmosphere of the planet in order to reproduce the observed radius. Under more realistic temperature conditions, an extra source of energy seemed to be lacking, to make the radius match the observations. These authors proposed one mechanism to account for this extra energy: if a fraction ($\leq$1%) of the incident stellar flux is transformed into kinetic energy at the planet atmosphere, then it could be converted into thermal energy at deeper levels (tens of bars) of the atmosphere, by dynamical processes.

Other studies proposed different extra sources of energy in the planet. Bodenheimer, Lin, & Mardling (2001) also find a difference of $\sim$0.3 R_J between the observed and predicted radius (without an extra source of energy). They suggest (Bodenheimer, Laughlin, & Lin 2003) that the energy arising from ongoing tidal circularization of the planet's orbit could account for such an increased radius. This would require the presence of a yet unseen companion to HD 209458 b, which can still be consistent with the residuals of the radial velocity measurements. In fact, they obtain a good fit to the spectroscopic measurements with an eccentricity of $e \sim 0.03$. This low, but nonzero eccentricity, could explain the increased radius of HD 209458b, if a model without a core for the planet is assumed. For models with a solid core, the eccentricity needed would be of the order of $e \sim 0.1$, which seems inconsistent with the current velocity measurements. A two-body fit of the radial velocity data seems to indicate a possible second companion (companion "c") with a period of $\sim$ 80 days, and mass of $\sim$ 0.12 M_J.

In the study carried by Chabrier et al. (2004), a simple model of one-dimensional irradiation, with incoming flux deposited uniformly over the day side and non-dynamical redistribution of the incident flux because of day-night temperature differences, is found to adequately reproduce the radius of OGLE-TR-56b. But, in order to reproduce the radius of HD 209458b, a significant fraction ($\sim$0.5%) of the incident flux must be transported downward and converted into thermal energy at the radiative-convective boundary. This confirms the results by Showman & Guillot (2002). But it is still necessary to invoke an unknown mechanism able to transport kinetic energy from the top of the atmosphere downwards to the adiabat level, which lies at P$\sim$500 bar for HD 209458b and P$\sim$4000 bar for OGLE-TR-56b (18 and 23 pressure scale heights, respectively). The calculated radii and the measured values are plotted in Figure 1.9. It seems, from these plots, that this mechanism might be taking place in HD 209458b, while for OGLE-TR-56b it is not necessary to invoke any extra source of energy.

Finally, Burrows, Sudarsky, & Hubbard (2003) argue that the radius measured in a transit is systematically larger than the radius that result from the planet evolution codes. This is a consequence of the stellar photons passing

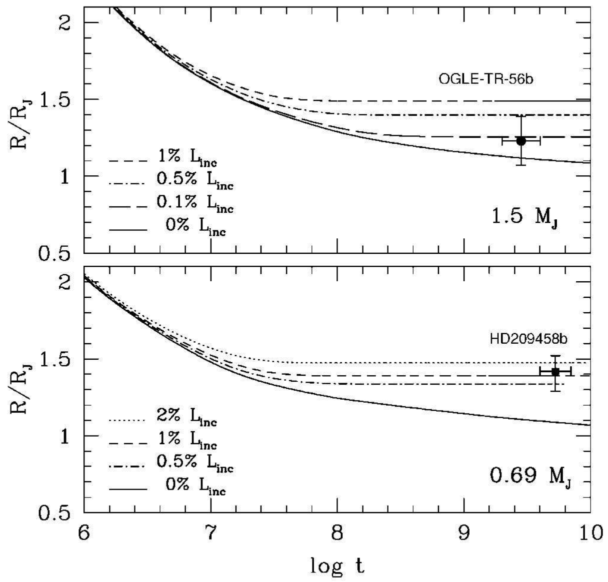

FIGURE 1.9— Evolution of the planetary radii of OGLE-TR-56 b (top) and HD 209458b (bottom), for models without invoking an extra source of energy (solid lines), and assuming conversion of several fractions of the incident luminosity into thermal energy deposited at the adiabatic level. From Chabrier et al. (2004)

obliquely to the limb of the planet. The measured radius of a transit implies an effective optical depth of $\sim$ 1. But the effective optical depth is for a chord that is parallel to the line between the centers of the planet and the star. This can be quite different from the optical depth measured radially from the center of the planet. In fact, there is a significant difference between the pressure level at which the transit beam becomes opaque (1 mbar, according to Fortney et al. 2003), and the one that is calculated for opacity equal to 1 with the models ($\sim$0.1 bar, Baraffe et al. 2003, Figure 5 in that work). Burrows, Sudarsky, & Hubbard (2003) estimated that this effect might add $\sim$0.1 R_J to the estimated radii, and, in the case that the real measurement of the radius of HD 209458b lies in the bottom part of the observational error bar, then no extra source of heating might be necessary to account for the observed radius.

To summarize, there have been three different proposed explanations for the radius of HD 209458b:

- The radius is anomalously large; the transport of a small fraction of the incident flux by kinetic energy (winds) to deep levels of the planet's atmosphere, and the subsequent conversion of this energy into thermal energy at this level can account for this increased radius. This effect might take place in all the Hot Jupiters, and consequently, all the transiting planets might show strongly inflated radii.

- The radius is anomalously large; this is due to ongoing tidal circularization, which needs the presence of a yet unidentified third body in the system. If this were the case, HD 209458b might be the anomalous case, and the next found transit planets should all show smaller radii.

- The radius is within theoretical expectations, taking into account the factors discussed by Burrows, Sudarsky, & Hubbard (2003). The newfound transiting planets, according to this approach, should all show bigger radii than estimated.

1.5 Transmission spectroscopy

The atmospheres of the transiting planets leave a signature on the observed stellar spectra as they cross the disk. The study of this signature and the extraction of physical information on the atmospheres of these object can be done with a technique called *transmission spectroscopy*. The observations of spectra in transmission are not new for exoplanets; they have been used to study binary stars (e.g. Eaton 1993), and occultations of stars by planets in our solar system (e.g. Smith & Hunten 1990). Several works have aimed to provide clues on what can be observed from the exoplanet's atmospheres with current or near future instrumentation. In this Section, we summarize the two main (and only) works on this subject: Seager & Sasselov (2000) and Brown (2001). We refer the reader to these works for detailed information.

The signal imposed by an exoplanet on the star's spectrum while it is transited is small. As a rough number, the outer parts of the planet that are not opaque to certain wavelengths (i.e. its atmosphere) are not bigger than 10% of the total planetary radius. When superposed on the star's disk, the total area that can act as a probe for the atmosphere is of the order of 10^{-3} to 10^{-4} of the star's area. This signal will be Doppler shifted by a significant amount during a transit of a Hot Jupiter, due to the high orbital velocities of these objects (for the case of HD 209458b, this Doppler shift is about $\pm$ 15 km/s). Out of the several varying sources of radiation that reach the observer from the star/planet system during the transit (namely, thermal radiation from the planet, scattered light from the day-side of the planet, and direct light blocked by the planet), the difference in direct light blocked by the planet at different wavelengths is the best diagnostic for the planet's atmosphere. The thermal contribution and the scattered light effects are at least 10 times smaller than the effect of having

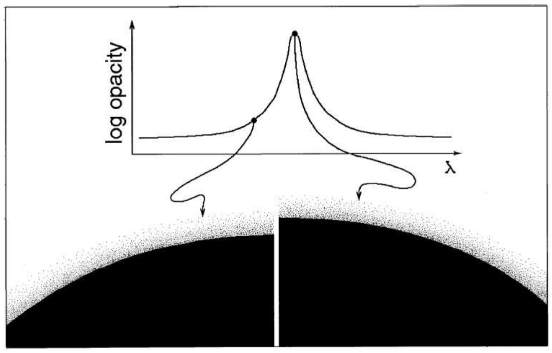

FIGURE 1.10— Atmospheric opacity (shown as a function of wavelength in the upper trace) corresponds directly to apparent radius of the planet, since in opaque regions of the spectrum, one must go to higher altitude and lower density before tangential rays are transmitted. High-opacity regions appear as absorption lines in the spectrum ratio because the planet appears larger at these wavelengths and blocks a larger part of the star's light. From Brown (2001)

material with different opacities at different wavelengths. This dependance of the planet's atmospheric opacity is translated into a variation of the observed planetary radius with wavelength (see Figure 1.10).

The main goal of the works by Seager & Sasselov (2000) and Brown (2001) was to derive theoretical expectations on the variation of the observed planetary radii with wavelength, and to seek the most promising features that might be observable with current instrumentation. To do so, Seager & Sasselov (2000) relied on a self-consistent transmission model based on atmosphere models of Hot Jupiters[6], together with assumptions on the (expected) cloud composition and grain size (10μ grains of $MgSiO_3$, Fe, and Al_2O_3). The cloud base (and cloud top) are fixed in their model once its composition and grain size is determined.

Under a slightly different approach, Brown (2001) cautions that poorly understood physical processes (such as meteorology, photochemistry, cloud processes, etc.) might be important in these objects, and thus constructs a non-self-consistent model, using reasonable assumptions when needed. His model is based on T(P) profiles provided by Sudarsky, Burrows, & Pinto (2000), and solar abundances of H, He, C, N, O, Na, Si and K. The partial pressures of the main molecules (H_2, H_2O, CO, CH_4, N_2 and NH_3) are calculated from the reactive atomic constituents (H, C, N, O), assuming thermodynamic equilibrium

[6]Described in Seager (1999) and Seager, Whitney, & Sasselov (2000), these models provide T(P) profiles, and assume an atmosphere composed of H_2, CO, H_2O and He

at each pressure level. Clouds are supposed to be composed of $MgSiO_3$, with a distribution of grains sizes that peak at 3 μm.

Neither model accounts for stellar photoionization, but Brown (2001) treats the ionization of the alkali metals at high atmospheric altitudes in a schematic way. Helium opacity is included in the model by Seager & Sasselov, but not by Brown. Both authors agree on that the likely extended atmosphere, where this compound is expected to reside, will be highly photoionized, and recombination might populate triplet states of the atom (which are long-lived). The calculation of the population of the low levels of this slow transitions would require a radiative transfer calculation involving not only He, but also H_2 and H, and it would be complicated by the near-horizontal incidence of the ionizing radiation. This led to the non-inclusion of the He opacity in the model by Brown (even if the He is included as a non-reacting component).

As final results of the calculations, both works provide expected transmission spectra for these objects. In order to visualize the dim signals of the planet, Seager & Sasselov (2000) plot the normalized spectra in-transit minus spectra out-of-transit (Figure 1.11). The work by Brown (2001) presents the ratios of spectra in-transit / spectra out-of-transit (Figure 1.12). Both works agree on the fact that the resonance lines of the alkali metals (Na and K) are promising absorption features, together with near infrared molecular absorption bands of CO, H_2O and CH_4. The He triplet line at 1083.0 nm is proposed by Seager & Sasselov (2000) as a "strong" signal, while the work by Brown (2001) doesn't quantify the absorption of this element, for the reasons stated above. Both models agree on the importance and present lack of knowledge of the composition and location of clouds, and the results are strongly dependent on this. The work by Brown (2001) further explores the possibility to measure heavy-element abundances, temperatures, and the vertical temperature structure; although these properties (and the composition and location of the clouds) tend to be somewhat degenerate.

Brown (2001) proposes a cross-correlation of observed spectra to templates from the theoretical models to establish the line strengths of the different elements.

Photoionization in his work apparently reduces the depths of the alkali metals resonance line cores, while there is little or no change in their wings. Altitude-dependent winds would also leave a signature on the spectral lines, but unrealistic values need to be considered for this effect to be detected in the next decades.

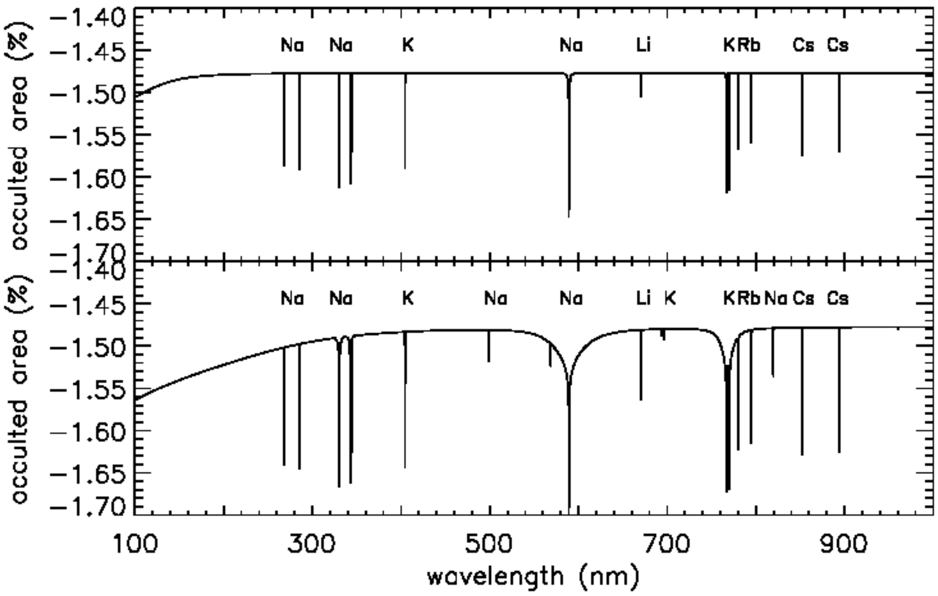

FIGURE 1.11— Upper plot: The normalized in-transit minus out-of-transit spectra, i.e., percent occulted area of the star. In this model the cloud base is at 2.4×10^{-3} bar. Rayleigh scattering is important in the UV. Lower plot: A model with cloud base at 0.2 bar. The stellar flux passes through higher pressures, densities, and temperatures of the planet atmosphere compared to the model in the upper plot. In addition, a larger transparent atmosphere makes the line depth larger. Observations will constrain the cloud depth. From Seager & Sasselov (2000).

1.6 Formation models of giant planets

Observational evidence that the mass function of young objects in star-forming regions extends down to below the deuterium burning limit (Zapatero Osorio et al. 2000) and the absence of good theoretical reasons against it, point towards the same formation mechanism for stars, brown dwarfs and isolated high mass planetary objects (fragmentation during collapse of a molecular cloud). On the other hand, the existence of a "brown dwarf desert" (no objects with masses in the brown dwarf regime orbiting close to a star) in all the radial velocity surveys, and the increasing number of planetary mass objects with smaller masses (see, e.g., Halbwachs et al. 2003) point to a different formation mechanism for orbiting exoplanets than for stars and isolated objects. The fragmentation model is not valid to explain the formation of these objects (Bodenheimer, Hubickyj, & Lissauer 2000). Out of the different formation models that have

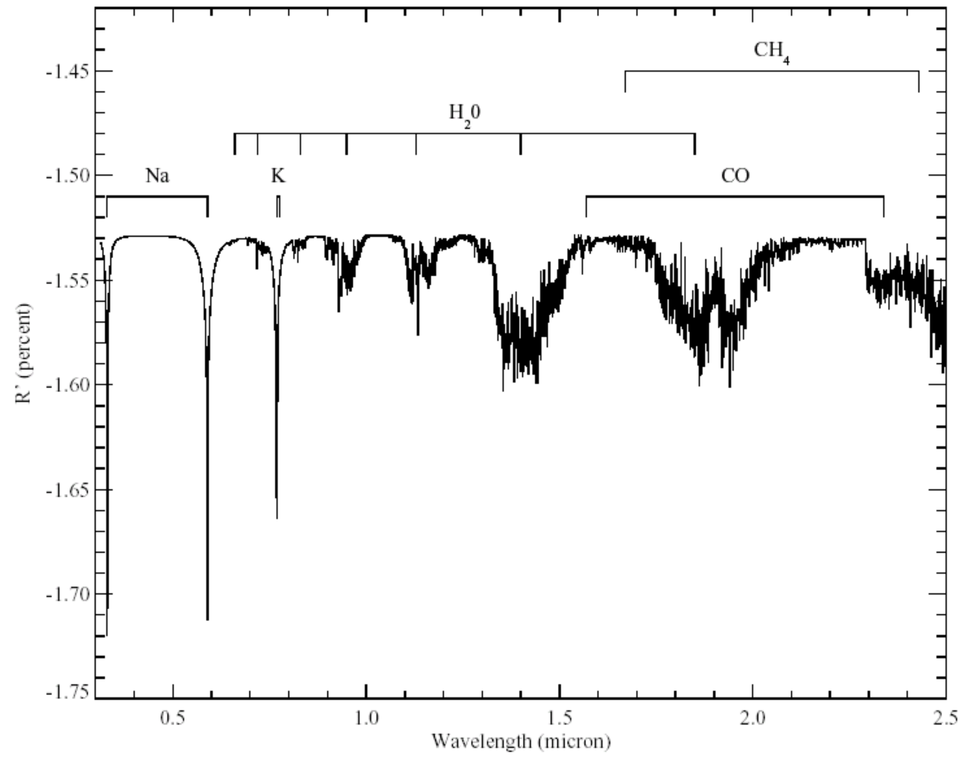

FIGURE 1.12— Fiducial model spectrum ratio vs. wavelength. The maximum value of -1.53 % corresponds to the fraction of the star's light blocked at the wavelengths where the atmospheric opacity is lowest. Over most of the wavelength range, the spectrum was computed at R = 15.000, but it is displayed here averaged and rebinned to R = 3000. Significant atomic and molecular absorption features are labeled. From Brown (2001).

been proposed (see Wuchterl, Guillot, & Lissauer 2000 and references therein for a review), the two hypotheses receiving most attention are the core instability model (or nucleated instability) and the disk instability (or gravitational instability) model.

According to the core instability model (see, e.g., Bodenheimer, & Pollack 1986), the planet is formed in a similar way as a terrestrial planet is, until it reaches a mass that allows to accumulate significant amounts of the surrounding gas in the disk. The gas accretion rate becomes comparable to the planetesimal bombardment when the core reaches a mass of $\sim$10 M_E. At this point, the gas accretion happens very fast, in a phase called runaway accretion. The primary question regarding this scenario is whether planets with small cores can accrete very massive gaseous envelopes within the lifetimes of gaseous protoplanetary disks (10^6-10^7 y, Strom, Edwards, & Skrutskie 1993, Alencar & Batalha 2002).

In the disk instability model (e.g. Cameron 1978, Boss 1997), the giant planet forms directly from the contraction of a clump formed by gravitational instability in the protoplanetary disk. It seems that this model has never been demonstrated for realistic disk conditions (c.f. Lissauer 2004). Besides, it has difficulties explaining the supersolar abundances of heavy elements in Jupiter and Saturn, and it does not explain the origin of planets like Uranus and Neptune. But the timescales for this process are smaller than those derived from the core instability model (few hundred years).

There is some theoretical controversy associated with the possibility that the planets experience orbital migration, as a consequence of the gravitational torque between the disk and the planet. This torque may allow planets to clear gaps around themselves (Goldreich & Tremaine 1980; Ward 1986; Bate et al. 2003; see Thommes & Lissauer 2005 for a review). Planetary orbits can migrate towards (or, in some circumstances, away from) their parent stars, as a consequence of angular momentum exchange between the planet and the disk. It is thus possible that planets may form at several AU away from their parent star and then migrate inwards to the locations where they are currently observed. This raises several problems, such as the necessity for a stopping mechanism to avoid the planet falling onto the star. We will not get into the details on this and we refer the interested reader to the Thommes & Lissauer (2005) review, and references therein.

1.7 Motivation for the following study

As has been explored in this Introduction, exoplanets that transit their host stars can provide us with valuable physical information, such as a mass measurement (without the degeneracy imposed by the inclination of the orbit in the non-transiting planets), and a radius estimation that is inaccessible by other means. With the occurrence of transits, a new set of follow-up studies becomes possible, as was discussed in Section 1.3. The discovery of transits in the HD 209458 system allowed the development of a series of techniques and studies that served to increase the knowledge on these objects.

However, at the time of beginning this thesis, HD 209458b still remained the only planet to produce transits, and any knowledge about its physical parameters could not be extrapolated to the rest of the known Hot Jupiters. This thesis work was intended principally to search for more transiting planets, in order to establish what is common and what is peculiar in these kind of objects. Though it seems obvious, we point out that this field of investigation is strongly governed by observations; this will be demonstrated in the following chapters.

As we saw in the previous sections, there are different proposed theories to explain the apparently "too big" size of the planet HD 209458b. Some of them would implicitly require that the newly found transiting planets should also exhibit an increased radius. This subject remained an open question until the new transiting planets were detected (even after that, it remains an open question, as we will see at the end of Chapter 5).

One important obstacle we had to overcome was to establish techniques that allow the identification of the many false positives that would arise from transiting planet surveys. These will be described in Chapter 3.

Finally, the 2004 transit of Venus provided, for the first time ever, the opportunity to test the transmission spectroscopy technique, in a object whose atmosphere is at least better known than those of the far away planets orbiting stars other than the Sun. These observations will be described in Chapter 6.

2

The STARE instrument

In this chapter we describe the STARE (STellar Astrophysics and Research on Exoplanets) project, which involves the STARE instrument (a ∼10 cm wide field Schmidt camera) and its data analysis (based on Differential Imaging techniques), needed to identify the transiting planet candidates.

2.1 Introduction: The STARE instrument

THE telescope is a field-flattened Schmidt design (Figures 2.1 and 2.2), with an aperture of 102 mm and a effective focal length of 296 mm, giving an f ratio of 2.9. To make the focal plane accessible, it has a diagonal mirror that is mounted to the aluminum tube assembly with a delrin spacer. The length of this spacer is chosen to compensate temperature-induced focus drifts. After the diagonal mirror and near the focal plane there is a system of three manually changeable filters. These were chosen to resemble the Johnson's standard filters B, V and R. Due to the poor sensitivity of the CCD detector to the blue wavelengths, the filter response of the B and V filters were shifted to the red. Thus, the absolute photometric calibrations would require special care. For our purposes, though, time series will be obtained in the R filter, and B and V color images of the stars are taken once per field (typically on a clear moon-less photometric night, with the field close to the zenith), to estimate the spectral types of the stars. Our interest will reside in the relative magnitudes of the stars obtained in the R filter; thus, these shortcomings in the absolute calibrations are of little importance.

The wave front coming out from the filter slide is not flat, and it needs to

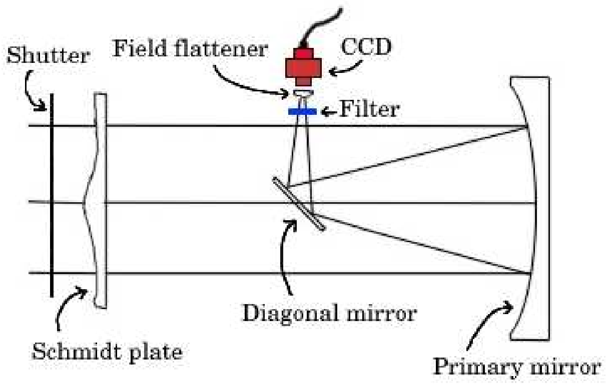

FIGURE 2.1— Optical scheme of the STARE telescope.

be flattened before it arrives to the CCD detector. This is achieved by a plano-convex lens that is oiled to the front surface of the dewar's window. In order to minimize the distance between the detector and the diagonal mirror, we placed the shutter in the entrance pupil. This is achievable thanks to the small diameter of the mirror. The main drawback of this action is that the shutter takes an non-negligible time to open an close (∼0.4 s, with several tenths of a second between the center and the corners of the frame), and this difference in exposure times needs to be taken into account in the data reduction scheme.

The CCD detector is a 2Kx2K front-illuminated Loral device installed in a camera fabricated by Pixel Vision Inc. The square pixels are 15-microns wide. It is cooled down to -35° C with a 3-stage thermoelectric cooler. The readout time is 13s at a speed of 400kHz; at this rate, the read noise is 10 electrons. We operate the system with a gain of 6.8 electrons per analog-to-digital converter unit (ADU).

The dark current of the camera at its operation temperature is ∼0.8-0.9 photoelectrons per pixel per second. To avoid negative counts, it has an additional signal (bias) that is typically 200 ADU's. This signal can be measured with null-time exposures or with a region of the CCD that is never exposed to light (the overscan region).

The sky signal at its current emplacement on the Observatorio del Teide of the Instituto de Astrofísica de Canarias, for a moon-less sky is always above 400 counts in a typical 107 s exposure. Thus, the dark and readout noises are always lower than the sky background photon noise ($\sqrt{400 * 6.8} = 52$ e^{-} $= 7.7$ ADU's).

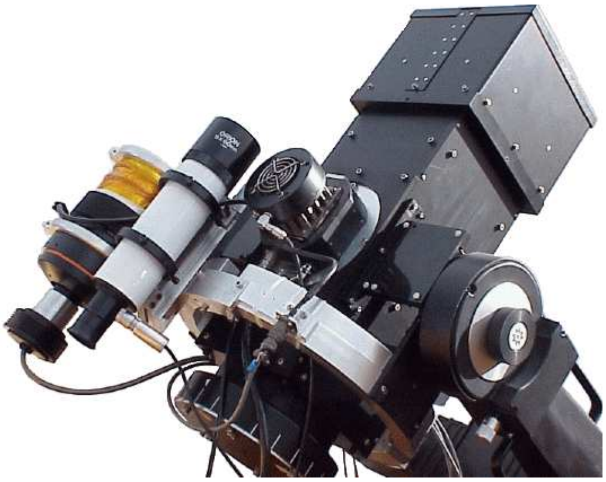

FIGURE 2.2— The STARE telescope.

With this optical assembly, the total field of view covered in the sky is 6.1×6.1 deg^2. The image scale is then 10.8 arcsec per pixel.

2.1.1 The mount

All the above components of the telescope are attached to a commercial Meade LX-200 fork mount (made for a 12-inch telescope). This mount allows continuous following of a field from dusk to dawn. But it is not precise enough as to maintain all the stars within the same 1 - 2 pixels all night. To accomplish this, the telescope has a 90 mm Maksutov reflector piggy-backed, equipped with a Santa Barbara Instrument Group ST-4 autoguider. This system takes images of a bright ($\sim$5 mag) star every 2 s, and corrects the mount drifts to guide on the star. There is flexure between the main telescope and the guiding system during a night that needs to be compensated. To achieve this, every science image taken with the main CCD is compared to a couple of 128×128 sub-images of the field[1], and corrections to the position of the star in the ST-4 camera are done if necessary. This comparisons are performed at the same cadence as the science data is arriving, which is typically once every two minutes.

The telescope and mount are inside a 3.2 m diameter Ash-Dome, which

[1]One image is the central part of a reference image taken at the beginning of the campaign. The second image is the central 512×512 pixels of the same reference image, re-sampled to 128×128 pixels.

needs to be manually opened, and it is connected to the *Cielo Nocturno* building with optical fiber. Several views of the instrumentation are given in Figures 2.3 and 2.4.

2.1.2 The computers

The UPS (Uninterrupted Power Supply), computers and data storage devices are inside the *Cielo Nocturno* building. Two linked Pentium PC computers operate the whole system: Butch and Sundance. Butch is responsible for the dome and mount control, while Sundance controls the CCD acquisition and storage. The communication between Sundance and the CCD is done with a dual optical fiber serial line. Both computers operate under Windows 98, and the user interface consists of several programs written in Visual C++. These invoke scripts which are based on "Orchestrate Scripting Software" for the telescope control, and "AutomaDome" for the dome control; both are by Software Bisque. STARE's operation is not fully autonomous, however. It depends on an operator who decides to start the system if observing conditions are acceptable. The operator has to remove the telescope covers, open the dome manually, and start a telescope control script. This script will begin the observations at a specified hour, once a sample field reaches a prescribed altitude or when the sky is dark enough. The telescope will then perform the entire observing programme autonomously. At the end of a night, or once a sample field moves too low, the telescope parks itself in a safe position (no direct sunlight on the telescope), and waits for the return of the operator. He/she will then close the dome and create copies of the acquired data. The operator is also required to monitor meteorological conditions and has to shut down the instrument in case of adverse conditions. These tasks are performed by operators who are responsible for several instruments at Teide Observatory, avoiding the need for dedicated manpower.

2.2 Data Analysis

The state-of-the-art concept to perform photometry on crowded CCD images is the Differential Imaging Analysis (Alard & Lupton 1998, Alard 2000). Basically, it consists of choosing one high quality image of the field, taken at the best possible conditions of seeing and atmospheric transparency. We will refer to this image as the reference image. Every science image is shifted, interpolated to the same grid as the reference frame and convoluted with a kernel image, in order to correct for possible seeing and focus variations, and then subtracted from the reference image. The photometry is later done on the resultant image, which should only have significant signal in the objects whose flux has changed

FIGURE 2.3— Different views of the STARE instrument. From top left to bottom right: dome, telescope shutter, out-of-limits sensor, control computers, mount keypad, telescope electronics rack.

from the reference image. These include variable stars, asteroids, artificial satellites and trailing stars, among others. In this section, we describe in more detail all the process, from the calibrated images and the standard star list to the final light curves.

2.2.1 Calibrating the images

All the science images are corrected for the usual effects needed to perform CCD photometry, namely:

- Bias subtraction. 20 images with the shortest exposure time allowed by the software (1s) and the telescope covered are a relatively good measurement of the ideal 0s exposure time image. They are taken every observing night, and averaged (and sigma-clipped) to produce one master bias im-

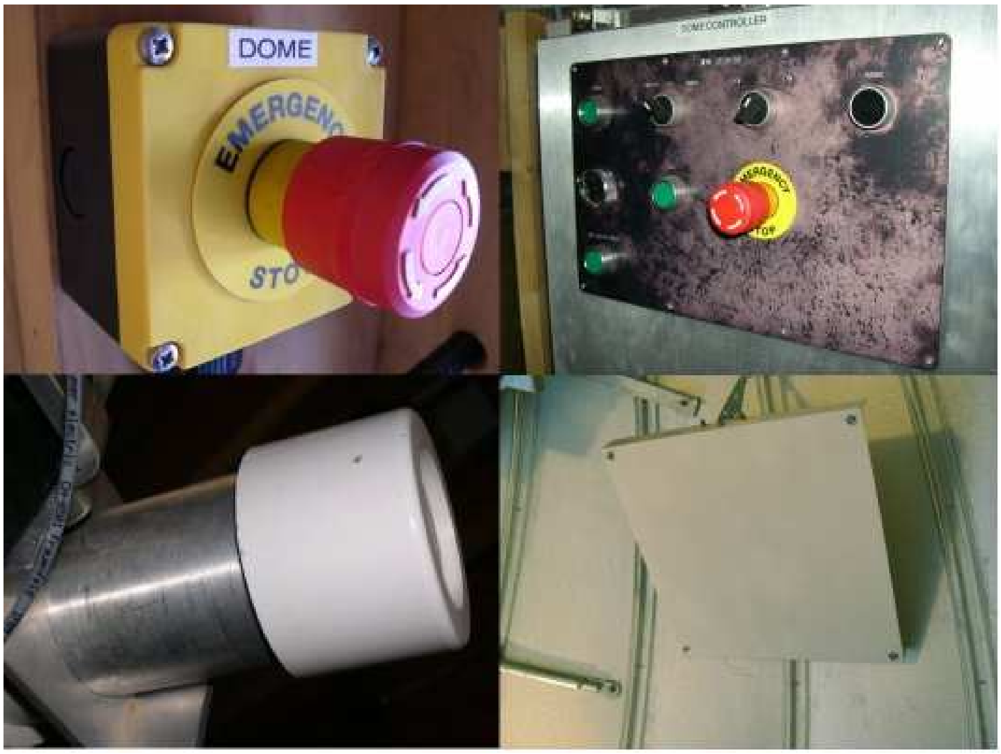

FIGURE 2.4— Different views of the STARE dome. From top left to bottom right: emergency stop button, dome control panel, flat-field lamp, flat-field screen.

age for that night. This image is zero-scaled with the overscan region of every science image taken on that night, and subtracted from it.

- Flat field correction. The differences in the response of the different CCD pixels, and the effect of the vignetting affecting the telescope are corrected with a division of every science image by an image of an uniformly illuminated field. These images are taken following two approaches: images taken at twilight, and images taken pointing to a screen located at the dome, which is illuminated by a lamp. The twilight images provide a measurement of the large-scale structures, but it is difficult to accumulate enough photons to measure the small-scale gain structure accurately. This is achieved with the dome images, in which more photons can be accumulated, but it is hard to achieve a constant illumination throughout the field of view. Thus, a combined flat-field is constructed using the sky-twilight images as a measurement of the large-scale structures, while the small-scale structures are measured with the dome flats. Typically, one master flat field, constructed using a combination of all the available flat images in the observing period of one specific campaign, is used to correct all the images of the campaign.

- Dark current correction. The non-zero temperature operation of the CCD causes several ADUs to arise from thermal action. The signal depends on the temperature of the CCD and on the pixel impurities. This signal can be measured taking long exposures with the telescope covered (the electrons due to dark current accumulate at a constant rate for each pixel). All the signal appearing in these images is the bias + the effect of the temperature. Typically, 20 images of 600 s exposure time are taken in cloudy nights, and averaged to get a master dark image that is scaled to the science images exposure time before being subtracted.

- Shutter correction. The non-negligible open-close time of the shutter located at the entrance of the telescope makes the final exposure time of the science images be bigger at the center of the images than at the corners. Dome flat field images taken with the same illumination and with different exposure times are used to build an artificial image that will contain the shutter open+close time at every pixel.

Nine 128x128 subimages of a reference image (ref1) are chosen to estimate the translation, rotation and scale changes on a nightly basis. The position of one reasonably isolated star in the field is used to get a first rough measurement of the sky background level and the atmospheric transmission. Quality-control plots are computed and stored for each observing night; an example of these plots for one typical night is presented in Figure 2.5. These plots are used to better filter the data, eliminating from the further analysis the images with doubtful quality due to weather or technical problems.

2.2.2 Building a star list

After a visual inspection of the quality-control plots, one image with one of the lowest sky background levels is chosen to construct a star list of all the objects whose light curves are desired. This image (ref2 hereafter) is inspected for unusual signals, such as satellite or plane trails, meteors, diffuse light, etc. Using DAOPHOT/ALLSTAR (Stetson 1987, Stetson & Harris 1988, Stetson 1992), a star list containing the PSF magnitudes of several tens of thousands of stars is built (typically, from $\sim$8000 stars until $\sim$40000, depending on the

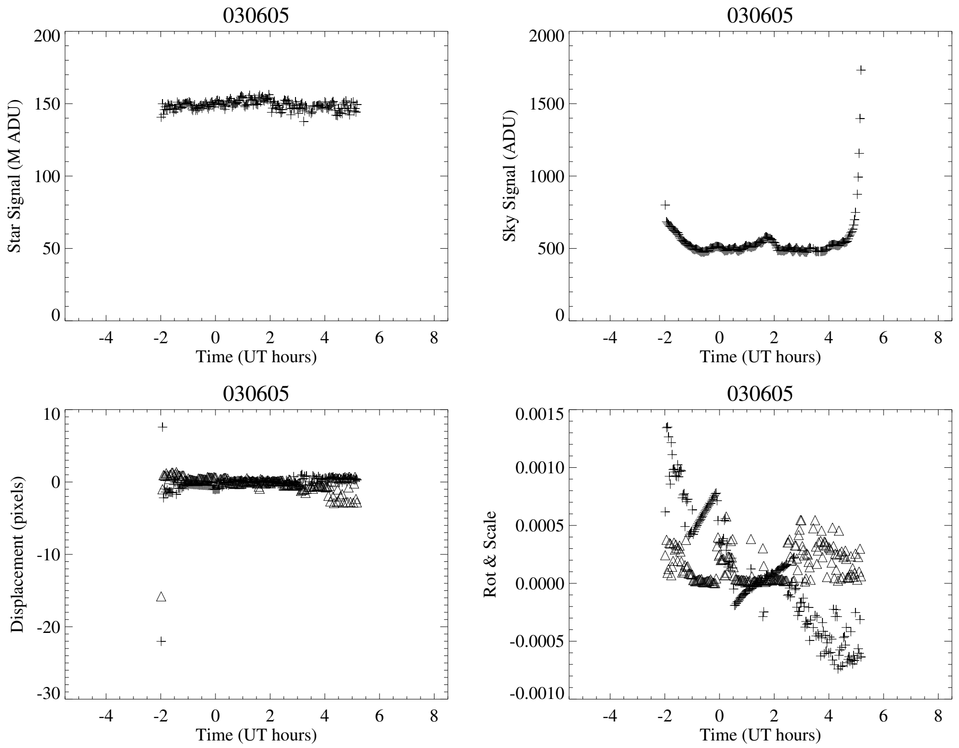

FIGURE 2.5— Plot for quality evaluation in a good night of observation. Top left: The signal of a bright unsaturated star. Top right: The sky signal. Bottom left: The displacement of the image from the ref1 image. Bottom right: The field rotation and scaling trends during the night.

stellar crowding). A few dozen stars distributed through all the field of view are identified with the Tycho-2 catalogue[2], and the transformation between the CCD's X and Y coordinates and J2000.0 Right Ascension and Declination is extrapolated for the rest of the stars in the star list.

2.2.3 Interpolation to the same X-Y grid

Before performing the image subtraction, all the images have to be interpolated to the same X-Y grid as the ref2 image. This is done with the routine *interp.csh* of the ISIS package, which requires as input parameters the coefficients for the transformation. These are calculated by the least square solution to the

[2]Available at http://www.astro.estec.esa.nl/hipparcos_scripts/hipMultiSearch.pl

relations:

$$x = a_0 + a_1 y_{ref2} + a_2 x_{ref2} + a_3 y_{ref2}^2 + a_4 x_{ref2} y_{ref2} + a_5 x_{ref2}^2 \tag{2.1}$$

$$y = b_0 + b_1 y_{ref2} + b_2 x_{ref2} + b_3 y_{ref2}^2 + b_4 x_{ref2} y_{ref2} + b_5 x_{ref2}^2 \tag{2.2}$$

where the x and y coordinates are from the image to be interpolated, and x_{ref2} and y_{ref2} are those of the ref2 image. The x and y coordinates for each star in the star list and in each data image are calculated with aperture photometry (APHOT), and matched to the same stars with x_{ref2} and y_{ref2} coordinates in the ref2 image with DAOMATCH/DAOMASTER (Stetson 1993).

2.2.4 Image subtraction

A higher S/N image (hereafter ref3) is built from a set of typically 10-20 images taken the same night and at similar times as the ref2 image. All these images have to be interpolated, and they are combined with the routine *ref.csh* of the ISIS package. The ref3 image is then convolved with an optimal kernel K to match each data image's psf profile, and the data image is subtracted from this ref3 image. The kernel K is computed by a least square minimization of the expression (Alard 2000):

$$\sum_i ([R \otimes K](x_i, y_i) - I(x_i, y_i))^2 \tag{2.3}$$

in which the kernel is assumed to be well decomposed in the basis functions:

$$K(u, v) = \sum_n a_n K_n(u, v) \tag{2.4}$$

with:

$$K_n(u, v) = e^{-(u^2+v^2)/2\sigma_k^2} u^i v^j \tag{2.5}$$

and the generalized index $n = (i, j, k)$.

The resulting image will have only significant signal in the variable and moving objects (Figure 2.6). As a consequence of the undersampling of the STARE's PSF, there will also be some residuals in the positions of the bright stars.

After image subtraction on a typical field of a STARE campaign, there are several thousand of residual images that are in the same x-y grid. It is thus straightforward to perform aperture photometry to measure the residuals centered on the positions of the stars in the star list. Let's write the residual flux of a star s in the ith image as $\Delta F_{s,i}$, with its associated standard error

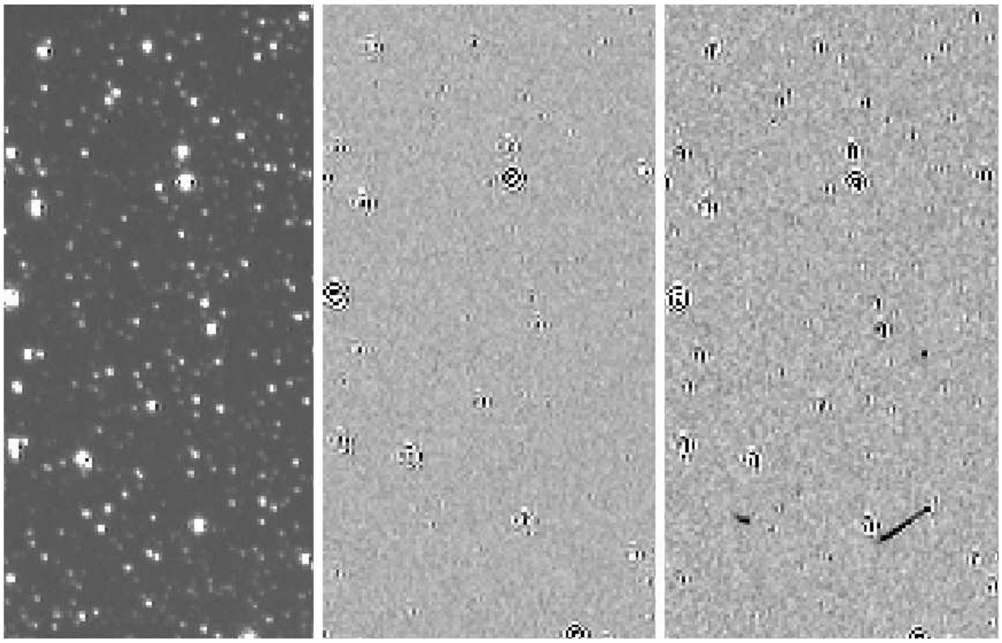

FIGURE 2.6— Left: A 100×200 pixels subimage of the ref2 image. Center: The same part of the image for the subtracted ref2 image. Right: The same part, for another image of the campaign, with worse weather conditions. The diagonal line is consequence of a falling star (present in the image i, but not in the ref2 image).

of $\sigma_{\Delta F_{s,i}}$. This set of images will include the ref3 image subtracted from itself. We will write the flux of the star s in this subtracted image as $\Delta F_{s,R}$. The flux of the star in the ref3 image is, to a good approximation, the measured flux in the ref2 image, used to build the star list. We will refer to this flux as $F_{s,R}$. Then, the magnitude difference of the star s in the ith frame with respect to its magnitude in the ref3 image is obtained by:

$$\Delta m_{s,i} = -2.5 \log \left(\frac{F_{s,0} - \Delta F_{s,i}}{F_{s,0}} \right) \tag{2.6}$$

where $F_{s,0} = F_{s,R} + \Delta F_{s,R}$ is the flux of the star in the ref3 image. The associated error can be estimated from the error in the ref3 image: $\sigma_{\Delta m_{s,i}} = 1.0857(\sigma_{F_{s,i}}/F_{s,0})$, where $\sigma^2_{F_{s,i}} = \sigma^2_{F_{s,0}} + \sigma^2_{\Delta F_{s,i}}$.

The resulting photometry is reformatted and collected in files which contain a manageable number of stars (typically 2000) with all the measurements for those stars, ordered in HJD.

These light curves are highly correlated, showing systematic trends that could not be removed in any of the previous steps. To correct for these trends, each star's light curve is regressed with the rest of the stars. This is done by a general linear least squares solution using Singular Value Decomposition (SVD) techniques (see, for instance, Press et al. 1988). In our case, each star's light curve ($m_s = m_{s,0}, m_{s,1}, \ldots, m_{s,M-1}$, with M the total number of observations) can be expressed as:

$$\begin{pmatrix} m_{s,0} \\ m_{s,1} \\ \vdots \end{pmatrix} = \begin{pmatrix} m_{0,0} & m_{1,0} & \cdots \\ m_{0,1} & m_{1,1} & \cdots \\ \vdots & \vdots & \ddots \end{pmatrix} \cdot \begin{pmatrix} x_0 \\ x_1 \\ \vdots \end{pmatrix} \tag{2.7}$$

The solution vector $\mathbf{x} = x_0, x_1, \ldots, x_{N-1}$ (with N the total number of stars), for non-square matrices, is calculated as the vector that minimizes the expression:

$$\boldsymbol{\chi^2 = |A \cdot x - b|^2} \tag{2.8}$$

where **A** is the first matrix in the righthand side of the Equation 2.7 and **b** is the term on the lefthand side, i.e., the magnitudes of the star *s*. The solution of the least-squares problem can be written as:

$$\boldsymbol{x = \sum_{i=0}^{M-1} \left(\frac{U_{(i)} \cdot b}{w_i} \right) V_{(i)}} \tag{2.9}$$

where **U** is an column-orthogonal M×N matrix, **V** is a N×N orthogonal square matrix, and w_i are the *singular values*, or the elements in the diagonal of a N×N diagonal **W** matrix that satisfy:

$$\boldsymbol{\Big(A \Big) = \Big(U \Big) \cdot \begin{pmatrix} w_0 & & & \\ & w_1 & & \\ & & \ddots & \\ & & & w_{N-1} \end{pmatrix} \cdot \Big(V^T \Big)} \tag{2.10}$$

The variance in the parameter x_j is:

$$\sigma^2(x_j) = \sum_{i=0}^{M-1} \left(\frac{V_{ji}}{w_i} \right)^2 \tag{2.11}$$

The final light curves will have part of this least square solution subtracted, i.e.:

$$\boldsymbol{m'_s = m_s - A' \cdot x} \tag{2.12}$$

where the matrix **A'** is an approximation of the matrix **A**, built with only the largest singular values w_i. We obtain good results in a typical field of STARE by de-correlating no more than 500 stars at once, because this method requires more data points than stars. The final light curves of real variable stars remain basically unaffected, while the variations that are common to the majority of the stars are mostly removed with this method. We noticed, though, that the amplitude of the genuine events (such as transits) are decreased by a 10-20%, which can affect to the detectability of the low depth transit events.

The last step in the light curve building is the averaging of the data into 0.0062 d ($\sim$9 min) wide bins (typically, 4-5 data points per bin). This reduces the final dispersion of the brightest stars from $\sim$6 mmags to $\sim$3 mmags.

2.2.5 Transit search

The binned light curves of all the stars are searched for transit shaped signals with the BLS algorithm (Kovács, Zucher, & Mazeh 2002). This algorithm computes the Signal Detection Efficiency (SDE), defined as:

$$SDE = \frac{SR_{peak} - < SR >}{\sigma_{SR}} \tag{2.13}$$

where SR is the Signal Residue of the time series at any given trial period (defined below). SR_{peak} is the SR at the highest peak, $< SR >$ is the average, and σ_{SR} is the standard deviation of SR over the frequency band tested. The SR at a trial period is computed as:

$$SR = MAX \left\{ \left[\frac{s^2(i_1, i_2)}{r(i_1, i_2)[1 - r(i_1, i_2)]} \right]^{1/2} \right\} \tag{2.14}$$

where i_1 and i_2 are the sorted points in the phase-folded light curve with the trial period, that define a step function (box-shaped) with the values L in $[i_1, i_2]$, and H in $[1, i_1)$ and $(i_2, n]$, with n the total number of points. The values of s and r are given respectively by:

$$s = \sum_{i=i_1}^{i_2} w_i x_i \tag{2.15}$$

$$r = \sum_{i=i_1}^{i_2} w_i \tag{2.16}$$

with x_i the phase-sorted magnitude values, associated to a weight w_i, defined as $w_i = \sigma_i^{-2}[\sum_{j=1}^{n} \sigma_j^{-2}]^{-1}$. The σ_i are the measurement errors of each data point. Each light curve needs to verify that $\boldsymbol{wx}$ has a zero arithmetic average.

The algorithm is run in each 2000 stars file, trying periods typically in the range 1 to 10 days, with 50 phase bins and fractional transit durations in the range [0.01, 0.1]. All the stars returning values of the SDE above typically 2.7 are visually inspected, to discard obvious false positives, such as variable stars, eclipsing binaries and stars with problematic photometry. This value of the SDE was chosen after an inspection of the SDE distribution of all the stars, retaining those that have SDE above the point in which this distribution falls to ∼1/3 of its maximum value.

2.3 Noise sources and performance

There are several factors that contribute to the final dispersion of the unbinned light curves. These are:

- Photon noise from the star: assuming a Poisson distribution of the photon (or shot) noise, the associated uncertainty in mags is given by: $\sigma_{star} = 1.0857/\sqrt{N}$, being N the total number of electrons ($= N_{ADU} \cdot gain$) recorded at the detector inside the star aperture, with the sky background subtracted.

- Photon noise from the sky background: the relative uncertainty in mags is given by $\sigma_{sky} = 1.0857 \cdot \sqrt{N_{sky} \cdot gain \cdot n_{star}}/N$, where N_{sky} is the measured sky level around the star (typically in an annulus with inner radius of 6 pixels and an outer radius of 12), and n_{star} is the number of pixels inside the stellar aperture.

- Scintillation noise: estimated using the empirical relationship by Young (1967):

$$\sigma_{sci} = 1.0857 \cdot 0.09 \cdot D^{-2/3} \cdot (1/\cos Z)^{1.75} \cdot \exp -h/h_0/\sqrt{2 \cdot T} \tag{2.17}$$

  where D is the aperture of the telescope, in cm, Z is the angle in degrees from the zenith, h is the observatory altitude, in meters, h_0 is the typical altitude scale height (8000 m), and T is the exposure time, in seconds.

- Detector noise sources: the reported read noise level (R) for the detector we use is 10 e$^-$. We can estimate the implied uncertainty in a single measurement from Everett & Howell (2001):

$$\sigma_{read} = 1.0857 \frac{R\sqrt{n_{star}[1 + n_{star}]/n_{sky}}}{N} \tag{2.18}$$

where n_{sky} is the number of pixels used to measure the sky level (in the annulus defined above).

The dark current standard deviation will be as well:

$$\sigma_{dark} = 1.0857 \frac{\sqrt{N_{dark} \cdot T \cdot n_{star}[1 + n_{star}]/n_{sky}}}{N} \tag{2.19}$$

where N_{dark} is the number of e$^-$ per second per pixel registered at the detector. Typical values in our case are 0.8-0.9 e$^-$ s^{-1} px^{-1}.

- Uncorrected atmospheric extinction The wide field of view of the STARE images make it challenging to achieve good atmospheric extinction corrections throughout the whole field, specially when the observing conditions were not photometric.

In the case of a field observed by STARE (a field in the constellation of Lyra, whose reduction will be described in Chapter 4), the observed dispersion of the unbinned (2-min sampled) data together with the modelling of the main noise sources are plotted in Figures 2.7 and 2.8. In those Figures, it can be seen that the main noise sources are the sky background noise for faint stars (fainter than R=10.4 in full moon conditions, and R=12.2 if there is no moon), and the scintillation noise for the brightest stars (estimated at an altitude of 2400 m, and at a zenithal distance of 50°, which corresponds to an airmass of 1.56; the values for n_{star} and n_{sky} are 13 and 339 respectively). It seems that the bright end of the sample is still above the expected noise value, which may be due to an underestimation of the scintillation noise level, uncorrected atmospheric extinction, flux errors introduced by the interpolation of the images, a non perfect guiding of the telescope, or a combination of all these factors.

2.4 STARE as a part of TrES

Since spring 2003, the STARE observations are coordinated inside the TrES (**Tr**ansatlantic **E**xoplanet **S**urvey) network. This consists of two other small instruments with similar characteristics as STARE, namely PSST (Dunham 2004) and Sleuth (O'Donovan, Charbonneau, & Kotredes 2004); these characteristics are summarized in Table 2.1. The advantages of these coordinated efforts, with instruments located at different longitudes, lie in:

- Less observing time per telescope is needed to detect planets with 3-5 d periods, and thus a survey of more stellar fields, without losing detection capabilities, is possible.

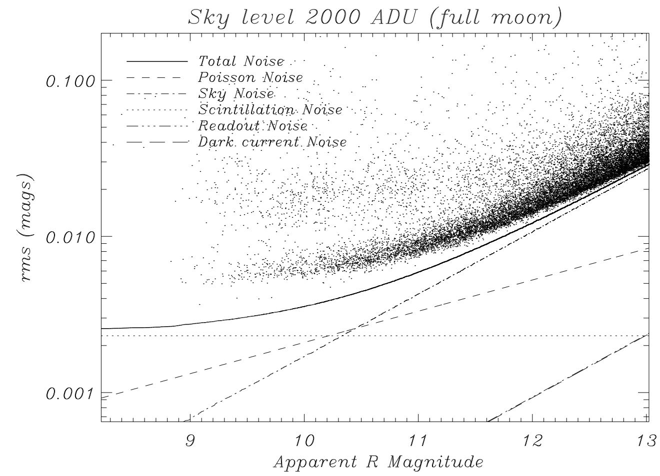

FIGURE 2.7— The unbinned decorrelated rms of all the stars in a whole STARE campaign centered on a field at the constellation Lyra (described in detail in Chapter 4). Also plotted are the main noise sources, for a typical full moon sky background. See text for details.

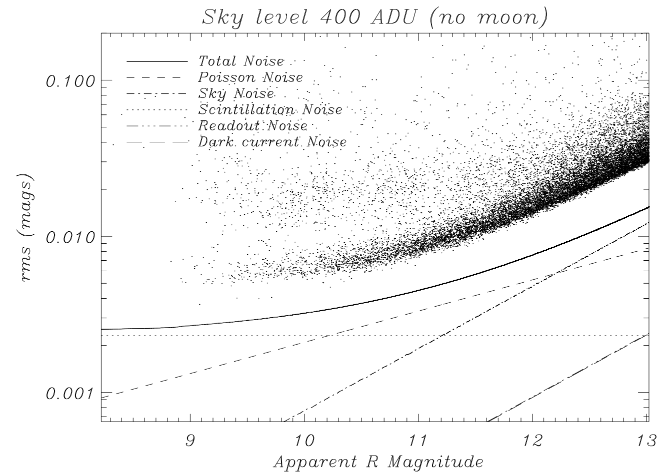

FIGURE 2.8— Same as Figure 2.7, but with the noise sources estimated for the best achievable sky background conditions at the Observatorio del Teide.

TABLE 2.1— The TrES telecopes

	STARE	PSST	Sleuth
Diameter (cm)	10.2	10.7	10
Focal Length (mm)	296	300	280
f/ ratio	2.9	2.8	2.8
Camera + pixel size	2k×2k×15μm	2k×2k×15μm	2k×2k×13.5μm
Camera type	front-illuminated	back-illuminated	back-illuminated
FOV	$6^\circ.1\times6^\circ.1$	$5^\circ.6\times5^\circ.6$	$6^\circ\times6^\circ$
Mount	Meade	Celestron	Meade
Autoguider	SBIG ST-4	SBIG ST-4	SBIG ST-4
Filters	Johnson	Bessell	SDSS
Location	Tenerife (Spain)	Arizona (USA)	California (USA)
Reference	This work	Dunham 2004	O'Donovan et al. 2004

- Confirmation of doubtful candidates, and isolated events, such as candidates only showing ingress-egress of a transit.
- Reduced aliasing in the spectra of the pulsating stars.
- Higher probabilities of detecting relatively long-period planets (P>10 d).

3

The follow-up techniques

Fingimos lo que somos;
seamos lo que fingimos.
Pedro Calderón de la Barca

In this chapter, we propose, study and review different approaches that can be used to verify the true nature of an eclipsing object after presumable transits are detected in the photometric light curves. There are several eclipsing stellar systems that can mimic the signal of a planetary transit. The techniques described in this chapter are intended to identify these false positives. As the final confirmation of a planetary transit requires the use of a few state-of-the-art spectrographs, other less-expensive methods need to be developed for an improved use of the time in these instruments.

3.1 Introduction

NOT everything that looks like a transit is caused by a Hot Jupiter. There are a number of stellar systems that can mimic transit shapes, specially when dealing with data whose signal is close to the noise level. For wide-field searches as STARE, the expected most common cases are (as we saw in the Introduction, Brown 2003):

3.1.1 Stellar binaries

An eclipsing binary not affected by the contribution of light coming from a third system can be confused with a transit signal in two cases:

- The stars have a similar $\frac{R_{\star 1}}{R_{\star 2}}$ as a main sequence star and a planet (typically, the star radius is 10 times bigger than the planet radius to produce

TABLE 3.1— Ratios of radii for main sequence stars. Evaluated from Cox (2000).

	A0	**A5**	**F0**	**F5**	**G0**	**G5**	**K0**	**K5**
M0	4.00	2.83	2.50	2.17	1.83	1.53	1.42	1.20
M2	4.80	3.40	3.00	2.60	2.20	1.84	1.70	1.44
M5	8.89	6.30	5.56	4.81	4.07	3.41	3.15	2.67
M8	24.0	17.0	15.0	13.0	11.0	9.20	8.50	7.20

1% eclipses): this can be the case if one of the stars has an age as to have burned all the hydrogen in its nucleus and have started the post-main sequence stage, increasing its radius. Also, several combinations of main-sequence binary stars can have similar ratios of radii (see Table 3.1, evaluated from the values in Cox 2000). Of particular importance in wide-field searches are the pairs of stars composed by a F and a M star, because of the large percentage of F stars in such a search (∼20% of the total number of stars[1]).

A recent observational proof of the similar sizes for the lowest mass stars and the Hot Jupiters is the detection by Pont et al. (2005) of a $1.17^{+0.2}_{-0.13}$ R_J object with a mass of 96±9 M_J and a period of 7.3 days. This was one of the transiting planet candidates identified by the OGLE survey (Udalski et al. 2003), and it constitutes the lowest mass star for which the radius has been measured. It is, thus, the densest (measured) main sequence star.

- The stars can also be similar in size, but only produce grazing eclipses. These will be usually triangular in shape, but with signals close to the noise level, they can be confused with a transit. Planetary transits can also be grazing, and produce triangular-shaped transits if there are no 2^{nd} and 3^{rd} contacts. For this to be possible, the inclination must be between the values:

$$\arccos(\frac{R_s + R_p}{a}) \leq i \leq \arccos(\frac{R_s - R_p}{a}) \tag{3.1}$$

in such a case, the maximum duration of a transit of a 1 R_J planet as a function of its period and the mass of the central star is plotted in Figure 3.1.

[1]evaluated from the 2MASS colors of a TrES field in the constellation of Cygnus; J–K

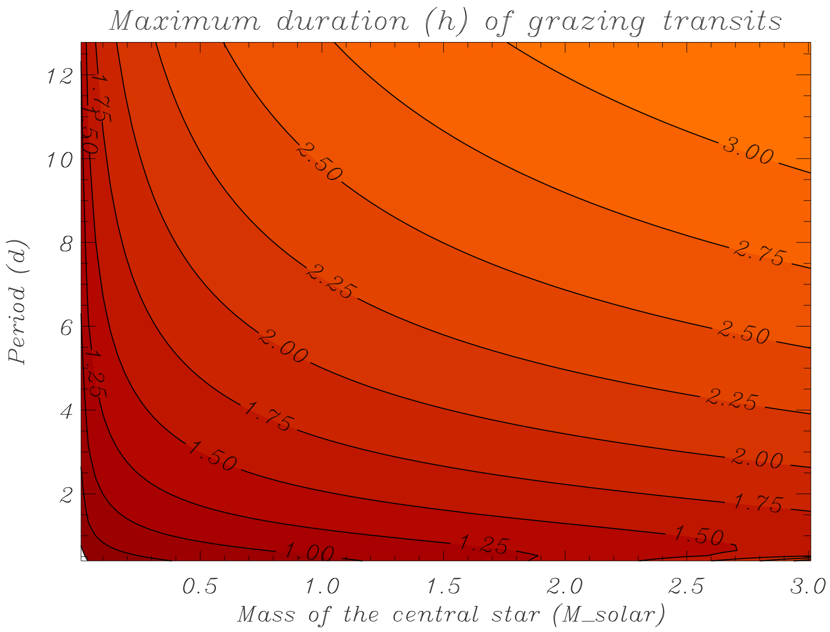

FIGURE 3.1— Maximum duration (in hours) of a grazing (i=arccos($\frac{R_s-R_p}{a}$)) transit (no 2^{nd} nor 3^{rd} contacts) , as a function of the star's mass (in Solar units) and the planet's period (in days). Circular orbits, a 1 R_J planet, and M_s=R_s (main sequence stars) have been assumed.

3.1.2 Triple (or multiple) systems

The depth of a binary eclipse can be diluted by the light of a third component. This third star can be a part of the system (*hierarchical system*) or just at a sky-projected distance of $\lesssim$ 1 FWHM of the line of sight (in the case of STARE, the FWHM is typically 15″). In the next sections, we provide some techniques that can unravel these systems.

3.2 Careful analysis of the light curves

A first inspection of the transit shape and the parts of the light curve without transits can quickly identify a false positive. This is the cheapest way, in time and cost, to identify false positives (i.e., no further telescope time is needed).

colors for main sequence F stars extracted from Bessell & Brett (1988)

3.2.1 Inspection of the parts without transits (out of eclipse modulation)

A known effect of several binary stars is the ellipsoidal variability (see Shobbrook et al. 1969 and references therein): the tidal forces are responsible for making the primary star elongated towards the companion. The changes in the angular size of the star, and the gravity darkening produce a sinusoidal modulation of the light curve with half the period of the system. The maximum light will be provided in the quadratures of the binary, and the minima will happen in the primary and secondary eclipse. This effect will be more evident when the companion is closer to the star and more massive. The ellipsoidal variability induced by a planetary companion would produce a signal that is not detectable from ground (Pont et al. 2005 estimate an ellipsoidal variability of 0.06 mmags for OGLE-TR-122, which is a 96 M_J star; in the case of planets, this would be of the order of a few μmags, assuming a theoretical dependence of the variability of M_s/P^2). Using this knowledge, Drake (2003) and Sirko & Paczyński (2003) fitted the data of the OGLE candidates (Udalski et al. 2002, 2002b, 2002c), and identified ellipsoidal variability in several of the candidates, with different statistical significance. Sirko & Paczyński (2003) claim that 50% of the 117 OGLE candidates they analyzed might have stellar companions, based only on the study of the photometric data.

Another known effect is the reflection effect, caused by the emission of the heated hemisphere of the secondary, that is commonly tidally locked. This event shows in the light curve as a sinusoidal shape, with maximum at the secondary eclipse, and with the same period as the system. In some cases (when the secondary eclipse is not detected), it is difficult to distinguish among this effect in the data and the ellipsoidal variability of a system with double the period (and thus having indistinguishable primary and secondary eclipses). This is the case in some of the OGLE candidates studied by Sirko & Paczyński (2003).

To recognize any of these effects in the light curves of the candidates, they propose a fit of the folded time series to a function:

$$I_k = < I > + a_{c1} \cos p_k + a_{s1} \sin p_k + a_{c2} \cos 2 * p_k + a_{s2} \sin 2 * p_k \tag{3.2}$$

where I_k is the observed intensity, and p_k is the folding period of the candidate.

We can define the significance D_i of any of the amplitude terms in the Equation 3.2 as:

$$D_{s1} = a_{s1}/\sigma_{s1} \tag{3.3}$$

and similarly the rest of the terms. The σ values are the standard deviation of the non-linear fit to the folded data. This fit can be implemented by the use of the Levenberg-Marquardt algorithm (Levenberg 1944, Marquardt 1963). The ellipsoidal variability will produce non-zero values of the term a_{c2}, while the reflection effect will cause non-zero values of a_{c1}.

3.2.2 Inspection of the transit shape

Seager & Mallén-Ornelas (2003) provide a simple test to identify the more valuable candidates. It consists of estimating the stellar density from the transit shape (with known P, t_F, t_T, and ΔF, see Equations 1.9 and 1.11 of the Introduction), and then comparing this stellar density with the one expected for a main sequence star. If the stellar density obtained from the transit shape is typical of a giant star ($\log(\rho/\rho_\odot)$ <-1.5, see Cox, 2000, for stellar densities as a function of the spectral type, in main sequence and giant stars), then the depth of the transit cannot be due to a planetary-sized object. If the stellar density closely resembles the density of the star obtained by a different approach (for instance, estimation of the spectral type by photometry or spectroscopy, and a value of the density for that spectral type taken from Cox 2000), then the candidate should be further observed. The input parameters t_T and t_F are crucial in this test, and can be obtained by a Levenberg-Marquardt fit of the folded time series to a function:

$$y = \begin{cases} 0 & x < t_c - t_T/2 \\ (t_c - x - t_T/2)\frac{\delta}{t_{ie}} & t_c - t_T/2 < x < t_c - t_F/2 \\ -\delta & t_c - t_F/2 < x < t_c + t_F/2 \\ (x - t_c - t_F/2)\frac{\delta}{t_{ie}} - \delta & t_c + t_F/2 < x < t_c + t_T/2 \\ 0 & x > t_c + t_T/2 \end{cases} \tag{3.4}$$

where the four fitted parameters are the center of the transit t_c, the total duration t_T, the depth in magnitude units δ, and the ingress-egress time t_{ie}. The duration of the transit between second and third contacts (t_F) can be inferred from t_F=t_T-2×t_{ie}. The relationship between the depth expressed in magnitudes (δ) and the $\sqrt{\Delta F}$ is $\sqrt{\Delta F} = 1 - 10^{-0.4\delta}$.

3.3 Multicolor photometry

To first order, a planetary transit is achromatic. The depth and shape of the transit only changes as a consequence of the dependence of the limb darkening of the star with wavelength. The limb darkening effect is more noticeable at shorter wavelengths (see, e.g., Claret 2000). Instead, a triple stellar system with different colors will, in some cases, produce eclipses with different depths when observed at different band passes. In the next paragraphs, we study in some detail, as illustrative examples, the dependence with color of a triple system where the two eclipsing stars are identical in color and the third star (diluting star) has a different color. A more general case in which the components of the eclipsing star are different is studied later, under the assumption that no secondary eclipses are detected in the photometric data.

3.3.1 Triple systems of main sequence stars. Two identical eclipsing stars.

Let's assume that the eclipsing stars (stars 1 and 2) are both main sequence stars, of the same color and spectral type. In a first approximation, let's suppose that within eclipses, one star completely blocks the flux emitted by the other. The diluting star (star 3) can vary its color and distance with respect to the eclipsing system's distance (1: same distance, <1: closer to the observer, >1: farther from the observer). A schematic plot of this configuration is given in Figure 3.2a.

To evaluate the variation in color of the blended system in and out of eclipses, a 5^{th} order polynomial was used to fit M(V) vs. B-V for stars in the main sequence, using the values tabulated in Cox (2000). A denser grid of 500 colors (B-V, V-R, R-I, V-I) corresponding to main sequence stellar types between 05 and M5 was built. In this first approach, reddening was not considered. In Figure 3.2b (and Figure 3.5 at the end of the Chapter), we show the differences in the observed colors inside and outside an eclipse, for all the possible configurations of the color of the stars 1 (the same as 2) and the color of the star 3. The precision of the color measurements can put serious constraints on the color that the third star may have in order to produce achromatic transits. Contour plots of these surfaces are given in Figure 3.2c (and Figure 3.6 at the end of the Chapter). From these figures it can be seen that, if a precision of 0.01 mags in V-I can be achieved, then there is a narrow range of colors for the star 3 to produce achromatic transits (basically, it should have almost the same color as stars 1 and 2). A practical application of these concepts will be presented in Chapter 4, Section 4.5.12.

If the observed color differences inside and outside an eclipse are not de-

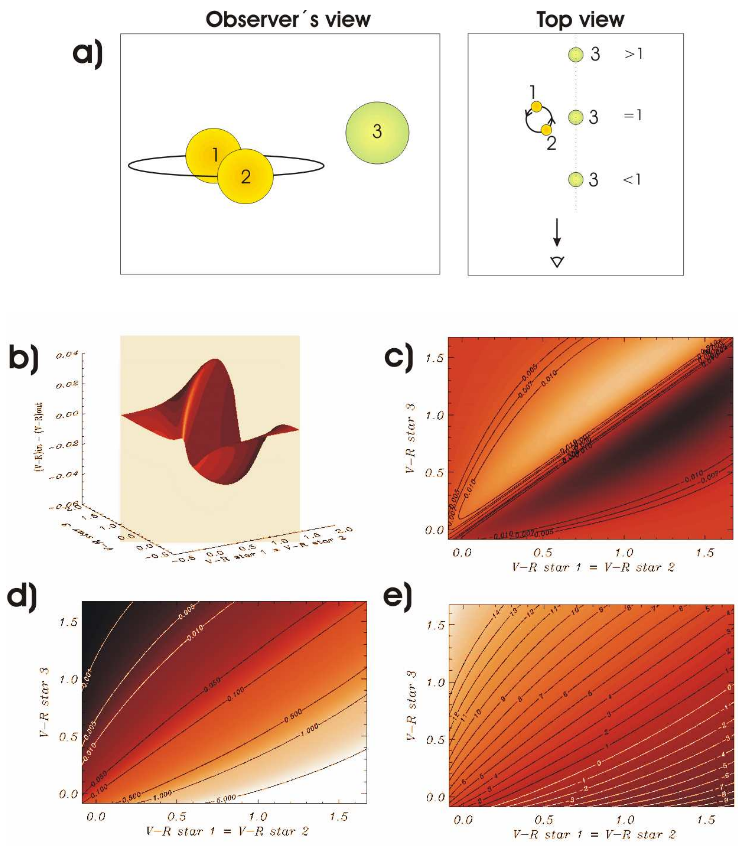

FIGURE 3.2— **a)** Schematic plot of the case discussed in the Section 3.3.1: two identical eclipsing stars (1 and 2), and a third star (3) providing light to the system. The third star can be physically associated (at a relative distance = 1), or be in the line of sight, with no gravitational binding. The three stars are assumed main sequence stars. **b)** The surface represents the differences in the observed V–R color, inside - outside an eclipse, of this blended case when the star 3 is at the same relative distance (=1). Note that the differences in colors can be of several cents of a magnitude. Positive values imply that the system becomes redder within the eclipses. **c)** Contour plots of the surfaces plotted in *b*. Levels are 0, 5, 7 and 10 mmags. Only triple systems between the negative and positive values of these contours (depending on the measurement precision) can not be detected by multicolor observations (basically, only combinations in which the three stars are of the same color would pass this test). **d)** Required relative distances of the star 3 to the eclipsing system, to reduce 50% eclipses up to 1% eclipses. Lines are the contour maps for relative distances (0.01, 0.05, 0.1, 0.5, 1, and 5) of the star 3 with respect to the eclipsing system. **e)** Magnitude differences between the stars 3 and the eclipsing 1-2 system, for an extreme dilution of 50% eclipses of 1-2 to an observed 1% eclipse.

tectable, it is still possible to constrain the possibility of a third diluting star. Considering, for instance, that the eclipsing stars 1-2 totally eclipse each other (50% eclipses), and that the observed depth is 1%, there is a limited range of main sequence colors for star 3 where it can be part of the system (in Figure 3.2d and 3.7, lines with a value of 1.0). It is not possible in this case that these three conditions are met: *i)* the three stars are main sequence stars, *ii)* there are no observed differences in color inside and outside an eclipse, and *iii)* the three stars are gravitationally bound. If conditions *i* and *ii* are met, then there is only a limited range of relative distances where the star 3 can be, in order to reproduce the observed achromatic eclipses (the values at the diagonal of the plots in Figure 3.2d and 3.7 are the maximum relative distances between the three components, corresponding to a dilution of 50% eclipses up to 1%).

In a more general case, if the eclipses of the system 1-2 reduce their total flux to a factor of d_1 ($0.5 \leq d_1 < 1$), the required relative distance D of the star 3 in order to dilute the (blended) observed eclipses to a final factor of d_2 (e.g. equal to 0.99 to explain a 1% decrement in the total flux) is:

$$D = \sqrt{\frac{F_3(1-d_2)}{2F_1(d_2-d_1)}} \tag{3.5}$$

where F_3 is the flux of the third star, and F_1 is the flux of each of the stars 1 and 2. The maximum relative distance will happen when the two stars 1 and 2 totally eclipse each other (d_1=0.5), and the blended eclipse is detected in the data (d_2 ~0.99). This distance is plotted in the Figure 3.2d and 3.7. The difference in magnitudes between the system 1-2 and the diluting star 3 is:

$$m_{12} - m_3 = -2.5log\Big(\frac{2F_1D^2}{F_3}\Big) \tag{3.6}$$

thus, the maximum difference in magnitudes for a background stellar eclipsing binary to explain an observed achromatic transit candidate is given by ($F_1 = F_3$):

$$m_{12} - m_3 = -2.5log\Big(\frac{1-d_2}{d_2-d_1}\Big) \tag{3.7}$$

which, for the extreme case of d_1=0.5 and d_2=0.99 is 4.23. Grazing eclipses of the system 1-2 (i.e., 0.5< d_1 <1.0) will reduce this number. This provides useful constraints on the faintness of a background eclipsing binary that could explain a transit candidate; high spatial resolution images, as those described in the next Section, should be planned to detect these extreme cases.

If there is no color photometry of a transit event available, but there is information on the colors of the stars (or their spectral type), Figure 3.2e (and

Figure 3.8 at the end of the Chapter) plots the extreme magnitude differences of an eclipsing system to account for the observed transit depth. If there are no detected objects within this magnitude difference from the brightest star in a higher resolution image, then the eclipses must be happening on the brightest star, and thus their dilution can be considered negligible.

3.3.2 Triple systems of main sequence stars. Only primary eclipses are detected.

If the colors of the stars 1 and 2 are different, then their relative fluxes will also be different, due to their respective position in the H-R diagram. Thus, the primary and secondary eclipses might show different depths, which would disqualify the object as a planetary transit candidate. If the secondary eclipse is within the noise of the measurements, then the contribution of the star 2 to the total (star 1+2+3) flux can be neglected. In this case (plotted schematically in Figure 3.3a), the color differences between the star 1 and star 3, if present, might show up as different depths of the eclipses when observed at different band passes. A plot of the change in B–V color as a function of the color of the star 1 and star 3 (neglecting the contribution from star 2), is given in Figure 3.3b and 3.3c (and Figures 3.9 and 3.10 at the end of the Chapter). In this case, star 2 has been treated as a dark object that blocks 1.5% of the flux of the star 1 within eclipses.

For a secondary eclipse to be undetectable in a set of data with average dispersion per point of σ, its depth must be lower than:

$$\Delta F_{secondary} \leq \frac{3\sigma}{\sqrt{N}} \tag{3.8}$$

where N is the number of data points that sample the secondary eclipse (equal to the number of points that sample the primary, if we assume circular orbits), and 3 is the threshold needed to consider a non-detection with a significance of 99.87 % (assuming a normal distribution of the noise). In a typical ground-based survey such as STARE, with a conservative value of σ=0.01 per 10 minutes data point, and sampling 3 secondary eclipses of 3 hours each, the secondary should have a depth smaller than 4×10^{-3} to remain undetected in the data. Thus, if the primary eclipse is 1.5% deep and no secondary eclipse is seen, then the surface brightness of the eclipsing object (star 2) must be at least 3.8 times fainter than that of the eclipsed star (star 1). To have such a low surface brightness, it must also be redder by an amount that can be estimated given the properties of the eclipsed star 1. If the color of this star is known, and no secondary eclipse is detected, then Figure 3.3d (and Figure 3.11 at the

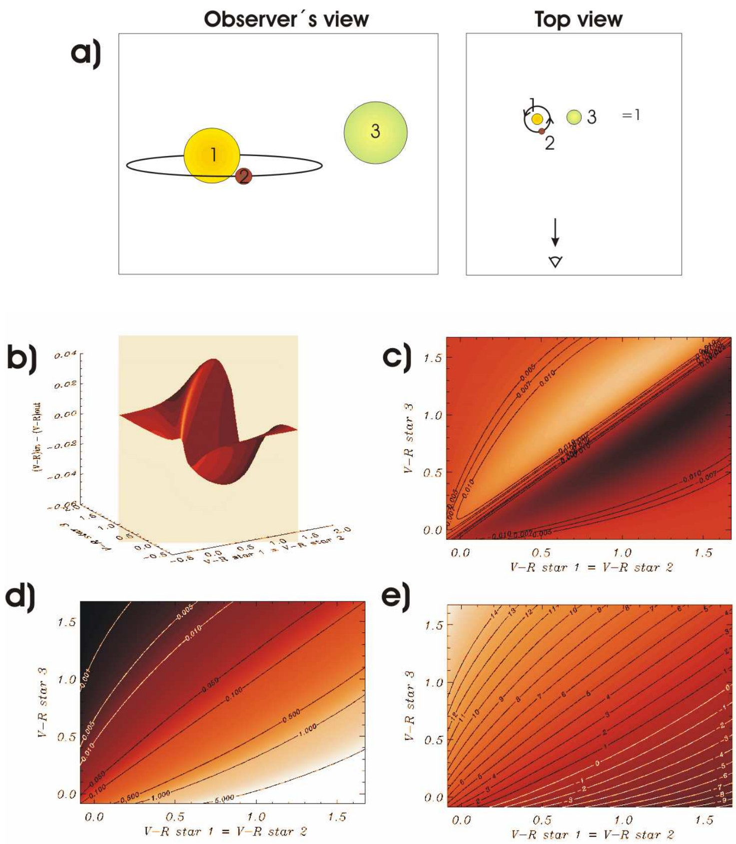

FIGURE 3.3— **a)** Schematic plot of the case discussed in Section 3.3.2: two eclipsing stars (1 and 2), being the star 2 smaller and fainter, and a third star (3) providing light to the system. The third star can be physically associated, or be in the line of sight, with no gravitational binding. **b)** The surface represents the differences in the observed colors, inside - outside an eclipse, of the blended case plotted in *a)*. The flux of the star 1 is reduced by a 1.5% within eclipses. Note that the differences in colors are now barely detectable from ground. Positive values imply that the system becomes redder within the eclipses. **c)** Contour plot of the surface plotted in *b)*. **d)** Contour plot of the minimum V–R color of the star 2 in a gravitationally bound triple system, under the assumption that no secondary eclipses are detected in a total of N=54 points of the data (with an average quadratic dispersion σ=0.010). **e)** Maximum depth, in magnitudes, of the primary eclipse of the star 1-2 system, under the same assumption as in *d)*.

end of the Chapter) provides the minimum color differences between the two stars.

As a further step, this minimum color difference can be used to establish the maximum eclipse depth in the undiluted primary eclipses, considering that these are not grazing (Figure 3.3e and 3.12 at the end of the Chapter). Plots similar to those represented in Figures 3.9 and 3.10 can be constructed with this maximum eclipse depth, and the color change of the triple system inside and outside eclipses can be calculated. As inferred from these figures, in this stellar configuration, the detected color differences will be typically below 1 mmag, and thus hardly reachable from ground-based instruments.

Special caution should be taken with these stellar configurations, as the observed color differences are of the order of the expected color changes due to limb-darkening effects (see, for instance, Seager & Mallén-Ornelas 2003). In this case, though, the observations in redder wavelengths lead always to equal or deeper eclipses, and changes in the transit shape. The eclipses are more U-shaped when observed at bluer wavelengths. The difference in colors treated in this Section due to the presence of a third star would contribute to this effect. Contrary to the limb-darkening wavelength effect, this difference does not change the transit shape; only its depth is modified.

The precision levels required make this case hardly detectable from ground-based multicolor observations. The situation is even worse in the case of only two eclipsing stars with a radii ratio similar to those of exoplanets (first case in Section 3.1.1, no extra flux from a third blended star); this is not possible to be detected from multicolor photometry. Thus, this technique should be seen as a necessary but not sufficient condition that every transiting planet should verify (within the limb darkening expected variations).

3.4 Adaptative Optics

Increasing the spatial resolution is a good tool to detect unbound triple (or multiple) systems (where the non-eclipsing star is not part of the system). The probability to detect such a star in the line of sight on an eclipsing binary with an improvement in the diameter of the PSF (Point Spread Function) from d_{psf1} to d_{psf2} is:

$$P_{detect} = 1 - \frac{d^2_{psf2}}{d^2_{psf1}} \tag{3.9}$$

Catalogued images, such as 2MASS, offer an improvement of the STARE's PSF (from $\sim 15''$ to $\sim 2''$), and in that case the probability to detect the star providing light to the stellar system is 98.2 %. With the use of AO, this probability

TABLE 3.2— Projected separation (in AU) of a companion detected at angular distances of 2" and 0.2" to a star situated at a distance D.

α	**D=50pc**	**D=100pc**	**D=150pc**	**D=200pc**
2"	100	200	300	400
0.2"	10	20	30	40

can be as high as 99.982 % (d_{psf2}=0.2$''$).

For stars at a typical distance of D ($\simeq$100 pc), the projected separation of a hierarchical companion would be d=D$\tan\alpha$, with α the observed angular separation of the stars. Table 3.2 presents values of this quantity for several different D, and α. For comparison, Pluto's orbit at the Solar System is at $\sim$40 AU, and the closest stars to the Sun are at distances of $\sim$250000 AU.

As an example, Figure 3.4 shows the detection of a multiple system we found in a AO campaign using NAOMI/INGRID (for a description of this instrumentation, see NAOMI: Myers et al. 2003; INGRID: Packham et al. 2003) at the William Herschel Telescope (Roque de los Muchachos Observatory, La Palma). This campaign was aimed toward the detection of stellar triples (hierarchical or in the line-of-sight), and it will be described in the next Chapter. In this star (GSC 03186-01085), which was a candidate for a transiting planet found in a field centered at the constellation Cygnus, at least four companions at angular distances lower than 1" were detected. The probability density for a fortuitous alignment of five objects in a 1"×1" region of a 40"×40" image is $P_{5objects} = (\frac{1}{40^2})^4 = 1.53 \times 10^{-13}$. Considering that there is only another object with a flux above the faintest companion in the whole image, the total probability of finding such a configuration without physical association of the objects is then $P = \frac{6!}{5!} P_{5objects} = 9.2 \times 10^{-13}$. The 2MASS colors for the central star are compatible with an early-mid F-star. The companions are between 3 and 3.8 mags fainter in K band, which means that they are all early-mid K stars, assuming that all the stars in the system are in the main sequence. The maximum observed diluted depth of a 50% eclipse in a fainter star with a magnitude difference of Δm is[2]:

$$\delta = -2.5 \log \Big(1 - \frac{10^{-0.4\Delta m}}{2}\Big) \tag{3.10}$$

Even with these companions detected, the observed 0.05 mags depth of the

[2]This equation is different from 3.7 because in this case the flux from the second component of the eclipsing binary has been neglected. It provides a conservatively bigger value for the observed diluted eclipses, thus constituting a stronger condition.

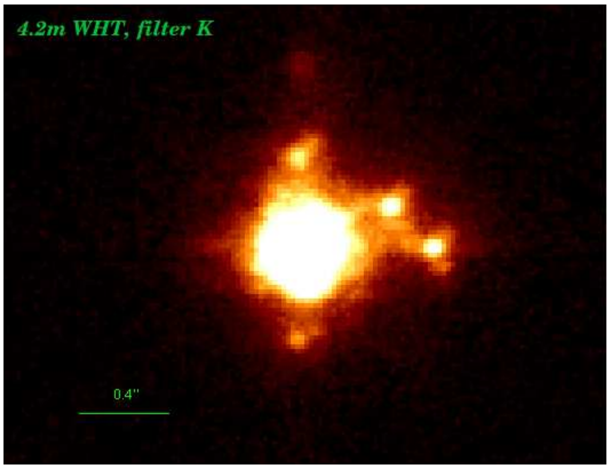

FIGURE 3.4— GSC 01386-01085, one of STARE's transit candidates, showing faint close companions when observed with NAOMI/INGRID at the 4.2 m William Herschel Telescope.

eclipses in this Cygnus candidate could not be explained by eclipses of any of these stars (a 3 mags fainter star with d_1=0.5 eclipses could only account for a $\sim$0.035 mags eclipse in the blended system, according to Equation 3.10).

3.5 Radial velocities

This technique, described in the Introduction, constitutes the final confirmation of a transiting planet; no other method can distinguish between the transit of a planet and that of an hypothetical brown dwarf in the same orbit, for instance. Only a few state-of-the-art spectrographs can provide the accurate radial velocity measurements needed to infer the presence of a planet. But the radial velocity variations in a star induced by a stellar companion can easily be measured with many spectrographs, at the km/s level. Double-lined spectroscopic binary systems can be recognized with a single exposure, and triple systems can be inferred by a close inspection of the correlation peak (which gives an idea of the mean spectral line). Double stellar systems with one fainter companion (not detected in the exposures) show variations of several tenths of km/s, in spectra taken at two or more different epochs. Thus, spectra of the stars and radial velocities at the km/s level constitute an efficient tool to detect the false positives. The TrES collaboration makes use of the *CfA Digital Speedometers*. This instrument (described in detail in Latham 1992) records 4.5 nm of spectrum centered near 518.7 nm, which samples the Mg *b* lines, with spectral resolution of about 8.5 km/s. For the typical magnitudes of the TrES candidates, and if the star is not a rapid rotator, precisions of better than 0.5 km/s can be achieved, allowing the detection of objects with masses above $\sim$5-10 M_J.

Another indication for a false positive is provided by the star's projected rotational velocity (vsin i). The tidal synchronization time scales for a star to be tidally locked with a planet is (Marcy et al. 1997):

$$\tau_{synch,s} = 1.2\Big(\frac{M_s}{M_p}\Big)^2\Big(\frac{a}{R_s}\Big)^6 yr \tag{3.11}$$

which is of the order of 10^{13} yr for Hot Jupiters around solar-like stars, and thus negligible. If the companion is not a planet but a star, then this a value is reduced to $\sim 10^7 - 10^8$ yr (for an F-M binary case orbiting with an a/R_s=10). Consequently, the observation of a star whose rotation is tidally locked with the companion is a strong indication for a stellar binary. In fact, with the information on the surface gravity and effective temperature of the primary star recorded in the spectra, it is possible to estimate a radius for the primary star. If the period of the eclipses is P, and the stars are tidally locked, then the mean observed stellar rotation is related to the stellar radius by:

$$v \sin i = \frac{2\pi R_s}{P} \sin i \tag{3.12}$$

for stars with eclipses, a reasonable approximation is $\sin i \sim 1$. If the measured vsin i value is consistent with the ratio on the right side of the equation, then the main star is tidally synchronized with the companion, which strongly points towards a stellar nature for it.

A final test that must verify a transiting planet is that the motions of the host star spectral lines must be the same in the cores of the lines as in the parts close to the continuum. This can be measured by means of the line bisector spans, defined usually as the velocity difference between the top and the bottom of the line bisectors (e.g., Queloz et al. 2001, Torres et al. 2004b; a more sophisticated analysis is the line shape and depth study, described by Brown et al. 1998b). A fainter unresolved eclipsing binary will produce distortions on the top of the spectral lines, while the bottom will remain unaffected. Thus, line asymmetries which are time dependant, and phased with the photometric period, are a consistent proof for a fainter eclipsing companion. A recent case in which the line bisectors were phased with the orbital period, and changing by a few km/s allowed the detection of a diluted triple system in a candidate that was a promising transiting brown dwarf candidate. This is described in more detail in the next Chapter, Section 4.7.

3.6 Summary and proposed scheme for efficient follow-up

The effort that needs to be settled in the follow-up observations and analysis of transit candidates is very large. An organized chain of tests that these candidates need to pass can improve the speed of the detection of false positives. This allows to efficiently use the time needed for the mass determination of the planetary transits, which need state-of-the-art spectrographs, only available in a few telescopes. Sorted from simple and cheap methods to the more expensive and sophisticated ones, every transit candidate should verify:

- **Careful interpretation of the light curve**. The data from different sites can be folded and smoothed, to search for out of eclipse modulations or secondary eclipses (none of them should be detected from ground-based searches). A detailed study of the transit shape can be used to estimate the host star density. If this is consistent with the density estimated by another means, then the candidate should be further observed.

- **Low signal to noise radial velocity**. In many cases of eclipsing binaries, two spectra might show radial velocity variations of several km/s, which can not be due to planetary mass companions. The spectra might also be double-lined, which constitutes a quick detection of a false positive. The $v \sin i$ of the star, together with an estimation on its radius, must not be consistent with tidal synchronization with the object producing the eclipses with a known periodicity.

- **Multicolor transit photometry**. The eclipses must be checked for achromaticity. Most of the triple stellar systems can be detected with 1% multicolor photometry. For wide-field searches, photometry on all the stars within a Δm able to produce eclipses with a depth of δ mags (Equation 3.10) that fall within 2-3 FWHM of the wide-field instrument should be performed.

- **Imaging with very high resolution**. Adaptative Optics or Speckle interferometry techniques might show close (<1") companions with similar brightness that would either dilute or have diluted eclipses from the other star. These companions must be located typically at several tens of AU of the central star to be detected. There is a huge probability that a detected companion is gravitationally bound, and not fortuitously located in the line of sight.

- **High signal to noise radial velocities and bisector analysis**. As a final stage of the follow-up chain, these measurements can identify hard to find false positives (with the study of the bisector spans) or provide an orbital solution for the planetary companion producing the transits.

In the next Chapter, we will perform an application of all of the follow-up techniques described here, to a list of candidates obtained in a TrES field in the constellation Lyra.

3.7 Appendix to Section 3.3: Plots for different Johnson colors

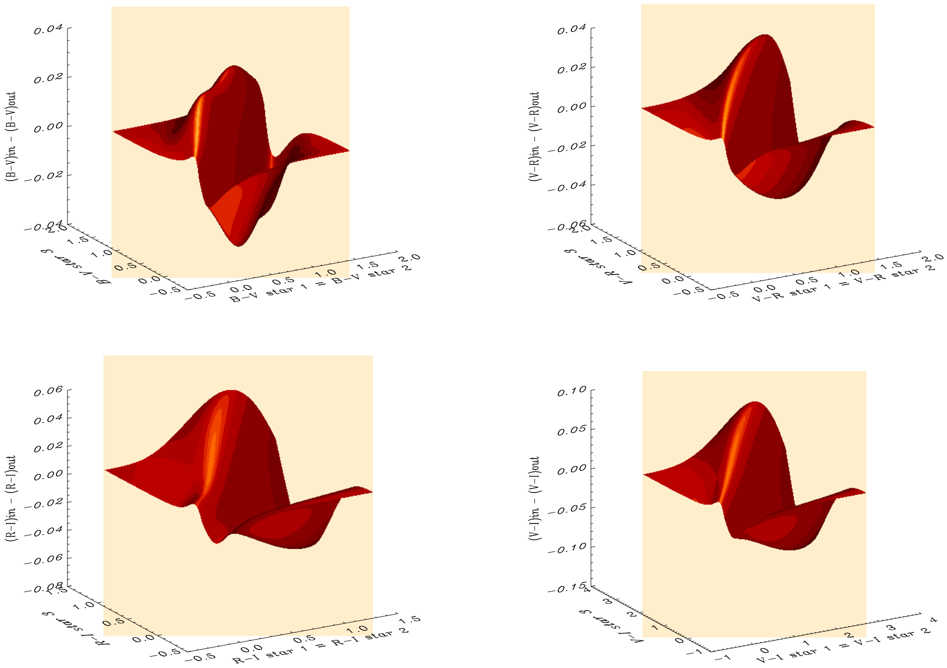

FIGURE 3.5— This surface represents the differences in the observed colors, inside - outside an eclipse, of a blended case, when there are two stars of the same color (1 and 2, x-axis) and a third diluting star of different color (star 3, y-axis), at the same distance. From top left to bottom right: (B-V), (V-R), (R-I) and (V-I). Note that the differences in colors can be of several cents of a magnitude. Positive values imply that the system becomes redder within the eclipses.

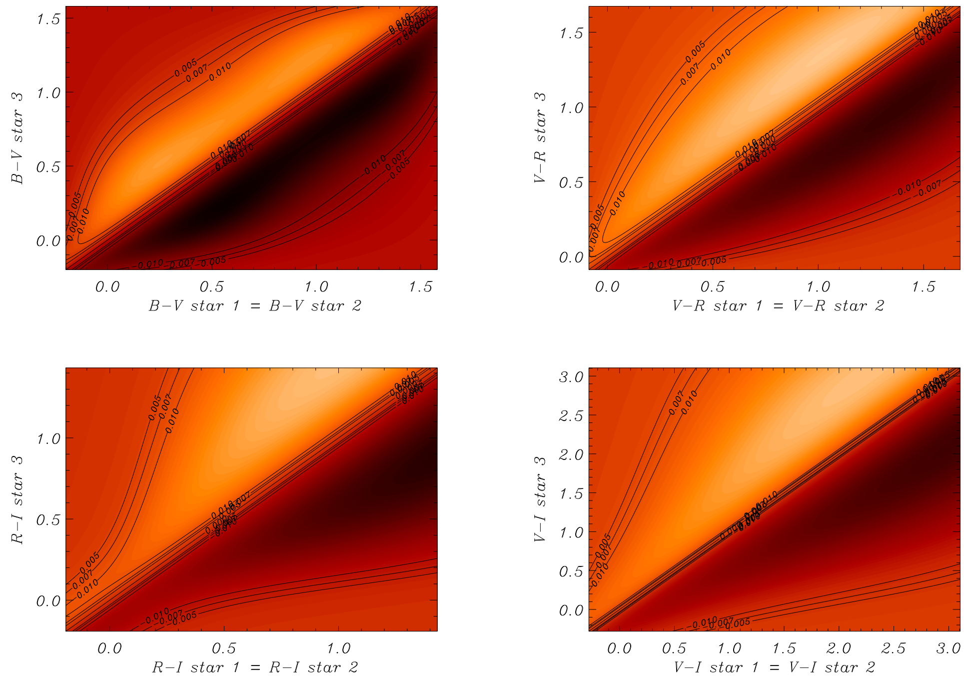

FIGURE 3.6— Contour plots of the surfaces plotted in Figure 3.5. Levels are 0, 5, 7 and 10 mmags. Only triple systems between the negative and positive values of these contours (depending on the measurement precision) can not be detected by multicolor observations (basically, only combinations in which the three stars are of the same color would pass this test).

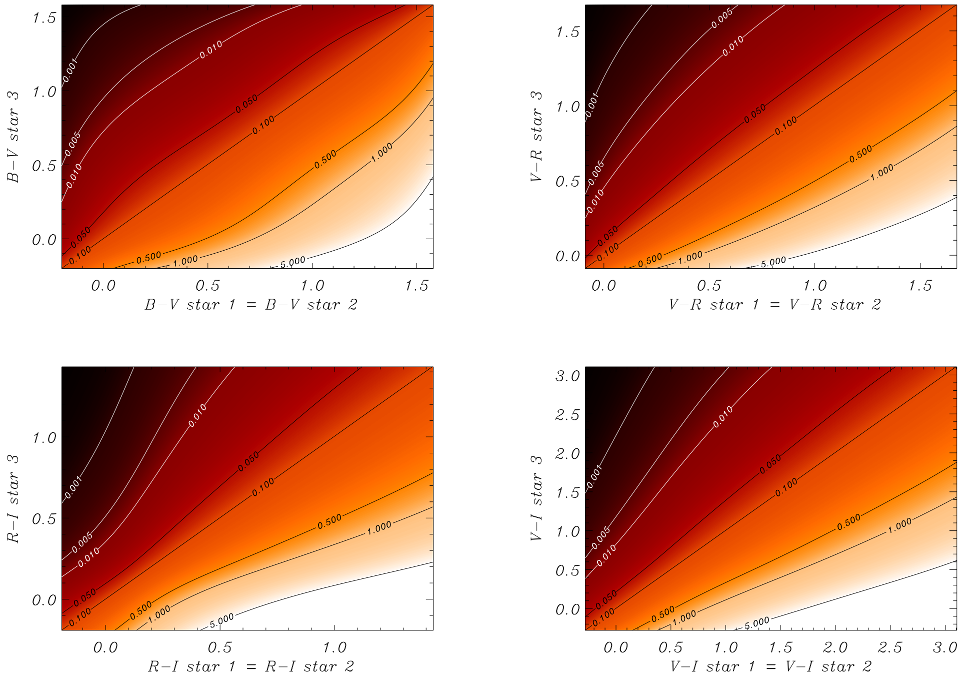

FIGURE 3.7— Required relative distances of a third diluting star to the eclipsing system, to reduce 50% eclipses up to 1% eclipses. X axis is the color of the star 1 and 2. Y axis is the color of the star 3. Lines are the contour maps for relative distances (0.01, 0.05, 0.1, 0.5, 1, and 5) of the star 3 with respect to the eclipsing system. The three stars are considered main sequence stars.

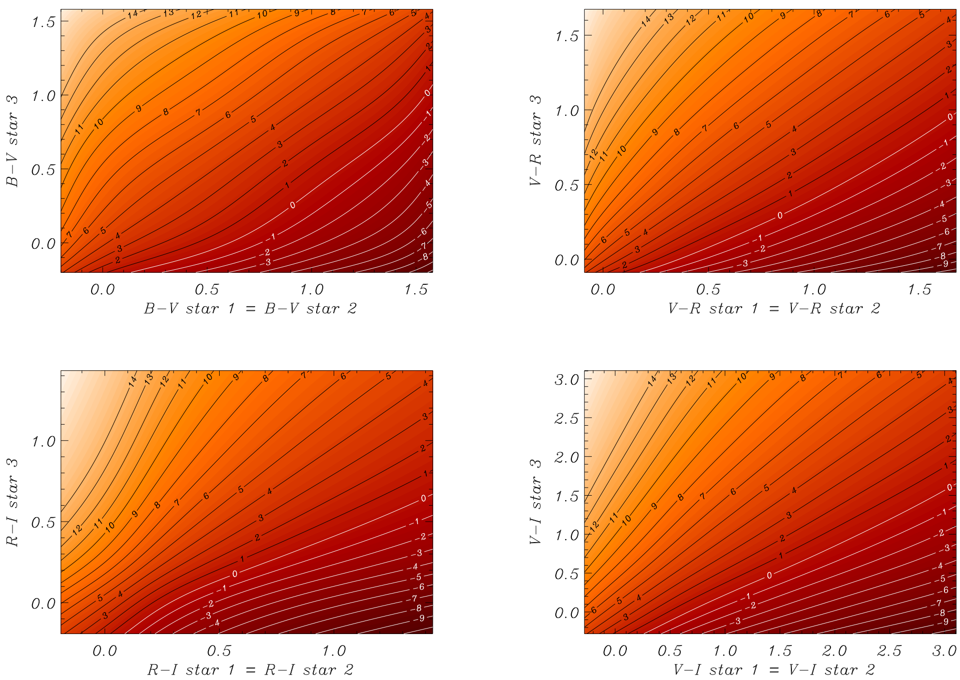

FIGURE 3.8— Magnitude differences between the stars 3 and the eclipsing 1-2 system, for an extreme dilution of 50% eclipses of 1-2 to an observed 1% eclipse. See text for details.

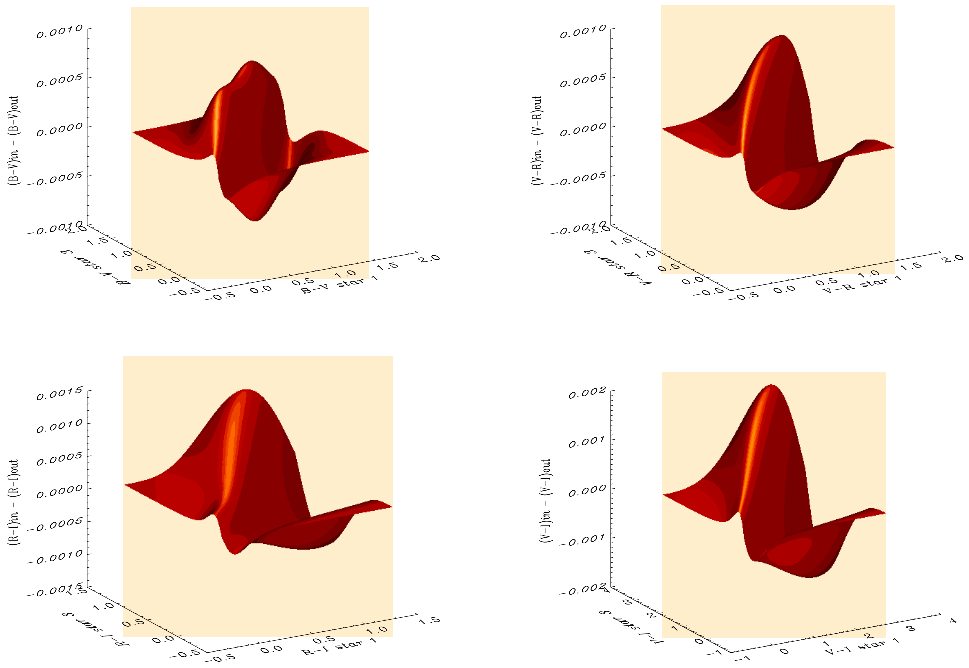

FIGURE 3.9— This surface represents the differences in the observed colors, inside - outside an eclipse, of a blended case, when there is a eclipsing 1-2 system, in which the flux of the star 2 is negligible, and a third diluting star of different color (star 3, y-axis), at the same distance. The flux of the star 1 is reduced by a 1.5% within eclipses. From top left to bottom right: (B-V), (V-R), (R-I) and (V-I). Note that the differences in colors are now barely detectable from ground. Positive values imply that the system becomes redder within the eclipses.

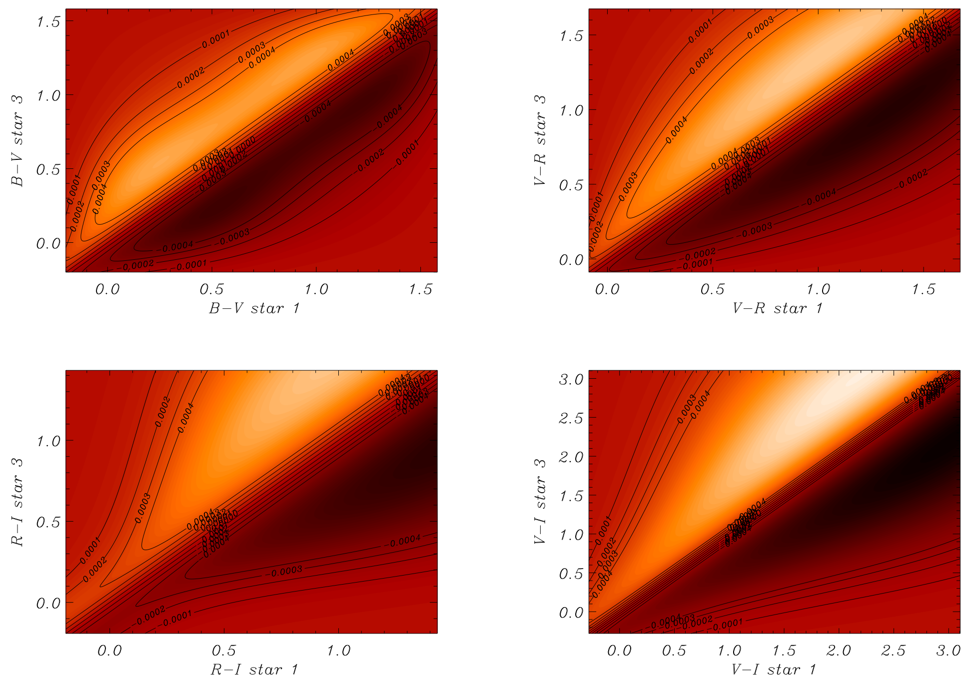

FIGURE 3.10— Contour plots of the surfaces plotted in Figure 3.9.

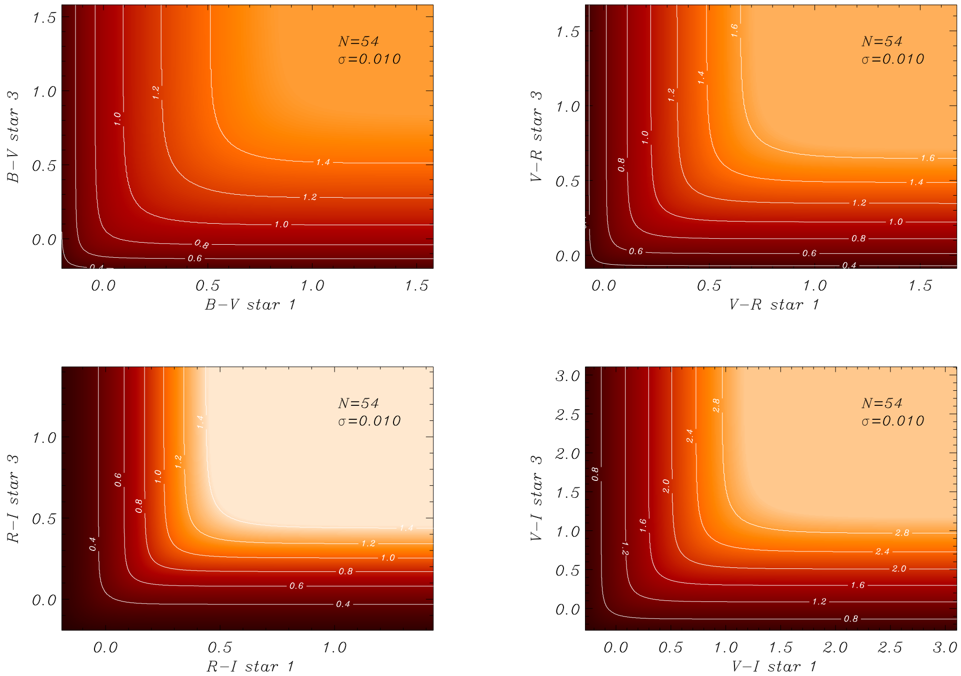

FIGURE 3.11— Contour plots of the minimum colors of the star 2 in a gravitationally bound triple system, under the assumption that no secondary eclipses are detected in a total of N=54 points of the data (with an average quadratic dispersion σ=0.010). The colors of the star 2 represented in each plot are the same as the ones presented in the x and y axis (from top left to bottom right: B–V, V–R, R–I, V–I.

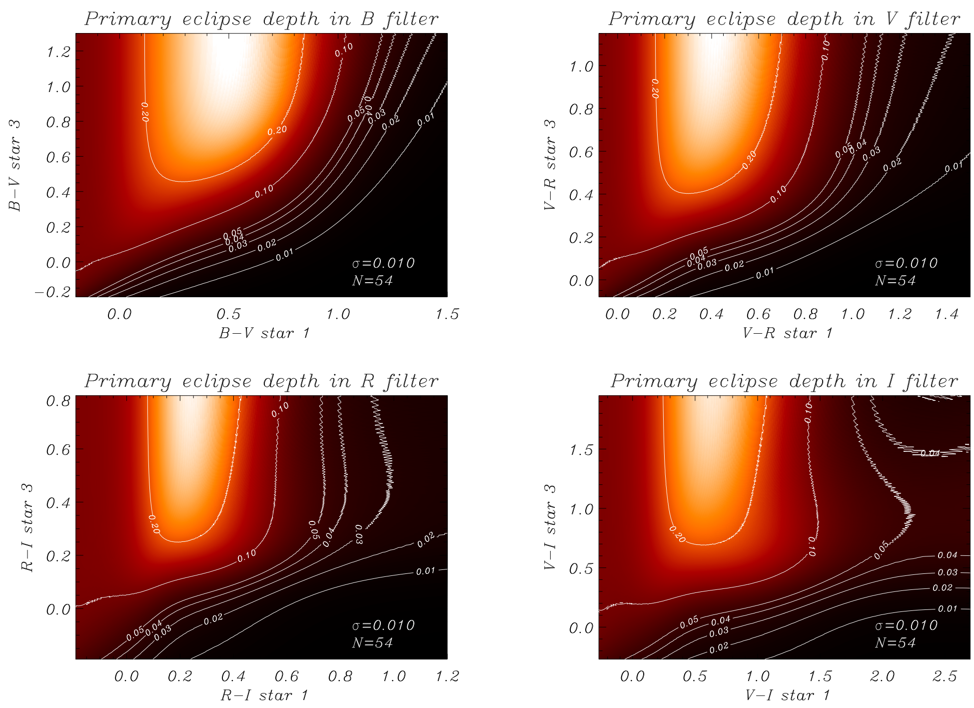

FIGURE 3.12— Maximum depths, in magnitudes, of the primary eclipse of the star 1-2 system, under the assumption that no secondary eclipses are detected in a total of N=54 points of the data (with an average quadratic dispersion σ=0.010).

4

Results from a field in the constellation Lyra

My God - it's full of stars!
David Bowman, in "2010: Odyssey Two"

In this chapter, we make a detailed presentation of the results of a TrES campaign pointed towards a field in the constellation of Lyra. A total of 16 transiting planet candidates were identified, and follow-up observations together with a detailed analysis of the light curves were performed to identify the false positives. We describe the results for each of the candidates, which finally allowed the identification of 15 false positives, and a transiting planet, TrES-1, which will be discussed in the next chapter.

4.1 Observations

THE field of Lyra was centered on the star Theta Lyrae (RA $=19^h16^m22.10^s$ $\delta = +38°08'01.4''$, J2000.0, V= 4.347, b=11.86°), and observed for 49 good nights (July 1st until September 16th), from the STARE site (Tenerife, Spain), and 25 good nights from the PSST site (Lowell, Arizona, USA). The Sleuth telescope was still under development at that time, and so did not observe this field. For about another 7 nights the STARE's guiding system didn't work properly, and these images were not further analyzed. PSST had also some technical problems for ~43 days during their observing season, and thus only the 25 nights mentioned above were useful.

Bias series of 20 images were taken at the beginning of each night, and later on averaged to have one master bias for every night. Dome and twilight flats were obtained approximately at the middle of the observing season, and a combination of these flats was performed as described in Chapter 2. Only one master flat field image was used to correct all the 10166 (final 8868) science images. Some experiments using more than one master flat field image for the reduction of a whole campaign resulted in significant (several percent) jumps in the final light curves, which arose from an incomplete correction of the different pixel sensitivities. This can be due to slight variations in the position of the telescope + dome while taking the dome flats, or to poor statistical significance of the master flat images (taken as an filtered average of 20 images in the case of dome flats and typically 8 images in the case of the sky flat images). Even with the risk of not achieving a correct absolute calibration (which would in any case need to be handled with care, as we saw in Chapter 2), we preferred to have the same flat field correction for every image, as we are interested in differential changes.

4.2 Data reduction

Data were processed as described in Chapter 2. Here we outline some details of interest.

When running DAOPHOT/PHOT (Stetson 1992) on the image used to obtain the standard star list, we got 56000 stars with a signal greater than 10 sigmas above the sky background. As we do not expect to have enough precision in the faintest stars to find planetary transits, we set a threshold of 25 sigma for the signal, resulting in $\sim$31000 stars in the final star list.

The master image for the field was built from an average of 17 images taken around the same time as the image used to build the star list. It is plotted in figure 4.1.

The standard deviation of the stars achieved for this field, for the 9-min binned STARE data, goes down to 3 mmag in the bright end, and rises above 10 mmag after 5700 stars. A plot of the rms of the stars versus magnitude is given in figure 4.2. The bright end of the plot shows some dispersion which can be due to saturation effects: the reference image used to build the standard starlist was chosen in a clear moonless night, with the lowest sky-background level. The brightest stars, in a night with a higher sky background level, will be closer to the saturation value, or even saturated.

As a comparison, we plot in Figure 4.3 the rms for the PSST observing run. This data set is shorter, and it becomes clear from this plot the advantage of having a back-illuminated CCD instead of a front-illuminated one such as STARE's (for details, see the Table 2.1 in the Chapter 2): the detector is sensitive to fainter stars, and the final dispersion in the light curves is smaller. We are planning to upgrade the STARE detector in the present year.

4.3 Transit candidates

We performed a search for transiting planet candidates with the BLS algorithm (Kovács, Zucher, & Mazeh 2002) on the brightest 12000 stars, divided in blocks of 2000 stars. The threshold was chosen by visual inspection of the final SDE (Spectral Distribution of Energy, see Equation 2.13) of the 2000 stars; typically, fixing the threshold where the approximately gaussian-shaped signal has $\sim 1/3$ of its maximum value, returns a number of false positives that are easily recognized by visual inspection of the light curves. This threshold was established as SDE=2.7 Examples of such false positives are plotted in Figure 4.4.

After the visual inspection of all the stars returning values above the threshold, and discarding the obvious outliers (eclipsing binaries, variable stars, stars too close to the edges of the CCD or to dirty parts, not fully corrected with the flat field images), we ended up with a list of 16 transiting planet candidates. Ordered in increasing period, they are plotted in Figures 4.5 and 4.6, and summarized in Tables 4.1, 4.2 and 4.3. After this first identification of the candidates, we refined the period determination, by running the BLS algorithm with a better phasing coverage and oversampling: The frequencies in region with a width of 0.1 c/d around the corresponding peak[1] were sampled, and a conservative period error estimate was computed as the difference between the values of the period in which the SDE peak amplitude decreased to half of its maximum level. The folded light curves in Figures 4.5 and 4.6 were constructed using this refined period estimation. We have kept the original values of the SDE (i.e., those obtained after the first BLS pass), even if the periods were not exact, to reflect the significance of each detection.

[1]In several of the candidates, we found that the highest amplitude peak was not the real period of the candidate, but an integer multiple of its period. Visual inspection of the folded light curves helps to identify the correct peaks. This was the case of T-Lyr0-03507, as we will see in the Section 4.5.9

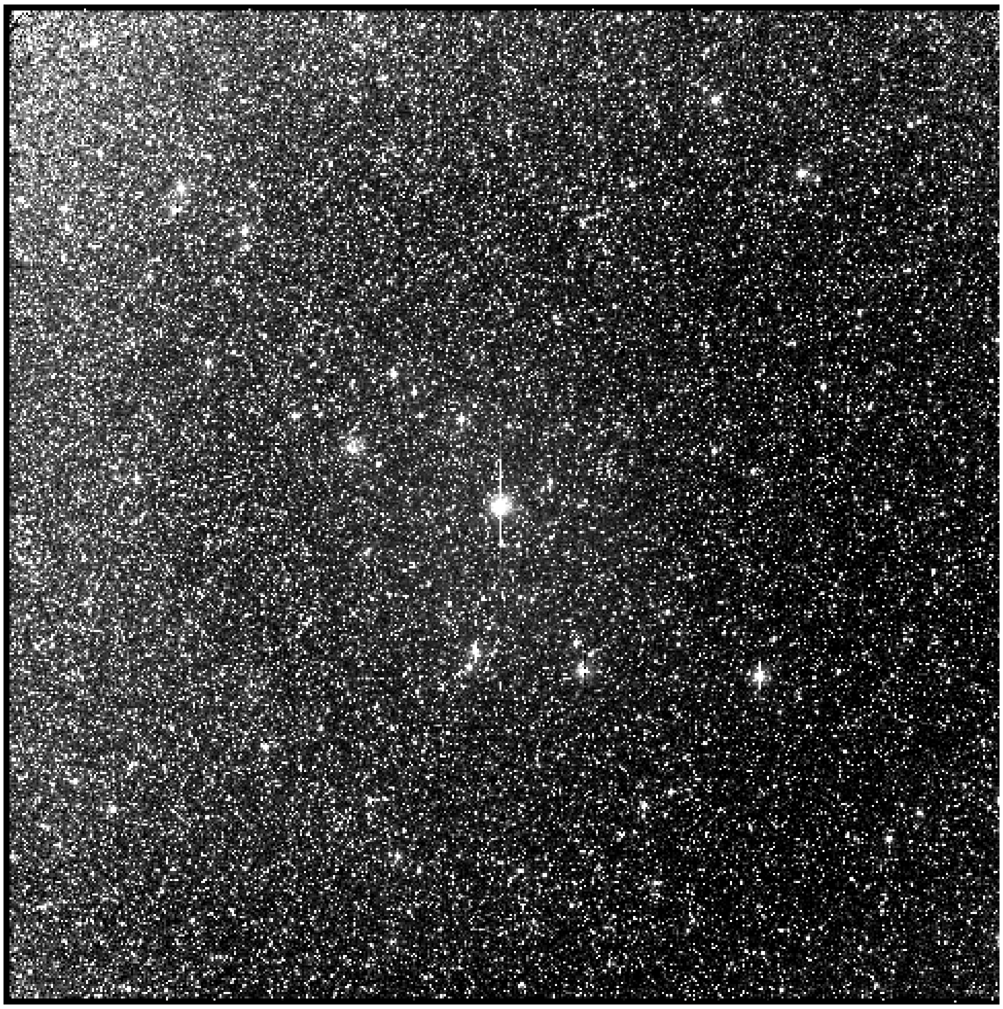

FIGURE 4.1— Master image of a field centered in the constellation Lyra.

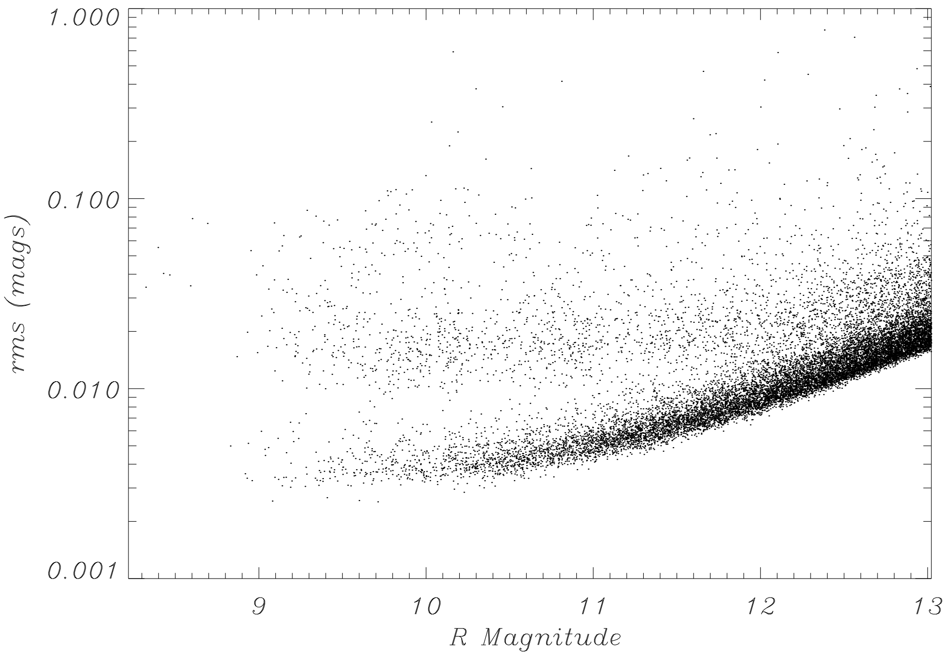

FIGURE 4.2— The rms versus magnitude for the Lyra run. Each point represents the rms of a star in the 9-min binned data, for the whole run. STARE data.

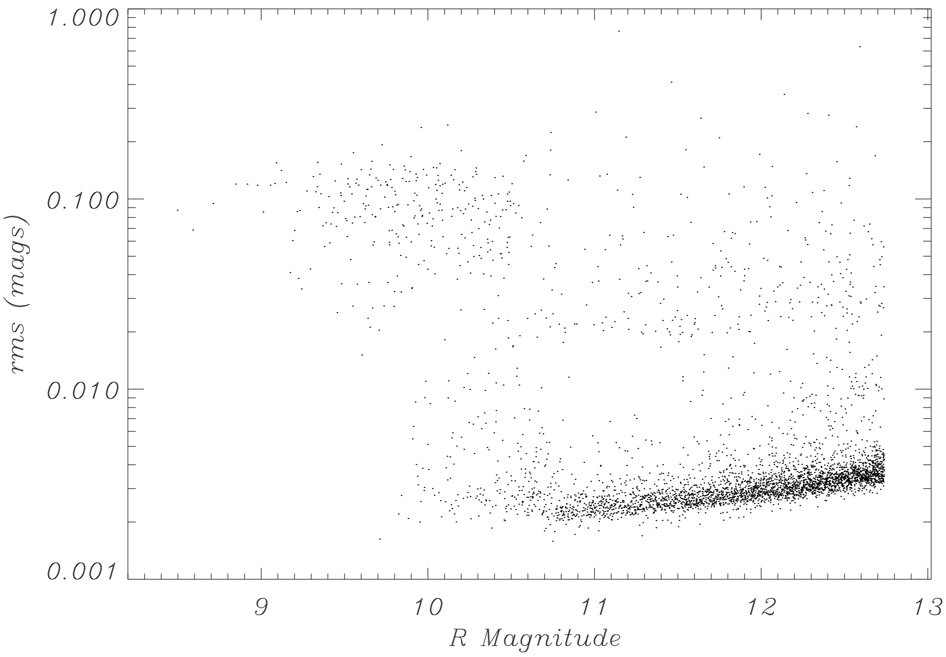

FIGURE 4.3— Same as Figure 4.2, but for the shorter PSST data set.

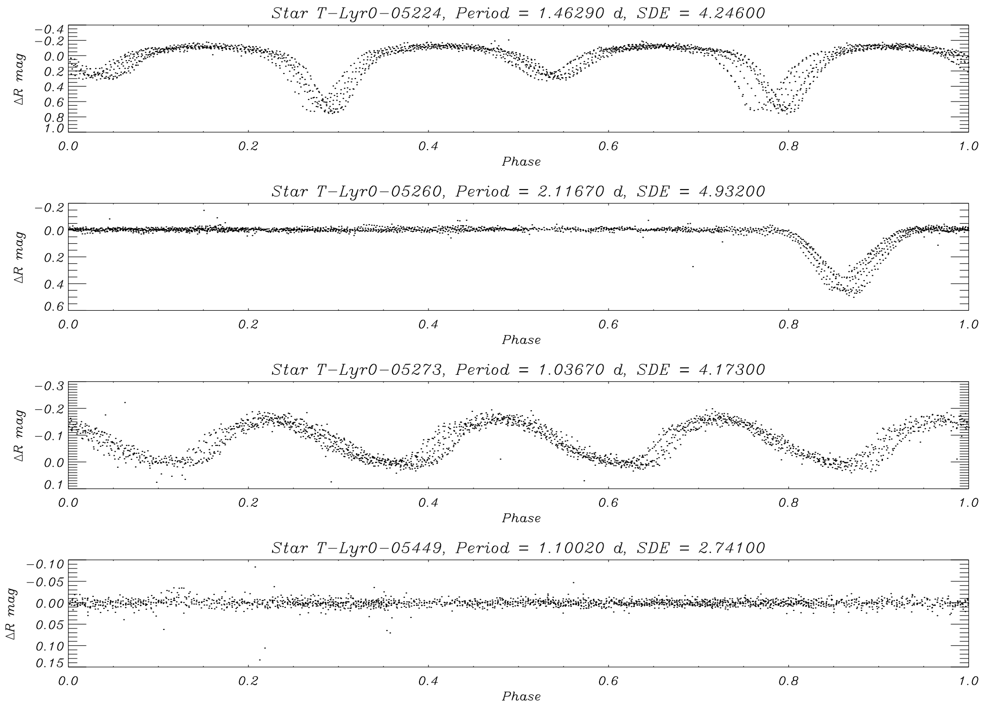

FIGURE 4.4— False positives from the BLS search, easily recognizable by visual inspection. From top to bottom: Two eclipsing binaries, one pulsating star and a star with a SDE close to the threshold of detection, not showing any evidence for a transit-shaped feature.

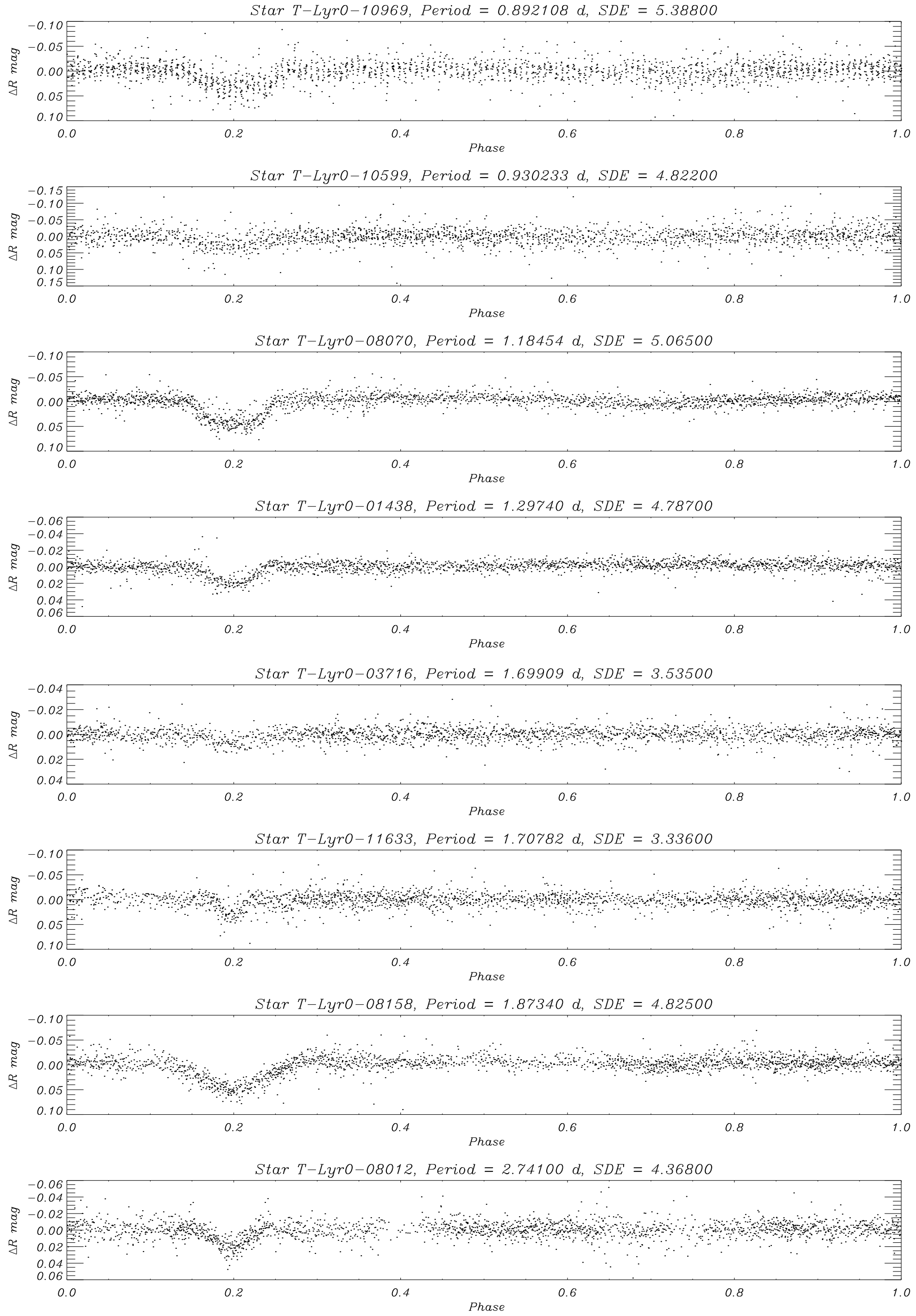

FIGURE 4.5— Folded light curves of transit candidates in the Lyra field.

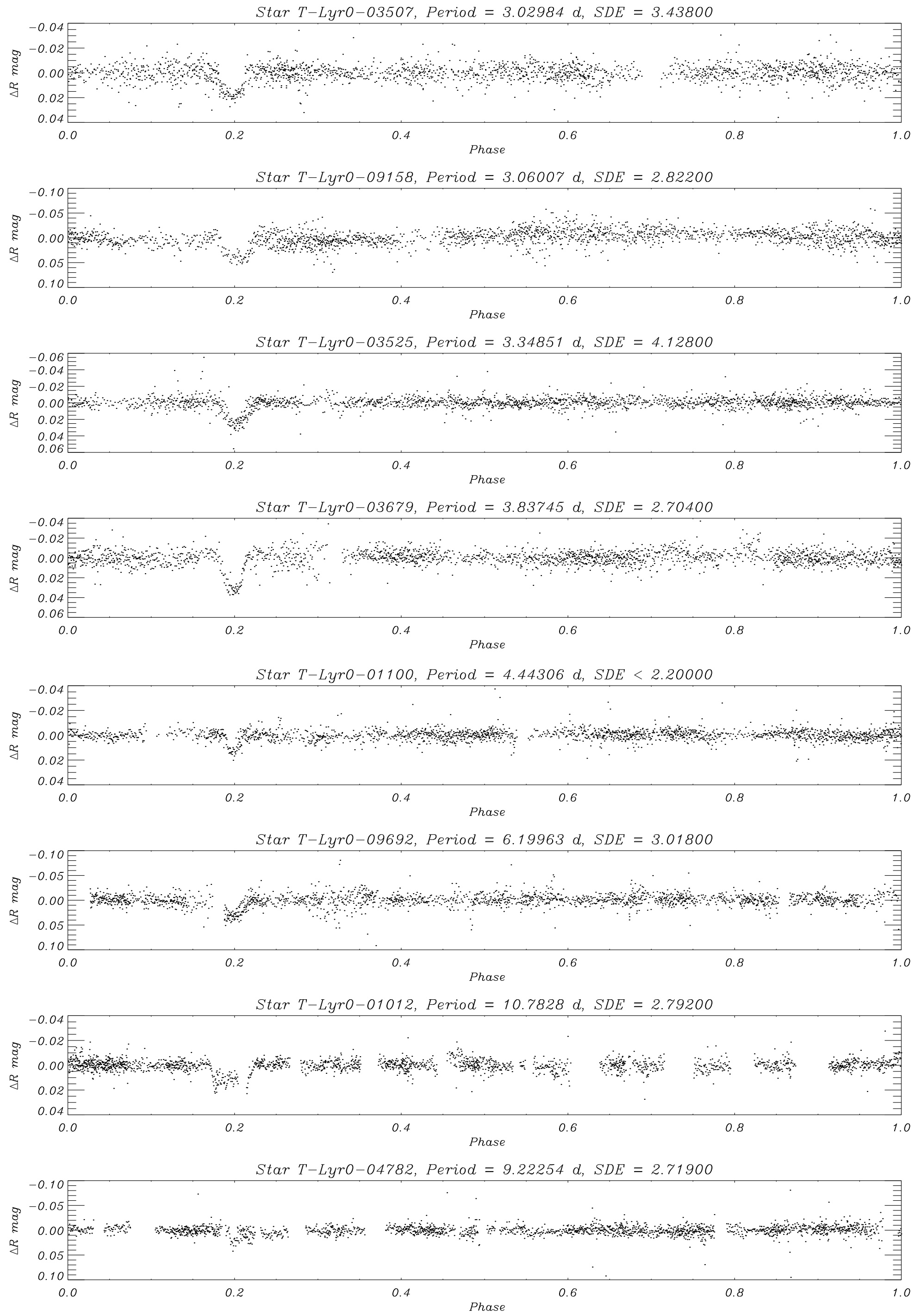

FIGURE 4.6— Folded light curves of transit candidates in the Lyra field.

TABLE 4.1— Characteristics of the stars showing transit-like events.

Candidate ID	GSC 1.2 ID	2MASS coordinates	2MASS J	2MASS H	2MASS K	USNO ppm ra (err)	USNO ppm dec (err)	Sp. Type (J-H)	Sp. Type (H-K)
T-Lyr0-10969	02666-01877	19 27 56.3 +36 13 19	11.857	11.667	11.638	0(0)	0(0)	F3	F0
T-Lyr0-10599	NO	19 29 47.7 +35 58 12	11.759	11.536	11.497	0(0)	0(0)	F5	F5
T-Lyr0-08070	03121-01659	19 19 03.6 +38 40 56	11.507	11.321	11.261	0(0)	8(0)	F3	G6
T-Lyr0-01438	02665-01287	19 17 08.6 +36 24 57	9.761	9.520	9.489	2(0)	8(0)	F6	F1
T-Lyr0-03716	02655-01344	19 16 41.1 +36 55 35	10.103	9.588	9.435	0(0)	0(0)	K2	K8
T-Lyr0-11633	02655-01623	19 14 58.7 +36 48 44	11.816	11.569	11.518	4(2)	-6(1)	F6	G1
T-Lyr0-08158	03134-00705	19 21 54.5 +38 25 37	10.935	10.375	10.253	0(0)	0(0)	K3	K6
T-Lyr0-08012	03121-00781	19 17 52.3 +38 52 02	11.162	10.907	10.820	-6(5)	10(1)	F6	K2
T-Lyr0-03507	02652-01324	19 04 09.8 +36 37 57	10.294	9.887	9.819	-42(0)	-22(0)	G8	G8
T-Lyr0-09158	02652-01397	19 11 39.? +36 49 03	11.201	10.829	10.780	8(2)	8(2)	G6	G0
T-Lyr0-03525	03125-00317	19 13 05.? +40 24 02	10.587	10.415	10.362	-4(0)	20(0)	F3	G3
T-Lyr0-03679	02665-00795	19 20 33.9 +36 37 32	10.362	9.870	9.748	0(0)	0(0)	K1	K6
			12.159	11.765	11.649			G8	K5
T-Lyr0-01100	03125-01126	19 13 53.3 +40 05 16	10.364	10.134	10.093	0(0)	0(0)	F5	F5
		19 13 53.8 +40 05 08	10.764	10.555	10.515			F4	F5
T-Lyr0-09692	03120-00359	19 04 37.1 +39 03 56	11.408	11.160	11.057	-4(5)	-14(0)	F6	K4
T-Lyr0-01012	02666-00345	19 28 09.1 +36 44 45	9.723	9.611	9.564	0(0)	-8(0)	A8	F8
T-Lyr0-04782	03124-02558	19 01 10.7 +39 56 49	9.664	8.821	8.621	-2(1)	-6(2)	M?	M1

TABLE 4.2— Characteristics of the transit-like events (I).

Candidate ID	Period (d)	Epoch (HJD-2450000.)	Duration (h)	Depth (mags)	Fainter close stars[1] Distance and ΔJ	Flat Bottom Duration (h)
T-Lyr0-10969	0.892108	2821.94014	2.45	0.031	20″,2.45 mags	1.53
T-Lyr0-10599	0.930233	2821.45589	3.13	0.026	27″,2.87 mags, 33″,1.47 mags	1.33
T-Lyr0-08070	1.184539	2824.46888	2.89	0.040	37″,0.81 mags	1.78
T-Lyr0-01438	1.297404	2821.22555	2.73	0.019	13″,2.61 mags	1.03
T-Lyr0-03716	1.699091	2822.32172	4.81	0.007	7.9″,2.87 mags	0.46
T-Lyr0-11633	1.707825	2822.33848	1.95	0.030	11″,2.00 mags, 14″,2.79 mags	0.52
T-Lyr0-08158	1.873396	2821.59657	6.64	0.052	9″,2.44 mags	0.38
T-Lyr0-08012	2.741003	2822.76567	4.50	0.025	21″,2.04 mags	-0.13(0)
T-Lyr0-03507	3.029844[a]	2820.16941	2.51	0.018	NO	1.64
T-Lyr0-09158	3.060069	2821.02118	3.25	0.040	34″,0.46 mags	1.69
T-Lyr0-03525	3.348513	2820.68971	3.56	0.026	22″,2.91 mags	0.51
T-Lyr0-03679	3.837446[a]	2821.01704	2.97	0.031	7.8″,1.80 mags	1.28
T-Lyr0-01100	4.443060	2820.86708	2.43	0.014	8″,0.40 mags	0.45
T-Lyr0-09692	6.199628	2821.23664	6.99	0.033	NO	1.37
T-Lyr0-01012	10.782834	2825.48893	13.46	0.013	NO	10.46
T-Lyr0-04782	9.222540	2834.49387[b]	?	0.028	NO	?

[1] At an apparent distance lower than 40″ and with ΔJ lower than 3 mags

[a] These epochs and periods are refined later on this thesis, with further observations.

[b] Epoch of the single observed eclipse.

TABLE 4.3— Characteristics of the transit-like events (II).

Candidate ID	Period (d)	N events W	I	E	Follow-up work resuts
T-Lyr0-10969	0.892108	5	6	3	Blended system, eclipsing F+brown dwarf system, or F+M system
T-Lyr0-10599	0.930233	3	3	2	Triple blended system
T-Lyr0-08070	1.184539	7	5	4	Binary system (F+M)
T-Lyr0-01438	1.297404	5	5	2	Binary system, double the period (similar components)
T-Lyr0-03716	1.699091	3	1	1	Triple blended system
T-Lyr0-11633	1.707825	5	0	2	Binary system
T-Lyr0-08158	1.873396	3	5	4	Blended system, double the period[b]
T-Lyr0-08012	2.741003	3	2	3	Blended system?[b]
T-Lyr0-03507	3.029844[a]	3	1	0	Transiting planet
T-Lyr0-09158	3.060069	2	0	1	Binary system
T-Lyr0-03525	3.348513	3	0	2	Binary system
T-Lyr0-03679	3.837446[a]	1	1	2	Blended system[b]
T-Lyr0-01100	4.443060	2	0	1	Blended system[b,c]
T-Lyr0-09692	6.199628	0	0	3	Triple blended system?
T-Lyr0-01012	10.782834	1	1	1	Binary system
T-Lyr0-04782	9.222540	1	0	0	Unsolved case

[a] These epochs and periods are refined later on this thesis, with further observations.

[b] Resolved in the 2MASS images.

[c] Resolved with AO observations (NAOMI at 4.2 m WHT).

TABLE 4.4— Stellar densities from *i*) values tabulated at Cox (2000), where the spectral types of the stars are estimated from the 2MASS J–K colors (Bessell & Brett 1988), and *ii*) the result of fitting the transit shape, as proposed by Seager & Mallén-Ornelas (2003). Main sequence stars and circular orbits for the companions have been assumed.

Candidate ID	J–K	Sp. Type (J–K)[1]	$\log(\rho/\rho_{\odot})_{(J-K)}$	$\log(\rho/\rho_{\odot})_{(Fit)}$	$\Delta = \log(\rho/\rho_{\odot})_{(J-K)} - \log(\rho/\rho_{\odot})_{(Fit)}$	10^{Δ}
T-Lyr0-10969	0.219	F5	-0.20	-0.46	0.26	1.82
T-Lyr0-10599	0.262	F5	-0.14	-0.63	0.49	3.09
T-Lyr0-08070	0.246	F5	-0.16	-0.35	0.19	1.55
T-Lyr0-01438	0.272	F5	-0.12	-0.66	0.54	3.47
T-Lyr0-03716	0.668	K5	0.15	-1.57	1.72	52.5
T-Lyr0-11633	0.298	F5	-0.09	-0.79	0.70	5.01
T-Lyr0-08158	0.682	K5	0.17	-1.37	1.54	34.7
T-Lyr0-08012	0.342	G0	-0.04	-0.99	0.95	8.91
T-Lyr0-03507	0.475	K0	0.05	-0.02	0.07	1.17
T-Lyr0-09158	0.421	G5	0.02	-0.23	0.25	1.78
T-Lyr0-03525	0.225	F5	-0.19	-0.66	0.47	2.95
T-Lyr0-03679	0.614	K0	0.11	-0.14	0.25	1.78
T-Lyr0-01100	0.249	F5	-0.16	-0.14	-0.02	0.95
T-Lyr0-09692	0.351	G0	-0.04	-0.99	0.95	8.91
T-Lyr0-01012	0.159	F0	-0.31	-1.48	1.17	14.8
T-Lyr0-04782						

[1] Spectral type of the star with the closest J–K color in the Bessell & Brett (1988) tables.

[2] From a 4^{th} order polynomial fit to the J–K vs $\log(\rho/\rho_{\odot})$ in the tables of Cox (2000)

4.4 Careful inspection of the transit candidates

As we saw in the previous Chapter, a careful interpretation of the light curves of the candidates can reveal false positives, without the need for further telescope time. In this Section, we apply two different tests to the candidates obtained in the Lyra field, based on the transit shape and on the out of eclipse modulation.

4.4.1 Stellar densities

To show the utility of a detailed light curve analysis, we applied the formulation described in Chapter 3, in Section 3.2.2, which allows a measurement of the host star density. This can be compared with the density inferred from the 2MASS colors, according to the values tabulated in Cox (2000). As there are few tabulated values in these tables, we performed a 4^{th} order polynomial fit of the J–K vs $\log(\rho/\rho_{\odot})$, and used the fitting coefficients to estimate the $\log(\rho/\rho_{\odot})$ of each candidate from its J–K color.

Fits of the transit shapes with the function defined in Section 3.2.2 are plotted in Figures 4.7 and 4.8. To provide a cleaner view of the transit shape, Figures 4.9 and 4.10 plot the phases of transit for each of the candidates, with the data points binned in 0.005 wide phase-bins. The error bars are the rms of the N points inside each bin, divided by the square root of N.

The results are summarized in Table 4.4, where the last column shows the ratio among the stellar densities estimated from the J–K 2MASS colors and those resulting from the transit shape fitting. There are only 3 stars for which this factor is in the range [0.4-1.6], which means that the two measurements of the densities differ by less than 60%.

This method eliminates 13 of the 16 candidates. These are T-Lyr0-08070, T-Lyr0-03507 and T-Lyr0-01100. For long-period candidates (in the frame of ground based transit searches, i.e., periods bigger than $\sim$7 d), this test should not be considered as a final test, as the eccentricities of the known exoplanets with these periods begin to become significant (e.g., HD 217107b, with a period of 7.11 d and an eccentricity of 0.14, Fischer et al. 1998), and the test intrinsically assumes circular planetary orbits. Of particular significance are the candidates whose J–K colors are typical of a K star; some of them have ratios among the two densities of several tens, which provides a clue that the K star is not a main sequence star (as assumed in the test) but a red giant. This is a strong indication for a blended system, as the typical radii of the giants (several tens of the solar radius) does not allow orbits with the short periods usually found by the observations (the orbit would be inside the stellar atmosphere).

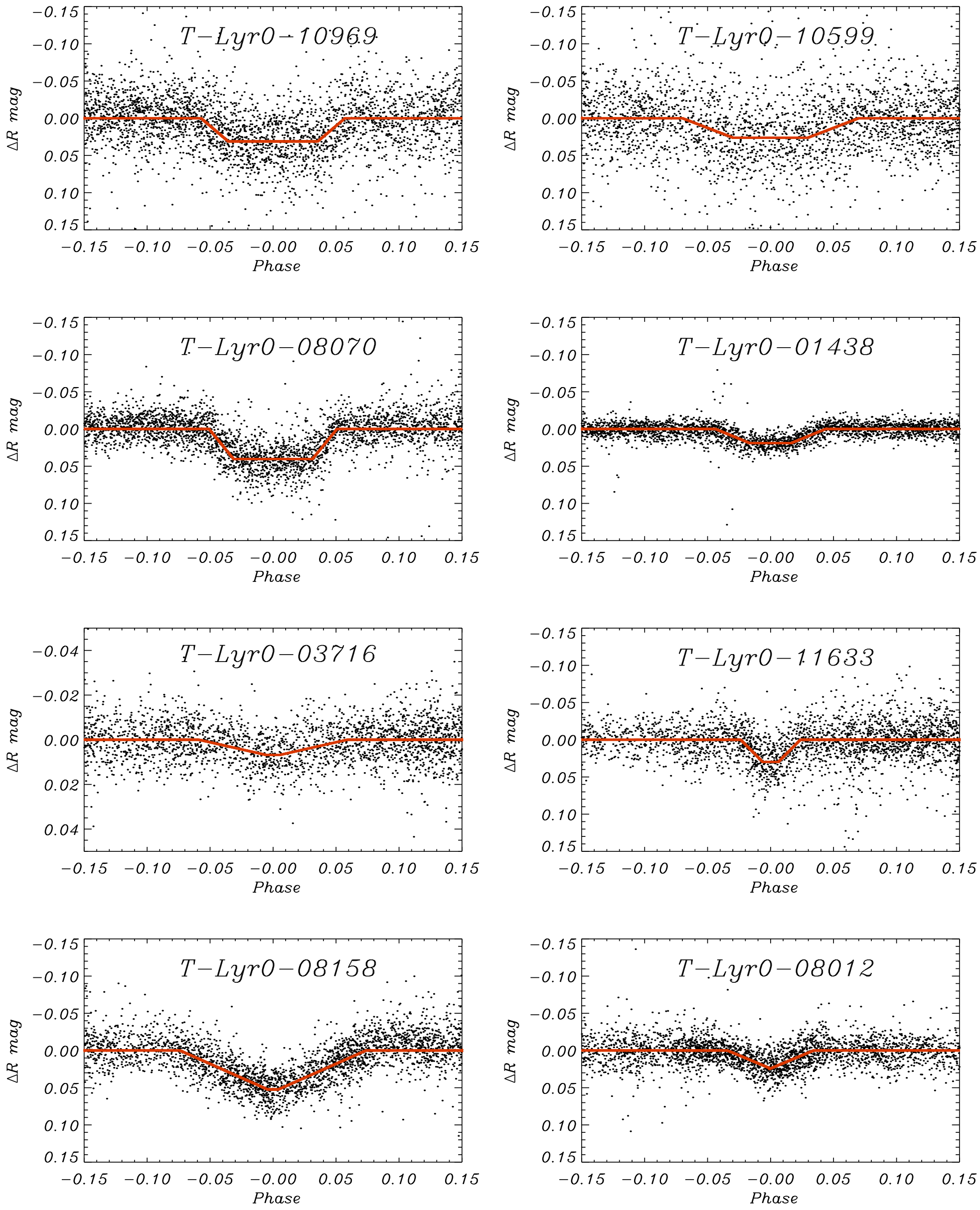

FIGURE 4.7— Transit shape fitting of the candidates in the Lyra field. The free parameters in the least square fit were the phase of the center of the transit, its total duration, depth and ingress (equal to the egress) time. See the text for details.

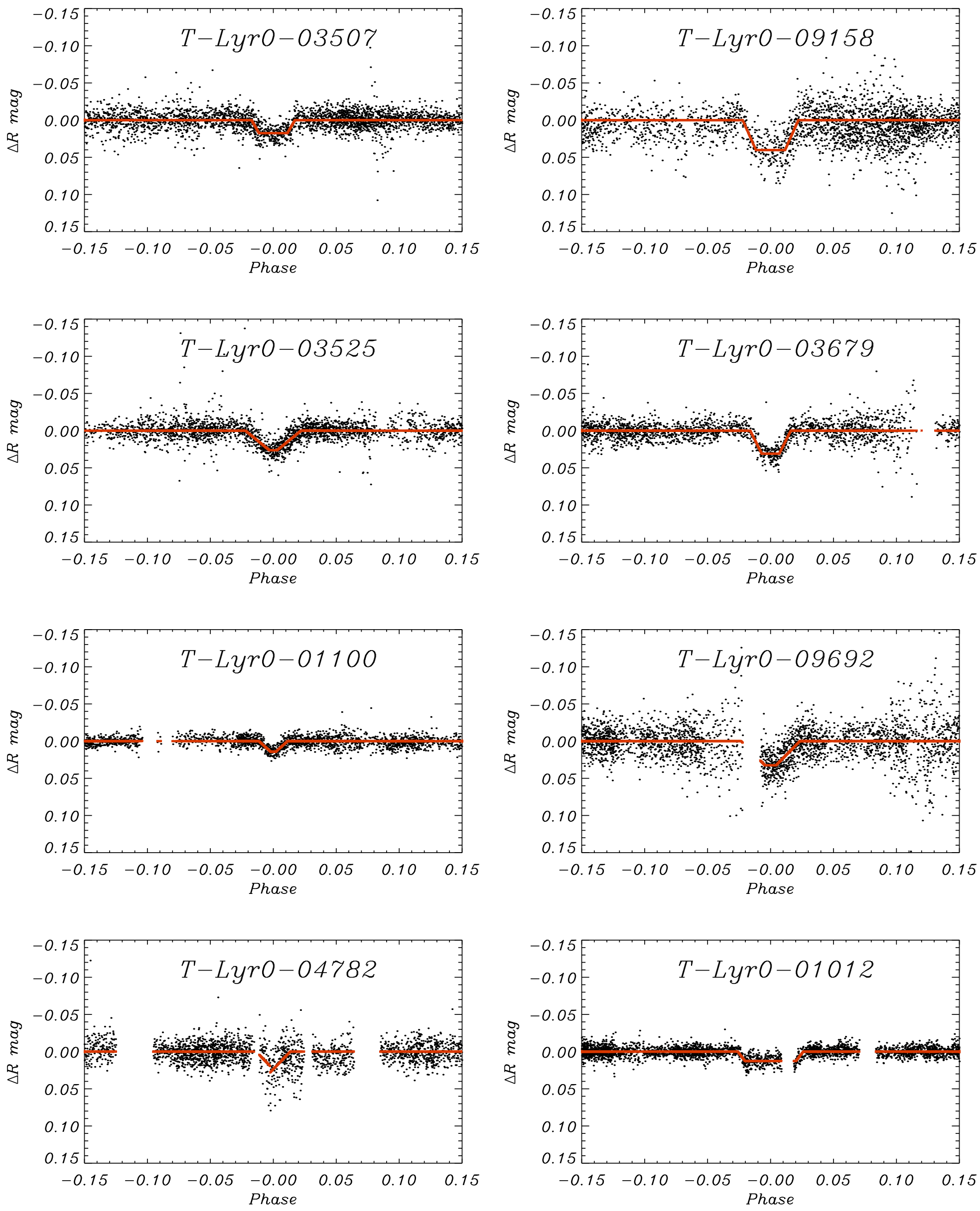

FIGURE 4.8— Transit shape fitting of the candidates in the Lyra field. The free parameters in the least square fit were the phase of the center of the transit, its total duration, depth and ingress (equal to the egress) time. See the text for details.

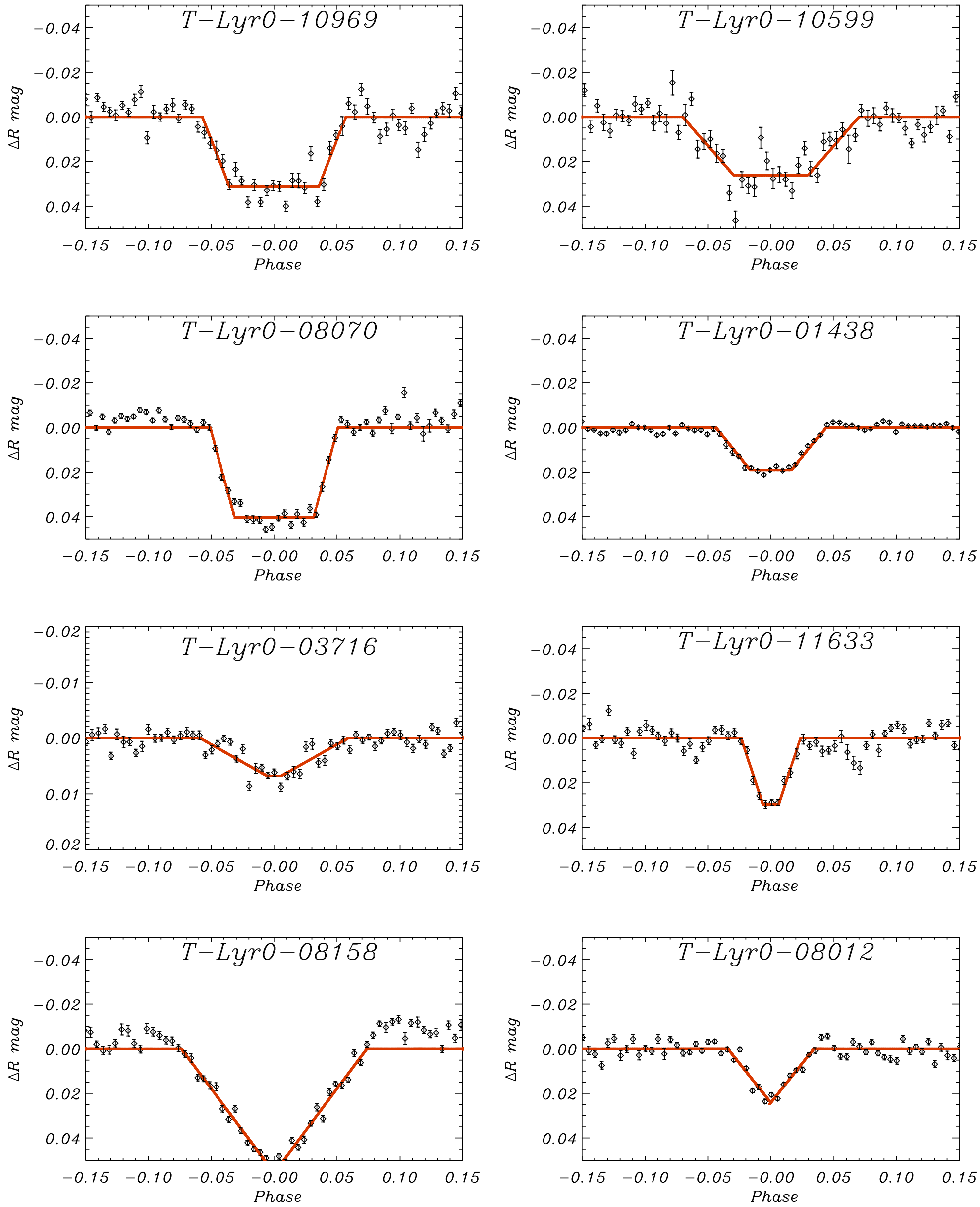

FIGURE 4.9— Same as Figure 4.7, with the data points binned in 0.005 wide bins in phase. The error bars are the *rms* of the N points inside each bin divided by the square root of N.

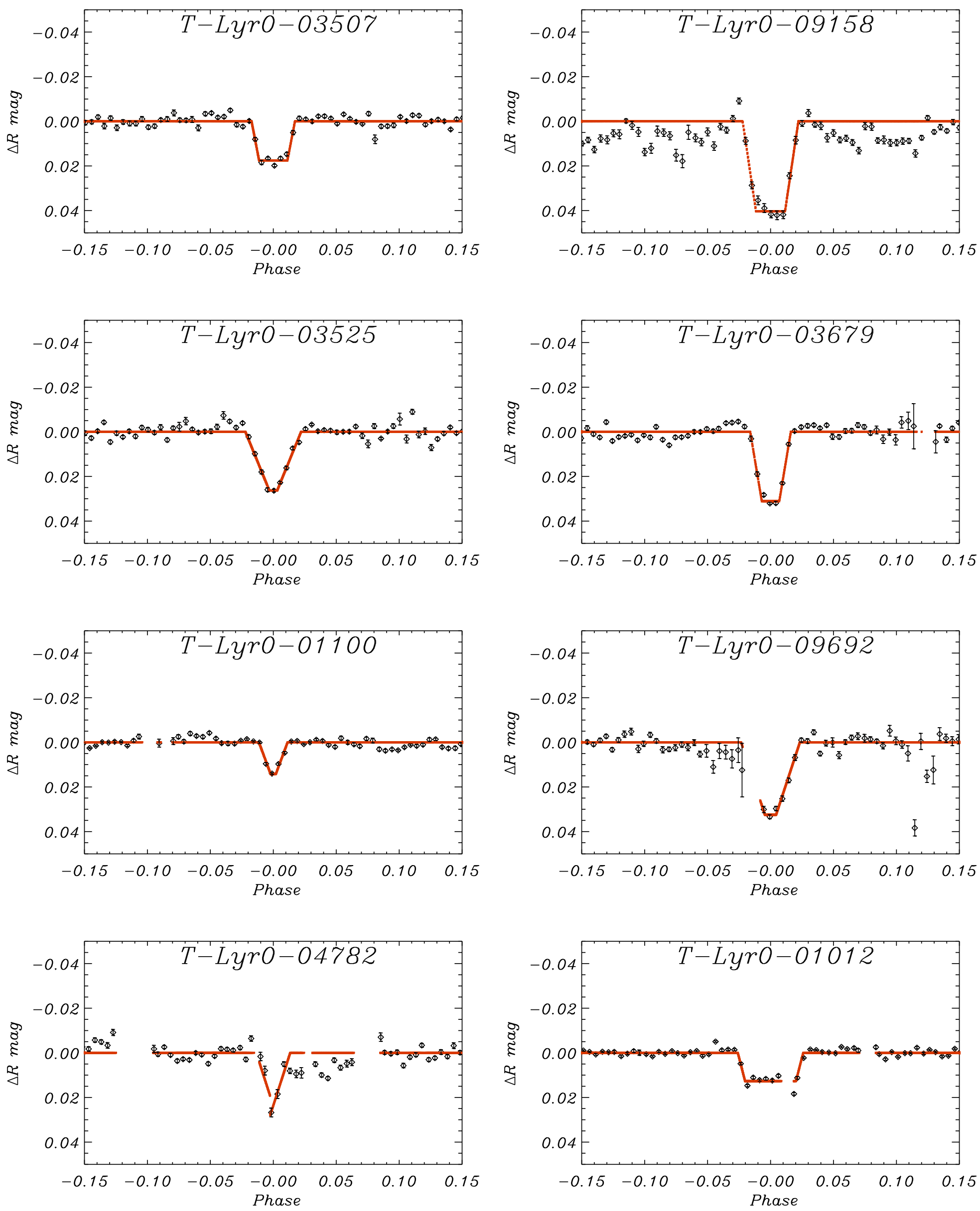

FIGURE 4.10— Same as Figure 4.8, with the data points binned in 0.005 wide bins in phase. The error bars are the *rms* of the N points inside each bin divided by the square root of N.

4.4.2 Out of eclipse modulation

We evaluated the significance of the out of eclipse modulation in each of the candidates, according to Equation 3.2. This was done by a non-linear fit of the phase-folded light curves to the 5 adjustable parameters ($<I>$,a_{c1},a_{c2},a_{s1},a_{s2}) based on the Levenberg-Marquardt algorithms (Levenberg 1944; Marquardt 1963). The eclipses, with a total duration measured in the previous section, were not taken into account in the fit. Figures 4.11 and 4.12 plot the fits to each of the candidates, superposed on the unbinned data. Figures 4.13 and 4.14 plot only the resulting fitting functions, to highlight the amplitudes of each of the modulations. The values of the significance D_i, defined in Equation 3.3 are printed in Table 4.5. Finally, Figure 4.15 plots the maximum values of these significance. The slash-dotted line in that plot, at a level of D = 3, separates candidates with significant out of eclipse modulation (at a 3σ level from those with non significant modulation). Surprisingly, only 3 out of the 16 candidates were consistent with no modulation. This gives an idea of the utility of this cheap test (i.e., no further observations are needed). The 3 candidates that survived this test were T-Lyr0-03716, T-Lyr0-03507 and T-Lyr0-03525.

Taking this result in addition to that from the previous Section, the only candidate that survived both tests was T-Lyr0-03507, which, as we will see in this and the next Chapter, proved to be the only transiting exoplanet among the 16 candidates. In the next Section, we summarize the spectroscopic and photometric follow-up observations of each candidate, to firm up this conclusion and to try to unveil the true nature of each of the impostors.

4.5 Spectroscopic and photometric follow-up of transit candidates

In this section, we summarize the spectroscopic and photometric follow-up work performed on the 16 candidates obtained in the Lyra field.

4.5.1 T-Lyr0-10969: An eclipsing brown dwarf, M star, or a blended system?

With a flat bottom eclipse lasting 2.45 hours, this short period candidate was compatible with a transit of a planet across a main sequence F-sized star (1.5 $R_\odot$). The 2MASS colors are consistent with an early-mid F star. Three spectra were taken with the CfA Digital Speedometers, revealing a rapidly rotating (80 km/s) F dwarf. The rapid rotation of the star causes the radial velocities to be less precise, but there are weak evidences for variations at the 10 km/s level. Assuming a mass for the primary of 1.5 $M_\odot$ (from Cox 2000),

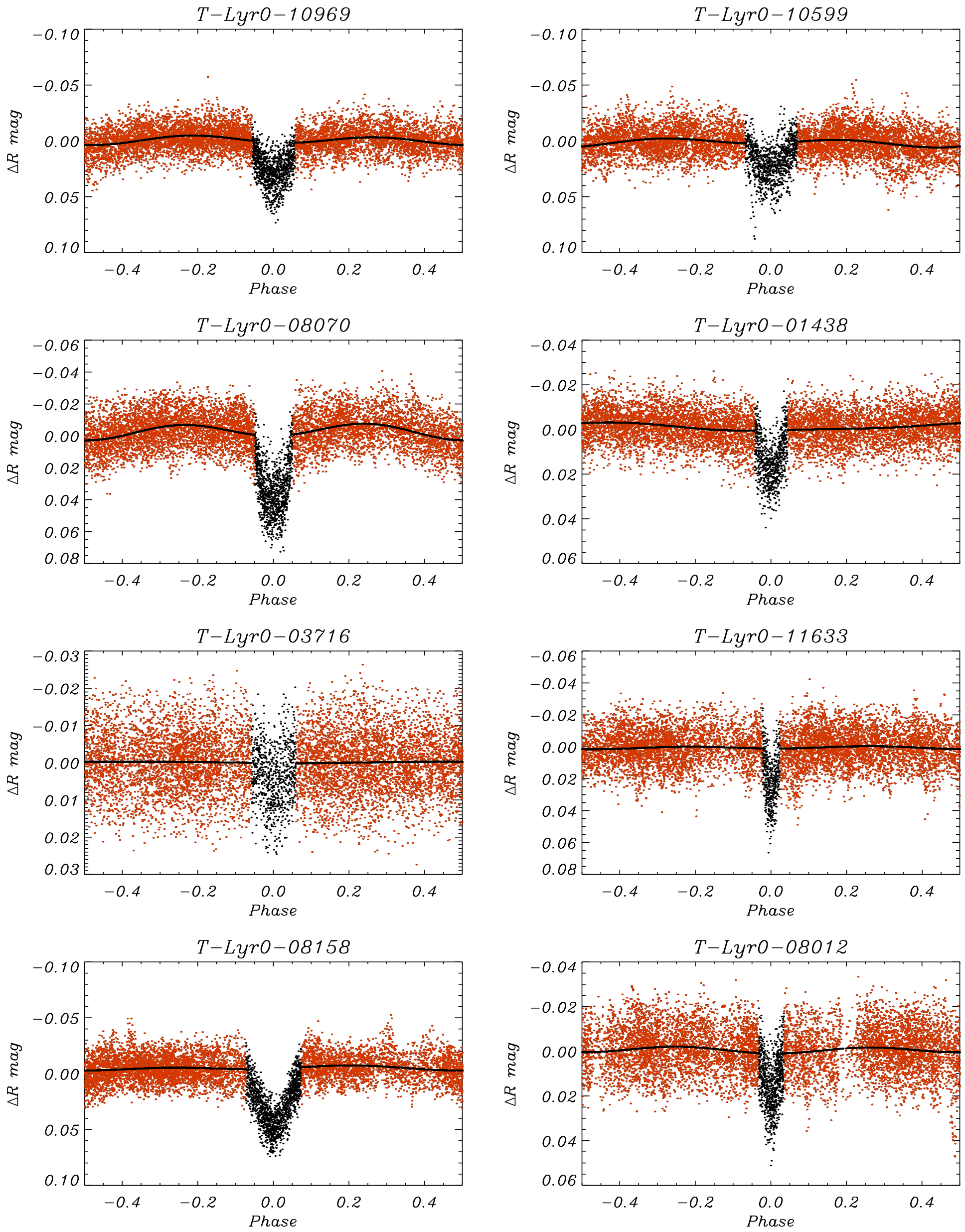

FIGURE 4.11— Folded light curves of the candidates in the Lyra field, together with the best fit to the out-of-eclipse part. The eclipses have not been considered in the fits.

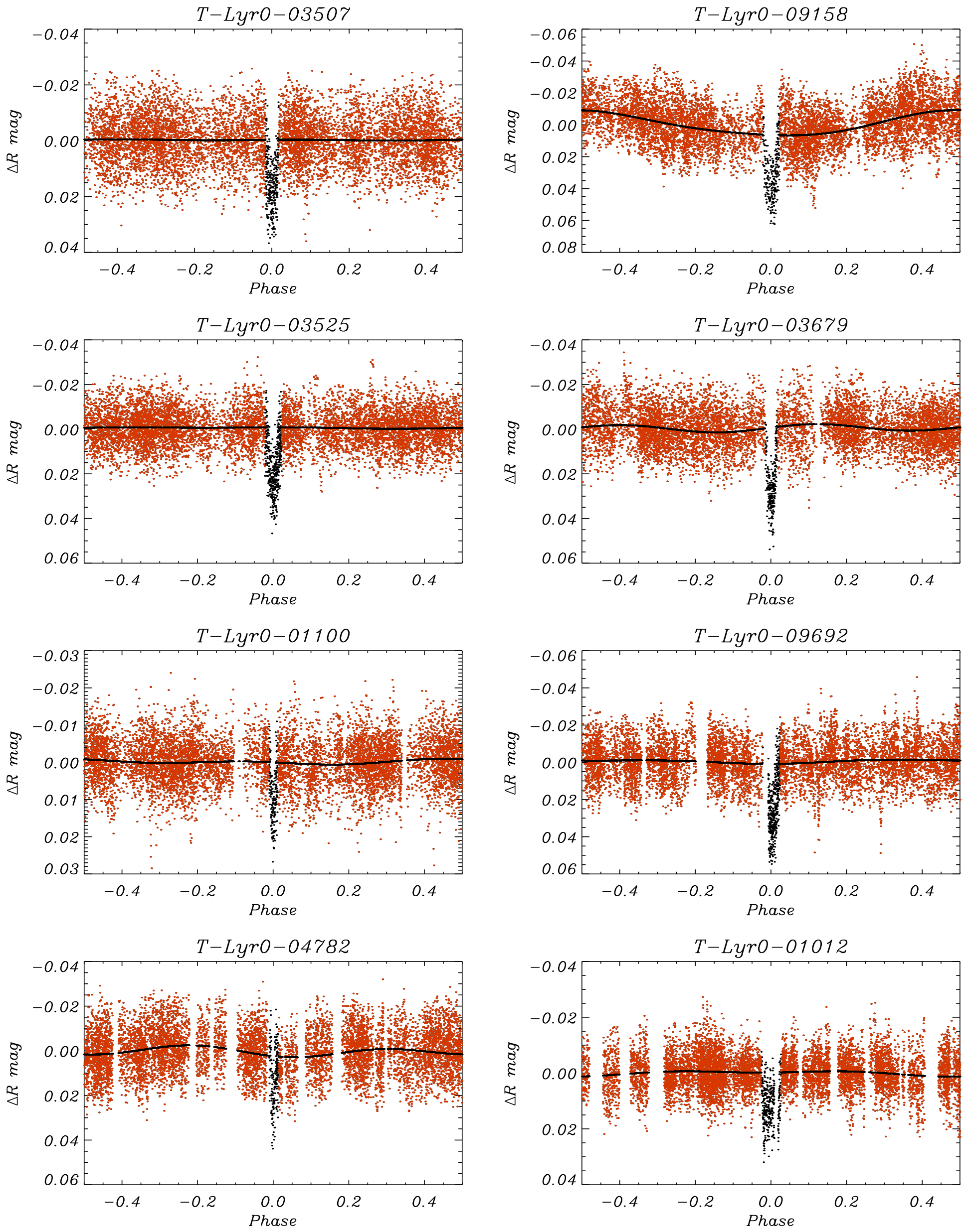

FIGURE 4.12— Same as Figure 4.11

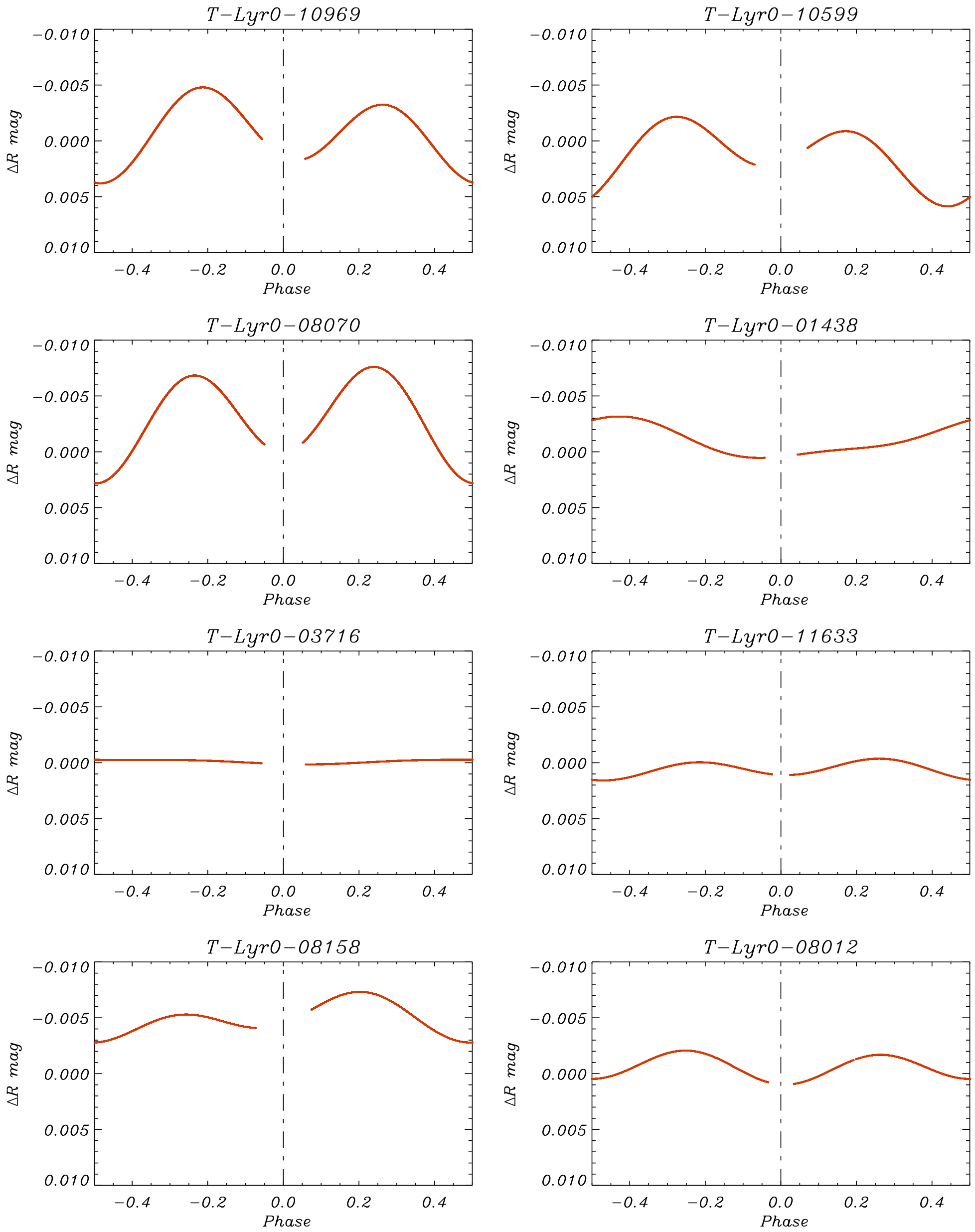

FIGURE 4.13— Ampliation of the best fit solution to the out of eclipse modulation on the candidates, plotted in Figure 4.11.

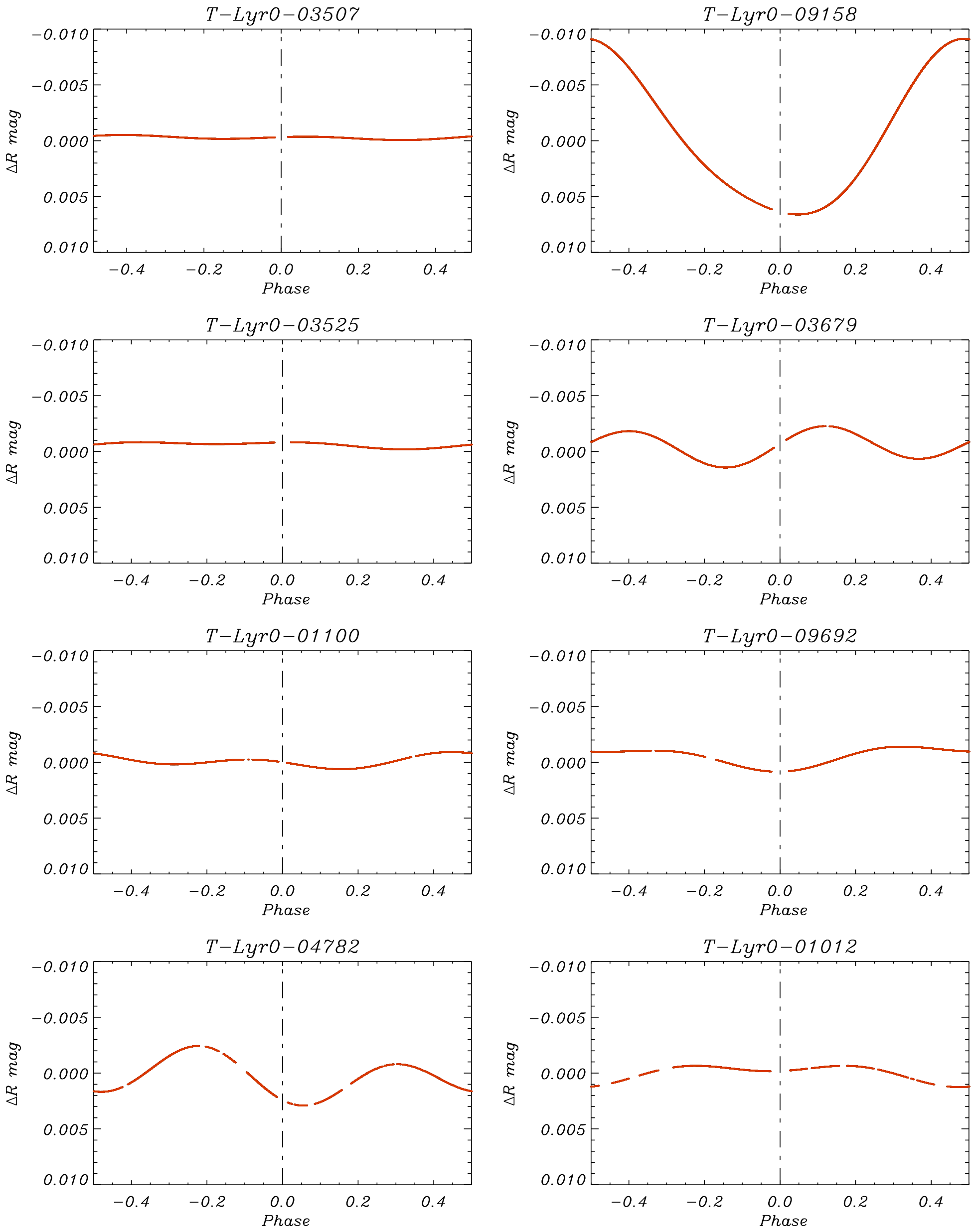

FIGURE 4.14— Same as Figure 4.13, for the candidates plotted in Figure 4.14

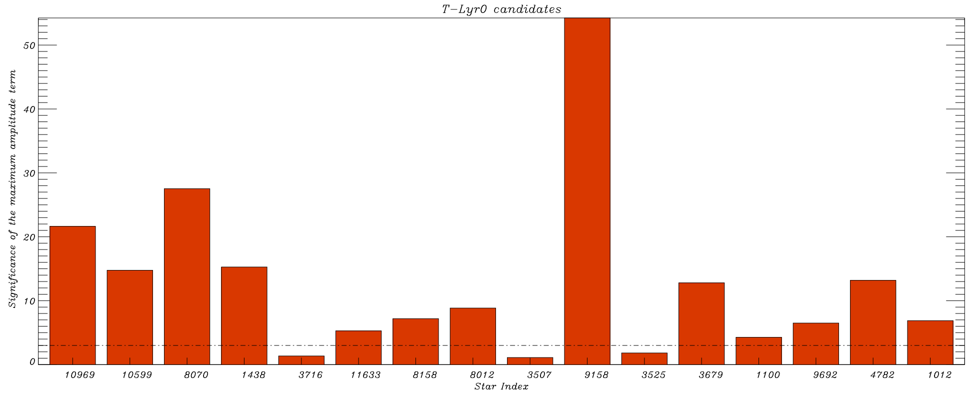

FIGURE 4.15— Values of the significance D_i defined in Equation 3.3 for the out of eclipse modulation in the candidates obtained in the field of Lyra. The 3σ level is overplotted with the slash-dot line. Only 3 of the 16 candidates remain below this level, and thus 13 of the candidates could have been ruled out by this simple method.

TABLE 4.5— Significances of the different terms to the fit described in Equation 3.2.

Candidate	D_{c1}	D_{s1}	D_{c2}	D_{s2}
T-Lyr0-10969	-7.75	4.92	21.63	8.12
T-Lyr0-10599	-9.72	10.47	14.76	-13.58
T-Lyr0-08070	-8.99	-2.93	27.53	0.60
T-Lyr0-01438	15.27	4.20	-1.48	-5.09
T-Lyr0-03716	1.35	0.63	0.34	0.36
T-Lyr0-11633	-1.51	-1.50	5.28	1.52
T-Lyr0-08158	-4.56	-6.03	7.19	-3.61
T-Lyr0-08012	1.70	1.44	8.85	0.56
T-Lyr0-03507	0.33	0.69	-0.67	-1.11
T-Lyr0-09158	54.24	1.65	-6.64	4.53
T-Lyr0-03525	-0.81	1.82	-0.94	-1.23
T-Lyr0-03679	0.61	-3.93	-2.32	-12.80
T-Lyr0-01100	4.27	0.68	-3.79	3.75
T-Lyr0-09692	6.50	-1.28	3.30	0.21
T-Lyr0-04782	2.97	7.00	13.19	6.22
T-Lyr0-01012	-6.88	1.34	5.28	-1.88

this range of velocities would imply a companion of 0.059 $M_\odot$, in the brown dwarf regime.

A companion with the masses in the brown dwarf regime would produce flat-bottomed eclipses when transiting in front of a F-sized star. But the existence of the so-called brown-dwarf-desert argues against this possibility. Better determined velocities could easily move the mass of the secondary to the M-star regime, which constitutes a much more plausible scenario.

In the case of a blended triple system, the rapidly rotating F star would be providing most of the light to the system, and a fainter eclipsing binary (not resolved in 2MASS nor AO images) would make the correlation peaks of the CfA spectra vary, which might be erroneously interpreted as variations in the radial velocities of the F star. The rapid rotation of the star makes it possible that a fainter stellar system remains undetected in the CfA spectra.

With the main star being a fast rotator it is difficult to disentangle which of the two possible explanations for this candidate is the real one. In any case, these transits can not be produced by an exoplanet.

4.5.2 T-Lyr0-10599: A blended triple system

With a period of less than 1 day, this candidate showed flat-bottomed eclipses in its light curve, and in the 2MASS images there were no other stars within 20" and 3 magnitudes in J. The 2MASS colors point to a mid F star. The total duration of the transits (3.1 h) are inconsistent with transits of a planet in a circular orbit around a main sequence star (see Figure 1.6).

The analysis of one CfA spectrum indicated a composite spectrum, with a slowly rotating primary and a rapidly-rotating secondary. The flat-bottomed eclipses together with this evidence for a composite spectrum is a proof for an (at least) triple system. Furthermore, the presence in the spectra of two signals of stars with different rotations could only be explained if the system had not enough time to be tidally locked. With such a short period, the tidal timescale for locking of, for instance, an 1.5 $M_\odot$ F star and a 0.3 $M_\odot$ star, is $\sim$37000 years (from the Equations in Marcy et al. 1997). This reinforces the triple star hypothesis.

A plot of the light curve binned as in the previous case (average of 64 data points per bin) is given in Figure 4.16. If we add the results of the out of eclipse modulation and stellar density measurement from the previous Section, we can conclude that there must be an unresolved eclipsing binary, constituting a blended triple system.

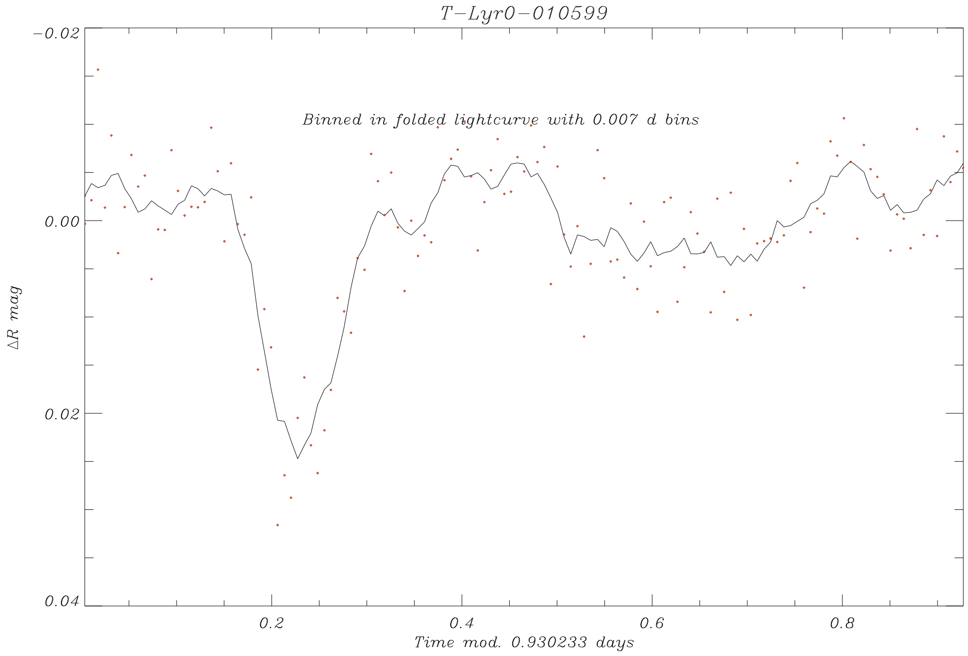

FIGURE 4.16— Light curve of T-Lyr0-10599 folded with the best found period and binned in phase. Each point is an average of typically 60-70 data points. The solid light curve is the 6-points median-filtered light curve. After follow-up observations, this candidate proved to be a blended triple system.

4.5.3 T-Lyr0-08070: A binary system

This candidate has clear flat-bottomed eclipses, that lasted for 2.9 hours, with 1.8 hours in a flat bottom stage. This duration is longer than expected for a solar radius star and the low period of the transits (1.18464 d). If the star is made bigger, so that the duration can match the observations ($\sim$2 $R_{\odot}$, according to Figure 1.6), then the depth is far too big to be explained with a Jupiter sized object (the implied radius would be 3.7 R_J). Some eccentricity might help to explain the long duration of the eclipses, but then a problem arises on how to explain a non-negligible eccentricity in an object with a period of roughly 1 day. A light curve binned in phase shows an out of eclipse modulation with a semi amplitude of $\sim$5 mmags (Figure 4.17), as expected from the analysis of the out of eclipse modulation carried out in Section 4.4.2.

Four spectra were taken with the CfA Digital Speedometers. These are consistent with a main sequence star of T_{eff} = 6500 K, rotating with a vsini of 64 km/s. Even with such a high rotational velocity (which broadens the spectral lines, decreasing the precision of the radial velocities measurements), radial velocities changes have a range of ~20 km/s. This is evidence for a stellar companion to the star. The rotation of the primary, and the period of the secondary, yield a radius of the star of 1.5 $R_\odot$ (assuming tidal synchronization, see Equation 3.12), which is to first order consistent with the determined T_{eff}.

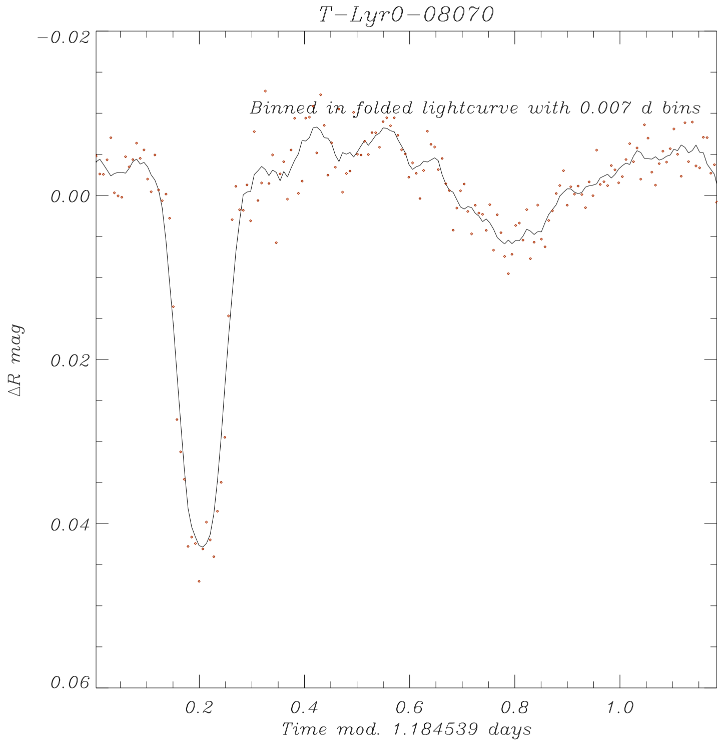

FIGURE 4.17— Light curve of T-Lyr0-08070 folded with the best found period and binned in phase. Each point is an average of typically 50 data points. The solid light curve is the 6-points median-filtered light curve. After follow-up observations, this candidate proved to be a binary system.

4.5.4 T-Lyr0-01438: A binary system

With a period of 1.297404 d, the fit of the transit shape of this candidate revealed 2.7 hour eclipses with a flat bottom duration of 1 hour. If main sequence stars and circular orbits are assumed, then the mass of the central star should be $\gtrsim$1.5 $M_\odot$ in order to reproduce the transit duration (see the Figure 1.6 of the Introduction).

The spectral type of the star from the 2MASS colors pointed to an early-mid F type star. As expected from the result of the Section 4.4.2, binning in phase the light curve showed out of eclipse modulation with an amplitude of $\sim$3 mmags (Figure 4.18). This was a clue that the system had stellar components. There are no significant differences between primary and secondary eclipses when the light curve is folded with double the period. Two spectra taken at the CfA showed variations of 50 km/s, and a rotational velocity that implied one solar radius for the star, assuming synchronization with a companion with double the reported period. This confirmed the stellar nature of the system, thus rejecting it as a planetary candidate.

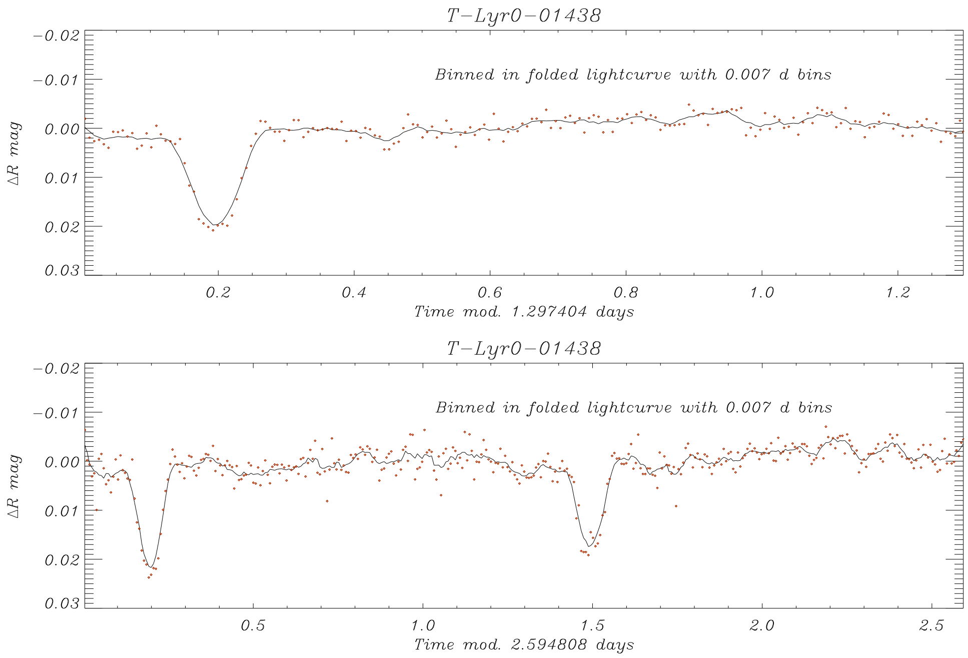

FIGURE 4.18— Light curve of T-Lyr0-01438 folded with the best found period and binned in phase (top). Each point is an average of typically 45 data points. Bottom: the same candidate, but folded with double the reported period. The solid light curve is the 6-points median-filtered light curve. After follow-up observations, this candidate proved to be a binary system, with double the reported period.

4.5.5 T-Lyr0-03716: A blended triple system

Even though the STARE light curve shows a ~6.8 milli-magnitudes depth transit, the PSST data helped to confirm this as a candidate, with the lowest transit depth of all. The combined and binned data showed a triangular eclipse, as seen in Figure 4.19. The 2MASS colors are compatible with a K star. But, the spectra taken at CfA favor a K giant, and there is no velocity variation at a level of 0.14 km/s. The period of the transit and typical radii for K giant stars (a KIII star has a radius of 15 $R_{\odot}$, Cox 2000) would imply that the companion would be in orbit inside the atmosphere of the star. However, this problem can be solved if we explain the observations with a triple system, where one component is the K giant, and there is a faint main-sequence eclipsing binary in the glare of the giant.

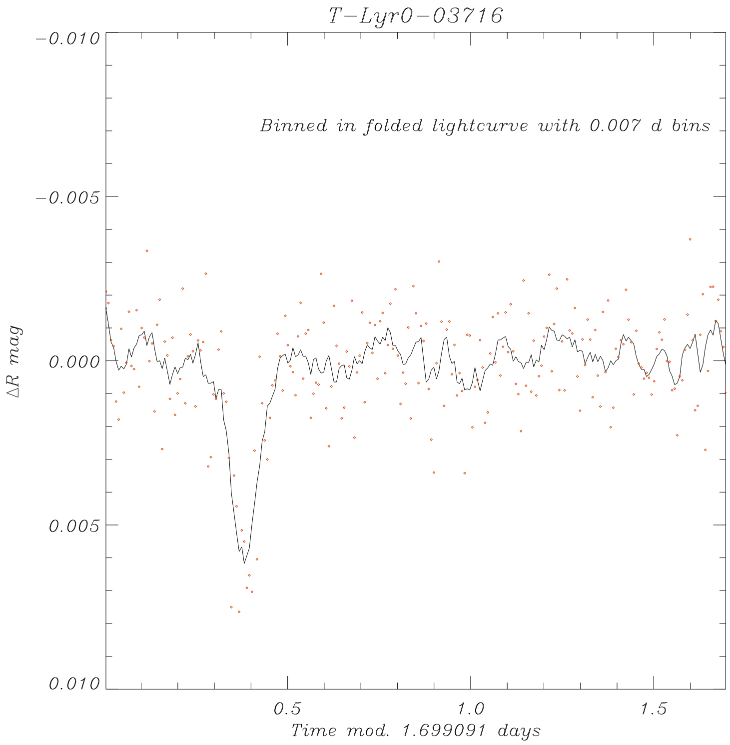

FIGURE 4.19— Light curve of T-Lyr0-03716 folded with the best found period and binned in phase. Each point is an average of typically 50 data points. The solid light curve is the 6-points median-filtered light curve. After follow-up observations, this candidate proved to be a blended triple system.

4.5.6 T-Lyr0-11633: A binary system

The light curve of this candidate showed eclipses lasting for 2 h, and the fit to the transit shape is consistent with a flat transit part of half an hour. Binning the light curve folded in phase with the reported period, and twice this value, showed some tentative differences between primary and secondary eclipses (Figure 4.20). However, these were not conclusive, mainly due to the faintness of this candidate in the STARE images, what causes the dispersion of the data to be 0.024 mags in the raw (unbinned) data.

The 2MASS colors indicate a mid F or an early G type star. Three CfA exposures showed a variation in radial velocities with a total range of almost 60 km/s. This is not consistent with a planetary mass companion, so this object was not further observed.

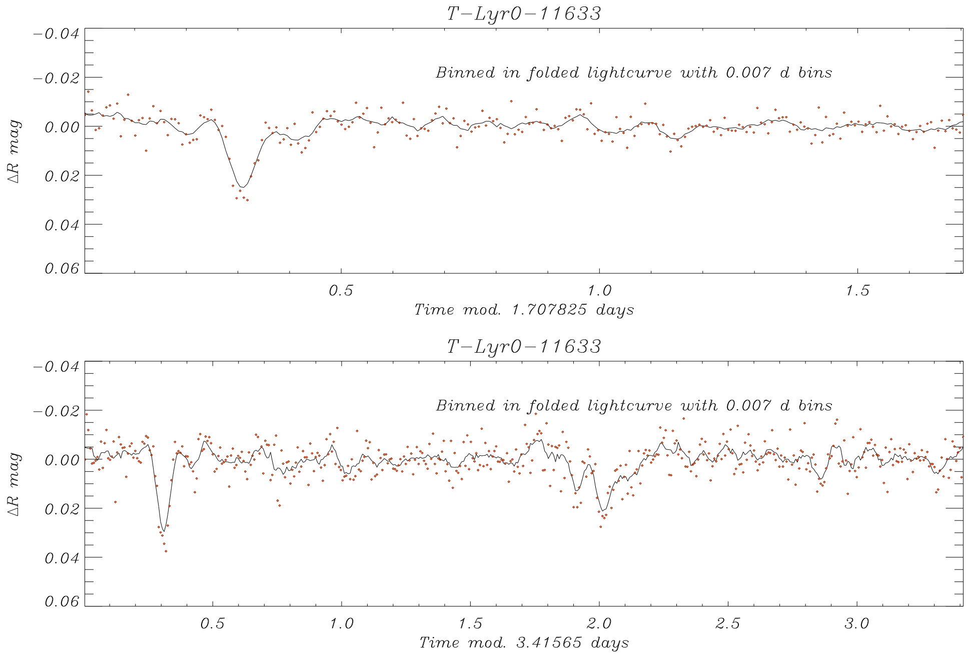

FIGURE 4.20— Folded light curve of T-Lyr-11633, with the reported period (top) and twice this value (bottom). The CfA radial velocities showed this was a stellar binary system.

4.5.7 T-Lyr0-08158: A blended stellar system

This star exhibits triangular-shaped eclipses. A binning in phase with the photometric period (1.873396 d) and twice this value does not show detectable differences among a primary and a secondary eclipse (Figure 4.21). There is a star 2.4 magnitudes fainter in J at 7″, easily resolved in the 2MASS images. The duration of the eclipses is ∼7 hours, inconsistent with a transit of a planetary companion with this period, in a circular orbit. 2MASS colors point to a mid-K star, while the CfA spectra (not showing detectable radial velocity variations) favor a G dwarf. Both the duration and the shape of the eclipses can not be explained by a transiting planet, and the most plausible scenario is the star at 7″ being an eclipsing binary with almost equal components. In this case, the undiluted eclipse depth would be of ∼48.5%, which favors the hypothesis of undistinguishable primary and secondary eclipses, both stars being of similar size and luminosity. The J–K colors of this star are compatible with a mid-G spectral type.

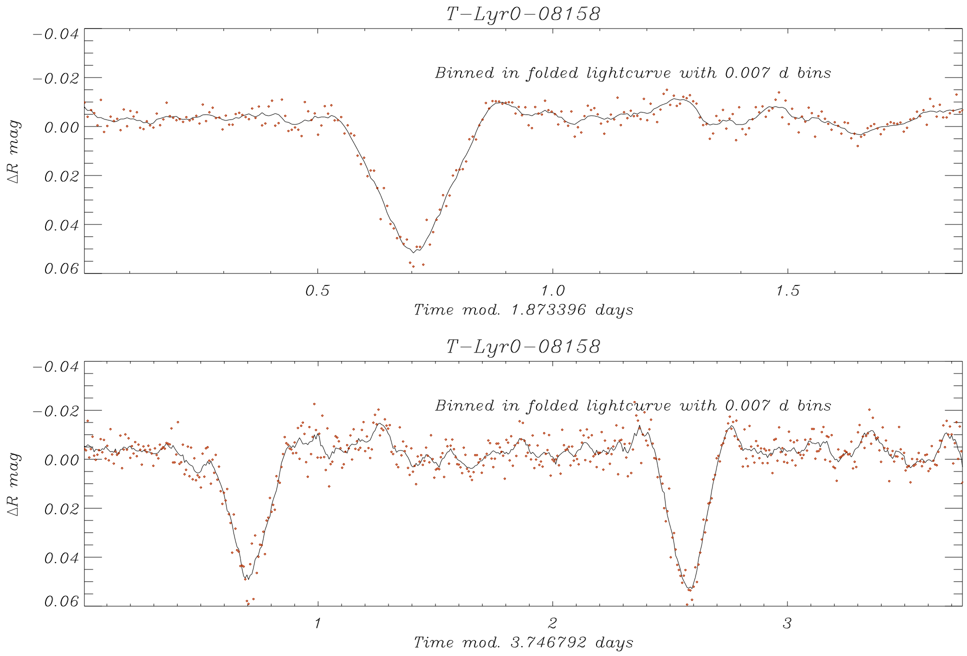

FIGURE 4.21— Folded light curve of the candidate T-Lyr-08158 with the best-found period (top), and twice this value (bottom). There are no significant differences among the primary and secondary eclipse in the bottom plot. After follow-up observations, this candidate proved to be a blended stellar system.

4.5.8 T-Lyr0-08012: A blended stellar system

As we saw in Section 4.4.2, this star showed significant out of eclipse modulation, and the fit to the transit shape revealed a triangular eclipse, with no flat bottom (see Table 4.2). The duration of a grazing planetary transit, for a 1 $R_{\odot}$ star, would be of $\sim$1.6 h, which is much smaller than the fitted total transit duration of 4.5 hours. Four spectra of this candidate were taken at the CfA, showing a slowly rotating star with a T_{eff} of 6000 K, consistent with the J–K determined spectral type (late F or early G). The measured radial velocities are consistent with no variation, down to residuals of 0.6 km/s.

There is a companion 2 mags fainter at a distance of $21''$. The out of eclipse modulation, the transit shape fitting and the absence of radial velocity variations suggest that this companion is an eclipsing binary, whose light is diluted by the candidate, thus constituting an obvious blended case. As the angular separation of the components is relatively high, the more plausible scenario is a fortuitous alignment of the two resolved stars, with no gravitational binding. The undiluted eclipse depth of the binary would be 17.2% in J.

4.5.9 T-Lyr0-03507: A transiting planet

This candidate will be discussed in further detail in the next Chapter. After the confirmation that this star had a Hot Jupiter producing transits, this star was renamed as TrES-1 parent star. The period that returned the maximum value of the SDE was half the real period. This circumstance is due to the period being close to an integral number of days, which causes the phases at a distance of 0.5 from the transits to be poorly sampled (see Figure 4.5). The PSST data served to identify the real period, as no transits were observed in the phases that were poorly sampled in the STARE data.

4.5.10 T-Lyr0-09158: A binary system

This star showed flat-bottomed eclipses in the binned light curves, and there was evidence for out of eclipse modulation, greater than 10 mmags amplitude (Figure 4.14). Both J–H and H–K are consistent with a G type star. The CfA spectra are also consistent with a G type star, but the rotation is bigger than that expected for a dwarf star synchronized with a stellar companion. Three spectra spanning 6 days showed velocity variations of more than 10 km/s, also rejecting this star as a planetary candidate. A plausible model for this system is a slightly evolved G star with a stellar companion. The evolved stage of the star would result in an increased radius, and thus the eclipses of the secondary component could have depths comparable to those produced by a transiting planet across a dwarf star, and also a flat part of the transit. The results of the out of eclipse modulation test performed in Section 4.4.2 showed a significant contribution of the $\cos p_k$ term into the fit. A more realistic situation would be that the real period is twice the reported period, showing an eclipsing binary with indistinguishable primary and secondary eclipses, and with the out of eclipse modulation being a consequence of the ellipsoidal variability instead of the more improbable reflection effect. In Figure 4.22 we show plots of the binned data, for both cases.

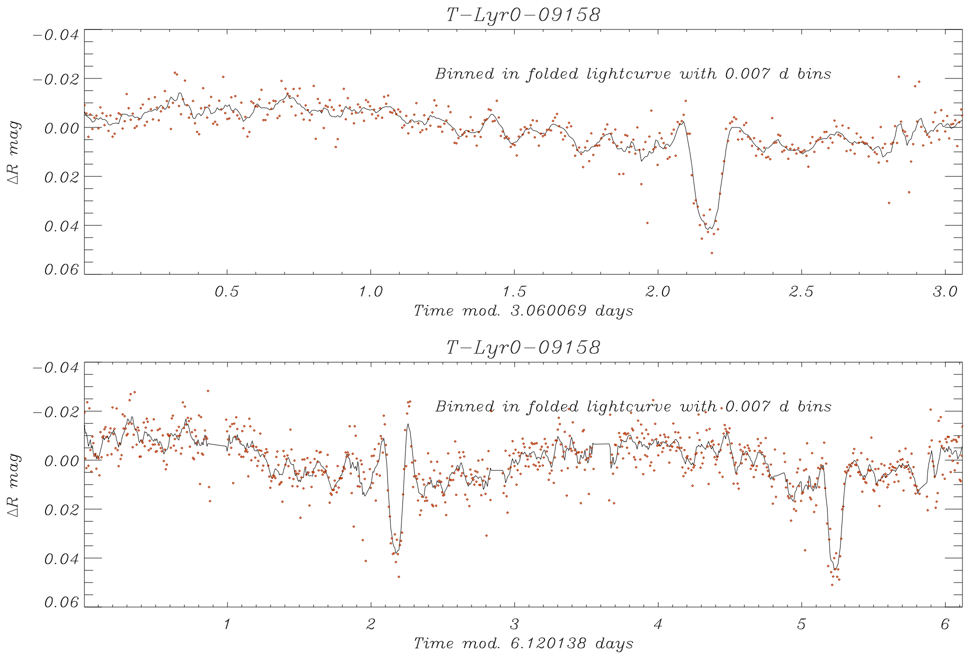

FIGURE 4.22— Folded light curve of the candidate T-Lyr-09158 with the best-found period (top), and twice this value (bottom). There are no significant differences among the primary and secondary eclipse in the bottom plot. After follow-up observations, this candidate proved to be a binary system.

4.5.11 T-Lyr0-03525: A grazing binary

Even though the raw light curve does not show evident flat-bottomed transits, the fit to the transit shape is compatible with a short flat part, of ~30 min. If there is a transiting planet at high enough latitudes, it could produce transits without a flat bottomed part (if the orbital inclination of the system is between the values stated in Equation 3.1.1). The depth could be compatible with a planetary transit, and the 2MASS colors are consistent with a F-G dwarf star. There are two stars, at 22″ and 42″ respectively, that are less than 3 mags fainter in J. In the case that these are eclipsing, the depths would have to be of less than 12% in order to reproduce the observed depths (equal to 12% for the star 2.9 mags fainter located at 22″). However, two exposures taken at the CfA showed a double lined binary with almost equal components. This rejects the hypothesis that the relatively close companions are eclipsing. The system is a grazing binary.

4.5.12 T-Lyr0-03679: A blend

The light curve of this candidate shows a 0.031 mags flat bottomed eclipse lasting for ∼2.9 hours, consistent with transits of an object with a radius of 1.7 R_J across a 1 $R_\odot$ star. If the star were smaller, of a size of 0.6 $R_\odot$, then a planet with a radius of 1 R_J could explain the observed depth. But, in this case, the total duration of the transit would be bigger than the maximum duration for circular orbits (see the Figure 1.6 of the Introduction). Some eccentricity might explain the longer duration of the transits, if these are happening closer to the apastron than to the periastron.

The 2MASS images (Figure 4.23) showed two close stars, at an apparent distance of 7.9″, and with a difference in J magnitudes of 1.8. As both stars fall inside the PSF of the STARE images, we can not know which of the two stars is being eclipsed. We will refer as component A to the star GSC 02665-00795 (the brightest one) and component B to the star 2MASS 19203383+3637402 (the faintest). If the component A is having the eclipses, the real depth would be diluted, and the corrected depth, taking into account the flux from component B, would be 3.35% instead of 2.81%[2]. This way, a planetary object might be the source of the transits, even if they are diluted (a 1.3 R_J planet would match the observations if we assume a radius for the A component of 0.75 $R_\odot$, based on its 0.614 J–K color.). But, if the eclipsing companion is around component B, the corrected depth would be of 17.6%[3], and thus it could not be explained by transits of a planetary object (the implied radius would be of 3 R_J).

In order to find out which of the component was having the eclipses, we observed the system at the 82-cm IAC80 telescope, on the night of June 28th 2004. Due to the nature of this case, we observed completely in focus, to be able to perform aperture photometry on each of the two stars, as well as in several reference stars. The final light curves, obtained in V an I filters, are plotted in figures 4.24 and 4.25. In those figures, we have also plotted the signal we

[2] $k = 1 - \frac{(F_A+F_B)10^{-0.4*0.031} - F_B}{F_A}$, where $F_A = 10^{-0.4*m_A}$ and similarly with F_B

[3] $k = 1 - \frac{(F_A+F_B)10^{-0.4*0.031} - F_A}{F_B}$

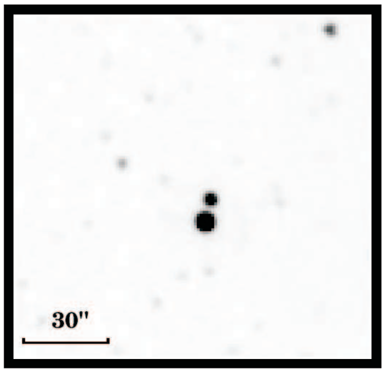

FIGURE 4.23— 2MASS image of the candidate T-Lyr0-03679, revealing the presence of two close stars, at a separation of 7.9″.

would have obtained if the system had not been resolved, by adding the fluxes of both stars. A flat bottomed eclipse is clearly seen in the V filter. The V–I color of the blended system would have shown a slight signal in the transit phase (Figure 4.26), which indicates that the blended system appears redder while in transit. This is the opposite effect as the limb-darkening wavelength dependence; in this case, the limb-darkening effect is more noticeable at shorter wavelengths (e.g., Claret 2000). The transit shape, in the case of a planet, would thus be flatter at longer wavelengths. This would leave a colored signal that would make the star appear slightly redder in the ingress and egress phases, and bluer in the central parts of it (see, for example, the colored light curves of HD 209458b by Charbonneau et al. 2003). The observed contrary effect means that *i)* the companion can not be a transiting planet, and *ii)* the "third" star (i.e., the one that is providing most of the flux to the system, component A in our case) is redder than the brightest star in the eclipsing system (component B). This is confirmed with the 2MASS colors ((J–K)$_A$ = 0.614, (J–K)$_B$ = 0.510).

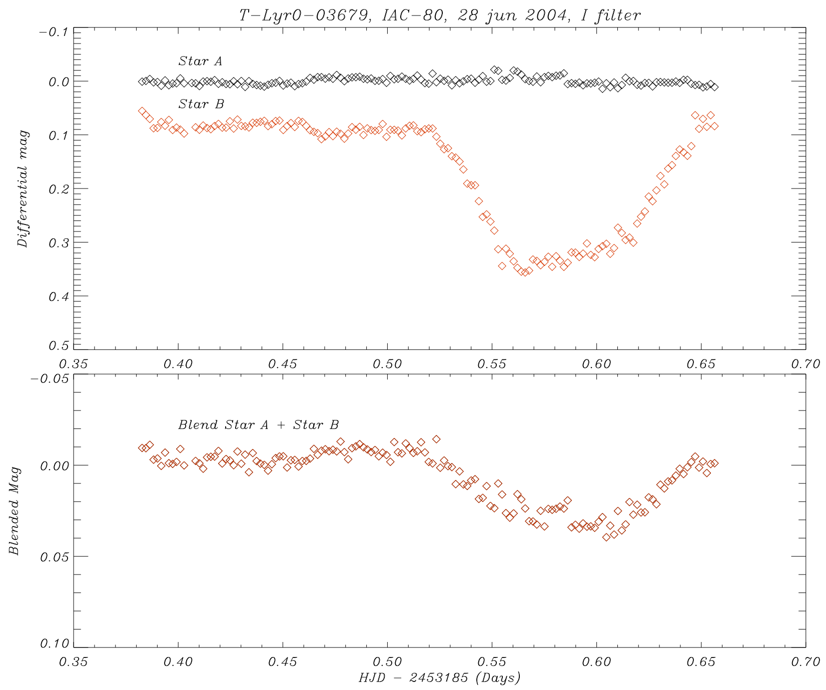

FIGURE 4.24— I-filter differential light curves obtained at the IAC80 telescope. Top: the two individual light curves of each of the components, revealing a flat-bottomed eclipse in the faintest star. Bottom: the observed light curve if we add the fluxes of the two components (the same effect as if we had not resolved the system).

4.5.13 T-Lyr0-01100: A blend

The light curve of this object seems to show a flat bottomed eclipse. The 2MASS images reveal two close ($8.2''$) stars with similar brightness. Assuming both stars are of identical brightness, the undiluted depth of the transits would then be 0.028 mags. The 2MASS colors of these stars point to two mid-F stars. Thus, the radius of an object capable of producing 0.014 mags depth transits in the blended system would be of 2 R_J (assuming a radius for the F star of 1.3 $R_\odot$).

The observations obtained at the WHT with NAOMI showed that one of these two stars was indeed a double star (see later, Figure 4.29). All the three stars have a similar brightness in K filter. The distance of this third star to its closest companion is $\sim 0.8''$. With three stars of similar brightness blended, the radius of an object that can cause the observed transit depths is now $\sim$2.5 R_J, if we assume that it is orbiting around one of the two F stars. There are no big

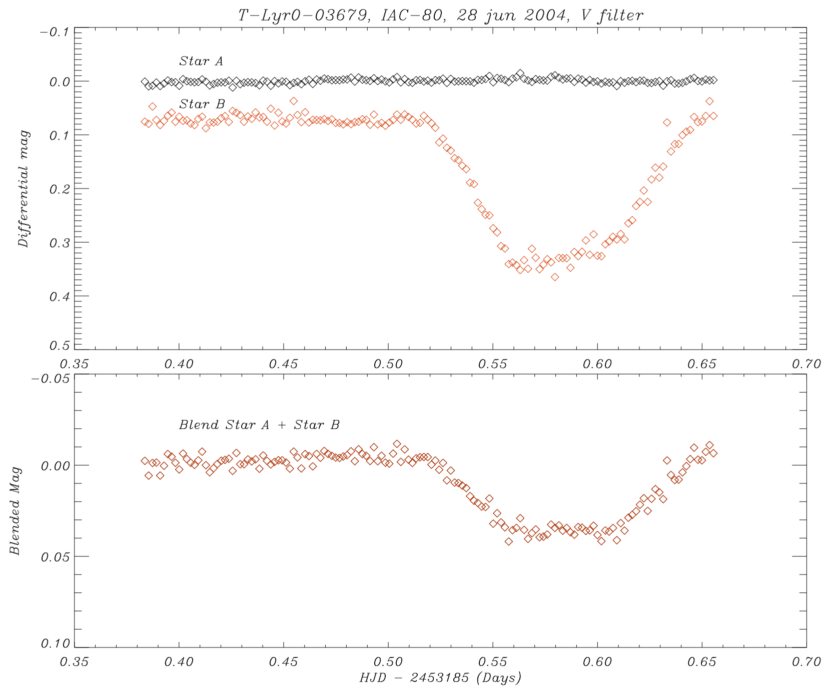

FIGURE 4.25— Same as Figure 4.24, for the V filter.

inconsistences among the spectral types of the two stars resolved in the 2MASS images, when estimated from the J–H and from the H–K colors (see Table 4.1). This indicates that the newly found star might have a spectral type similar to the other two, and thus also a similar radius.

4.5.14 T-Lyr0-09692: A diluted triple system?

The STARE light curve of this candidate showed evidence for three egresses of a transit with a period of 6.199628 d. J–H colors suggest an F6 spectral type, while the H–K point to a K4 star. This discrepancy might be resolved with the assumption of a blended system. There are clues for out of eclipse modulation, as we saw in Section 4.4.2. The CfA spectra showed radial velocity variations of more than 30 km/s, and rotational velocities not compatible with tidal synchronization. This circumstance can arise if the stellar system is composed of an eclipsing binary diluted by a third star (the measurement of the rotational velocity being affected by the contribution of a secondary unresolved moving correlation peak).

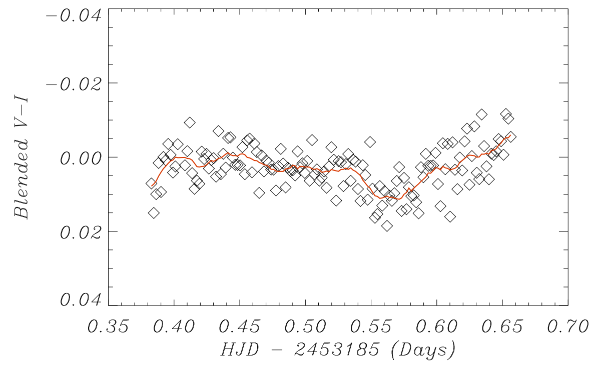

FIGURE 4.26— V–I color signature of the eclipse of the system T-Lyr0-03679, as would have resulted if the system had not been resolved. The color pattern of the eclipse is the opposite as expected for a transiting planet (see text).

4.5.15 T-Lyr0-01012: A binary system

This candidate showed a flat-bottomed eclipse lasting for at least 12 hours. Its period, of more than 10 days, was specially interesting, as a transiting planet found with such a long (in terms of transit searches) period would provide some clues on the dependence of the inflation of the planet due to the central star insolation, and thus to solve the paradox of the radius of HD 209458b (see the Introduction, 1.4).

STARE recorded one whole night in transit, one ingress and one egress. PSST recorded also one ingress, one egress and a whole night in transit, but all were different events (after that whole night in transit in the STARE data, the egress of the transit was recorded in the PSST data set). Combining both data sets gave a clearer light curve, but, when folded with double the period, there is still place for a secondary eclipse that would have not been observed. As seen in Figure 4.27, the ingress recorded from the PSST site seems to go further down than the bottom flat part of the primary eclipse. The total duration of the transit is also incompatible with a transiting planet across a F star, if its orbit is circular (∼5.2 h, see the Figure 1.6). Adding some eccentricity to the system[4] could solve the problem of the transit duration, as the orbital velocity at apastron varies from the circular orbital speed by a factor of $\sqrt{(1-e)/(1+e)}$.

[4]With periods in this range, the eccentricities can be significant, as is the case of HD 217107b with a period of 7.11 days and eccentricity of 0.14 (Fischer et al. 1998), or HD 108147b with a period of 10.9 days and eccentricity of 0.49 (Pepe et al. 2002b)

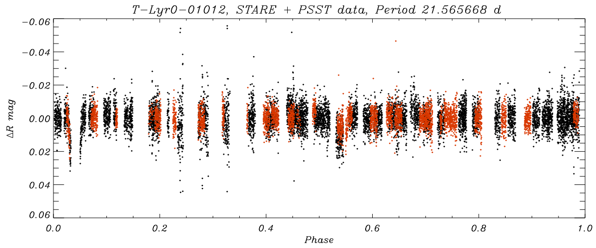

FIGURE 4.27— Phase folded light curve of the combined STARE + PSST data, with double the period reported in Table 4.2. There is still the possibility for deeper primary eclipses that would have not been recorded in any of the data sets (at a phase of ∼0.04). After follow-up observations, this candidate proved to be a binary system.

In this case, though, eccentricities bigger than 0.8 are needed to explain a 12 hours-long transit, and the orientation of the orbit should be such as to produce the transits near the apastron.

Three CfA spectra spanned in 6 days showed velocity variations of more than 50 km/s, thus rejecting it as a transit candidate. The J–K colors are significantly bluer than the effective temperature determined from the spectra, thus suggesting a hot blue companion.

4.5.16 T-Lyr0-04782: An unsolved case

There is only one whole transit event of this candidate, showing a ∼0.028 mags eclipse with a duration of ∼6 h. Folding the light curve with a period of 9.22 d gives a possible solution, and a SDE value that allowed its identification. But, as only one transit event was recorded in the STARE data, and none were detected in the PSST data set, this period should be considered with skepticism, and as a minimum value of the period, under the assumption that this event is real and not an artifact of uncorrected atmospheric extinction or other instrumental effects. Two CfA exposures taken 4 days apart showed no velocity differences, and a slowly rotating star.

4.6 Adaptative Optics observations of the candidates

Some of the candidates in the Lyra field were observed at the 4.2 m WHT, with the NAOMI AO system (Myers et al. 2003), and recorded in the infrared INGRID detector (Packham et al. 2003), on the nights of 4 and 5 July 2004. The brightness of the candidates identified by any of the TrES telescopes makes it possible that the stars themselves act as the reference stars necessary to close the AO loop. The data were taken mostly in J filter, moving to H and K when the target showed interesting features, or some doubts were raised on the single nature of the candidates (i.e., no close companions). A dithering pattern of 5 points was used in each candidate to avoid bad pixels and to perform better measurements of the sky level. The resulting snapshots of the candidates that were observed at this stage are plotted in Figures 4.28 and 4.29. As a consequence of these observations, the candidate T-Lyr0-01100 was found to consist on three unresolved stars with similar brightness, two of them lying at an angular distance of only $0.8''$.

4.7 A challenging false positive detected by TrES: the case of GSC 01944-02289[5]

As an example of a particularly difficult false positive identified by the TrES network, we describe in this section the case of GSC 01944-02289, found in a field in the constellation Cancri. Both multicolor photometry and radial velocity observations (see Figure 4.30) suggested that the system was formed by a substellar object in orbit around an F-type star. The companion mass was estimated (from the CfA radial velocities) as $\sim$32 M_J, which would have placed the object in the brown dwarf regime, and thus would constitute the first observations of transits of this type. Merely the detection of such an object in a tight orbit (with a period of 3.35 days) would have been of great interest, because of its location in the so-called "brown-dwarf desert" (see the Introduction). But the fact that it transited its host star would allow measurements of the sizes and densities of these objects, something that has never been done. Thus, special care was needed in the follow-up of this system.

A careful analysis of the spectral line shapes revealed a non-symmetrical behavior that could be explained assuming the presence of a fainter star whose movement would affect only the upper parts of the stellar lines. A model consisting of three blended stars, in which two are eclipsing and the other is providing light to the system (thus diluting the eclipses), served to derive the properties of the three components. With these properties, it was possible to identify a second set of spectral lines, corresponding to the primary star in the eclipsing system (Figure 4.31). Under this consideration, the photometric and spectroscopic observations can be explained by a hierarchical triple, in which a slightly evolved F5 primary (with $v\sin i\sim$34 km/s, providing $\sim$89% of the total flux) dilutes the eclipses of an M3V star passing in front of a G0V star.

Until today, this TrES candidate has proven the most difficult case of false positive to identify, a cautionary to be remembered when identifying a transiting

[5]A complete description of this work is found in Mandushev et al. (2005)

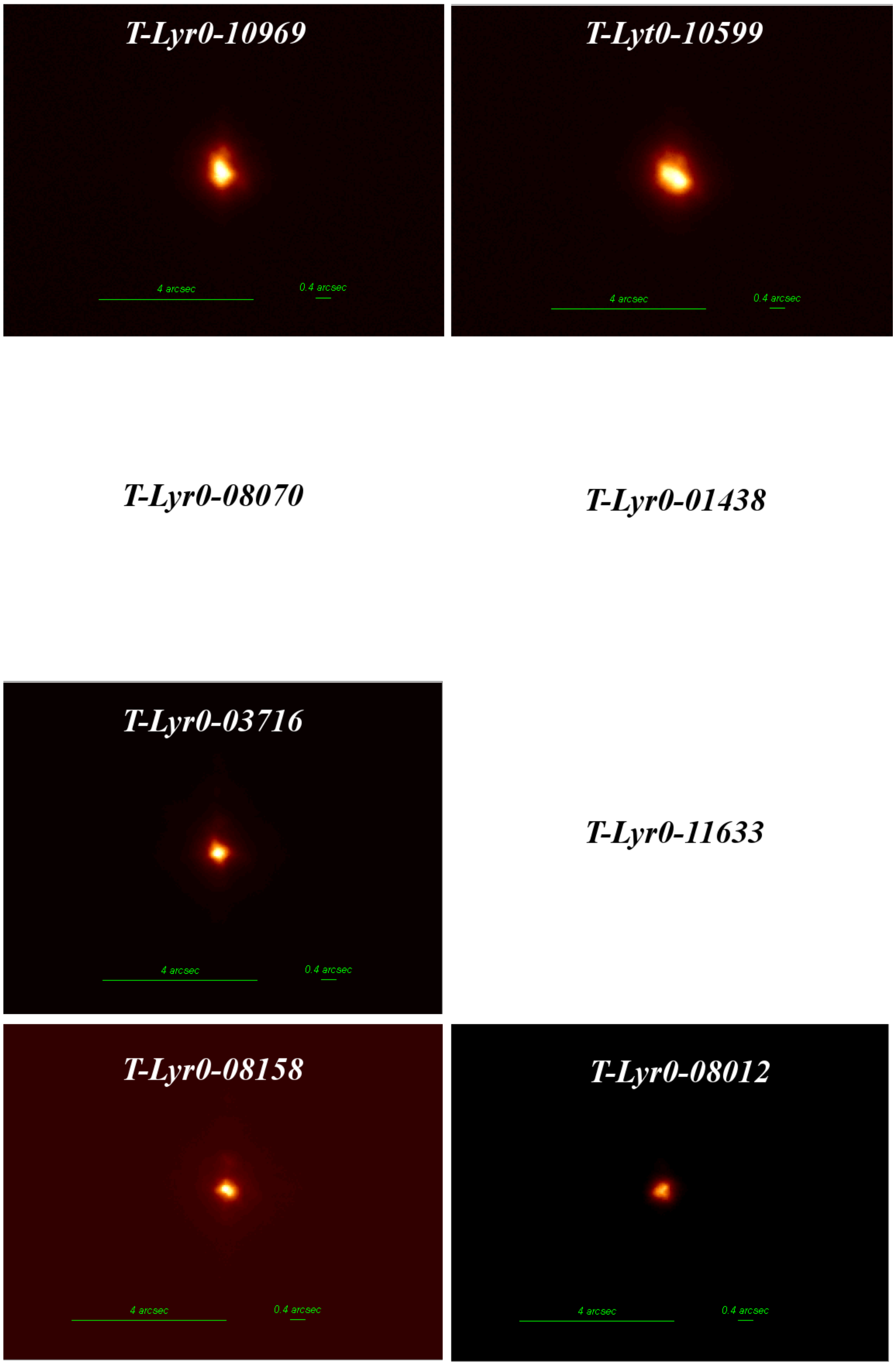

FIGURE 4.28— AO of the candidates, observed with the NAOMI/INGRID system at the 4.2 m WHT telescope. Each image samples roughly a single STARE's pixel (11″).

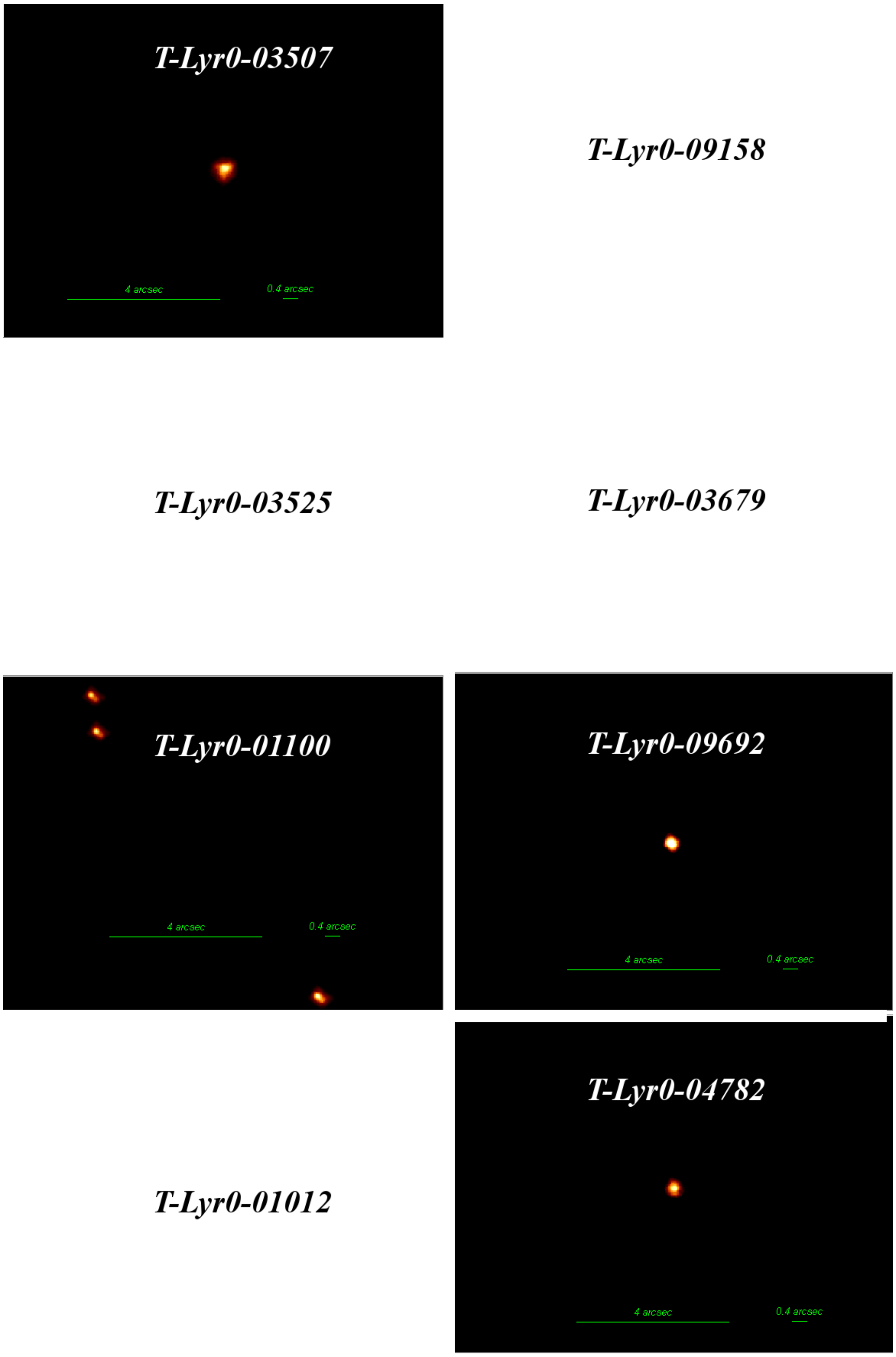

FIGURE 4.29— AO of the candidates, observed with the NAOMI/INGRID system at the 4.2 m WHT telescope. Each image samples roughly a single STARE's pixel (11″). Note the triple system T-Lyr0-01100.

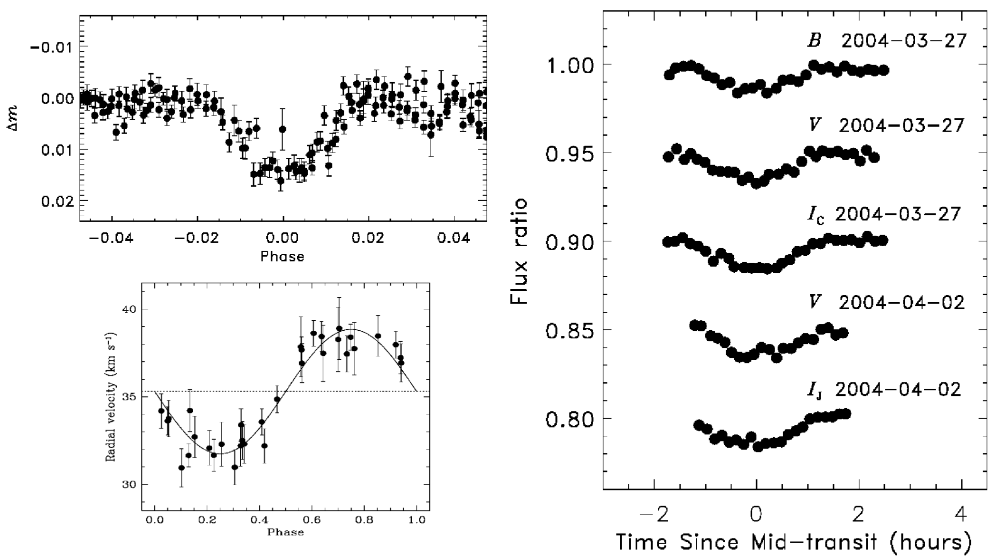

FIGURE 4.30— Top left: The PSST binned phased light curve of the star GSC 01944-02289 (with a period of 3.35 d), showing a 1.4% eclipse with a total duration of 2.7 h. Right: Multicolor photometry of transits of the same star. Bottom left: The CfA radial velocity curve, with an amplitude consistent with a brown dwarf companion.

planet (or brown dwarf) candidate around an F star.

4.8 Results on other stellar fields: a summary of the follow-up on TrES transiting planet candidates.

After almost two years of coordinated observations of STARE as a member of the TrES network, a total of 14 fields have been observed (see Figure 4.32), and the data reduction and analysis of most of them are continuously under way. Typically between 5 and 20 transiting planet candidates in each field are identified, depending on the number of stars present in the field. In this Chapter, we have provided a detailed analysis of one of these fields pointed towards the constellation Lyra, paying special attention to the details of the follow up observations and analysis of the candidates. We have shown that a careful analysis of the light curves can help to discard most of the candidates without the need for extra observations, a philosophy that will be adopted by the members of the TrES collaboration from now on, to provide priorities in the spectroscopic follow-up of each candidate.

To date, a total of 46 false positives in 9 reduced fields have been identified

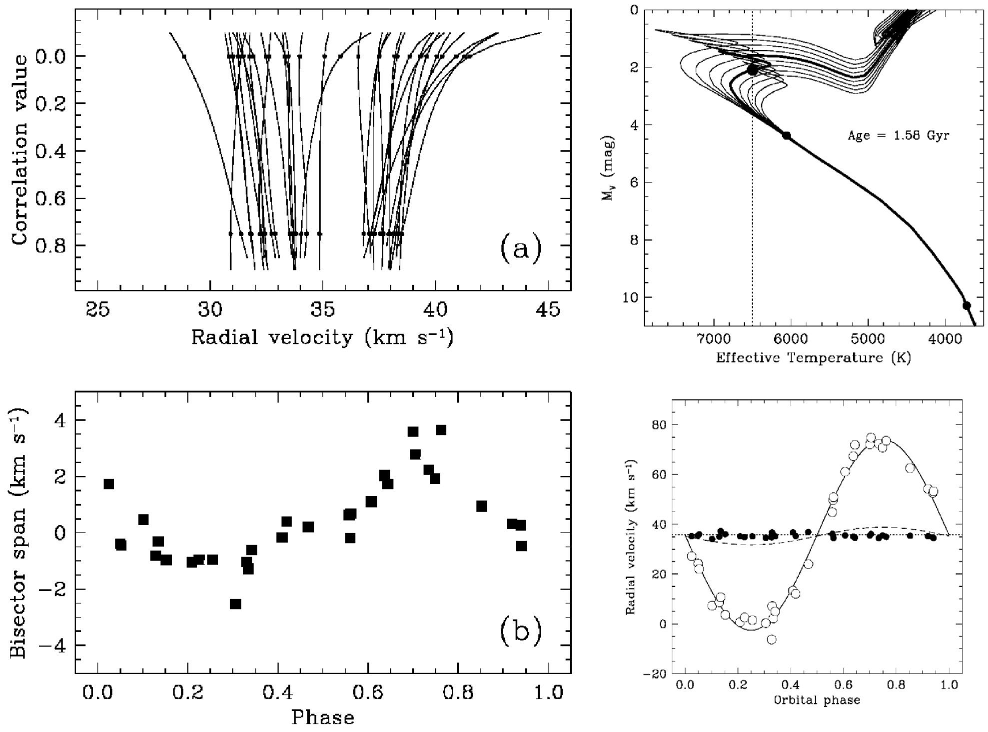

FIGURE 4.31— Top left: The line bisectors of the CfA spectra, showing a wider velocity range in the top of the lines than in the bottom. Bottom left: The bisector span, defined as the velocity difference between the top and the bottom of the spectral lines. Top right: The location in the H-R diagram of the three stars that best explain the data. Bottom right: The extracted radial velocity curve of one of the stars in the eclipsing system (the G0V star, open circles) and the star providing most of the light to the system (the evolved F5 star, filled circles).

in the TrES light curves, 17 of them were discussed in this Chapter, and the follow up work on the rest of them revealed:

- 15 Binary systems
- 7 Blended systems (three or more stars)
- 7 Unsolved cases: binary or triple systems, but, in any case, false positives. If the star is too hot, it is not possible to determine the radial velocities with accuracy. In this case, its radius will also be large, and thus the depth of the transits can not be reproduced by a Jupiter-sized object.

Another 42 candidates are scheduled for follow-up observations, or have survived the low S/N radial velocity measurements. With these number of candidates and detected false positives, it is still too early to provide detailed statistics on the detection rates of false positives, in order to compare them with the expected detection rates stated by Brown (2003). This argument is reinforced by the fact that these expected detection rates are approximate by a factor of a few, due to the number of (necessary) approximations performed in that work. A more detailed analysis of both the expected detection rates (for instance, extending it to other galactic latitudes) and the observed detection rates (considering non trivial factors as the dependance of the detectability of a transit on its duration, depth, crowding, photometric precision, etc.) is out of the scope of this thesis, but might be the objective of future works.

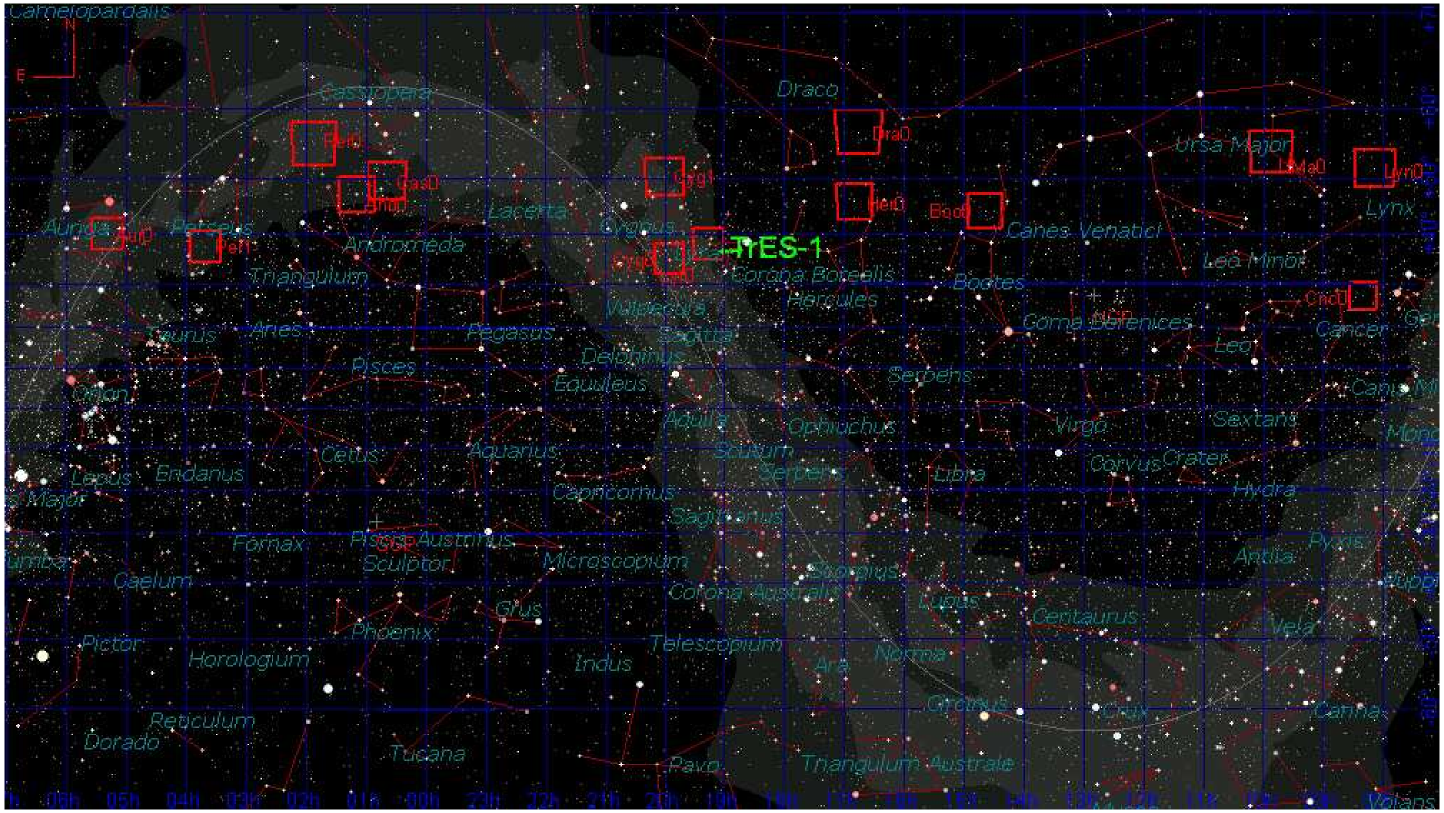

FIGURE 4.32— Location of the TrES network observed fields, in a Mercator projection.

4.9 Conclusions

We have obtained a total of 16 transiting planet candidates, from the observation of a field in the constellation Lyra. Careful analysis of the light curves, spectra taken for the determination of radial velocities, multicolor photometry at 1-m class telescopes, and AO imagery at the WHT have allowed us to classify these candidates as:

- 6 Binary systems: Two stars with ratios of the radii similar to the ratio of a main sequence star-giant planet, or eclipsing stars with grazing eclipses.
- 7 Blended systems: At least three stars, with two of them forming an eclipsing system, and the third star diluting the depths of the eclipses. This third star can be a part of the system, or in the line of sight.
- 2 Doubtful candidates:
  - One seems to be either a triple system, an F+brown dwarf binary or an F+M star binary. The rapid rotation of the brightest star makes it difficult to distinguish among these options.
  - Another has only one observed transit event, and thus undetermined ephemerides. There is also the possibility that the transit event is an instrumental effect.
- A planetary transit candidate, the only one that survived a detailed analysis of the light curve and all the follow up observations aimed to detect false positives. A detailed follow up on this object is the subject of the following Chapter.

5

TrES-1: The transiting planet of a bright K0V star

Los astros despliegan sus órbitas
imposibles. Luego congelan
la luz esclava. Reina el hombre
en el centro del Universo.
José Hierro (*Cuanto sé de mi, 1957)*

We report the detection of a transiting Jupiter-sized planet orbiting a relatively bright (V=11.79) K0V star. We detected the transit light-curve signature in the course of the TrES multi-site transiting planet survey, and confirmed the planetary nature of the companion via multicolor photometry and precise radial velocity measurements. We designate the planet TrES-1; its inferred mass is 0.75±0.07 M_J, its radius is $1.08^{+0.18}_{-0.04}$ R_J, and its orbital period is 3.030065 ± 0.000008 days. This planet has an orbital period similar to that of HD 209458b, but about twice as long as those of the OGLE transiting planets. Its mass is indistinguishable from that of HD 209458b, but its radius is significantly smaller and fits the theoretical models without the need for an additional source of heat deep in the atmosphere, as has been invoked by some investigators for HD 209458b.

5.1 Introduction

OUT of the 16 candidates detected in the Lyra field, and described in the previous chapter, T-Lyr0-03507 (renamed TrES-1 from here after) did pass all the tests that were performed to detect false alarms. These included a careful analysis of the light curve (a search for out of eclipse modulation and a determination of the mean stellar density from the transit shape), high-resolution observations using the AO system at the 4.2 m William Herschel Telescope (Observatorio del Roque de los Muchachos, La Palma, Spain), and relatively low signal-to-noise radial velocity observations. In the next sections we describe the more detailed observations that were carried out on this candidate, that led to the first transiting planet discovered by a wide-field survey.

5.2 The star in the on-line catalogues

Due to the relatively bright nature of the stars observed by the TrES network, there are a number of useful catalogues that can help to constrain the characteristics of the stars in the field. In the case of TrES-1, for instance, the 2MASS catalogue [1] provided a J-K color of 0.48, which suggests a star with late G or early K spectral types (Cox 2000). The Digitized Sky Survey plates showed no bright companions closer than a radius of $20''$ (basically the size of a STARE star image), which could produce a blend case. The AO observations in J and K helped to further constrain the possibility of a close companion, placing a secure limit of no stellar companions within 2 mags of the star, further than $0.3''$ of the star (see Figure 4.29 of the previous Chapter).

The SIMBAD B and V magnitudes of several stars in the field were used as calibrators to measure the B and V magnitudes of the TrES-1 star from the images of the PSST telescope. Johnson's R filter Observations taken at the IAC80, of the star and several Landolt fields (Landolt 1992) at different airmasses were used to measure the R absolute magnitude of the star. These values, together with the information available on the on-line catalogues, are summarized in Table 5.1.

Ignoring interstellar extinction, the observed V magnitude of 11.79 implies a distance to the star of approximately 150 pc. The USNO-B1.0 proper motion of the star is 47 mas/yr (Monet et al. 2003), which results in a transverse velocity of 26 km/s, when combined with the previous distance. This transverse velocity is fairly typical for low-mass field stars in the solar neighborhood.

5.3 Multicolor observations

There are several blending scenarios that might show a color dependance of the transit depth (Chapter 3), that lead us to perform multicolor observations of TrES-1 transits. At the IAC 80 cm telescope, we observed a partial transit (missing the egress) with Johnson V and I filters; at the University of Colorado

[1] http://www.ipac.caltech.edu/2mass/

TABLE 5.1— Parameters for the TrES-1 Parent Star

Parameter	Value
R.A.	$19^h04^m09^s.8$ (J2000.0)
Declination	+36°37'57″ (J2000.0)
R	11.34
V	11.79
B–V	0.78
J	10.294
J–H	0.407
J–K	0.475
Spectrum	K0 V
M_s	0.88 ± 0.07 $M_{\odot}$
R_s	$0.85^{0.10}_{-0.05}$ $R_{\odot}$
GSC	02652-01324
2MASS	19040985+3637574
USNO-B1.0 ppm (RA)	-42 mas yr^{-1}
USNO-B1.0 ppm (Dec)	-22 mas yr^{-1}

Sommers-Bausch Observatory (SBO) 61 cm telescope, we observed a full transit with Johnson B and R filters; at the CfA's Fred L. Whipple Observatory (FLWO) 1.2 m telescope, we observed one full and one partial transit with Sloan g, r, and z filters. The PSST telescope also observed four transits in R during the 2004 season. Figure 5.1 displays all of these observations, along with a fit to a model, which we shall discuss bellow.

5.3.1 The IAC-80 observations

As an example of the observations and data reductions carried out by the previous telescopes, in this subsection we describe in detail the observations performed of the TrES-1 system, at the IAC-80 telescope, the nights of 2004 August 29 and 2005 April 19, using Johnson's R filter.

The raw images were taken using a 2x2 binning of the CCD pixels; this allows a faster readout, reducing it a factor of ∼4, from ∼40 seconds to ∼10 seconds. A slight defocus of the image was applied, in order to reduce the effects of changes in the PSF due to atmospheric and instrumental conditions (seeing, temperature changes, flexures in the system), and also the effect of the intrapixel different sensivities of the CCDs (see, e.g. Penny & Leese 1996).

Calibration of the images involved flat-fielding, subtracting the CCD zero

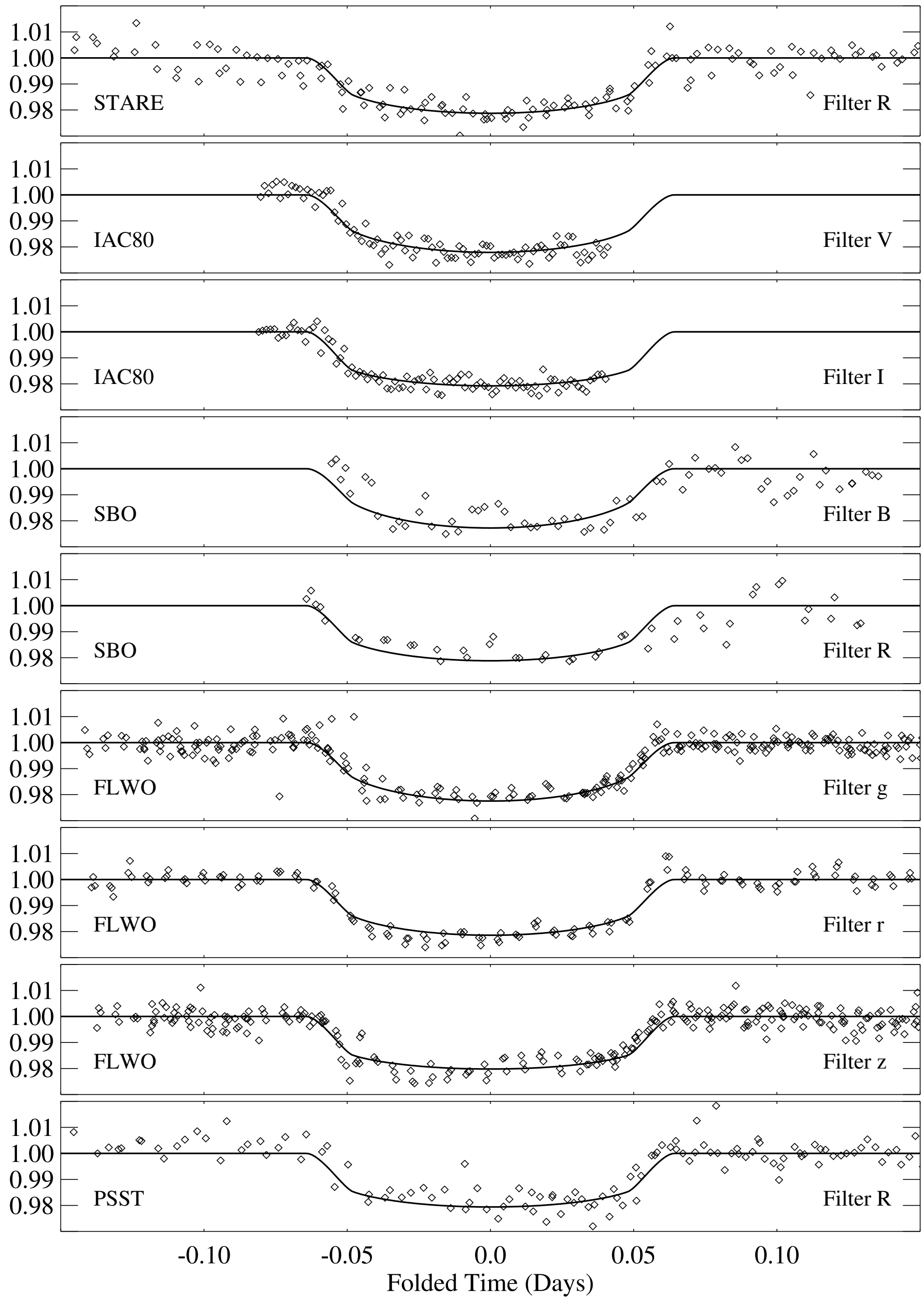

FIGURE 5.1— Time series photometry used in estimating the radius and inclination of TrES-1, plotted against heliocentric time modulo the orbital period from Table 5.2. The telescope and filter bandpass used are indicated on each plot, and discussed in the text. Each set of observations is overplotted with the predicted light curve for that color, given the parameters of Table 5.2

level, using the IRAF's (Tody 1986)[2] CCDPROC routine. All the images were aligned and aperture photometry was performed in the target star and 7 reference stars. The aperture to perform the photometry was allowed to vary, according to changes in the PSF that still were not removed by the defocussing. The typical FWHM of the stars was ∼4 arcsec. Different apertures for each star were chosen in a reference image (brighter stars having bigger apertures), and the ratios between the apertures of the stars were kept constant in every image, varying from image to image by a constant value. This was performed with the Vaphot IRAF routine developed by Deeg & Doyle (2001).

An artificial reference star is then built with the measured instrumental magnitudes of the 7 reference stars. The construction of this average reference star assigns more weight to the brightest stars, for which the photon noise is lower, and thus the dispersion of the points. Visual inspection of the magnitudes of each of the reference stars with the artificial star subtracted allows one to identify variable stars. This variability can be intrinsic of the star, or an instrumental artifact, which can be due to the location of the star close to a dirty part of the CCD which was not completely corrected with the flat-field correction, or confusion due to close fainter stars. Once these variables are identified, they can be removed from the construction of the artificial reference star. For the TrES-1 light curve, three of the seven reference stars were removed from the mean, due to intrinsic variability, or because their inclusion into the mean resulted in a noisier artificial reference star. The Johnson's R light curve, and a 6-points binned light curve is plotted on Figure 5.2. A final light curve in the R filter, sampled in a regular grid of phase points, is plotted in Figure 5.3. The error bars in the binned plots have a total size of the standard deviation of the average divided by the square root of the number of points in the bin.

5.4 Low signal to noise radial velocity observations

This star was observed with the CfA Digital Speedometers (Latham 1992, described in Chapter 3) at seven different epochs spanning 60 days, giving coverage of the full orbital phase. From these exposures, we determined a mean velocity of –20.52 km/s. The average internal error estimate and actual rms achieved were both 0.39 km/s, suggesting that any companion orbiting with a 3.03 day period must have a mass smaller than 5 M_{Jup}. This conclusion is not firm, however, if there is blending light from a third component. Comparisons of our observed spectra with synthetic spectra (calculated by J. Morse using Kurucz models, J. Morse and R.L. Kurucz, private communication), allowed us to estimate that the TrES-1 parent star has T_{eff}=5250±200 K, log$g$=4.5±0.5,

[2] IRAF is distributed by the National Optical Astronomy Observatories.

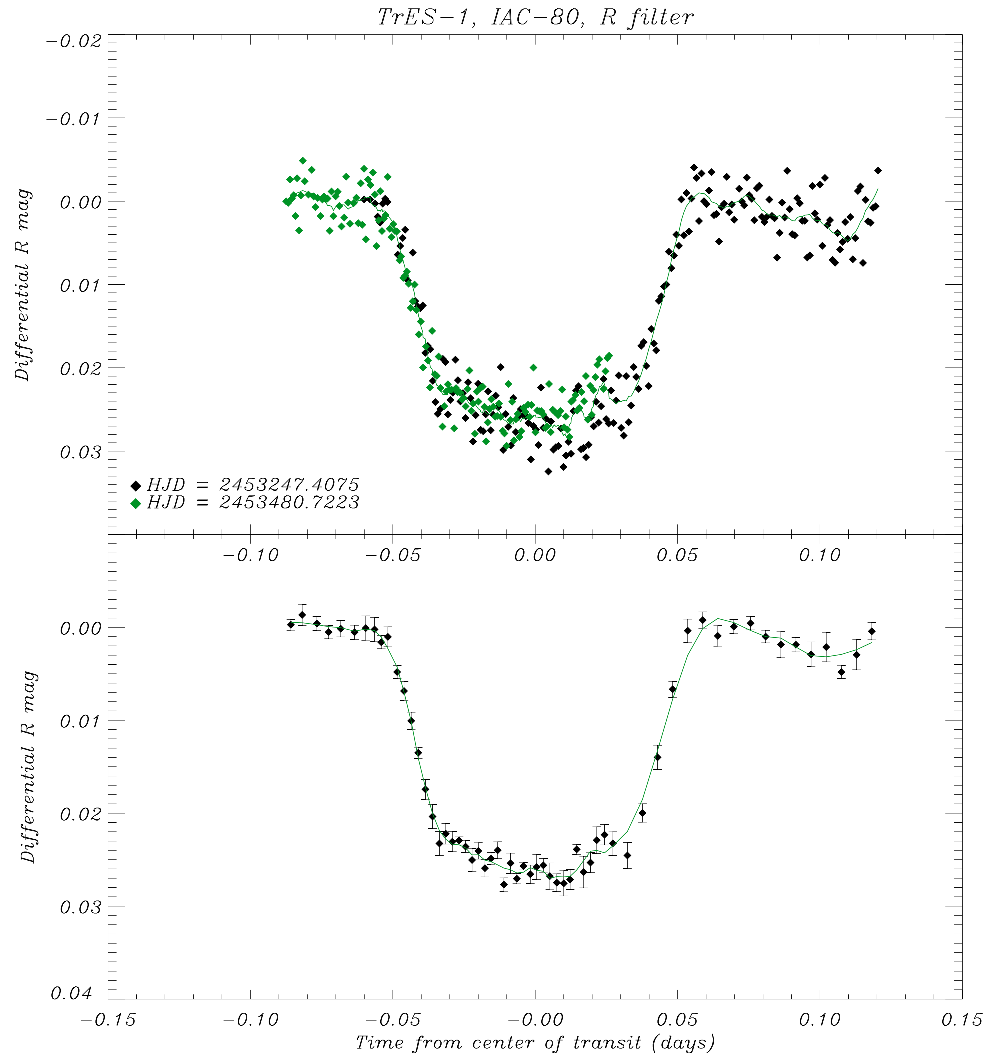

FIGURE 5.2— Top: Light curve of TrES-1 in R filter obtained at the IAC-80 telescope, on two different nights, HJD 2453247 (August 29, 2004) and 2453480 (April 19, 2005). The ephemerides listed in Table 5.2 were used to put the data in phase. Bottom: Same light curve, but averaged in 6 points bins; the error bars are the standard deviation of the average divided by the square root of the number of points in the bin.

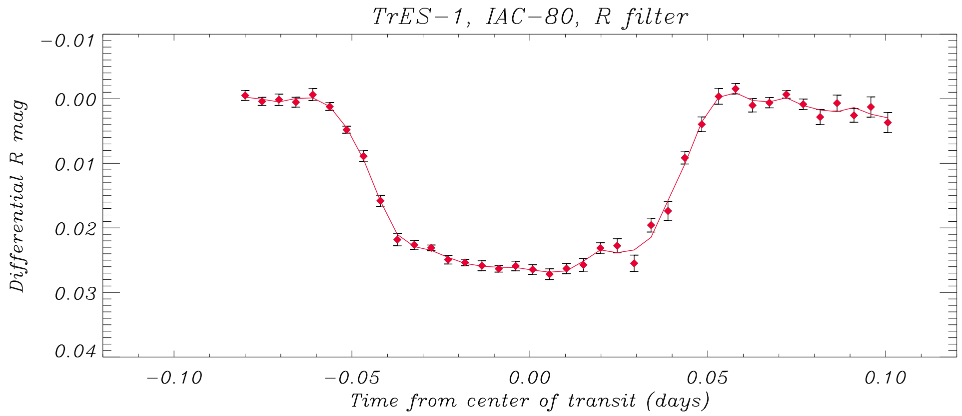

FIGURE 5.3— Same as Figure 5.2, but with the data binned in a regular grid of points with an interval of 0.0048 days (6.8 min). The error bars are the standard deviation of the average divided by the square root of the number of points in the bin.

$v\sin i \leq 5$ km/s, and a metallicity similar to that of the Sun. The slow rotation is particularly significant, for several reasons: it indicates that the star has not been spun up by tidal interactions with a massive secondary, it forecloses some blending scenarios, and it means that more precise radial velocity measurements can be obtained fairly readily.

5.4.1 A whole visible range spectrum

In order to confirm the photometric classification of the star, we also obtained a moderate-resolution echelle spectrum covering the entire visible wavelength range, using the Palomar 1.5 m telescope. Based on the comparison of this spectrum with the spectral standards of Montes et al. (1999), we classify the star as K0V. It shows no sign of a composite spectrum or of other peculiarities.

5.5 High signal to noise radial velocity observations

We obtained precise radial velocity measurements using the I_2 absorption cell and High Resolution Spectrometer on the Keck I telescope. Eight observations were collected over a period of 18 days in July 2004, providing good coverage of critical phases. The data reduction involved modeling of the temporal and spatial variations of the instrumental profile of the spectrograph (Valenti et al. 1995), and it is conceptually similar to that described by Butler et al. (1996). Internal errors were computed from the scatter of the velocities from the echelle

TABLE 5.2— Parameters for the TrES-1 Planet

Parameter	Value
	Orbital
P	$3.030065 \pm 8 \times 10^{-6}$ days
T_c	2453186.8060 ± 0.0002 (HJD)
a	0.0393 ± 0.0011 AU
i	$88.5^{+1.5}_{-2.2}$ deg
K	115.2 ± 6.2 m s^{-1}
	Physical
M_P	$(0.75 \pm 0.07) M_{Jup}$
R_P	$1.08^{+0.18}_{-0.04} R_{Jup}$
R_P/R_s	$0.130^{+0.009}_{-0.003}$

orders containing I_2 lines and are typically 10-15 m/s. Figure 5.4 shows the radial velocity measurements, along with a fit to a sinusoidal variation that is constrained to have a period and phase determined from the photometric data. This constrained fit matches the data well and yields a velocity semiamplitude of $K = 115.2 \pm 6.2$ m/s. The rms residual of the fit is 14 m/s, in good agreement with the average of the internal errors. Examination of the spectral line profiles in our Keck spectra by means of the bisector spans (Torres et al. 2004a) indicated no significant asymmetries and no correlation with orbital phase, once again ruling out a blend.

5.6 Discussion

To provide an initial estimate of the planetary mass and radius, we used the main-sequence calibration from Cox (2000), and assumed that TrES-1 parent star is a K0V with solar metallicity, a mass M_s=0.80 $M_\odot$ and a radius R_s=0.86 $R_\odot$. We took limb darkening relations from Claret (2000) and from Claret (2004, private communication), for models with solar metallicity, log(g)=4.5, and T_{eff}=5250 K. We assign (somewhat arbitrarily) an uncertainty of ± 0.07 $M_\odot$ to M_s. We also take $0.80_\odot \leq R_s \leq 0.95 R_\odot$, since adequate fits to the photometry cannot be obtained for stellar radii outside this range.

From the observed reflex stellar velocity and Kepler's laws, we estimated the semi-major axis a and the planetary mass M_p, using the constraints and assumptions just described. We then performed a minimum-χ^2 fit to all of the photometry (with errors estimated from the scatter of the input data), to obtain estimates on the planetary radius R_p and orbital inclination i, and to

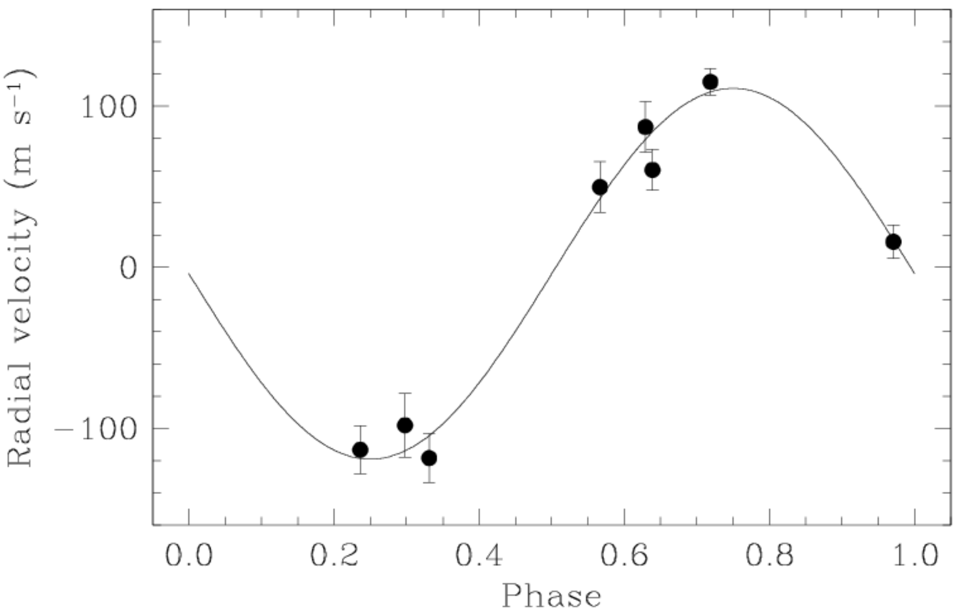

FIGURE 5.4— Keck I/HIRES radial velocity observations of TrES-1, overplotted with the best-fit orbit.

refine the estimates of the epoch of transit center T_c and the orbital period P. Our best estimates for the stellar, planetary and orbital parameters are given in Table 5.2, and the solid curves in Figures 5.1 and 5.4 show the fitted photometric and radial velocity variations overplotted on the data.

The error estimates given in Table 5.2 include errors that follow from our uncertainty in the radius and mass of the parent star (which is assumed to be a main-sequence object), as indicated in Table 5.1. These uncertainties (especially in R_s) dominate errors in the photometry as regards estimates of R_p and i. If the stellar radius and mass were known more accurately, the uncertainties in these parameters would be smaller by about a factor of 10. Contrariwise, if the star is actually a subgiant (photometric constraints notwithstanding), R_p could exceed the upper limit in Table 5.2. The error in M_p arises about equally from the radial velocity measurement precision and from our uncertainty in M_s.

The quantities in Table 5.2 allow us to estimate some further properties of the planet. We find the equilibrium surface temperature:

$$T_e = T_s(R_s/2a)^{1/2}[f(1-A)]^{1/4} = 1250(1-A)^{1/4} \tag{5.1}$$

where A is the Bond Albedo, and we assume efficient energy redistribution over

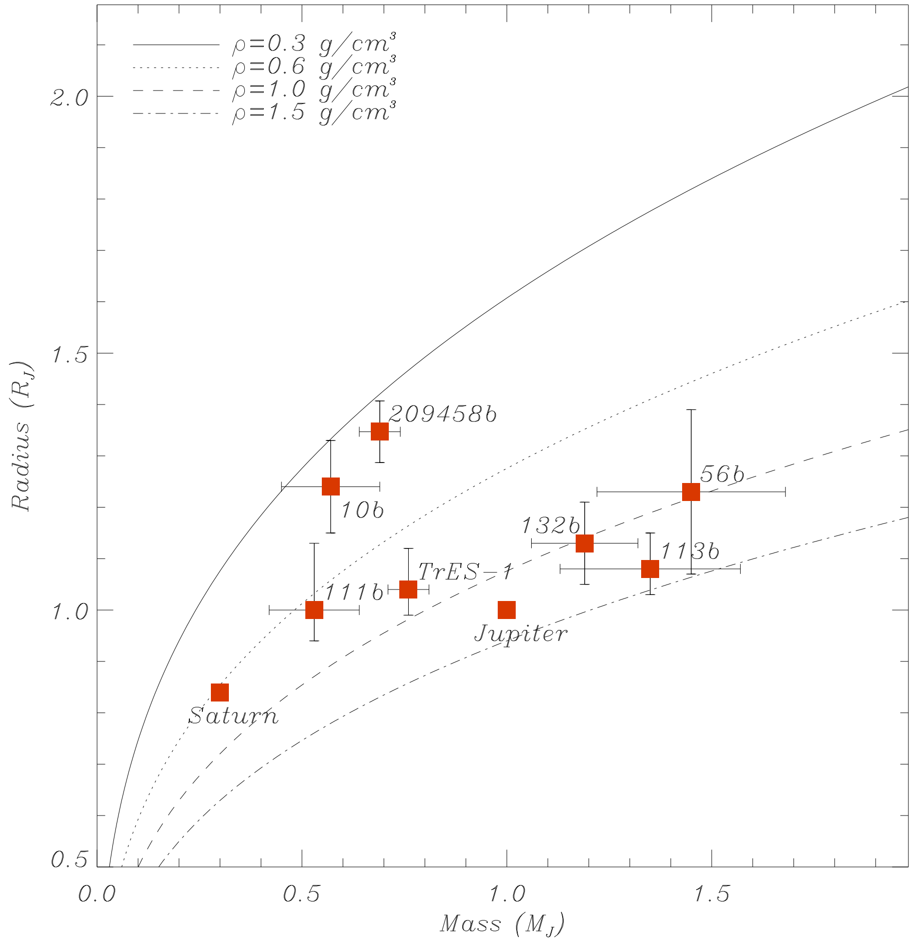

FIGURE 5.5— Radii of transiting extrasolar planets plotted against their masses. Dashed curves are lines of constant density. Data are from Brown et al. (2001) for HD 209458b, Torres et al. (2004a) for OGLE-TR-56b, Bouchy et al. (2004) for OGLE-TR-113b, Moutou et al. (2004) for OGLE-TR-132b, Pont et al. (2004) for OGLE-TR-111b, Konacki et al. (2005) for OGLE-TR-10b, and Sozzetti et al. (2004) for TrES-1.

the surface of the planet ($f = 1$). We also obtain the mean density 0.74 g/cm^3, the surface gravity 1373 cm/s^2, and the escape speed, v_e=47 km/s.

The mass, orbital radius, and radiative equilibrium temperature of TrES-1 are quite similar to those of HD 209458b, yet the former planet's radius is about 20% smaller. Indeed, as shown in Figure 5.5, the radius of TrES-1 is more similar to those of the OGLE planets, as it closely matches current models for irradiated planets without internal energy sources (Chabrier et al. 2004, Burrows et al. 2004). This discrepancy between the radii of HD 209458b and TrES-1 reinforces suspicion that HD 209458b has an anomalously large radius.

5.7 On-going and future works

To provide a better confrontation between theory and observation for this object, the stellar radius (and to a lesser degree, mass) could be better constrained. A more detailed analysis of the Keck spectra (Sozzetti et al. 2004) together with spectra obtained at the Hobby-Eberly Telescope allowed these authors to further constrain the stellar parameters of the TrES-1 Parent Star, deriving $T_{eff} = 5250 \pm 75$ K, $\log g = 4.6 \pm 0.2$ and [Fe/H] $= 0.00 \pm 0.09$, $M_s = 0.89 \pm 0.05 M_{\odot}$, $R_s = 0.83 \pm 0.05 R_{\odot}$. The star showed activity (measured by the Ca II indicator) and no Li down to the measurable level ($\log \epsilon(Li) < 0.1$), which led these authors to constrain the age of the system to the values 2.5 ± 1.5 Gyr. The improved planetary mass, radius and inclination of the orbit were:

- $M_p = 0.76 \pm 0.05\ M_J$
- $R_p = 1.04^{+0.08}_{-0.05}\ R_J$
- $i = 89.5^{+0.5}_{-1.3}$ degrees

5.7.1 HST observations

Additionally, we have undertaken a HST 15-orbit (3 visits of 5 orbits each) Director Discretionary's Time observing run on TrES-1, using the ACS/HRC with a grism. With this configuration, we estimate that we can achieve only a factor of 2.2 loss in precision with respect to the 40 times brighter HD 209458 star's photometry performed with STIS by Brown et al. 2001. This is mainly due to the much higher efficiency of the grism on ACS than the medium resolution STIS grating used in the HD 209458b case. With photometry of sufficient accuracy, it is possible to fit independently 4 key parameters of the star/planet system: the star radius, the planetary radius, the limb darkening coefficient and the orbital inclination. Although these refinements of the parameters (which are expected to reinforce the difference in radius of HD 209458b and TrES-1, thus providing a theoretical challenge for the explanation of the radii of the two objects) were the major objective of this run, there were also other by-products: these observations should allow for searches of few-earths sized hypothetical satellites (even if they are not expected due to the strong tidal

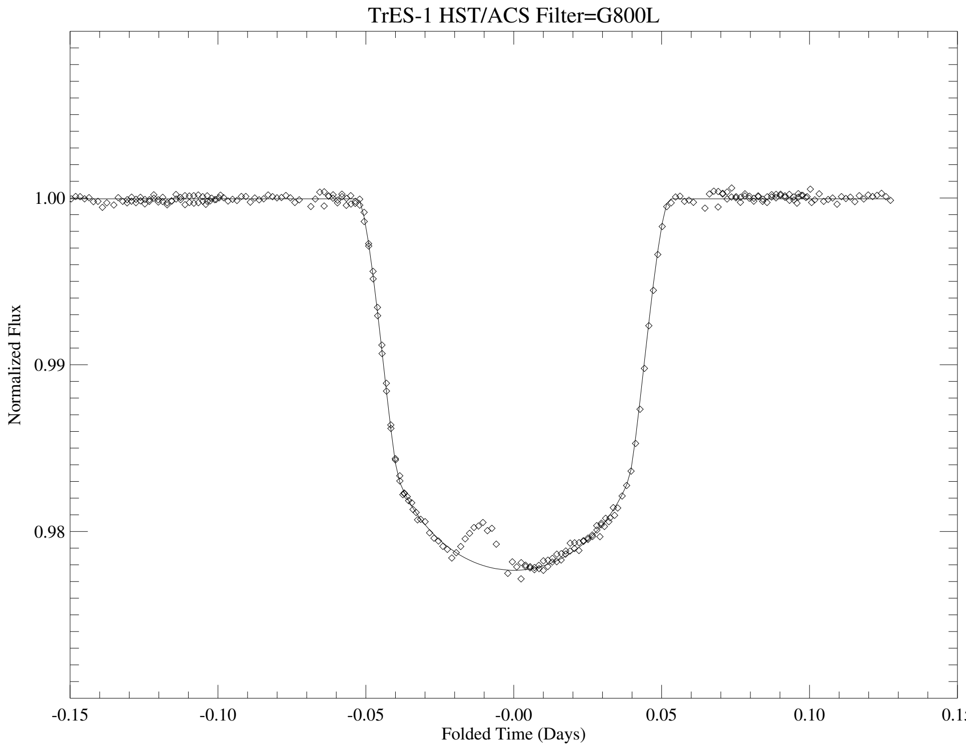

FIGURE 5.6— Preliminary HST/ACS light curve of TrES-1, showing a feature that can be interpreted as a spot being eclipsed by the planet.

forces in the close Hot Jupiter's orbits), either from residual photometric information of satellite's transits (constraining the satellite's size) or from the time-shift induced by the companion (constraining the satellite's mass; see, e.g. Sartoretti & Schneider 1999). Upper limits will be placed on the presence of opaque rings around the planet. With the data still under analysis, in Figure 5.6 we can advance a preliminary light curve. This shows an increase in brightness close to the center of the transit. This event was only observed in one of the three visits, and this phase of the transit was not observed again. There are two scenarios that could explain the presence of this feature: *i)* a big warm stellar spot (warm because otherwise there would be a color dependance of the feature that is not observed in this preliminary analysis), with a size of $\sim$1 R_J, being occulted by the planet, and *ii)* a hypothetical second planet in an outer orbit that would have been in transit at the moment that TrES-1 was in transit. The latter is a much more improbable explanation, as it works if

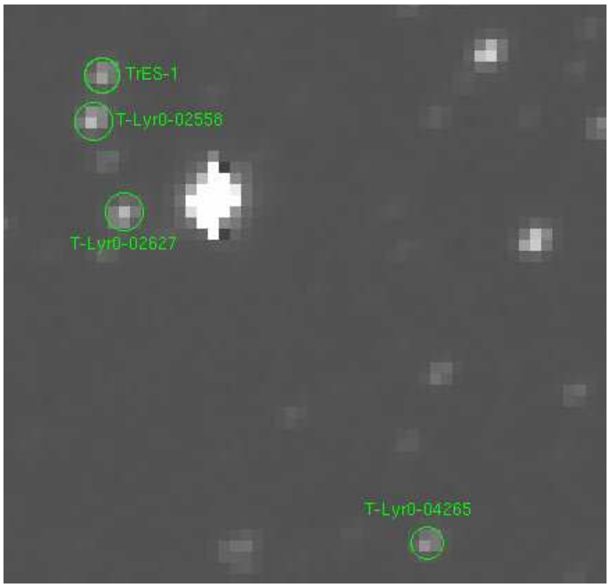

FIGURE 5.7— The location of TrES-1 and the three reference stars used to study its long term variability, summarized in Figure 5.8.

the planet is at a distance of roughly 1 AU. The chances to have observed this second planet in transit are thus quite low.

The presence of a spot in the HST data is not surprising, considering the known activity of the star, based on the Ca II indicator (Sozzetti et al. 2004). In order to establish if the activity of the star is detectable in the STARE data, we binned the raw light curve in 2 hour bins, whenever there were more than 50 data points inside each bin. To provide a comparison sample, we repeated the same operation in three close stars to TrES-1 (plotted in Figure 5.7), and estimated the standard deviation of each of the binned light curves. These plots are given in Figure 5.8, and the final standard deviation of the binned points for TrES-1 is larger by ∼24% than the mean standard deviation of the rest of the stars, that again points towards stellar activity on TrES-1 parent star.

5.7.2 Spitzer observations

With another experiment in a different wavelength range, we have pursued the detection of the TrES-1 planet secondary eclipse (the planet passing behind the host star), with the use of the IRAC detector on board the Spitzer Space Telescope. Even though there had been several attempts, only upper limits

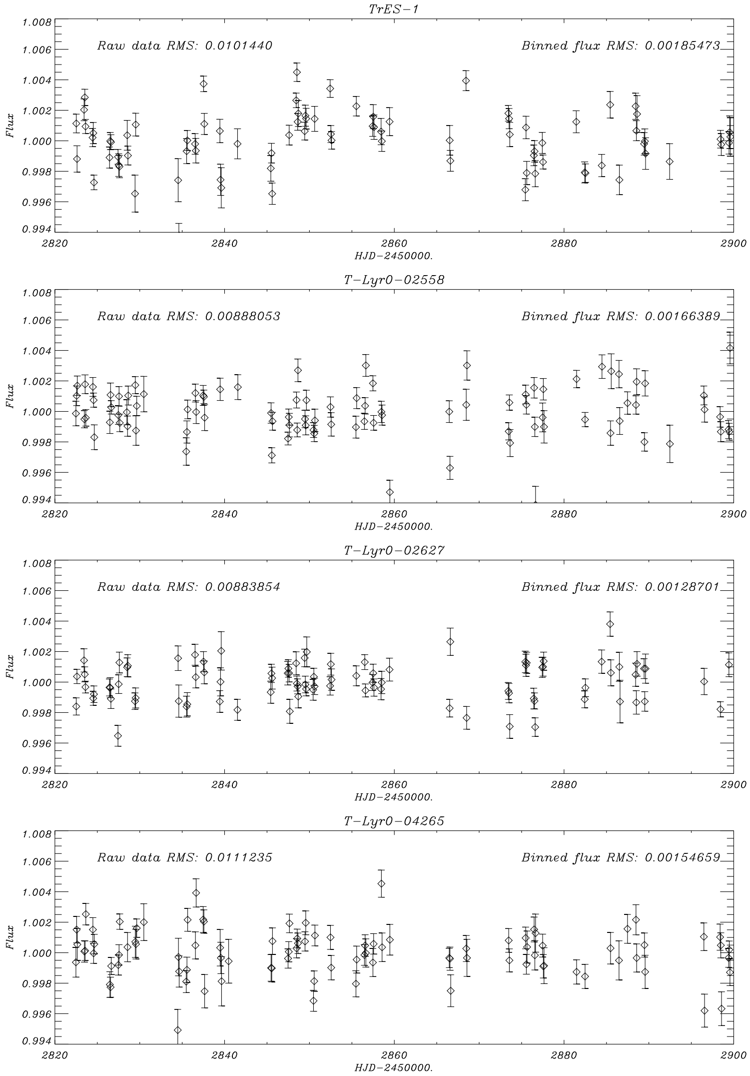

FIGURE 5.8— 2-hours binned light curves of TrES-1 and 3 close comparison stars with similar brightness (the location of the comparison stars is plotted in Figure 5.7). The error bars are the standard deviation of the data points inside each bin divided by the square root of the number of points. The RMS dispersion of the raw data is shown at the top left of each plot, and the dispersion of the binned light curves at the top right.

on the detection of thermal emission from an exoplanet have been published (Charbonneau et al. 1999; Collier Cameron et al. 2002; Leigh et al. 2003).

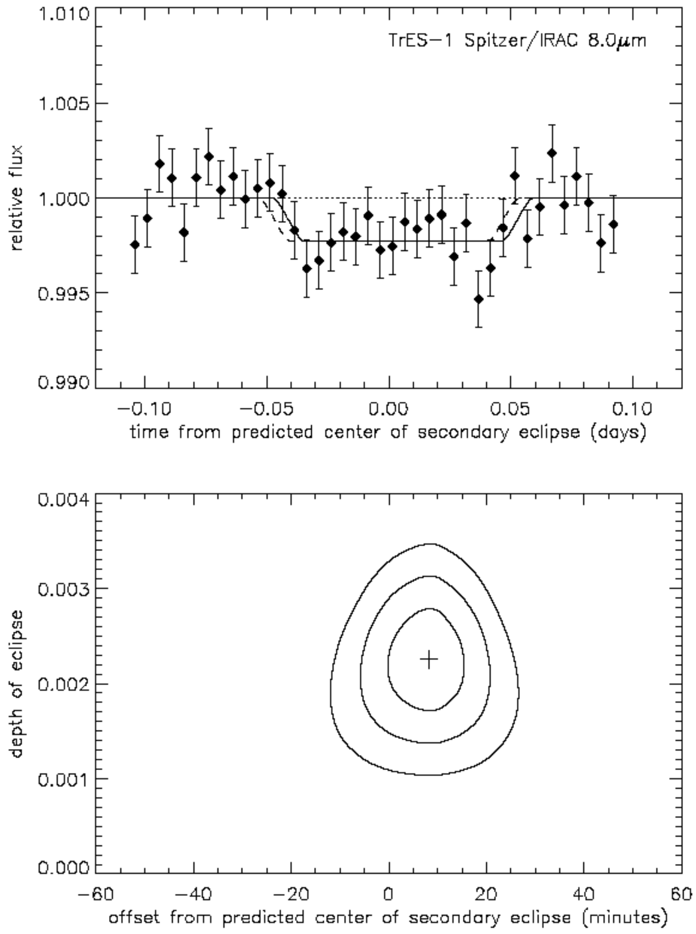

FIGURE 5.9— Upper panel: The binned 8.0 μm time series The best-fit model eclipse curve has a depth of ΔF=0.00225 and a timing offset of Δt=+8.3 minutes, and is plotted as the solid black line. A model of the same depth but Δt=0 is shown as the dashed line. Lower panel: The 1σ, 2σ and 3σ confidence ellipses on the eclipse depth and timing offset. From Charbonneau et al. (2005).

A second objective of these observations was to constrain the planetary orbit's eccentricity. A non-zero eccentricity detection could provide a mechanism for deposition of energy in the planet's interior (and thus increase its radius), a mechanism that has been proposed to explain the apparently anomalous radius of HD 209458b (Bodenheimer, Laughlin, & Lin 2003). The observations were carried during 5.6 hours on the night of Oct 30-31 2004, in two wavelength

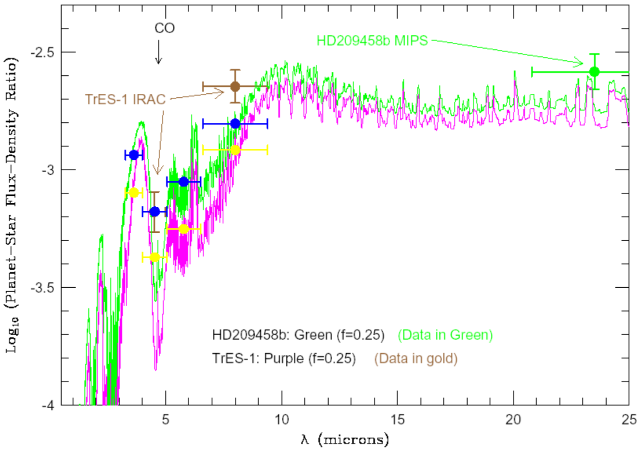

FIGURE 5.10— The logarithm base ten of the planet-to-star flux density ratio as a function of wavelength for the models of Burrows, Hubeny, & Sudarsky (2005) for TrES-1 (purple) and HD 209458b (green), assuming f=0.25 (a parameter that represents isotropic infrared emissions). Superposed are the secondary eclipse data: the gold dots with corresponding error bars are the TrES-1 data (Charbonneau et al. 2005), while the green dot with error bar is the HD 209458b data from Deming et al. (2005). From Burrows, Hubeny, & Sudarsky (2005).

bandpasses centered at 4.5 and 8 μm. The analysis revealed the first detection of thermal emission from an extrasolar planet[3] (Charbonneau et al. 2005), with a 6-σ detection of the secondary at 8 μm (Figure 5.9), and a 5-σ detection at 4.5 μm. The observed depths are 0.00225$\pm$0.00036 and 0.00066$\pm$0.00013, respectively. Under the assumption that the planet emits as a blackbody, the effective temperature of the planet is estimated as T_p=1060$\pm$50 K. There is no significant eccentricity detected, which forecloses the scenario proposed by Bodenheimer, Laughlin, & Lin (2003) for this planet. The same conclusion was obtained by Deming et al. (2005) for HD 209458b. If the planet is assumed to emit isotropically, then the implied Bond albedo is A=0.31$\pm$0.14. A comparison of these results with published models of planetary thermal emission (Sudarsky, Burrows, & Hubeny 2003) indicates that the measured flux at 4.5 μm might be explained by CO absorption (see Figure 5.10), while the absolute level of the 8 μm data point might be due to water absorption (Burrows, Hubeny, & Sudarsky 2005).

[3]There is another simultaneous detection by Deming et al. (2005) of the secondary eclipse of HD 209458b at 25 μm, also with Spitzer

In this Chapter we have described the observations that led to the discovery of the transiting planet TrES-1, which, at the moment of writing these lines, remains as the second better known exoplanet. The precision on its orbital and physical parameters is at the level of the planet orbiting the brighter star HD 209458. Its brightness in the infrared has made it possible to detect the secondary eclipse, and thus, thermal emission from an exoplanet. This detection provided the effective temperature of the planet, and it gives clues, according to some authors, for a tentative detection of CO and water absorption in its atmosphere. It does also argue against a proposed mechanism for energy deposition in the interior of the planet, which does not seem to be taking place in the bigger HD 209458b planet either. More transiting planets and theoretical effort are needed to understand the sizes of these objects. This implies adding more points in the Figure 5.5. In the next Chapter, we apply the technique for exoplanetary atmospheres investigation called transmission spectroscopy to the 2004 Venus transit. This technique will help to study the atmospheres of the newly found transiting planets.

6

Dreaming of the future: The 2004 Venus transit

For the first time ever, the Venus 2004 transit provided the opportunity to test the technique called *Transit Spectroscopy*, in a planet whose atmosphere is better known than those of the planets orbiting another stars. In this chapter we describe infrared spectroscopy of the 2004 Venus transit taken at the Vacuum Tower Telescope (VTT) located at the Observatorio del Teide, which allowed to detect $^{12}CO_2$ and $^{13}CO_2$ absorption lines in its atmosphere, thus demonstrating the capabilities of the technique.

6.1 Introduction

IN June 2004, Venus passed in front of the solar disk, producing a transit of a solar planet. This alignment only occurs typically twice every century, the previous one having occurred in 1882. There is an important difference with the more frequent Mercury transits: the dense Venus atmosphere. At the Venus limb position, the light coming from the solar disk will be blocked by the atmosphere at those wavelengths in which the opacity of the atmospheric components is high. Measuring the ratio between the solar spectra in a region where there is no Venus atmosphere and in a region with atmosphere will thus provide clues about the components of the atmosphere and their temperatures and densities. We saw in the Introduction the basics of this technique and its application to the transiting planet HD 209458b. On this occasion, the atmosphere of the planet has been studied and measured from ground and space probes, and thus the findings with transit spectroscopy can be directly compared and checked with the current knowledge of its atmosphere. We planned the observations of the Venus transit to not only validate the technique, but also provide some information on a poorly-known region in the Venus atmosphere: the mesosphere.

6.1.1 The Venus mesosphere

The Venus mesosphere is a transition region which separates the thermosphere, with a subsolar to antisolar (SSAS) wind regime, at altitudes above $\sim$ 120 km (Bougher et al. 1997) from the troposphere, with an intense zonal retrograde flow (below 60 km altitudes or 250 mbar, Gierasch et al. 1997). The first measurements of this region were derived from Pioneer Venus observations (Taylor et al. 1980), and revealed an inverted equator-to-pole temperature gradient at 70 to 100 km (p=3×10^{-5} bar), which was associated with the decay of the cloud-top (located at $\sim$65 km altitude) super-rotation. The mesospheric temperature varies from $\sim$240 K at 60 km down to $\sim$170 K at 100 km, and a "cold collar" structure has been detected at $\sim$65°N with an associated vertical temperature inversion of $\sim$15 K at the morning terminator and 0-5 K at the evening. This structure has shown significant variability with time (Newman et al. 1984). Almost all the data on this region comes from spacecraft[1]; the only other information on this region has been obtained through visible observations of CO_2 lines[2], 10-μm measurements of CO_2 bands[3], and millimeter and sub-millimeter wave CO observations[4]. Thus, the region between $\sim$80 and $\sim$100 km has very few observations which use the CO_2 spectral lines. The CO measurements are complicated by the still not well understood mechanism of photochemical production and redistribution, as suggested by a controversial

[1]Thermal field measurements from CO_2: observations of the Pioneer Venus Orbiter Infrared Radiometer, the Venera 15 Infrared Fourier Spectrometer Experiment and the Galileo Near-Infrared Mapping Spectrometer; Temperature measurements from Radio Occultations: Pioneer Venus, Veneras and Magellan; Temperature measurements from Pioneer Venus Probe data, and wind measurements at the cloud tops obtained from tracking ultraviolet features, on the Pioneer Venus and Galileo missions; see Lellouch et al. (1997) for a complete revision on these measurements.

[2]These lines provide wind information of a region just above the clouds, 65-85 km. The first observations generated some controversy in the late 1970s; they are finally consistent with a rapid decrease of the zonal super-rotation above the cloud tops (Young et al. 1979).

[3]Produced in a $\sim$20 km layer centered at 109 km (Deming & Mumma 1983), and dominated by the SSAS flow, with an tentative detection of the return branch of the thermospheric flow at mesospheric levels (Goldstein 1989).

[4]Sampling a region between 75-105 km, with vertical resolutions of 4-5 km, and allowing the detection of a *mesopause* at $\sim$91 km in the dayside and $\sim$87 km in the nightside (Clancy, Sandor, & Moriarty-Schieven 2003).

morning peak in CO abundance: it was observed to occur at 0.6±0.6 a.m local time above 95 km, while it appeared shifted to 8.5±1 a.m. below 90 km (Clancy & Muhleman 1985); these authors needed significant retrograde zonal winds at this altitude levels to explain this distribution, which has been criticized by Goldstein (1989), and also contradicts the conclusions of the Young et al. (1979) work.

The few wind velocities measurements show SSAS wind velocities at the Venus terminator (and altitudes around 100 km) in the range 105-140 m/s (typical uncertainties of 15-20 m/s, Goldstein et al. 1991, Betz et al. 1977), while the retrograde zonal flow is not so well constrained at the upper mesosphere-lower thermosphere altitudes (there are reported values from +5 m/s, thus a prograde flow, Goldstein et al. 1991, to -90 m/s, Goldstein 1989, Betz et al. 1977); this strong variability in the reported values is suspected to be related to wave activity (Bougher et al. 1997).

The mesosphere is thus a transition region in which the retrograde zonal flow observed at the cloud tops is expected to decrease with altitude, while the SSAS thermospheric flow behavior gets more important. But there is a lack of direct wind measurements on this region, and, as we have seen, the few observations are a matter of controversy. The transmitted spectral CO_2 lines in the Venus 2004 transit were expected to sample this poorly known region.

6.2 Observations

Four days at the Kiepenheuer Institut für Sonnenphysik's (KIS) VTT were assigned to the project, from June 5 to June 8. The Sun rose at ~06:30 UT on the morning of June 8 with Venus already in front of the disk, and the third and fourth contacts happened at 11:07 and 11:26 UT. The VTT consists of a 46 m effective focal length, 70 cm solar telescope, equipped with an Echelle spectrograph that, when used in the infrared mode and with a slit width of $0.4''$, provides a resolving power of 200000. The detector used was the 256×256 pixel Tenerife Infrared Polarimeter (TIP, Martínez Pillet et al. 1999), in the Spectrograph mode (no polarimeter). The image scale in the focal plane was of $0.36''$/pixel, and at the distance of Venus at the moment of transit, 200 km were translated in $\sim 1''$. The total field of view was $\sim 92''$, and the Venus disk had a maximum diameter of $58.2''$. In the spectral axis, the wavelength range covered at the regions around 1.5 μm is of 8 $\AA$; thus, each pixel samples a total of 0.031 $\AA$. Series of 50 ms exposures were accumulated to provide 1 s integration time images every ~3 s (the rest of the time is spent by the system in writing the images to disc, reading the CCD, communicating with the telescope, etc.). All the images show a fringe pattern, a central horizontal line that divides the two

TABLE 6.1— Observing log. Spectral region *Favorite* = 1.5965-1.5973μm, *Grab bag* = 1.61245-1.6132μm, *Favorite +* = 1.5975-1.5983μm, Slit position 1 = 45.5°, position 2 = 315.5° (measured from the Venusian north anti-clockwise).

Time (UT)	Spectral Region	Slit position	Comments
06:51:27-06:54:10	Favorite	2	Dark images
06:57:20-07:02:17	Favorite	2	Flat field images
07:33:16-07:55:55	Favorite	2	Full scan
08:02:08-08:06:51	Grab bag	2	Flat field images
08:15:06-08:43:07	Grab bag	2	TESOS-leaded
08:55:25-09:00:23	Grab bag	2	Flat field images
09:10:25-09:26:32	Grab bag	2	Full scan
09:31:32-09:36:11	Grab bag	1	Flat field images
09:52:48-09:55:01	Grab bag	1	Partial scan, no AO, telescope failure at the end
10:02:51-10:24:09	Grab bag	1	Manual full scan, no AO
10:29:21-11:19:22	Favorite +	1	Manual partial scan, AO?
11:19:36-11:29:05	Favorite +	1	Manual partial scan, Venus close to limb, TESOS-leaded
11:30:27-11:35:09	Favorite +	1	Flat field images
11:36:07-11:40:45	Favorite +	1	Dark images

upper 128×128 chips from the two lower ones, and a region with a noticeable number of bad pixels in the upper-left corner (where we define the orientation as in the figures plotted further down). A gain jump between the left and right chips is also visible.

Flat field images were obtained by moving continuously the telescope through a part of the disc close to the center and without magnetic regions. These images were obtained before and after every scan of the Venus disk, and after changing the slit orientation and/or the spectral range (the fringe pattern depends on both changes). Also, to correct for the temperature dependence of the chip, sets of 30 dark images were obtained, by putting a cover in the entrance of the spectrograph.

The system is equipped with Adaptative Optics, that was used after the $\sim$ 1st hour of data acquisition, when the Sun was at a suitable altitude above the horizon. The sky conditions were very good, with a clear sky, no dust, and seeing conditions varying around 1″. Several technical problems happened the morning of the transit, causing a total of $\sim$ 1 hour of lost observing time. The need for manually-controlled drift scans of the Venus disk limited the use of AO to only one of the two used slit orientations.

Three complete scans of the disc of Venus and three partial scans were obtained (see Table 6.1), in two different slit orientations and three different spectral regions close to 1.5 μm.

6.3 Data analysis

In this section we describe the details of the process followed to obtain the spectral absorption lines. Two main problems in the images had to be treated carefully: the fringe pattern, which is time-dependant, and the diffuse light in the Venus limb, which has a signal a factor of $\sim$10 smaller than the solar disk.

6.3.1 Calibration

Average flat-fields and dark currents were obtained combining typically 30 exposures of each type of image. Bad pixels are detected by subtracting each image from a 4 points smoothed image and establishing a certain threshold. Those points above or below the threshold are substituted with the smoothed value, and the process is repeated two more times, with different image smoothing and thresholds.

Even though if the images are bias-corrected at the time of storage of the images in the computers at the telescope, a division with a normalized flat-field images doesn't work properly. As seen in the subtracted image shown in Figure 6.1 (in the next subsection we'll describe how these images were obtained), whilst the fringes disappear in the solar disk, there are fringes in the venusian disk, and consequently in the limb. This is a consequence of diffuse light in the Venus disk. To investigate this diffuse light component, we made a linear fit of the minimum signal of the Venus disk as a function of its width in the image. The coefficients of this fit were used to estimate the diffuse light from the measured width of the disk in each of the images. Subtracting this value (multiplied by a constant value of around 0.45 as explained below), and flat-fielding, results in a subtracted image where, contrary as in Figure 6.1, the fringes are now evident in the part of the solar disk, and they have been successfully removed from the venusian disk (Figure 6.2). This is a consequence of the diffuse light affecting to the pixels with lower signal. Thus, we used in every image a wavelength-averaged image profile to build a "diffuse light" image that has $\sim$0 value in the parts with solar disk, and the diffuse light constant in the center of the venusian disk. A cut in the wavelength axis of this "diffuse light" image is plotted in Figure 6.3. The fringes are optimally removed from the final images if this diffuse light image is multiplied by a constant value before subtracting it from the data images[5]. Figure 6.4 plots one random subtracted image, to show that there are few remains of the fringe pattern.

[5]These constant values are different at each of the spectral regions, probably as a consequence of the different average solar continuum signal at each wavelength. The spectral regions with more solar signal will be more affected by diffuse light. For the Favorite and the Favorite + regions, this constant value is estimated as 0.45; in the Grab Bag region the fringes are better removed if a constant value of 0.25 is used.

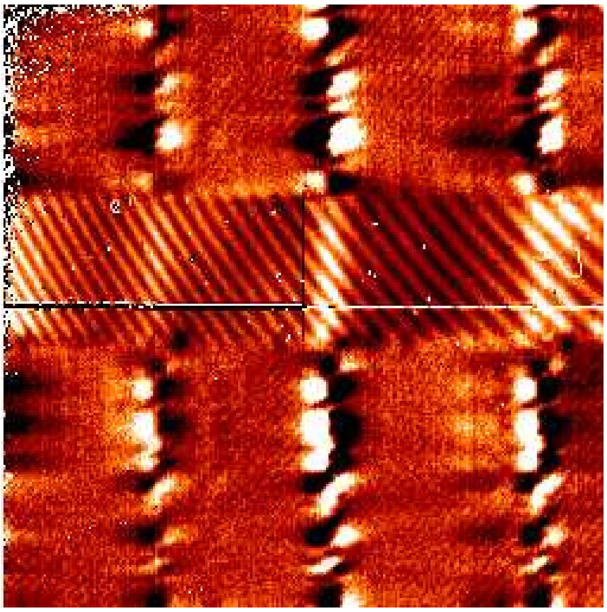

FIGURE 6.1— Difference of a flat fielded (as typically done) image and a model image (see text for details); wavelength is increasing to the right, and the central part is the Venus disk. The fringes have not been well removed from the disk.

6.3.2 Obtaining the spectral lines

In order to get rid of the parts that do not vary from image to image, we built, for every image, an artificial image that is the vectorial product of an average in the x direction times the average in the y direction. The subtraction of this image from the original leaves only the parts that are not common to all the images. In Figure 6.4 there are several features easily distinguishable:

- The solar spectral lines appear with positive and negative values, due to the different speeds of the plasma in the granules.
- There is still some residual fringing.
- In a few places in the Venus limb, absorption lines are clearly visible. They have not the same depth in the two limbs.

6.3.3 Final spectra

In every calibrated image, the ratio was built between the intensity at the limb locations (3 pixels were considered) and the intensity 11 pixels away from the

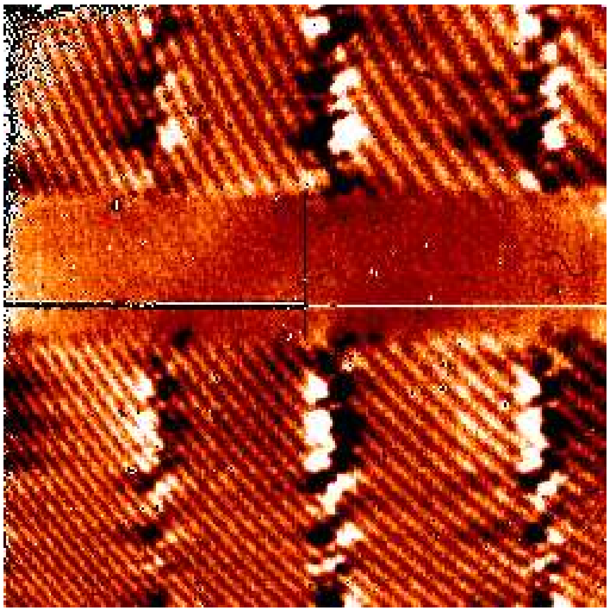

FIGURE 6.2— Same as Figure 6.1, but where a constant value has been subtracted to the image before flat fielding. Now, the fringes have been well removed from the Venus disk, but not from the Solar disk.

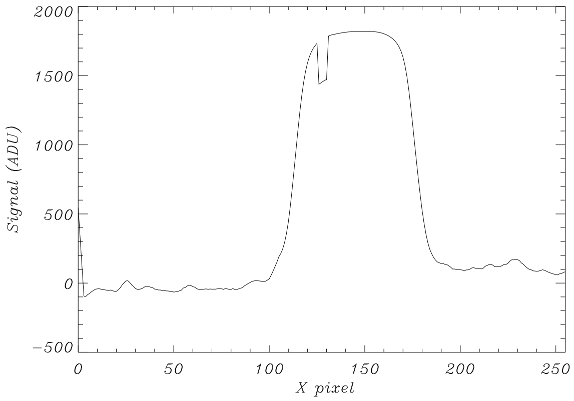

FIGURE 6.3— A vertical cut in a typical "bias" image, constructed as described in the text. It will subtract a constant value to the venusian disk, while the rest of the image will remain basically unaffected.

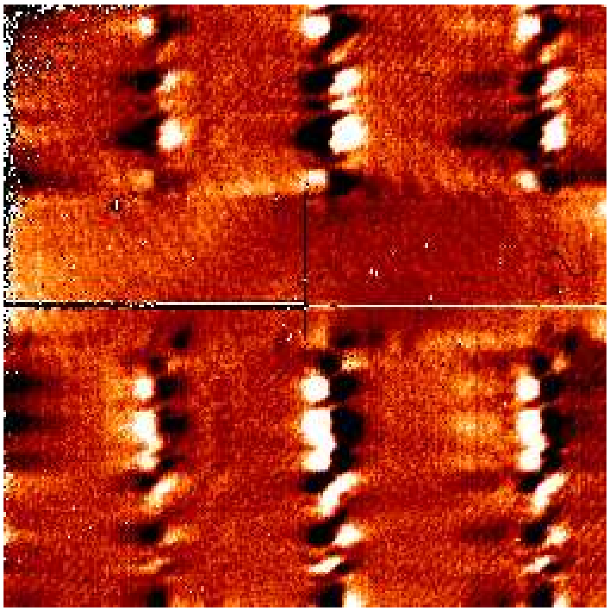

FIGURE 6.4— Final difference image, after correction with the artificial image whose cut is shown in Figure 6.3. Now, the fringes have been efficiently removed from all the image, and Venus absorption lines appear in both of the Venus limbs.

Venus disk. The ratio was normalized and corrected for gradients in the two segments of the CCD by a parabolic fit to regions of the spectra where no strong solar lines nor $^{12}CO_2$ absorption lines were expected. A visual inspection of the subtracted images allowed to reject bad exposures, in which the telescope was being moved, or the absorption lines were not clear, due to worst atmospheric conditions. The total final spectrum in each of the spectral regions was built as the median value of all the individual spectra. The final spectra in two of the three different spectral regions are plotted in Figures 6.5 and 6.6.

Absorption features in those spectra are evident, in the expected wavelengths. All the lines seem to appear in doublets, which is due to fortuitous overlaps with the $^{13}CO_2$ molecular absorption lines, not considered initially in the model.

The orientation of the slit at the time of third contact, in the slitjaw images, and the ephemerides for the transit impact parameter and orientation of the Solar and Venusian rotation axes were used to infer the latitude at which the two limbs were, in each of the images. This allowed to average several spectra in latitude-bins, in order to study possible differences in these. The spectral region

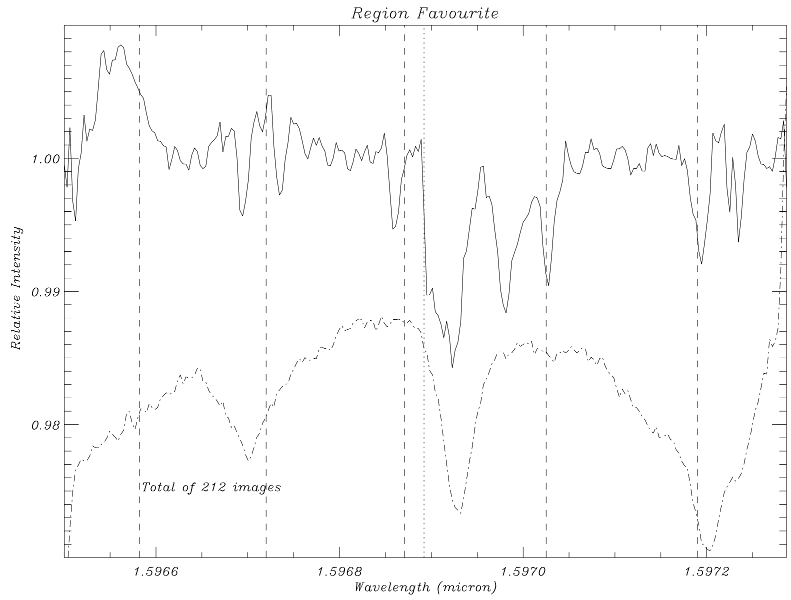

FIGURE 6.5— Final spectrum of the Favorite region, constructed as average spectra of the two limbs. Each spectra of the limbs is the median of 212 spectra, which are the ratio of the signal at 3 pixels centered on the Venus limb and 3 pixels located 11 pixels away on the solar disk. The individual spectra are fitted to a 2nd order polynomial in each of the CCD left and right halves (see text for details). Vertical dashed lines show the expected CO_2 absorption features, from the model described in the Introduction. The vertical dotted line marks the division between the two left and right chips. The dash-dotted line plots the mean solar + telluric spectrum at this region. Features that appear close to strong solar + telluric lines should be considered with special care.

Favorite + was used for this purpose, as the lines are more clearly detected in this wavelength range, and ~40 minutes were spent in a narrow set of latitudes. The Figures 6.7 and 6.8 show these binned spectra.

A total of 534 good images in the Favorite + region, sampling venusian latitudes between 0-30° (one limb) and 55-85° (the other), were used to obtain two averaged transmission spectra. These are plotted in Figure 6.9. The low-latitude absorption lines are less deep, specially the doublet close to 1.59792 μm. Further work will be devoted to establish wether this latitude dependence is real or an instrumental effect, such as an asymmetric PSF behavior.

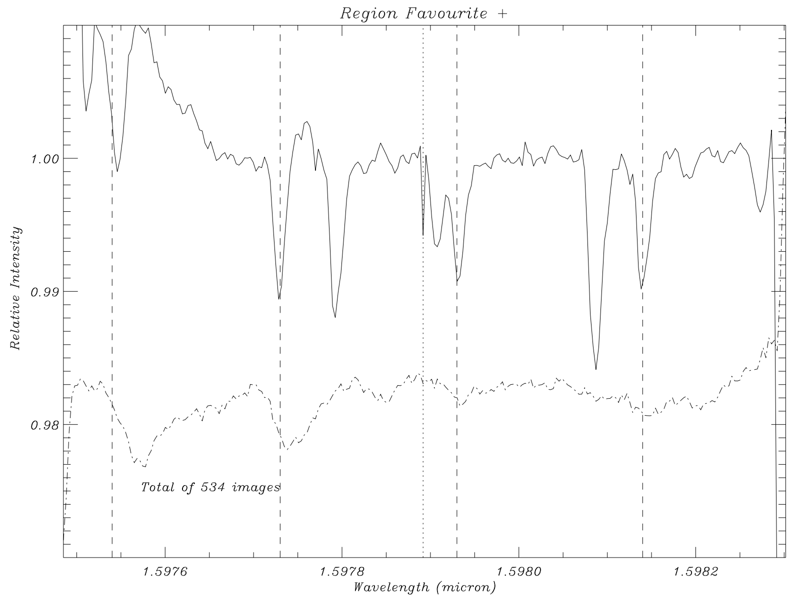

FIGURE 6.6— Same as Figure 6.5, for the Favorite + region. The S/N level of this spectrum is higher than in the other regions, due to the few solar + telluric features at these wavelengths and to the bigger amount of collected data.

6.4 Summary and future improvements

The spectral signatures of CO_2 have been detected for the first time as absorption features at the limbs of Venus while it is passing across the disk of the Sun. The relative strengths of the $^{13}CO_2$ and $^{12}CO_2$ close spectral lines have been observed to be different from the terrestrial cases, an effect that can be due to temperature differences between the terrestrial and Venusian atmospheres. Variations in the strengths of these features with the Venusian latitude of the limbs at which the slit cuts the disk of Venus are consistent with the increased temperatures at higher latitudes, an effect observed by the Pioneer Venus Orbiter for the first time.

Unfortunately, the fringes and diffuse light at the detector have placed a limitation on the expected performance of the observations. Our initial plans, to continuously rotate the slit in steps of a few (3-5) degrees, had to be changed due to the importance of the fringing on the detector, which required specific calibration images at each position of the slit, thus involving a precious amount of time. This has also limited our plans to perform a Doppler analysis of the absorption lines, which could provide information on the winds at the meso-

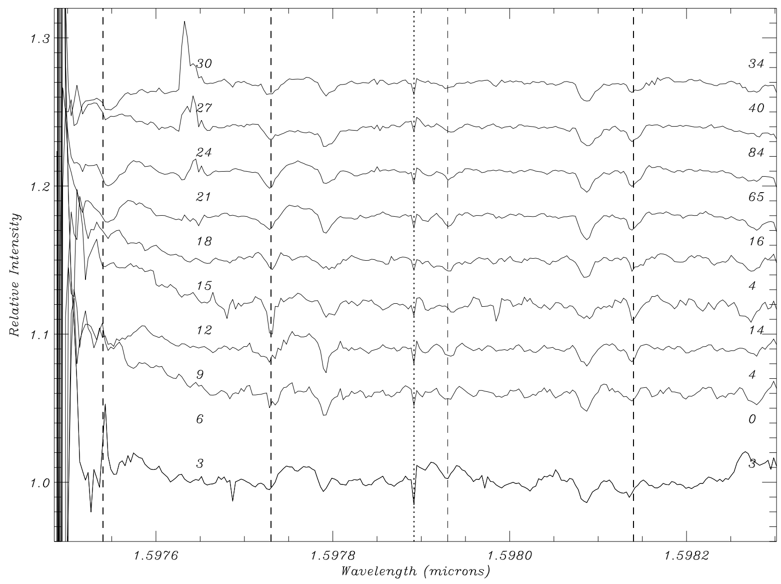

FIGURE 6.7— Latitude-binned spectra at the Favorite + region. The numbers on the left are the mean latitude of each bin, while the number on the right represents the number of averaged spectra in that bin. A total of 264 spectra have been considered. The apparent "emission lines" at ∼1.59763μm and 20-30° are due to residual bad pixels. All latitudes are in the Northern hemisphere.

spheric level, and at different altitudes. The S/N level of even our best averaged spectra (Figure 6.6) is not enough as to provide the minimum useful velocities precision of a few tens of m/s. The FWHM of the absorption lines in this spectrum is ∼6 pixels, which at this wavelengths translates in a Doppler shift of ∼3.5 km/s ($v=c*\Delta\lambda/\lambda$)

This work demonstrates the capabilities of the transmission spectroscopy to detect spectral signatures of the atmospheres of transiting exoplanets. Despite the current technical impossibility to have any spatial resolution on the host star and on the planet, and thus to make any latitude-dependant study on an exoplanet be not more than a dream for the next (several) decades, there is one important advantage of the exoplanetary transits: its more frequent occurrence. To try to repeat or improve the measurements described in this Chapter, we have to wait to the next Venus transit on June 2012, and after that to December 2117, while the transits of planets like HD 209458b or TrES-1 happen roughly every 3 days. Thus, it seems that refinements on the transit spectroscopy technique for the study of planetary atmospheres will be preceded

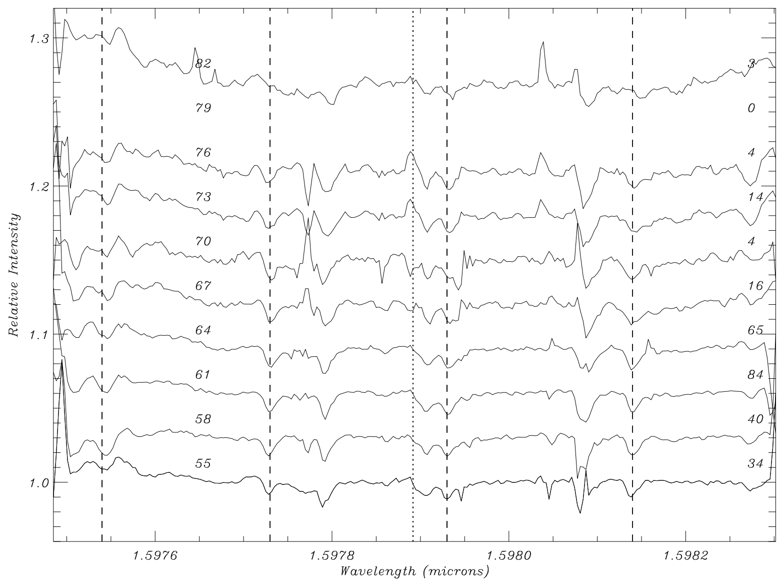

FIGURE 6.8— Same as Figure 6.7, for higher latitudes.

by the study of the exoplanet's atmospheres in the next decades.

As possible future improvements, more care could be payed to the time dependance of the fringing pattern. We noticed that it showed detectable variations after ∼30-50 images (∼1 minute); a way to try to reduce this variations would be to construct intermediate "flat field" images with the data. This false flat field images would show some real structure (such as granulation), but they would provide a better removal of the fringe pattern. The images where the Venus disk is small (slit almost tangential to the disk) might be used for this purpose; the fringes would not need to be optimally removed at the disk center, as only the signal at the limb and close to the limb in the solar part are used.

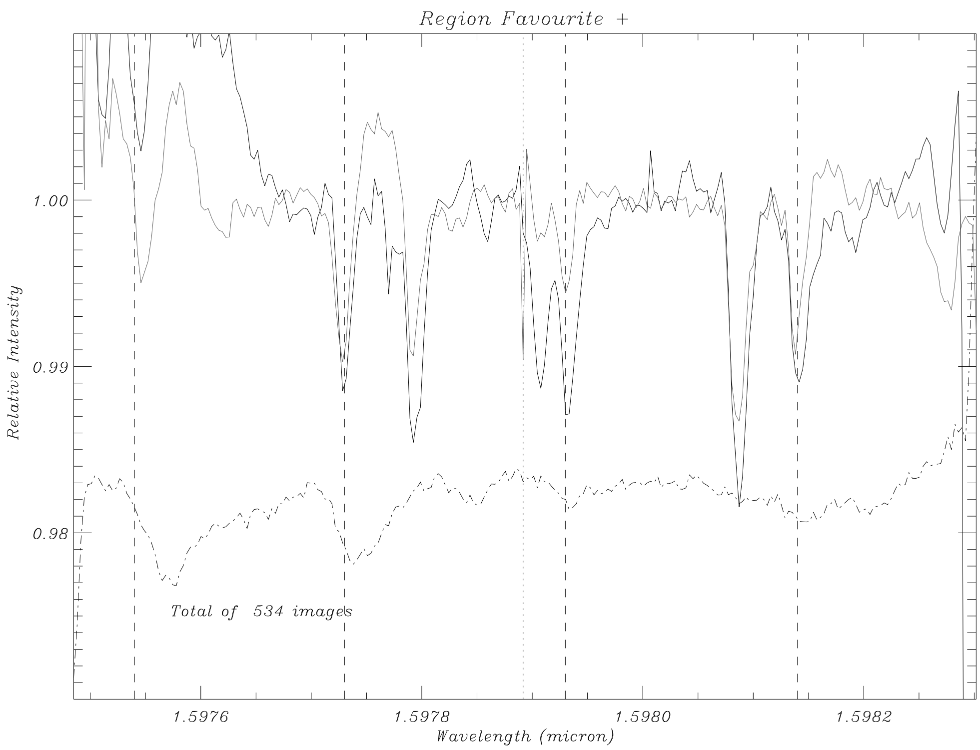

FIGURE 6.9— Median of the transmission spectra at the two limbs, separately. The solid line is for the limb at higher latitudes (55-82°) while the dotted line plots the limb located at lower latitudes (3-30°) of the venusian northern hemisphere.

7

Conclusions and future work

The field of exoplanet research is evolving at astonishing velocities since the first discovery of an exoplanet around a solar-like star, 51 Peg (Mayor & Queloz 1995). Among the different detection techniques, the transit method provides the strongest tool to date to measure physical parameters of these intriguing Hot Jupiters. Combined with the measurement of the radial velocity of the host star, it can yield the planetary density, which can provide clues about its formation history. The discovery of new transiting planets by ground and space projects in the next few years will certainly increase our knowledge of these objects. We are beginning to be able to perform comparative planetology, and new insights on the *real* mass distribution of these objects will be provided in the near future. The current situation has been compared by some authors to the state of the stellar evolution knowledge just before the first H-R diagram was built. With more than 150 exoplanets discovered to date, we are approaching the status in which the statistical studies on these objects begin to be meaningful.

7.1 Conclusions on exoplanet research

The conclusions of this work are summarized in the following points:

- We have discovered the first transiting planet detected by a wide-field telescope (STARE), TrES-1. It is orbiting a moderately active K0V star that shows no Lithium down to the detectable levels. The measured mass of 0.76 ± 0.05 M_J and radius of $1.04^{+0.08}_{-0.05}$ R_J make this planet the second best known in terms of precision of its physical parameters. Contrary to the currently best studied exoplanet, HD 209458b, the radius of TrES-1 is well matched by models of planetary evolution under intense radiation of the host star. There is no need for an extra source of internal energy in the planet. Further work (Charbonneau et al. 2005) has allowed the detection of the secondary eclipse, which constitutes the first detection of thermal emission at 4.5 and 8 μm from an exoplanet. With this detection, the effective temperature of the planet is estimated in T_{eff}=1060±50 K, and the eccentricity is strongly constrained to a circular orbit ($e \cos w$=0.0030±0.0019).

- A detailed analysis of the different follow-up techniques needed to confirm or reject a planetary transit candidate has been performed, and a tentative chain of tests, ranging from the cheapest ones to the most expensive, in terms of telescope needs and effort, has been proposed. This consists of:

  - Careful interpretation of the light curve: search for out-of-eclipse modulation and transit shape fitting.
  - Low signal to noise radial velocity, to detect eclipsing stellar systems.
  - Multicolor transit photometry, aimed to the detection of triple systems.
  - Imaging with very high resolution, to resolve triple stellar systems (hierarchical or unbound).
  - High signal to noise radial velocities and bisector analysis, to finally measure the orbital reflex motion of the parent star, and thus the mass of the planet.

- A sample field of the TrES network in the constellation Lyra has been analyzed in detail, paying special attention to the follow-up observations of the 16 objects identified as transiting planet candidates. These resulted in the detection of 6 binary systems, 7 blended triple systems, 2 unsolved cases and the transiting planet TrES-1.

- The 2004 Venus transit has permitted the first detection of $^{12}CO_2$ and $^{13}CO_2$ traces in the atmosphere of the planet by the use of the *transit spectroscopy* technique. Further work will be devoted to interpret the obtained transmission spectra, and the preliminary measured dependance of the depths of the features as a function of the sampled Venusian latitude.

7.2 Conclusions on stellar variability

Several studies have been performed with the STARE data in the field of stellar variability; these are summarized in the next two appendixes. The main conclusions that follow from these studies are:

- The STARE (or any of the TrES) light curves achieve enough precision as to perform serious studies of stellar variability.
- The STARE light curve of the δ Sct V1821 Cygni has been studied in detail, detecting 4 clear pulsation frequencies on this star. One frequency had not been detected in previous observations of the star. Another 3 frequencies close to the noise level might serve to explain the apparent amplitude variability of the main frequency f_1. However, it is not possible to reject the possibility that f_1 is intrinsically variable, and the 3 close frequencies are an artifact of the frequency analysis tool used.
- Frequencies, amplitudes and phases of 5 newly discovered pulsators in the constellation Cygnus have been provided as a by-product of the investigation on V1821 Cygni.
- As a result of a collaboration for the COROT space mission, a total of 38 variable stars have been discovered with STARE in the potential fields accessible to the spacecraft. Some of them are either too faint to be observed with the COROT seismology CCDs or too far from the main COROT targets, but 18 stars have been identified as potential secondary targets in the COROT seismology CCDs. These are mostly δ Sct stars, but also γ Dor pulsators and eclipsing binaries have been discovered.

7.3 Future work

Preliminary analysis of observations of TrES-1 using HST/ACS results in a determination of the planet parameters that is within the error bars of the parameters stated in this work, and in the probable detection of a large star spot that was occulted by the planet during one of the HST visits. The detailed shape of the ingress-egress phases in these data will serve to search for planetary rings on the planet. The precise eclipse timing and the study of the residuals of the transit fitting will be used to search for TrES-1 satellites.

Further work is needed to interpret the observations carried on the 2004 Venus transit, specially to establish the origin of the observed latitudinal dependance of the spectral features. In particular, a measurement of the ratio of equivalent widths between two clear $^{12}CO_2/^{13}CO_2$ lines can provide insights on the temperatures at the altitudes in which those lines become opaque to the tangential solar rays.

While many of the TrES transiting planet candidates are rejected as eclipsing binary (or triple) systems, there is valuable information on the sizes of eclipsing M stars within these candidates. Some of the TrES team members are working on obtaining the orbital and physical parameters of these binary systems (some of which were detected in the field of the constellation Lyra that was discussed in this Thesis). As a first result, the up-to-now fourth known eclipsing binary with two M star components has been detected in one field of the constellation Hercules (Creevey et al. 2005).

And, finally, the TrES network will be working for at least three more years, surveying the night sky in search for new TrES exoplanets.

When a significant number of transiting planet candidates are detected, it will be worthwhile to perform a detailed analysis of the rate of detections of false positives, and on the nature of each of those. This might serve to establish if the rate of occurrence of transiting planets is in good agreement with the rate of occurrence of planets detected so far by the radial velocity technique.

A

δ Scuti studies with the STARE data

We study a particular case of a δ Sct star (V1821 Cygni) observed by the STARE telescope in a field centered in the constellation of Cygnus. This star had been observed by several authors to be multi-periodic, and there were clues for variations in the amplitudes of one of its modes. The light curve obtained with STARE is used to confirm this amplitude variability, to investigate on its origin (close frequencies vs. intrinsical mode variability), and to detect previously unseen low amplitude pulsation modes. This provides an example of the use of the STARE (and TrES) light curve databases to perform investigations on stellar pulsations that can compete with those that use much bigger aperture telescopes.

A.1 Introduction

V1821 Cygni is a δScuti type pulsator that was discovered in a search for variable stars in the open cluster NGC 6871 (Delgado et al. 1984, D84 hereafter). It was found by these authors that the star is not a member of the cluster, but a foreground object. A period analysis of their set of 3 observing nights allowed them to identify two frequencies, $f_1 = 9.245$ and $f_2 = 11.076$ c/d. A second intensive study of this star was done by Zhou, Liu, & Du (2001), observing a total of 21 nights spanning 354 days. In their period analysis, they detected two different frequencies, 8.8218 and 8.2439 c/d. These authors also re-analyzed the D84 set of data, obtaining two terms at 8.9788 and 11.0674 c/d. The different results in the period analysis of the same set of data is a consequence of the short duration of the series, according to the authors. They noticed that a 1 day alias of the D84 f_1 roughly coincides with the 8.2439 c/d frequency. A fit of the D84 data with the frequencies obtained by Zhou, Liu, & Du (2001), allowing for phase and amplitude variations, was carried by these authors, and they observed an amplitude variability on the 8.8218 c/d frequency. No evidence was found for a frequency close to 11.076 c/d in the new set of data, making them suggest that, if this frequency is real, it has to be produced by an unstable mode.

The issue of amplitude and phase variations in several observed modes (in XX Pyx, Handler et al. 1998, Handler et al. 2000; V1162 Ori, Arentoft et al. 2001) is a controversial point. It is not well established if these observed values are produced by the effect of close frequency pairs (as suggested by Alvarez et al. 1998 for the case of BW Cnc), or if the variations are intrinsic to each mode. To illustrate the difficulties in disentangling these two interpretations, we mention a study carried by Handler et al. on XX Pyx in 1998. This star seemed to show long-term variations in the amplitude of the highest amplitude frequency f_1, that had a different time scale than the phase variations of the same mode. However, a new set of observations (Handler et al. 2000), allowed them to identify a new frequency close to f_1, that was the final cause of their detected frequency and amplitude variability. After developing and applying a non-linear analysis to the series, they claimed to find evidences for short-term amplitude and frequency variations in other 8 modes of the star.

Breger & Bischof (2002) performed a literature search for detected close frequencies in δ Scuti stars, and for one of these stars (BI CMi), they found phase variations in three of the modes when their amplitude reaches a minimum, thus favoring the close-frequency model instead of simple amplitude variability. They provide several possible explanations for these close-frequency pairs: mixed modes, trapped modes, rotational splitting, small spacing, and mode coupling. Some of these explanations (small spacing, trapped modes) can account for two detected close frequencies, but can not explain a group of three or more close frequencies.

A.2 Observations

The observations were obtained as a by-product of a planetary transit search in a field centered in HD 188650, carried by the STARE telescope (Chapter 2). A field containing V1821 Cygni was observed during summer 2001, for a total duration of 205 hours, obtained in 36 nights spanning 87 days. The filter used was roughly an R filter, and the exposure time was fixed at 107 s, producing typically one point every two minutes, due to the readout time. As a final result of the data reduction, there are a total of 820 points, sampled every

TABLE A.1— The light curves. N stands for number of data points. JD0 is Julian Date 2450000.

ID	N	Begins (JD - JD0)	Ends (JD - JD0)	Spans (days)
1	112	2136.5846	2143.7245	7.14
2	162	2145.4089	2151.4952	6.09
3	154	2153.4424	2162.5291	9.09
4	167	2165.3411	2172.5640	7.22
5	167	2183.3684	2205.5394	22.17
6	161	2487.3917	2493.7206	6.33

15 min. A good night of observation, sampled every two minutes, is plotted in Figure A.1. The amplitude spectrum of one close, 0.5 mag fainter constant star (HD 227732) is plotted in Figure A.2, to evaluate the precision level attained. It can be seen that there are no peaks detected above the 1 mmag level.

To study possible variations in amplitude of some of the frequencies (as stated in Zhou, Liu, & Du 2001), we made a subdivision of the data set, in an arbitrary number of 5 groups. This was done subjectively, trying to keep good runs of $\sim$ 6 days together, and, when not possible, trying to obtain enough data points. The length, number of points, and time span of each subdivision is summarized in Table A.1. The total number of data points is 762. The discrepancy between this value and that stated above (820) is due to three nights of data at the beginning of the observing run. These nights were too isolated in time (15 days) from the rest of the time series, and thus not considered for the study of the variations in the frequencies and amplitudes. The subdivision *5* in that table spans longer than the others. We made this subdivision trying to get enough points to allow a spectral study, thus compensating for the short durations of each nightly observation.

V1821 Cygni is the only cataloged δ Scuti star in this field, but several non-cataloged δ Scuti stars were discovered in the same field (Alonso, Belmonte & Brown 2003, see Figure A.3). Some of these stars will be used in this study to check for amplitude and frequency variations, allowing us to detect possible systematic errors in the data acquisition and/or analysis.

A.2.1 The 2002 data set

During summer 2002, the same field was re-observed. Unfortunately, due to technical problems, only 16 nights in a total span of 78 days were useful. Of these, the best set of data consists of 6 nights spanning 7 days, that will be the time series used for our purposes. The rest of the nights are too isolated in time; we discarded them to avoid complicated aliasing in the spectra.

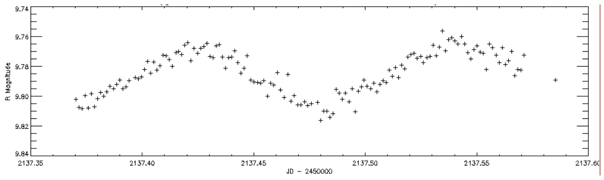

FIGURE A.1— Data from a night of observation on V1821 Cygni

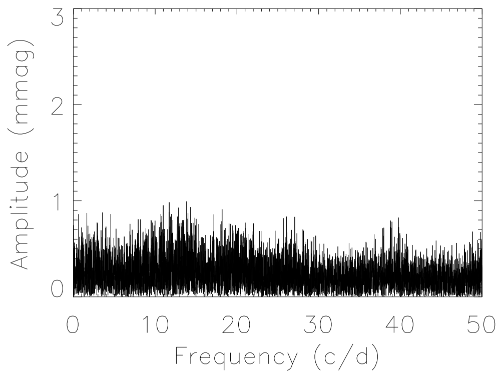

FIGURE A.2— Spectral analysis of a close, 0.5 mag fainter constant star (HD 227732, A0 type)

A.3 Data analysis

The frequency analysis was carried out with the tool Period98 (Sperl 1998), for consistency with the work of Zhou, Liu, & Du (2001). As a first analysis, we used the combined 2001-2002 time series to establish the best values of the frequencies, amplitudes and phases that matched with the observations. Table A.2 summarizes the results of this analysis. Zhou, Liu, & Du (2001) mention a possible amplitude variability of the frequency f_1, that is specially noticeable in the different time series of the star obtained by Delgado et al. (1984) and their new set of data. At this point, we should mention that both set of observations could be compared because they were obtained with the same Strömgren y filter. Our data cannot be directly compared to these results, as we used a roughly Johnson's R filter. The frequency resolution in the 2001 set of data is 0.011 c/d, if $1/\Delta T$ is used (ΔT is the span of the observations), or 0.016 c/d if the more conservative Loumos & Deeming (1978) approach is used.

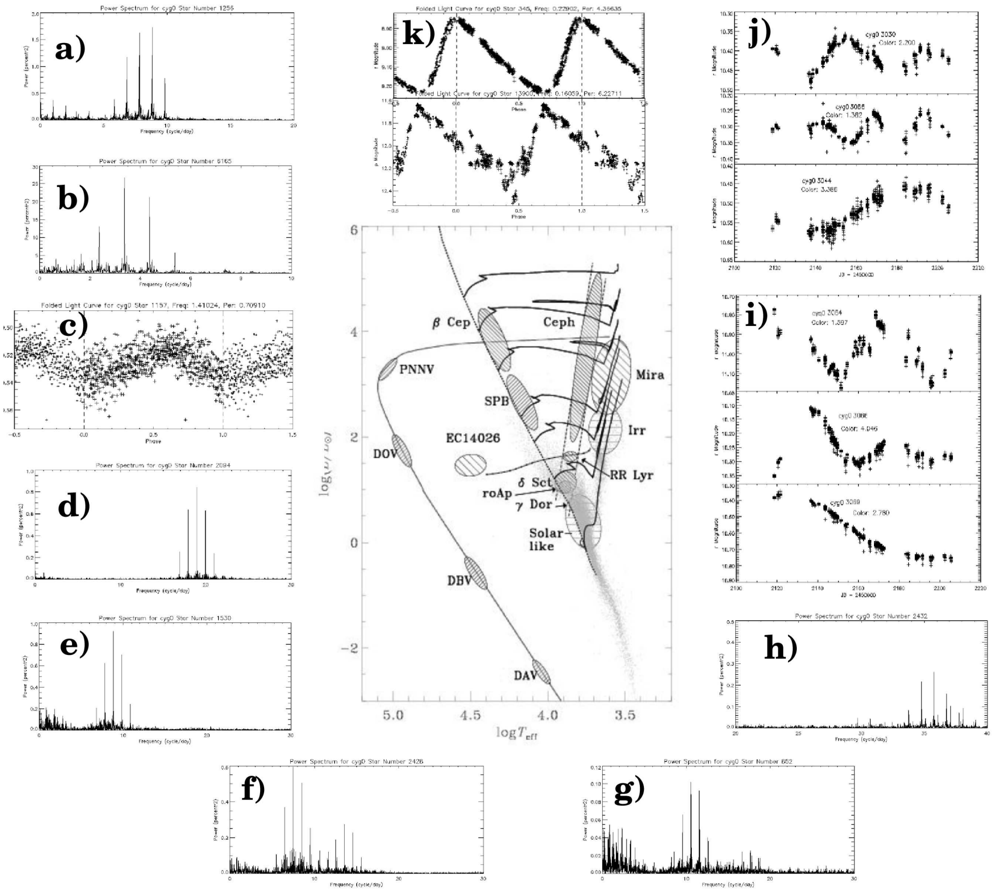

FIGURE A.3— Different examples of variability across the H-R diagram, from STARE data. a) Power spectrum of HD227977, probably a βCepheid star. b) and c) Two stars with oscillations in the range [1-5] cycles/day, thus probably γDoradus or SPBs. d),e),f),g),h) Power spectra of stars with oscillation periods in the range [6-40] cycles/day; d) shows a monoperiodic behavior, f) and g) show a complex spectrum, and h) shows frequencies higher than 30 cycles/day. i) and j) are plots of the light curves of long period or irregular red giant stars. k) are two folded light curves of classical Cepheids. Top: V547Cyg. Bottom: V402Cyg. The figure at the center is from Christensen-Dalsgaard (1999). From Alonso, Belmonte & Brown (2003).

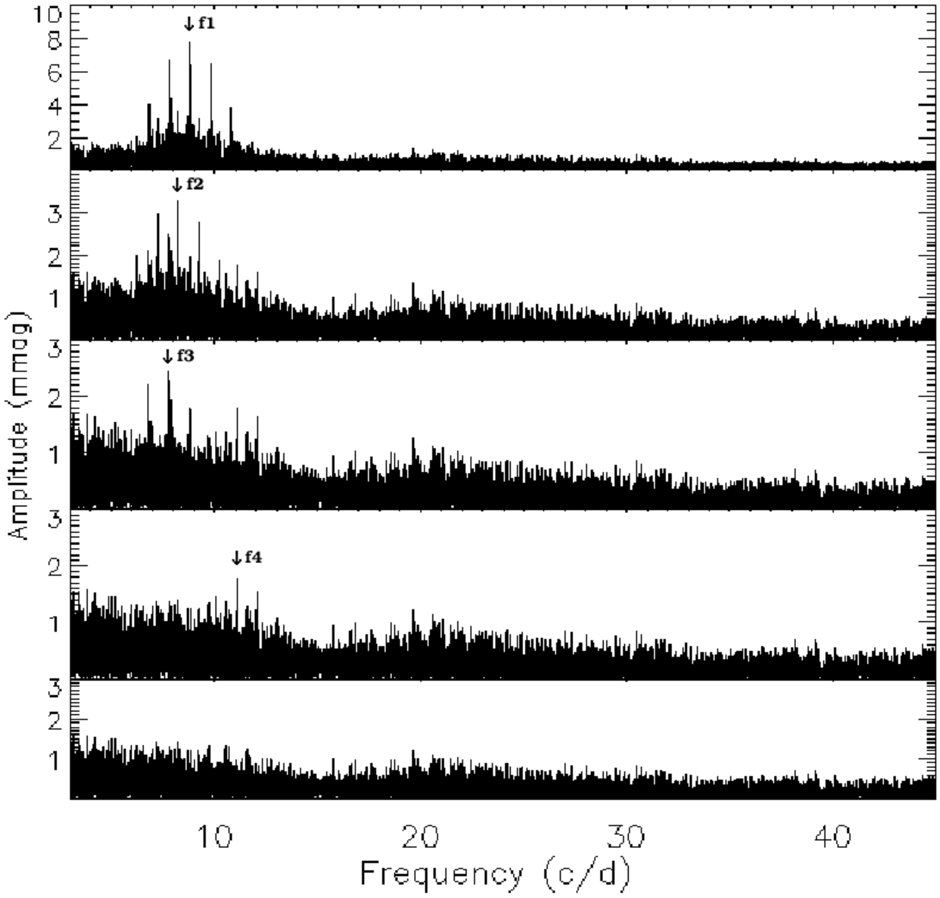

FIGURE A.4— Amplitude spectra of the 2001-2002 time series of V1821 in the region 3-45 c/d, obtained with Period98, after successive pre-whitening of the frequencies presented in Table A.2.

TABLE A.2— Results of the pre-whitening analysis. The noise was calculated in the residual spectra, as the mean amplitude level inside a 5 c/d box centered at each frequency. The frequency resolution for the 2001 data set is $\sim$ 0.016 c/d (see text for details).

ID	Frequency (c/d)	Amplitude (mmag)	S/N
f_1	8.819	8.4	17.8
f_2	8.243	3.4	6.9
f_3	7.775	2.6	5.3
f_4	11.086	1.8	4.4

A.3.1 Amplitude variability

To see if the amplitude variability reported by these authors is also present in our data, we used the different sets of data described in Table A.1. In each subset, we forced a least-squares fit to the data with the frequencies f_1, f_2, f_3 and f_4 fixed, letting the amplitudes and phases of these frequencies vary. The result of the standard deviations from the mean of the amplitude and phase of f_1 in each subset is respectively 1.69 mmag and 0.037 cycles. We need to determine if this variation is at the level of our detection capabilities. To accomplish this, in the next paragraphs we will remove the influence of f_1 in the light curve, and introduce a signal with the value of f_1, but with constant amplitude and phase. The results of the least-squares fit, as performed above, will give us an idea of the dispersions in amplitude and phase that we are able to detect.

To remove the signal of f_1, we made a least-squares fit to each subset. The fixed parameters were the frequencies f_2,f_3 and f_4, and the fitted parameters were the amplitudes and phases of these frequencies, together with the amplitude, phase and frequency f_1. We subtracted from the time series a sine wave with the values of the fitted frequency f_{1b}, amplitude and phase. Putting together all the subseries results in a time series with the influence of f_1 and possible variations in its amplitude and phase (i.e. frequency) removed.

As the next step, we added an artificial sine wave with fixed frequency, amplitude and phase to the whole (2001-2002) time series. We repeated the fit done to the initial light curve to this new time series, subdivided in the same subsets. The result is a much lower dispersion in the fitted values for the amplitudes and phases than the obtained with the real data: 0.19 mmag for the amplitude and 0.007 cycles for the phase.

It could be argued that with an a-priori knowledge of the frequency f_1 to be adjusted, it is obviously expected that the fit of this artificial light curve is better than the fit to the real data. To see if our results are affected by this effect, we made two different fits to the subseries, with a fixed frequency lower than the artificial inserted frequency ($f'_1 = 8.815$ c/d instead of 8.81853 c/d) and with a frequency higher ($f''_1 = 8.82179$ c/d, the value reported in Zhou, Liu, & Du (2001). The standard deviations of the amplitudes and phases of the fitted f'_1 and f''_1 are 0.33 and 0.18 mmag, and 0.068 and 0.092 cycles, respectively. The result of these fits shows that while an incorrect estimation of the frequency f_1 causes a linear drift or decrease in the fitted phase (and consequently a bigger dispersion in the measured phases), it does not produce variations in the amplitude of the order of the observed ones.

A.3.2 Phase variability

Once established that there are amplitude variations in f_1, we initiated a search for possible phase variability in this frequency. To do this, we need to model the amplitude variations of the frequency f_1. As a first approach, we will assume that the amplitude variability can be well described by a sinusoidal modulation. We used the measured amplitude and phase of f_1 in each subset, as described in the previous subsection, to calculate the parameters of this modulating sine wave. The analysis with Period98 returned a peak at a frequency of 0.0284 c/d (35.1854 d), amplitude of 1.83 mag, and phase of 0.49 cycles. This new frequency was used to modulate the amplitude of an artificial sine wave with frequency f_1. We added this signal to the time series, described above, with the influence of the *real* f_1 removed.

Finally, we performed least-squares fits to this new time series, in each of the subsets described in Table A.1. In these fits, as before, the fitted parameters were the amplitude and phases of the fixed 4 frequencies. In this case, the standard deviations of the amplitude and phases resulted in 1.28 mmag and 0.005 cycles, respectively. This shows that, while a sinusoidal variation of the amplitude of f_1 can account for the dispersion in the amplitude, the dispersion in the phase is not so big as in the real data. Once again, a similar analysis carried out with a fit to the frequency f_1 with an incorrect value causes the phase to change monotonically, which is not the case in the real data. This result motivated a more detailed analysis on the amplitude and phase behavior of V1821, that will be described in Subsection A.3.4.

A.3.3 Is the phase variation instrumental?

There is still another point to be checked before claiming a phase (or frequency) variation: could there be some instrumental problem in the data acquirement or data reduction pipeline that produces false phase variations? For instance, errors in the data acquisition PC clock (which is GPS-updated every hour), or truncations in the Julian Date vectors might be a source of phase variation. To test this possibility, we used other variable stars that are in the same field, with similar magnitude, and variations with similar frequencies as V1821 Cygni. These stars will have data at the same times as V1821 Cygni, and, if there were some instrumental problem with the times, all of them should reflect a similar behavior. As these stars were discovered in this run, there is no available information on their variability. Table A.3 lists these stars and the results of the frequency analysis on the 2001 data set.

For each star, we performed the same analysis as for V1821:

- Find the frequencies in the 2001 data set.

TABLE A.3— New δ Scuti stars in the field of V1821, used to test for amplitude and phase variability. When there is no ID of the star, the 2MASS coordinates are provided.

STARE ID	ID	RA (2000.0)	Dec (2000.0)	Frequency (c/d)	Amplitude (mmag)	Phase (cycles)
8267	-	$19^h55^m23.80^s$	$37°28'59.4''$	7.7073	65	0.50
				15.4142	20	0.31
2094	HD 225708	$19^h46^m07^s$	$35°25'07''$	18.9369	8.8	0.84
				27.2694	1.6	0.77
				21.1748	1.6	0.99
8663	-	$19^h48^m11.03^s$	$37°01'21.2''$	5.3137	7.1	0.95
				3.9744	2.3	0.74
				5.0191	2.1	0.97
1819	BD+36 3770	$19^h55^m17^s$	$37°21'30''$	15.8649	4.9	0.39
				18.2048	1.6	0.79
4566	-	$19^h40^m56.30^s$	$36°04'10.3''$	8.8316	13.2	0.82
				9.0416	2.1	0.20

- Construct the subseries.
- Fit the amplitudes and phases in each subseries, fixing the frequencies.
- Calculate the standard deviations of the amplitudes and phases in all the subseries.

The result of this analysis is summarized in Table A.4. Even if each star shows a different behavior, possibly due to the contribution of lower amplitude modes not taken into account, it can be seen that the standard deviation from the mean of the phase is around a value of $\sim$ 0.018 cycles, except for two cases: STARE 8663 and V1821 Cygni. The values of the standard deviations in the amplitude and phase of 8663 seem to indicate that this star also shows amplitude and phase variations, as we will demonstrate in the next subsection. The higher dispersion of the phase measurements in these two cases is a good proof of some phase (i.e. frequency) changes taking place in these stars, and disproves a possible instrumental origin of this result.

In the next section, we will try to disentangle if these amplitude and phase variations are intrinsic to the peak at f_1, or if they are caused by two or more close frequencies not resolved in each subseries.

A.3.4 A detailed study of the amplitude and phase variations

There are several possible effects that can produce amplitudes and phases variations. Among these, two close frequencies can in several cases explain these

TABLE A.4— Means and standard deviations of the amplitudes and phases for the fitted frequencies of the stars in Table A.3 to each subserie. See text for details.

STARE ID	Mean Amplitude	std amp	Mean phas	std phase
8267	67	0.73	0.50	0.017
2094	8.8	0.79	0.83	0.019
8663	7.2	1.56	0.95	0.031
1819	5.0	1.00	0.39	0.003
4566	13.1	1.15	0.82	0.012
V1821	7.8	1.57	0.82	0.026

variations (Breger & Bischof 2002), and favor this scheme against the single mode with variable amplitude hypothesis. A known effect of two close frequencies is a phase change that is steeper when the beating of the two frequencies reaches a minimum (see, for instance, Breger 1981). The amount of the phase change depends on the relative amplitudes of the two close modes. To try to establish which of these two favored explanations (single mode with variable amplitude vs. close modes) matches our data better, we made an amplitude - phase analysis, strongly inspired by the works of Arentoft et al. (2001) and Handler et al. (1998).

To avoid effects arising from the low amplitude frequencies, the time series first has to be cleaned of these. The way we accomplished this is as follows: first, in each subset described in Table A.1 we made a fit of the data to f_1,...,f_4. In this fit, the free parameters were the amplitudes and phases of f_2,f_3 and f_4, and the frequency, amplitude and phase of f_1. This ensures that we are removing the most powerful peak in the power spectrum of the subset. A synthetic light curve with the frequency, amplitude and phase of the best fit to f_1 in each subset was created and subtracted from the subset. Secondly, we put together these subsets having removed the contribution of f_1, and performed a frequency analysis, which gave a clearer fit to the low amplitude frequencies. The frequencies, amplitudes and phases of the four highest amplitude peaks coming out from this fit are in Table A.5. As a result of this analysis, a new frequency $f_{spurious}$ was detected, at a S/N level of 3.3. The value of this frequency, close to 7 c/d (at a distance lower than twice the spectral resolution), its lower S/N ratio, and the fact that it was not detected in the analysis carried out in Section A.2, makes us suspect that this is an spurious peak. The rest of the frequencies agree reasonably well with those tabulated in Table A.2, considering the spectral resolution (0.011 c/d). The final step was to construct a synthetic light curve with these low amplitude frequencies and subtract it from the original data. A frequency analysis of this last light curve shows a single peak at f_1, with the

TABLE A.5— Results of the pre-whitening analysis of the time series with the influence of f_1 removed. The noise was calculated in the residual spectra, as the mean amplitude level inside a 5 c/d box centered at each frequency.

ID	Frequency (c/d)	Amplitude (mmag)	S/N
f_2	8.241	3.3	7.1
f_3	7.773	2.5	5.3
f_4	10.082	1.5	3.8
$f_{spurious}$	6.980	1.6	3.3

low amplitude frequencies well removed.

To study the amplitude and phase variations with enough temporal resolution in this time series, we performed a *moving fit* to different subseries of the data. To construct these subseries, we fixed a duration (in time) and a step (in number of points) between two consecutive subseries. This ensures that all the subseries will have similar spectral resolution. We ended with $\sim N/step$ dependent subseries. In each of these subseries, we performed a 2 free-parameters (amplitude and phase) non-linear fit to a sine with frequency 8.818716277 c/d using the Levenberg-Marquardt algorithm (Levenberg 1944 and Marquardt 1963). We assigned the results of this fit (amplitude and phase) to the mean value of the time in each subseries. In Figure A.5 we plot the result, where the duration of each subseries is 10 days and the step is 4 data points. The error bars are 1-sigma above and bellow the estimated value. Choosing a shorter duration of the subseries results in poorly determined values of the amplitudes and phases, while with longer durations, the amplitude and phase variability begins to be artificially smoothed. We restricted this study to the data between JD 2452130 and 2452170, as there is good nightly coverage in this interval.

Surprisingly, in Figure A.5, a phase change is barely seen, but it does not occur when the amplitude reaches a minimum, as we would expect if it were caused by two unresolved close frequencies. The overall shape of the phase changes is well described numerically by two close frequencies of different amplitudes, with the lower amplitude peak also having the lower frequency. Anyway, as stated above, there is a significant shift of $\sim$ 14 days between the expected time of phase change and the observed one.

It remains to determine if the variations observed in V1821 Cygni can be attributed to the interference of more than two close frequencies. In fact, a spectral analysis of the time series of V1821 Cygni cleaned for the low amplitude f_2-f_4($+f_{spurious}$) frequencies (Figure A.6), shows at least two close peaks that are

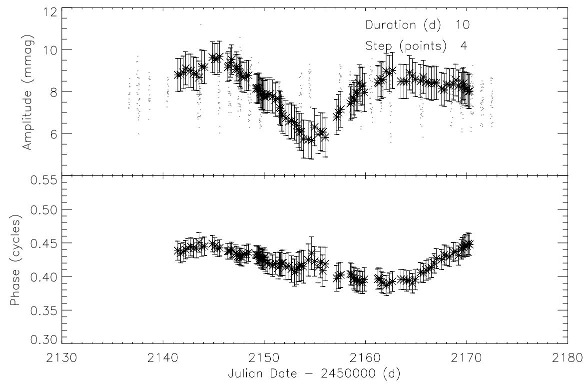

FIGURE A.5— Amplitude and phase variations of V1821 Cygni plotted versus time. Only one part of the whole time series with a good coverage is considered. Each point represents the best fit, in a 10 days length subseries around the point, to the amplitude (top panel) and phase (bottom panel) of a sine with frequency f1. The error bars are 1σ above and bellow the fitted value. The distance between each fitted subserie is 4 data points. The light points are the data points, shifted and scaled for the shake of clarity.

inside the resolution bin of a 10 days time-series (f_5 and f_6 in Figure A.6). As the signal to noise of these peaks is low (3.0 for f_5 and 2.8 for f_6), it is unclear if these are significant close frequencies, just from the spectral analysis. Moreover, there is a detectable daily alias for each of these peaks, with a frequency 1 c/d lower for the frequency close to 8.86 c/d, and in a frequency 1 c/d higher than 8.71 c/d. The single-site nature of these observations and the possible interference among these peaks with f_1 makes it impossible to decide which is the main peak and which the alias. If we restrict the spectral analysis to the part of the time series where the moving fit was applied, the spectrum shows three close frequencies to f_1, at 8.865 c/d (f_5), 8.71 c/d (f_6) and 8.746 c/d (f_7) (Figure A.7). We built an artificial light curve with the frequencies f_1 and these three close frequencies, choosing different values for the phases of the close frequencies. Performing the moving fit analysis to this artificial time series, it is possible to obtain amplitude and phase vs. time diagrams that closely resemble that of V1821 Cygni (Figure A.8). This result does not mean that these three close frequencies are *real* pulsation frequencies of the star. As pointed above, some of them could be aliases of a real frequency, and one (f_7) could be an artifact of the window function, because it is not noticeable in the spectrum of the whole 2001+2002 time series (Figure A.6). Some clarification on the aliasing of the f_5 and f_6 frequencies might be obtained with multi-site

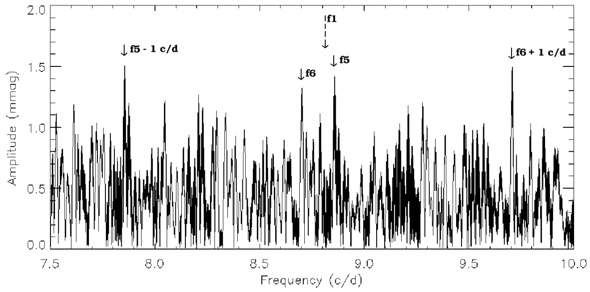

FIGURE A.6— The region around the cleaned frequency f_1, of the time series previously cleaned for the frequencies f_2-f_4.

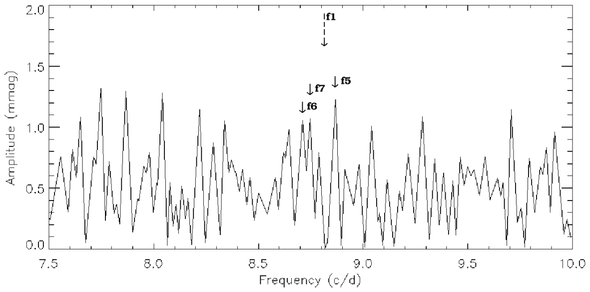

FIGURE A.7— Same as Figure A.6, but for the time interval used in the moving fit analysis.

photometry of this star. The importance of this result resides in that the amplitude and phase variability of the frequency f_1 in V1821 Cygni needs at least two close frequencies to be explained, and indeed it can be reasonably well modelled by three close frequencies that appear in the power spectra. Thus, it is not safe to conclude that the variations of f_1 are intrinsic to the mode, even if a phase change is seen without an apparent connection to an amplitude minimum. In this particular case, both explanations should be kept in mind, until more and/or better data on this star are available.

A.3.5 Comparison with other δ Scuti stars in the field

A similar study was carried for two another δ Scuties in the field, HD 225708 and STARE 8663. The first star has a f_1 frequency with a similar amplitude as V1821 Cygni, and the detected low amplitude frequencies are below a 2 mmag level. Using the same parameters of the *moving fit*, we obtained a behavior compatible with no amplitude nor phase variations (Figure A.9). This result argues once again against an instrumental origin for the phase and amplitude

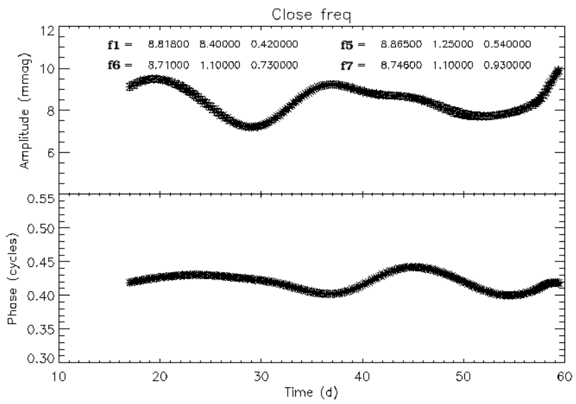

FIGURE A.8— Amplitude and phase variations of a model light curve, built with the three low amplitude peaks distinguishable in Figure A.7, and f_1, and manually adjusting the phases. Note how the first part of the curves resemble Figure A.5.

variations described in the previous sections. For the second star, STARE 8663, in section A.3.3 we had observed amplitude and phase variability of its main pulsation mode. The *moving fit* analysis in this star again shows evidence for this variability (Figure A.10), but in this case a change in phase seems to happen when the amplitude reaches a minimum. This behavior might easily be explained with the presence of two close frequencies in this star.

A.4 Summary and conclusions

A photometric study of the δ Scuti V1821 Cygni, performed with the STARE telescope, has provided a clear detection of 4 frequencies in this star. The frequencies f_1 and f_2 are close to the Zhou, Liu, & Du (2001) values, but f_1 is noticeably lower in our data set, probably due to a faint complex structure of at least two close frequencies to it (f_5 and f_6). We can not discriminate between f_5 and f_6 and their daily aliases due to the single-site nature of our observations. These frequencies close to f_1 can provide an (at least qualitative) explanation for the amplitude and phase variability of f_1. We performed an attempt to discriminate between this explanation and other possible description, namely intrinsical variation of the pulsation mode f_1. This second description could mean that f_5, f_6 and f_7 are just artifacts in the amplitude spectra that appear as a consequence of the variability of f_1, and don't represent real pulsation modes of the star. The moving fit analysis performed showed that we can not reject any of these explanations, even if a change in phase is seen uncorrelated

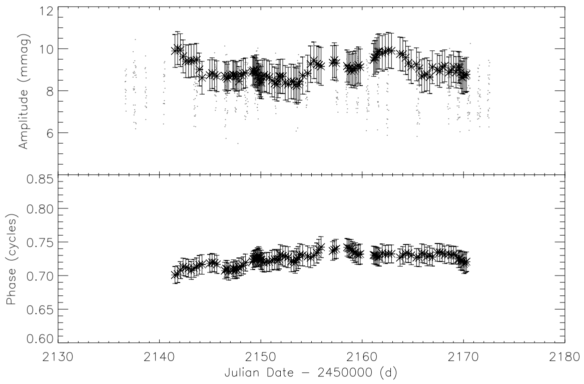

FIGURE A.9— Same as Figure A.5 for another δ Scuti in the same field (HD 225708), showing no evidence for amplitude nor phase variations.

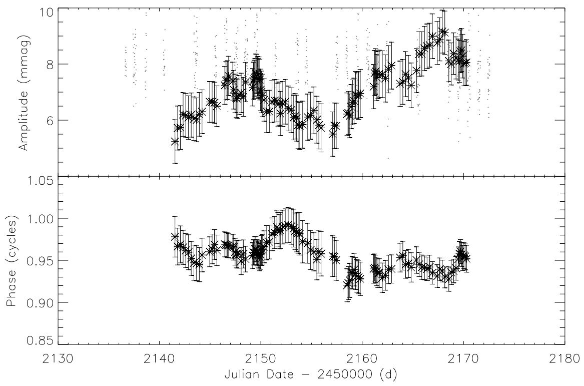

FIGURE A.10— Same as Figure A.5 for another δ Scuti in the same field (STARE 8663), showing evidence for amplitude and phase variations. In this case, a change in phase happens when the amplitude reaches a minimum.

with a minimum in amplitude. This is due to the presence of more than one close frequency. While the frequency f_3 is first reported in this work, the lower amplitude f_4 was detected in the discovery of this star by Delgado et al. (1984), but not seen in the better quality Zhou, Liu, & Du (2001) data set.

Putting all this together, we can conclude that V1821 Cygni suffers significant amplitude and frequency variability on at least two of its pulsation modes (f_1 and f_4).

Finally, an analysis of 5 newly discovered pulsators in the same field of view as V1821 Cygni, resulted in the detection of a δ Sct with at least amplitude variability (STARE 8663). Another one of these pulsators, HD 225708, seems to be consistent with no amplitude nor frequency variations of its highest amplitude pulsation mode, down to the precision of the observations. Frequencies, amplitudes and phases for all these stars have been obtained.

B

STARE observations for COROT[1]

This second Appendix summarizes the detection of new variable stars in the celestial regions accessible to the COROT telescope. The wide field of view of the STARE telescope allows a fast identification of variable stars. Some of these might be chosen to serve as secondary targets on the asteroseismic COROT CCDs, for its 150 d long runs, after the launch of the space mission expected for June 2006.

B.1 Introduction

THE european COROT (COnvection, ROtation and planetary Transits) space mission (Baglin et al. 2002) consists of a telescope with a pupil surface of 590 cm^2 (diameter ∼25 cm), planned for launch in June 2006, that will stare for long runs (∼150 days) at several pointings in two celestial regions: the galactic anti-center ($\alpha = 6^h50^m, \delta = 0°$) and the galactic center ($\alpha = 18^h50^m, \delta = 0°$). Each of the accessible zones for the telescope has a radius of 10°. Two CCD's with a total field of view of $\sim 2.8° \times 1.4°$ will be devoted to look at no more than 10 bright stars during each run, with magnitudes 5.7<V<9.5, with the aim of detecting solar-like oscillations, but also to study the pulsational behavior of different types of stars at several evolutionary stages. In this *asteroseismic* mode, one target is labelled as *primary*, while the other ∼9 are considered as *secondary* targets, for scheduling and planning

[1]Several of the results presented in this Appendix have been published in Alonso et al. (2003b), Poretti et al. (2003), Martín et al. (2004) and Poretti et al. (2005). I summarize in this appendix the STARE contribution to those works.

purposes. These objects are observed in a defocussed mode, to increase the number of collected photons, to minimize the intra-pixel and inter-pixels sensivity variations of the detectors, and thus to achieve noise levels at the order of 10^{-6} in flux after 5 days of observations. At least one δScuti star will be a primary target.

Two different CCD's will be situated after a prism, and photometry of at least ∼30000 stars (throughout the whole mission, a maximum of 12000 stars will be observed at each long run) with low resolution color information will be used for the search of transiting objects, aimed at the detection of the first telluric planets. In this *exoplanetary* mode, the magnitude range of the surveyed stars will be 11<V<16, (only those with V<15 will have color information) and the specifications are to achieve 10^{-4} noise levels for a 15.5 magnitude star after an integration time of 1 hour.

B.1.1 Motivation

The wide field of view of the STARE telescope implies that the objects accessible at all the possible orientations of the COROT CCDs around a primary target are within its reach. Thus, it was used as a tool to detect new variable objects of interest to serve as secondary targets around the primary targets on the asteroseismic CCDs. Two different philosophies were adopted in the center and anti-center directions, as the necessities were not the same in both cases.

B.2 Observations: Anti-center

In the case of the targets located at the anti-center direction, the request was to find suitable secondary targets around already fixed potential primary targets. The goal was to map the lower part of the instability strip, and the ideal COROT targets should be located between the ZAMS (Zero-Age Main Sequence) and the TAMS (Terminal-Age Main Sequence). The reason is that evolved stars show too dense frequency spectra that are very difficult to model. A total of six nights were spent to observe the fields around six primary targets: HD 43587 (16 March 2002), HD 45067 (17 March 2002), HD 49933+49434 (18 March 2002), HD 55057 (19 and 22 March 2002) and HD 43318 (18 Nov 2003). The observed fields and their position in the sky are plotted in Figure B.1. As the magnitude limit for the fainter stars in the asteroseismic CCDs is V=9.5, we reduced the integration time to 25 s, and we used the STARE "V" filter (see Chapter 2), for which the quantum efficiency of the CCD is lower. With this configuration, a total of 500-600 stars in each STARE field have V<9.5, and 500-700 images were obtained in each field.

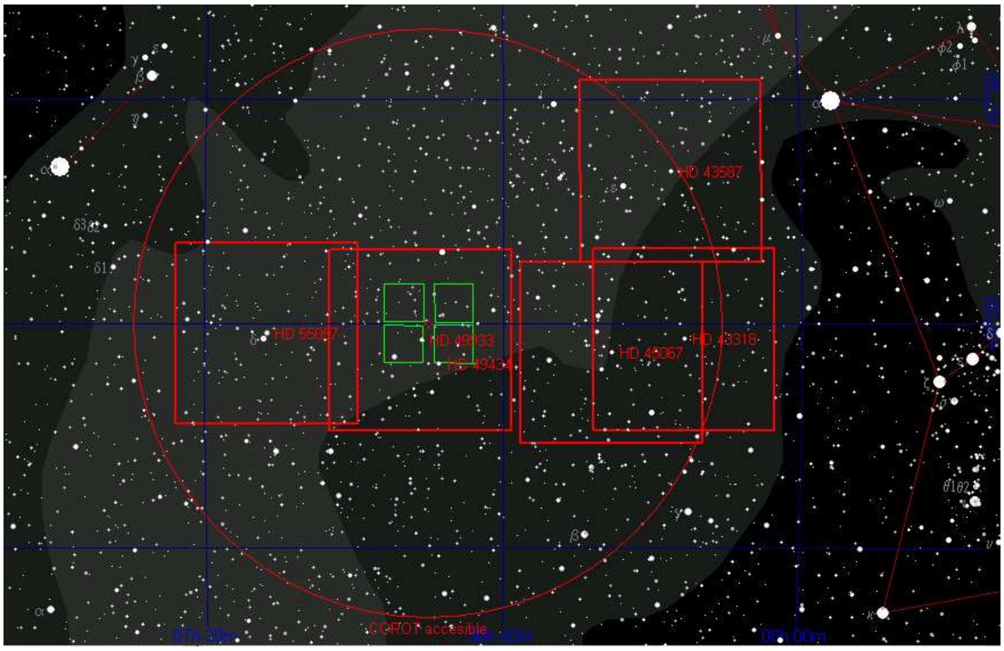

FIGURE B.1— Location of the COROT primary targets and the 5 STARE pointings in the anti-center direction. In green, the size of the COROT CCDs is plotted; the two CCDs on the left side will be devoted to asteroseismology, while the two on the right are used for exoplanet transit search. The circle marks the accessible sky for COROT on this region.

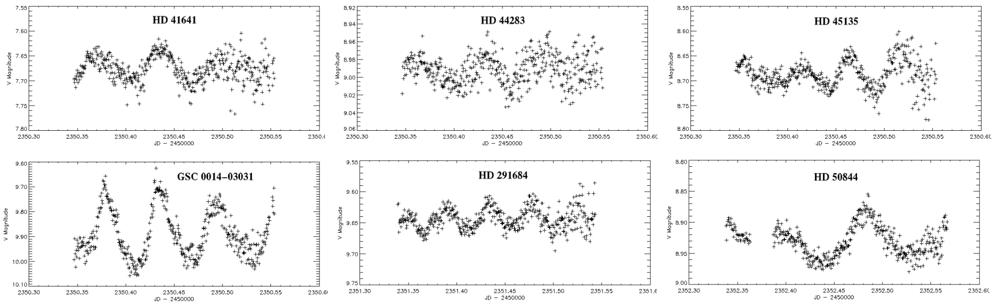

FIGURE B.2— Light curves of six stars found to be variable in the STARE images. Magnitude scale is instrumental V.

B.2.1 Results

A total of 38 clear variables have been discovered with the STARE observations in this exercise. They are listed in Table B.1. 11 of them meet all the conditions to be observed as secondary targets on the asteroseismic CCDs, and the rest are fainter than the V<9.5 limit (18) or too far from the primary targets (9). Possible future changes in the primary target choices might include some of the stars located too far from the current primary targets, and thus these have been included in the Table. A sample plot of six of the variable stars is given on Figure B.2.

B.3 Observations: Center

The observations in the center direction were conducted to try to detect new variables in the open cluster NGC 6633. If a star belongs to a known cluster, then parameters such as the age and the metallicity are better constrained, which might help in the inversion of the pulsation frequencies to study the interior of those stars. Several studies of δScuti stars have been preformed on the basis of this idea (e.g. Belmonte et al. 1994). A multi-site campaign coordinated by S. Martin in summer 2002 was intended to detect new variable stars and to confirm several doubtful candidates. The STARE telescope was used on the nights of July 13, 15 and 16 2002. The parameters for the observations were identical as those performed in the anti-center direction.

B.3.1 Results

A total of 7 stars brighter than V=9.5 and another 7 fainter stars were detected in the STARE observations. These are summarized in Table B.2; The stars

TABLE B.1— New variable stars discovered with STARE in the Anti-center direction.

Star	V[a]	Sp.	Ampl (mmag)[b]	Type and remarks[c]
		Potential secondary targets		
HD 43021	7.84	A0	45	δ Sct
HD 44283	9.36	F	<50	δ Sct
HD 44562	8.63	A3	20	δ Sct
HD 44872	8.40	A3	20	δ Sct
HD 45196	8.33		14	Geom.
HD 48719	9.19	A5	30	δ Sct
HD 50844	9.10	A2	80	δ Sct
HD 50870	8.88	F0	70	δ Sct
HD 55113	8.70	K5	~20	Red var.
HD 291684	9.83	A0	60	δ Sct
HD 293340	9.53	F0	40	δ Sct
		Too faint to be secondary targets		
HD 54780	10.17	A0	~220	E
HD 289732	10.8	B8	105	β Cep ?
HD 291635	10.4	B	400	E
HD 291791	10.5	F0	~80	δ Sct
HD 292402	10.10	F0	120	δ Sct
HD 292525	10.36	F2	150	δ Sct
HD 292864	10.45	A2	75	δ Sct
HD 292930	10.33	F0V	40	δ Sct
HD 292971	10.12	F2V	100	δ Sct
GSC 00142-00022	10.3		65	δ Sct
GSC 00143-00139	10.8		~120	HADS or E
GSC 00143-01718	10.3		~200	HADS or E
GSC 00144-03031	10.1		>400	HADS
GSC 04784-00830	11.5		600	E
GSC 04814-00028	11.1		~100	Red var.
		Too far to be secondary targets		
HD 41641	7.86	A5	70	δ Sct
HD 42561	8.89	A2	60	δ Sct
HD 45135	8.82	A2	100	δ Sct
HD 48866	9.0	A0	~300	E
HD 52239	9.06	A5	~30	δ Sct
HD 54331	7.94	A0	~40	Long per.
HD 292962	9.89	F0V	200	δ Sct
HD 293031	10.48	F8III	>200	E candidate
HD 293622	9.98	A	35	δ Sct

[a] Values reported in the SIMBAD and/or GAUDI (Solano et al. 2005) databases; in particular for GSC stars see GSC version 1.2

[b] Peak–to–peak amplitudes are in the V STARE instrumental system

[c]HADS stands for High Amplitude δ Sct star, E for eclipsing binary

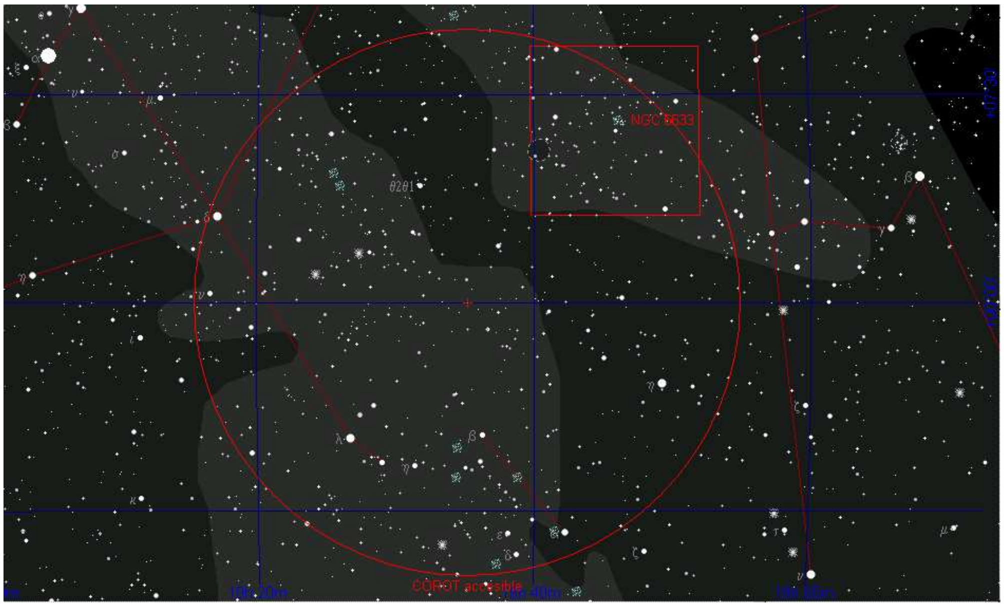

FIGURE B.3— Location of the NGC 6633 cluster in the COROT observable sky at the galactic center direction.

TABLE B.2— Variable stars detected with STARE in the center direction.

Star	Ampl (mmag)	Type and remarks
HD 169577	20	γ Dor discovered by Martín & Rodríguez (2002)
HD 169842	$\sim$20	γ Dor candidate; member of the cluster (Catalano & Renson 1998)
HD 169959	$\sim$20	Ap variability ?
BD+06 3737	70	δ Scuti
HD 169597	$<$20	Low amplitude
HD 170412	$<$20	Low amplitude, long period ($>$0.2d)
HD 170451	$\sim$300	W UMa (Koppelman, West, & Price 2002)
		Too faint to be secondary targets
NGC 6633 275	$>$70	γ Dor discovered by Martín & Rodríguez (2002)
BD+06 7348	20	δ Scuti?
NGC 6633 89	40	δ Scuti
BD+06 3803	30	δ Scuti
BD+06 3802	100	Candidate eclipsing binary
NGC 6633 14	40	Possible non-member
NGC 6633 108	30	Possible non-member

HD 169577 and NGC 6633 275 had been observed by Martín & Rodríguez (2002) and were suspected γ Doradus pulsators. Two new variables, HD 169842 and HD 169959, both with frequencies in the γ Doradus regime, are thought to be part of the cluster (Catalano & Renson 1998), and four other variable stars were identified in the STARE light curves. One is a W UMa eclipsing system, first detected by Koppelman, West, & Price (2002), and the other three had not been previously observed to vary.

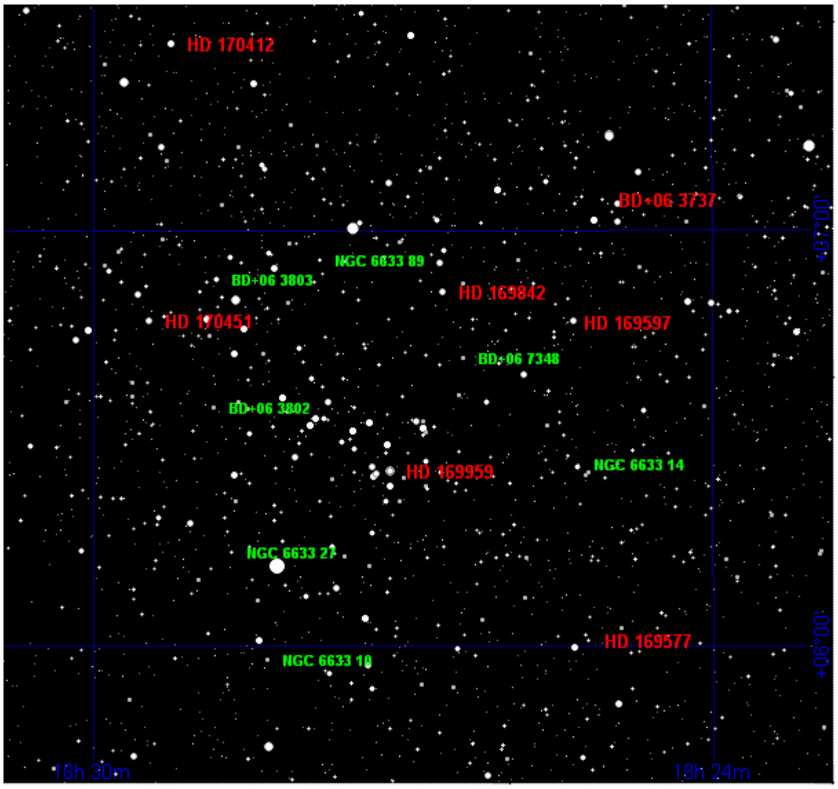

FIGURE B.4— Location of the identified variable stars in the NGC 6633 region. Red labels are for stars brighter than V = 9.5, while green labels are for fainter stars.

Bibliography

Alard, C. & Lupton, R. H. 1998, ApJ, 503, 325

Alard, C. 2000, A&AS, 144, 363

Alcock, C. et al. 1993, Nature, 365, 621

Alencar, S. H. P., & Batalha, C. 2002, ApJ, 571, 378

Alonso, R., Belmonte, J. A., & Brown, T. M. 2003, AP&SS, 284, 13

Alonso, R., Belmonte, J. A., Brown, T. M., Garrido, R., & Michel, E. 2003, in Asteroseismology Across the H-R diagram, proceedings of the Asteroseismology Workshop, ed. M. J. Thompson, M. S. Cunha, & M. J. P. F. G. Monteiro (Porto: Kluwer Academic Publishers), 284, 295

Alonso, R., et al. 2004, ApJ, 613, L153

Alvarez, M., et al. 1998, A&A, 340, 149

Arentoft, T., et al. 2001, A&A, 374, 1056

Baglin, A., et al. 2002, in First Eddington Workshop on Stellar Structure and Habitable Planet Finding, ed. F. Favata, I. W. Roxburgh, & D. Galadí-Enríquez (Noordwijk: ESA Publications Division), 485, 17

Baraffe, I., Chabrier, G., Allard, F., & Hauschildt, P. H. 2002, A&A, 382, 563

Baraffe, I., Chabrier, G., Barman, T. S., Allard, F., & Hauschildt, P. H. 2003, A&A, 402, 701

Baranne, A., et al. 1996, A&AS, 119, 373

Bate, M. R., Lubow, S. H., Ogilvie, G. I., & Miller, K. A. 2003, MNRAS, 341, 213

Belmonte, J. A., et al. 1994, A&A, 283, 121

Benedict, G. F., et al. 2002, ApJ, 581, L115

Bennett, D. P., & Rhie, S. H. 1996, ApJ, 472, 660

Bennett, D. P., & Rhie, S. H. 2002, ApJ, 574, 985

Bessell, M. S., & Brett, J. M. 1988, PASP, 100, 1134

Betz, A. L., Sutton, E. C., McLaren, R. A., & McAlary, C. W. 1977, in Proc. of the Symposium on Planetary Atmospheres, ed. A.V. Jones (Ottawa: Royal Soc. of Canada), 29

Bodenheimer, P., & Pollack, J. B. 1986, Icarus, 67, 391

Bodenheimer, P., Hubickyj, O., & Lissauer, J. J. 2000, Icarus, 143, 2

Bodenheimer, P., Lin, D. N. C., & Mardling, R. A. 2001, ApJ, 548, 466

Bodenheimer, P., Laughlin, G., & Lin, D. N. C. 2003, ApJ, 592, 555

Bond, I. A., et al. 2001, MNRAS, 327, 868

Bond, I. A., et al. 2004, ApJ, 606, L155

Boss, A. P. 1997, Science, 276, 1836

Bouchy, F., Pont, F., Santos, N. C., Melo, C., Mayor, M., Queloz, D., & Udry, S. 2004, A&A, 421, L13

Bougher, S. W., Alexander, M. J., & Mayr, H. G. 1997, in: Venus II, ed. S. W. Bougher, D. M. Hunten, & R. J. Phillips (Tucson: Univ. of Arizona Press), 259

Breger, M. 1981, ApJ, 249, 666

Breger, M., & Bischof, K. M. 2002, A&A, 385, 537

Brown, T. M., Kotak, R., Horner, S. D., Kennelly, E. J., Korzennik, S., Nisenson, P., & Noyes, R. W. 1998, ApJ, 494, L85

Brown, T. M., Kotak, R., Horner, S. D., Kennelly, E. J., Korzennik, S., Nisenson, P., & Noyes, R. W. 1998, ApJS, 117, 563

Brown, T. M, & Kolinski, D., *http:\\ www.hao.ucar.edu\public\research\stare\stare.html*

Brown, T. M., Charbonneau, D., Gilliland, R. L., Noyes, R.W., & Burrows, A. 2001, ApJ, 552, 699

Brown, T. M. 2001, ApJ, 553, 1006

Brown, T. M. 2003, ApJ, 593, L125

Burrows, A., et al. 1997, ApJ, 491, 856

Burrows, A., Sudarsky, D., & Hubbard, W. B. 2003, ApJ, 594, 545

Burrows, A., Hubeny, I., Hubbard, W. B., Sudarsky, D., & Fortney, J. J. 2004, ApJ, 610, L53

Burrows, A., Hubeny, I., & Sudarsky, D., 2005, submitted to ApJ, astro-ph/0503522

Butler, R. P., Vogt, S. S., Marcy, G. W., Fischer, D. A., Wright, J. T., Henry, G. W., Laughlin, G., & Lissauer, J. J. 2004, ApJ, 617, 580

Cameron, A. G. W. 1978, Moon Planets, 18, 5

Catalano, F. A., & Renson, P. 1998, A&AS, 127, 421

Chabrier, G., Baraffe, I., Allard, F., & Hauschildt, P. H. 2000, ApJ, 542, 464

Chabrier, G., Barman, T., Baraffe, I., Allard, F., & Hauschildt, P. H. 2004, ApJ, 603, L53

Charbonneau, D., Noyes, R. W., Korzennik, S. G., Nisenson, P., Jha, S., Vogt, S. S. & Kibrick, R. I. 1999, ApJ, 522, L145

Charbonneau, D., Brown, T. M., Latham, D. W., & Mayor, M. 2000, ApJ, 529, L45

Charbonneau, D., Brown, T. M., Noyes, R. W., & Gilliland, R. L. 2002, ApJ, 568, 377

Charbonneau, D., Brown, T. M., Gilliland, R. L., & Noyes, R. W. 2003, in Stars as Suns: Activity, Evolution and Planets, IAUS 219, ed. A. K. Dupree (San Francisco: ASP), 152

Charbonneau, D., et al. 2005, ApJ, 626, 523

Chauvin, G., Lagrange, A.-M., Dumas, C., Zuckerman, B., Mouillet, D., Song, I., Beuzit, J.-L., & Lowrance, P. 2004, A&A, 425, L29

Chauvin, G., Lagrange, A.-M., Dumas, C., Zuckerman, B., Mouillet, D., Song, I., Beuzit, J.-L., & Lowrance, P. 2005, A&A, accepted, astro-ph/0504659

Chauvin, G., et al. 2005, A&A, accepted, astro-ph/0504658

Christensen-Dalsgaard, J. 1999, Ap&SS, 261, 1

Clancy, R. T. & Muhleman, D. O. 1985, Icarus, 64, 157

Clancy, R. T., Sandor, B. J., & Moriarty-Schieven, G. H. 2003, Icarus, 161, 1

Claret, A. 2000, A&A, 363, 1081

Cody, A. M., & Sasselov, D. D. 2002, ApJ, 569, 451

Collier Cameron, A., Horne, K., Penny, A., & Leigh, C. 2002, MNRAS, 330, 187

Cox A.N. 2000, Allen's Astrophysical Quantities, 4th edition, Springer

Creevey, O. et al. 2005, ApJ, 625, L127

Cumming, A., Marcy, G. W., & Butler, R. P. 1999, ApJ, 526, 890

Deeg, H. J., Garrido, R., & Claret, A. 2001, New Astronomy, 6, 51

Deeg, H. J., & Doyle, L. R. 2001, in Third Workshop on Photometry, 85

Delfosse, X., Forveille, T., Mayor, M., Perrier, C., Naef, D., & Queloz, D. 1998, A&A, 338, L67

Delgado, A. J., García-Pelayo, J. M., Garrido, R., Vidal, S., & Alfaro, E. J. 1984, A&ASS, 58, 447

Deming, D., & Mumma, M. J. 1983, Icarus, 55, 356

Deming, D., Seager, S., Richardson, L. J., & Harrington, J. 2005, Nature, 434, 740

Drake, A. J. 2003, ApJ, 589, 1020

Dunham, E. W, Mandushev, G. I., Taylor, B. W., & Oetiker, B. 2004, PASP, 116, 1072

Eaton, J. A. 1993, ApJ, 404, 305

Everett, M. E., & Howell, S. B. 2001, PASP, 113, 1428

Fischer, D. A., Marcy, G. W., Butler, R., P., Vogt, S. S., & Apps, K. 1998, PASP, 111, 50

Fortney, J. J., Sudarsky, D., Hubeny, I., Cooper, C. S., Hubbard, W. B., Burrows, A., & Lunine, J. I. 2003, ApJ, 589, 615

Fridlund, M., Henning, T., & Lacoste, H. 2003, Towards Other Earths: DARWIN/TPF and the Search for Extrasolar Terrestrial Planets, ESA SP-539, ed. M. Fridlund, & T. Henning (Noordwijk: ESA Publications Division)

Gaudi, B. S., Seager, S., & Mallén-Ornelas, G. 2005, ApJ, 623, 472

Gierasch, P. J. et al. in Venus II, eds. S. W. Bougher, D. M. Hunten, & R. J. Phillips (Tucson: Univ. of Arizona Press), 459

Goldreich, P., & Soter, S. 1966, Icarus, 5, 375

Goldreich, P., & Tremaine, S. 1980, ApJ, 241, 425

Goldstein, J. J. 1989, PhD Thesis, Univ. of Pennsylvania, Philadelphia

Goldstein, J. J., Mumma, M. J., Kostiuk, T., Deming, D., Espenak, F., & Zipoy, D. 1991, Icarus, 94, 45

Gould, A. & Loeb, A. 1992, ApJ, 396, L104

Gray, D. F. 1997, Nature, 385, 795

Gray, D. F. 1998, Nature, 391, 153

Guillot, T., Burrows, A., Hubbard, W. B., Lunine, J. L., & Saumon, D. 1996, ApJ, 459, L35

Guillot, T. & Showman, A. P. 2002, A&A, 385, 166

Halbwachs, J. L., Mayor, M., Udry, S., & Arenou, F. 2003, A&A, 397, 159

Handler, G., Pamyatnykh, A. A., Zima, W., Sullivan, D. J., Audard, N., & Nitta, A. 1998, MNRAS, 295, 377

Handler, G., et al. 2000, MNRAS, 318, 511

Hansen, B. M. S. 2002, in ASP Conf. Ser. 263, Stellar Collisions, Mergers and their Consequences, ed. M. M. Shara (San Francisco: ASP), 22

Henry, G. W., Marcy, G. W., Butler, R. P., & Vogt, S. S. 2000, ApJ, 529, L41

Horne, K., in First Eddington workshop on Stellar Structure and Habitable Planet Finding, ed. F. Favata, I. W. Roxburgh, & D. Galadí-Enríquez (Noodwijk: ESA Publications Division), 485, 137

Israelian, G. 2003, in Stars as Suns: Activity, Evolution and Planets, IAUS 219, ed. A. K. Dupree (San Francisco: ASP), 57

Jha, S., Charbonneau, D., Garnavich, P. M., Sullivan, D. J., Sullivan, T., Brown, T. M., & Tonry, J. L. 2000, ApJ, 540, L45

Konacki, M., Maciejewski, A. J., & Wolszczan, A. 1999, ApJ, 513, 471

Konacki, M., Torres, G., Jha, S., & Sasselov, D. 2003, Nature, 421, 507

Konacki, M., & Wolszczan, A. 2003, ApJ, 591, L147

Konacki, M., Torres, G., Sasselov, D. D., & Jha, S. 2003, ApJ, 597, 1076

Konacki, M. et al. 2004, ApJ, 609, L37

Konacki, M., Torres, G., Sasselov, D. D., & Jha, S. 2005, ApJ, 624, 372

Koppelman, M. D., West, D., & Price, A. 2002, IBVS, 5327

Kovács, G., Zucher, S., & Mazeh, T. 2002, A&A, 391, 369

Kubas, D. et al. 2005, A&A, accepted, astro-ph/0502018

Kürster, M., et al. 2003, A&A, 403, 1077

Landolt, A. U. 1992, AJ, 104, 340

Latham, D. W. 1992, in Complementary Approaches to Double and Multiple Star Research, IAU Colloquium 135, ASP Conference Series 32, ed. H. A. McAlister, & W. I. Hartkopf (San Francisco: ASP), 110

Leigh, C., Collier Cameron, A., Udry, S., Donati, J., Horne, K., James, D., & Penny, A. 2003, MNRAS, 346, L16

Lellouch, E., Clancy, T., Crisp, D., Kliore, A. J., Ittov, I., & Bougher, S. W. 1997, in Venus II, ed. S. W. Bougher, D. M. Hunten, R. J. Phillips (Tucson: Univ. of Arizona Press), 295

Levenberg, K. 1944, Q. Appl. Math. 2, 164

Livio, M., Pringle, J. E. & Saffer, R. A. 1992, MNRAS, 257, 15

Lissauer, J. J. 2004, in Extrasolar planets: Today and Tomorrow, ASP Conf. Series 321, ed. J.-P. Beaulieu, A. Lecavelier des Etangs, & C. Terquem (San Francisco: ASP), 271

Lorimer, D. R. 2001, Living Reviews in Relativity, 4, 5

Lorimer, D. R., & Kramer, M. 2005, Handbook of Pulsar Astronomy (Cambridge: Cambridge University Press)

Loumos, G. L., & Deeming, T. J. 1978, Ap&SS, 56, 2, 285

Mandushev, G., et al. 2005, ApJ, 621, 1061

Mao, S., & Paczyński, B. 1991, ApJ, 374, L37

Marcy, G. W., Butler, R. P., Williams, E., Bildsten, L., Graham, J. R., Ghez, A. M, & Jernigan, J. G. 1997, ApJ, 481, 926

Marcy, G. W., Butler, R. P., Vogt, S. S., Fischer, D. A., Lissauer, J. J. 1998, ApJ, 505, L14

Marcy, G. W., Butler, R. P., Fischer, D. A., & Vogt, S. S. 2003, in Scientific Frontiers in Research on Extrasolar Planets, ASP Conf. Series 294, ed. D. Deming, & S. Seager (San Francisco: ASP), 1

Marquardt, D. W. 1963, SIAM J. Appl. Math. 11, 431

Martín, S., & Rodríguez, E. 2002, in First Eddington Workshop on Stellar Structure and Habitable Planet Finding, ed. F. Favata, I. W. Roxburgh, & D. Galadí-Enríquez (Noordwijk: ESA Publications Division), 485, 303

Martín, S., et al. 2004, in Second Eddington Workshop on Stellar Structure and Habitable Planet Finding, ed. F. Favata, S. Aigrain (Noordwijk: ESA Publications Division), 538, 349

Martínez Pillet, V., et al. 1999, in High Resolution Solar Physics: Theory, Observations, and Techniques, ASP Conf. Series 183, ed. T. R. Rimmele, K. S. Balasubramaniam, & R. R. Radick (San Francisco: ASP), 264

Mayor, M., & Queloz, D. 1995, Nature, 378, 355

Mayor, M., et al. 2003, The Messenger, 114, 20

Mazeh, T., et al. 2000, ApJ, 532, L55

McArthur, B.E., et al. 2004, ApJ, 614, L81

Miller, M. C., & Hamilton, D. P. 2001, ApJ, 550, 863

Myers, R. M. et al. 2003, SPIE, 4839, 647

Newman, M. G., Schubert, G., Kliore, A. J., & Patel, I. R. 1984, J. Atmos. Sci., 41, 1901

O'Donovan, F. T., Charbonneau, D., & Kotredes, L. 2004, in The Search For Other Worlds, AIP Conf. Proc. 713, 169

Packham, C. et al. 2003, MNRAS, 345, 395

Penny, A. J., & Leese, R. 1996, in Astronomical Data Analysis Software and Systems V, ASP Conf. Series 101, ed. G. H. Jacoby & J. Barnes, 29

Pepe, F., et al. 2002, The ESO Messenger, 110, 9

Pepe, F., Mayor, M., Galland, F., Naef, D., Queloz, D., Santos, N. C., Udry, S., & Burnet, M. 2002, A&A, 388, 632

Phinney, E. S., & Hansen, B. M. S. 1993, in ASP Conf. Ser. 36, Planets around Pulsars, ed. J. A. Phillips, S. E. Thorsett, & S. R. Kulkarni (San Francisco: ASP), 371

Podsiadlowski, P., Pringle, J. E. & Rees, M. J. 1991, Nature, 352, 783

Pont, F., Bouchy, F., Queloz, D., Santos, N. C., Melo, C., Mayor, M., & Udry, S. 2004, A&A, 426, L15

Pont, F., Melo, C. H. F., Bouchy, F., Udry, S., Queloz, D., Mayor, M., & Santos, N. C. 2005, A&A, 433, L21

Poretti, E., et al. 2003, A&A, 406, 203

Poretti, E., et al. 2005, AJ, 129, 2461

Press, W. H., Flannery, B. P., Teukolsky, S. A., & Vetterling, W. T. 1988, in Numerical Recipes in C, The Art of Scientific Computing, (Cambridge: Cambridge University Press), 534

Queloz, D., Eggenberger, A., Mayor, M., Perrier, C., Beuzit, J. L., Naef, D., Sivan, J. P., & Udry, S. 2000, A&A, 359, L13

Queloz, D., et al. 2001, A&A, 379, 279

Rhie, S. H. 2001, in Gravitational Lensing: Recent Progress and Future Goals, ASP Conf. Proc. 237, ed. T. G. Brainerd, & C. S. Kochanek (San Francisco: ASP), 267

Saar, S. H., Hatzes, A., Cochran, W., Paulson, D. 2003, in The Future of Cool-Star Astrophysics: 12th Cambridge Workshop on Cool Stars, Stellar Systems, and the Sun, ed. A. Brown, G. M. Harper, & T. R. Ayres (Boulder: University of Colorado), 694

Santos, N. C., Israelian, G., Mayor, M., Rebolo, R., & Udry, S. 2003, A&A, 398, 363

Santos, N. C., Israelian, G., & Mayor, M. 2004, A&A, 415, 1153

Santos, N. C., et al. 2004, A&A, 426, L19

Sartoretti, P., & Schneider, J. 1999, A&AS, 134, 553

Schneider, G., et al. , AAS, 205, 11 14

Seager, S. 1999, Ph.D. Thesis, Harvard University

Seager, S., & Sasselov, D. D. 2000, ApJ, 537, 916

Seager, S., Whitney, B. A., & Sasselov, D. D. 2000, ApJ, 540, 504

Seager, S., & Mallén-Ornelas, G. 2003, ApJ, 585, 1038

Shobbrook, R. R., Herbison-Evans, D., Johnston, I. D., & Lomb, N. R. 1969, MNRAS, 145, 131

Showman, A., & Guillot, T. 2002, A&A, 385, 166

Simkin, S. M. 1974, A&A, 31, 129

Sirko, E., & Paczyński, B. 2003, ApJ, 592, 1217

Smith, G. R., & Hunten, D. M. 1990, Rev. Geophys., 28, 117

Solano, E. et al. 2005, AJ, 129, 547

Sozzetti, A., et al. 2004, ApJ, 616, L167

Sperl, M. 1998, Master's thesis, University of Vienna

Stetson, P. B. 1987, PASP, 99, 191

Stetson, P. B., & Harris, W. E. 1988, AJ, 96, 909

Stetson, P. B. 1992, JRASC, 86, 71

Stetson, P. B. 1993, in IAU Coll. 136, Stellar Photometry- Current Techniques and Future Developments, ed. C. J. Butler, & I. Elliot (Cambridge: Cambridge University Press), 291

Stevens, I. R., Rees, M. J., & Podsiadlowski, P. 1992, MNRAS, 254, 19

Strom, S. E., Edwards, S., & Skrutskie, M. F. 1993, in Protostars and Planets III, ed. E. H. Levy, & J. I. Lunine (Tucson: Univ. Arizona Press), 837

Struve, O. 1952, The Observatory, 72, 199

Sudarsky, D., Burrows, A., & Pinto, P. 2000, ApJ, 538, 885

Sudarsky, D., Burrows, A., & Hubeny, I. 2003, ApJ, 588, 1121

Taylor, F. W., et al. 1980, J. Geophys. Res. 85, 7963

Thommes, E. W., & Lissauer, J. J. 2005, in Astrophysics of Life: Proceedings of the Space Telescope Science Institute Symposium, STScI symposium series 16, ed. M. Livio, I. N. Reid, & W. B. Sparks (Cambridge: Cambridge University Press) 41

Tody, D. C. 1986, in Proc. SPIE 627, Instrumentation in Astronomy VI, ed. D. L. Crawford, 733

Torres, G., Konacki, M., Sasselov, D. D., & Jha, S. 2004a, ApJ, 609, 1071

Torres, G., Konacki, M., Sasselov, D. D., & Jha, S. 2004b, ApJ, 614, 979

Udalski, A., et al. 2002, Acta Astronomica, 52, 1

Udalski, A., et al. 2002, Acta Astronomica, 52, 115

Udalski, A., Szewczyk, O., Zebrun, K., Pietrzynski, G., Szymanski, M., Kubiak, M., Soszynski, I., & Wyrzykowski, L. 2002, Acta Astronomica, 52, 317

Udalski, A., Pietrzynski, G., Szymanski, M., Kubiak, M., Zebrun, K., Soszynski, I., Szewczyk, O., & Wyrzykowski, L. 2003, Acta Astronomica, 53, 133

Udalski, A. 2003, Acta Astronomica, 53, 291

Udalski, A., Szymanski, M. K., Kubiak, M., Pietrzynski, G., Soszynski, I., Zebrun, K., Szewczyk, O., & Wyrzykowski, L. 2004, Acta Astronomica, 54, 313

Udry, S., Mayor, M., Naef, D., Pepe, F., Queloz, D., Santos, N. C., & Burnet, M. 2002, A&A, 390, 267

Udry, S., Mayor, M., Santos, N. C., 2003, A&A, 407, 369

van Straten, W., Bailes, M., Britton, M., Kulkarni, S. R., Anderson, S. B., Manchester, R. N., & Sarkissian, J. 2001, Nature, 412, 158

Vidal-Madjar, A., Lecavelier des Etangs, A., Desert, J. M., Ballester, G., Ferlet, R., Hebrard, G., & Mayor, M. 2003, Nature, 422, 143

Vidal-Madjar, A., et al. 2004, ApJ, 604, L69

Vogt, S.S. et al. 1994, in Proc. SPIE 2198,Instrumentation in Astronomy VIII, ed. D. L. Crawford, & E. R. Craine, 362

Watson, A. J., Donahue, T. M., & Walker, J. C. 1981, Icarus, 48, 150

Ward, W. R. 1986, Icarus, 67, 164

Wolszczan, A., & Frail, D. A., 1992, Nature, 355, 145

Wolszczan, A. 1994, Science, 264, 538

Wolszczan, A., Hoffman, I. M., Konacki, M., Anderson, S. B., Xilouris, K. M. 2000, ApJ, 540, L41

Wolszczan, A., Konacki, M. 2005, in Planet Formation and Detection, 2005 Winter Conference on Astrophysics, Aspen, www.astro.northwestern.edu/AspenW05/Talks/Wolszczan.pdf

Wuchterl, G., Guillot, T., & Lissauer, J. J. 2000, in Protostars and planets IV, ed. V. Mannings, A. P. Boss, & S. S. Russell (Tucson: University of Arizona Press), 1081

Young, A. T. 1967, AJ, 72, 747

Young, A. T., Schorn, R. A., Young, L. D. G., & Crisp, D. 1979, Icarus, 38, 435

Zapatero Osorio, M. R., Béjar, V. J. S., Martín, E. L., Rebolo, R., Barrado y Navascués, D., Bailer-Jones, C. A. L., & Mundt, R. 2000, Science, 290, 103

Zhou, A.-Y., Liu, Z.-L., Du, B.-T. 2001, A&A, 371, 233

Zucher, S., & Mazeh, T. 2002, ApJ, 568, L113

Some physical constants and useful identities

TABLE B.3— Masses

	Value (kg)	$M_\odot$	M_{Jup}	$M_\oplus$
$M_\odot$	$1.989 \cdot 10^{33}$	1	1047	$3.33 \cdot 10^5$
M_{Jup}	$1.899 \cdot 10^{30}$	$9.55 \cdot 10^{-4}$	1	318
$M_\oplus$	$5.974 \cdot 10^{27}$	$3.00 \cdot 10^{-6}$	$3.15 \cdot 10^{-3}$	1
M_{Sat}	$5.68 \cdot 10^{29}$	$2.86 \cdot 10^{-4}$	0.299	95
M_{Nep}	$1.03 \cdot 10^{29}$	$5.85 \cdot 10^{-5}$	0.054	17
M_{Ven}	$4.868 \cdot 10^{27}$	$2.45 \cdot 10^{-6}$	$2.56 \cdot 10^{-3}$	0.81

TABLE B.4— Radii

	Value (km)	$R_\odot$	R_{Jup}	$R_\oplus$
$R_\odot$	696000	1	9.75	109
R_{Jup}	71400	0.103	1	11.19
$R_\oplus$	6378	$9.16 \cdot 10^{-3}$	0.089	1
R_{Sat}	60240	0.087	0.84	9.45
R_{Nep}	25050	0.036	0.35	3.93
R_{Ven}	6051	$8.69 \cdot 10^{-3}$	0.085	0.95

$G = 6.67 \times 10^{-11}$ N m^2/kg^2

1 A.U. = 149590000 km

1 pc = 205615 A.U. = $3.08568025 \times 10^{13}$ km

Agradecimientos

Tras estos años en el IAC, quiero agradecer a las personas que han ayudado a que esta travesía llegue a buen puerto:

En primer lugar, a los causantes de la aventura, Juan y Tim, por enseñarme a navegar en cuanto soltamos amarras, y vigilar constantemente el rumbo, dejándome siempre la libertad de dirigir el timón.

A Hans quiero darle las gracias por mostrarme artes de la navegación. En concreto, por su ayuda en las observaciones, y por tantas conversaciones mantenidas.

A Clara y Teo les agradezco que me hayan permitido utilizar su camarote durante tanto tiempo.

El funcionamiento rutinario de STARE no sería posible sin todo el buen hacer de la gente del observatorio: Álex, Ángel, Antonio (Jiménez y Pimienta), Cristina (Abajas y Díaz), Héctor, Jose Manuel, Miguel, Luis, Orlagh, Paco, Pere, Ruymán, Santiago, Sergio, Teodoro, etc. En los (tantos) momentos en que el instrumento no respondía adecuadamente, conté siempre con el apoyo de la gente de mantenimiento del OT: Enrique, Ignacio, Jesús, Rafa, Ramón, así como de la gente del CAU. A unos y a otros, gracias de corazón por vuestro esfuerzo en hacer que la nave avance.

Many people in Boulder are continuously taking care of STARE: thanks to the work of Don, Alice, Kim, Greg and Ron.

From all the people involved in the TrES network, and the continuous exchange of e-mails, I've learned many things about Science and collaborations. And I feel we are all having fun out of this. Thanks, Dave (Charbonneau and Latham), Francis, Georgi, Guillermo and Ted.

I would also like to acknowledge the people that enjoyed the Venus transit: Wolfgang, Tim, Heike, Helmold, Manolo, Michael, etc.; unfortunately, I am afraid we will have some difficulties to repeat the experience, at least from Tenerife...maybe in another life.

A todos los amigos y familiares que compartisteis, voluntaria o involuntariamente, este viaje conmigo, con charlas y risas en cubierta, o muestras de ánimo en la bodega en los momentos de tempestad, un fuerte abrazo de agradecimiento.

A Mar, gracias por haber hecho que el barco flote.

Roi Alonso Sobrino